

# Towards better Calibration of Space Instrumentation for Measurements of Energetic Neutral Atoms

Inauguraldissertation  
der Philosophisch-naturwissenschaftlichen Fakultät  
der Universität Bern

vorgelegt von

**Jonathan Gasser**

von Langnau i.E.

Leiter der Arbeit  
Prof. Dr. Peter Wurz  
Physikalisches Institut der Universität Bern

## Abstract

Pre-flight instrument calibration is a key step in the development process of new instruments for the observation of Energetic Neutral Atoms (ENA) at low energies in space. This is important in regard of the IMAP-Lo instrument on the upcoming Interstellar Mapping and Acceleration Probe (IMAP) mission, which is currently under development.

The objective of this work was to improve the laboratory calibration capability for low-energy ENA instruments by obtaining more accurate knowledge of the calibration neutral beam fluxes and neutral energy at the instrument calibration. In order to achieve this goal, a laboratory device was developed and tested to measure the neutral atoms flux from a neutral-beam source at low beam energies in an absolute manner, independent of the detection efficiency. By application of the newly developed Absolute Beam Monitor (ABM), the low-energy neutral atom beam source of a calibration facility for space instruments was calibrated in preparation for the calibration campaign of IMAP-Lo at the University of Bern.

To support the IMAP-Lo instrument development, charge-state conversion surfaces were characterized experimentally in a dedicated particle-scattering test facility.



*This work is licensed under a Creative Commons Attribution 4.0 International License.*

*See details of this license at*

<https://creativecommons.org/licenses/by/4.0/>



# Acknowledgments

This Ph.D. project and this thesis would not have been realized without the strong endorsement of numerous good colleagues, close friends, and family. I am endlessly grateful for all the kind words of motivation, moral support, patience and understanding at times when I did not seem to take the time for them; technical, organizational and health difficulties and many more.

The first person to be thanked in the context of this thesis is of course my *Doktorvater* Prof. Peter Wurz: First of all thank you for the trust in me accepting me as his PhD student, but foremost for thank you for your solid supervision and competent support throughout my doctorate during the past 4+ years. I experienced several situations and periods during my PhD that were difficult for me and sometimes cast into doubt my intended path forward because of the external circumstances in the past years. However, fortunately, we always managed to find a solution that worked out – a huge thank you Peter!

Another huge thanks goes to André Galli: I surely learn(ed) a huge lot from him that goes far beyond space plasma physics, and his combined role of colleague and supervisor during this doctorate has been highly valued to me!

Auch möchte ich es nicht versäumen, *my dear friend* Martina Föhn zu danken, die sicherlich nicht ganz unschuldig war daran, dass es überhaupt mit diesem Doktorat geklappt hatte . . .

Weiterhin danke ich meinen Bürokollegen Noah Jäggi und Prof. em. Otto Eugster, dass sie mich über die nicht ganz vier Jahre hinweg mit viel Witz und Verständnis begleitet und ertragen haben.

I further express my heartfelt thank to the following colleagues:

Michela Gargano, for keeping all the IMAP-UniBe-stuff together and -staff connected. The IMAP-folks overseas: Nathan Schwadron, Réka Winslow, David Heitzler, Eberhard Möbius, Eric Hertzberg, Stephen Fuselier, Justyna Sokol, Clark Schiferl, Jonathan Bower, for the many committed and instructive presentations and discussions on all possible aspects of IMAP-Lo.

Daniele Piazza, for the great support in all mechanical engineering affairs of the ABM. Adrian Etter, Joël Gonseth and Raphael Hänggi for the huge support, knowledge, patience and the many hours in the Mefisto lab: with the ECRIS, the diverse

electronics issues, error fixing, vacuum. . . Without you, this thesis project and the ABM would not have been realized and finished. Plus, also thank you for all the nerves it must have cost you throughout the four years . . .

Mathias Brändli and Simon Studer for realizing the parts drawings for the ABM and the CEM device, respectively.

Alexander Stettler, for realization of the ABM power supply.

Thomas Gerber, Claudio Zimmermann and Sebastien Hayoz, for their help in solving all kinds of (re-)occurring electronics problems.

Iljadin Manurung, for his hands-on support whenever it came to fixing (and testing) erratic electronics devices.

Harry Mischler, Sacha Häusler and Martin-Diego Busch for their valuable help in sample ordering, preparation, storage and parts manufacturing.

Valentine Riedo-Grimaudo, Prof. Peter Broekmann, Vitali Grozovski, María de Jesús Gálvez Vázquez and Beatrice Frey for all their help and (more than superficial) knowledge in AFM, SEM, and microscopy surface analyses.

Gaetano Borrini and Urs Geissbühler, for all modern and ancient IT issues, in particular for their support on the data transfer from ILENA.

Dora Zimmerer, Tina Rothenbühler and Franziska Stämpfli for fighting with UPS (and numerous good deeds more!)

Harry and Raphi, again, for all the ‘practical’ stuff in and out of the lab!

. . . and to Andreas, Annette, Antoine, Audrey, Boris, Chantal, Clément, Coen, Daniel, Dănu, Diana, Georges, Hammad, Heinz, HP, Jan, Jannis, Jason, Jonas, Kristina, Lea, Leander, Luca, Marek, Martin, Matthias, Michi, Michu, Mirko, Mohammad, Nicolas, Niels, Nikita, Nora, Parastoo, PeterKe, Philipp, Reto, Rico, Roland, Rolf, Salome, Samuel, Sebastian, Severin, Stefan, Stephan, Susanne, Thierry, Thomas, Timm and Youcef.

Mi gröscht Dank u mi ganzi Achtig u Dankbarkeit gilt mine Eutere, Hans u Barbara.  
Si hei mer aues mitggäh wo's bis dahäre bbruucht het.  
Danke für aues!

Ganz fescht dankä sägeni ou mire Schwoscht Marie-Louise, wo mi so lang u guet kennt wie süsch chuüm öpper;

a Gotti u Fam., wo gäng es offes Ohr une offni Tür für mi hei,

a Götti u Beatrice, Christine, Hanny, Irène u Bani,

a Uschi u Bruno, woni ou ganz viu glehrt ha vone, u womi gäng wider bi Vorhabe unterstützt hei (nid zlescht Pilgerreis und Bewärbige),

u a Marianne u Rémy, zu ihne chönnti fasch zglyche schrybe. Danke!

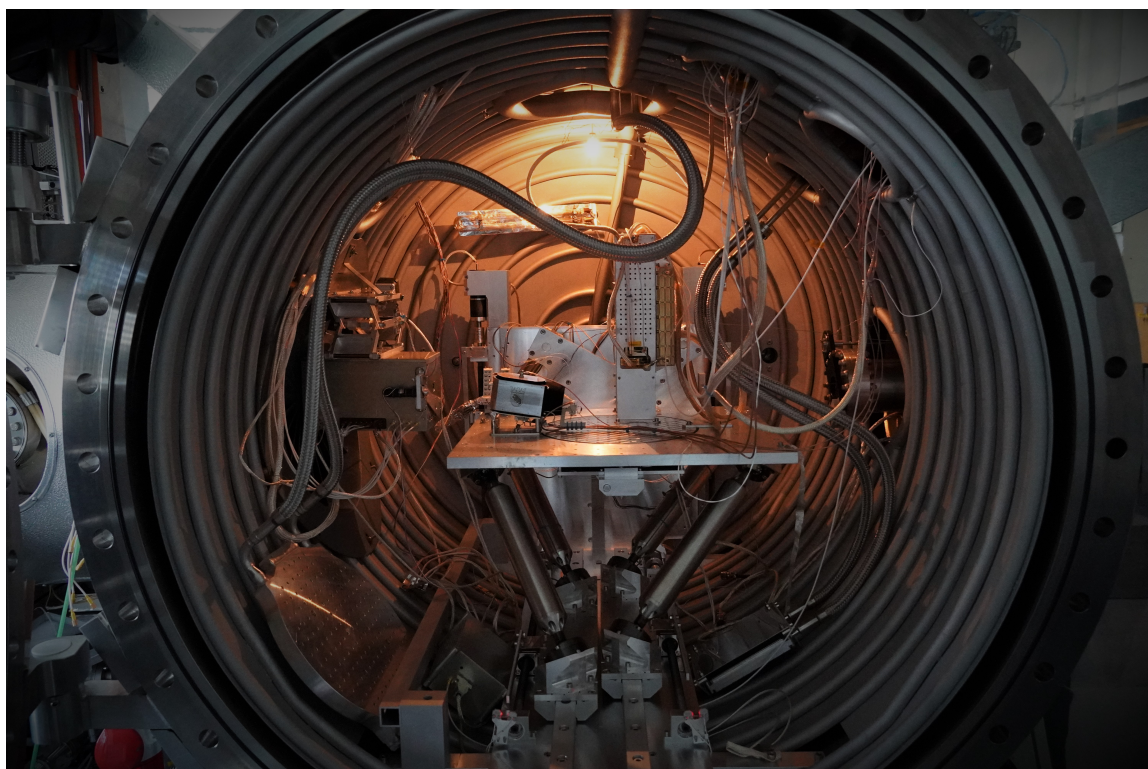
Merci ou viumau a mine guete Fründe u Kollege Fiona, Martina, Claire, Fabi, Marc, Sabrina, Vivi, Luk, Desirée, Colette, Diana, Yves, Armin, Levyn, Alê, Silas u Stefan.

. . . and to anyone I might have forgotten: please send me a message!

# Contents

<b>Abstract</b>	<b>i</b>
<b>Acknowledgments</b>	<b>ii</b>
<b>List of Abbreviations</b>	<b>vi</b>
<b>1. Introduction</b>	<b>1</b>
1.1. Heliosphere . . . . .	1
1.2. Energetic Neutral Atoms . . . . .	4
1.3. Space Missions . . . . .	5
1.4. Thesis Outline . . . . .	7
<b>2. Charge-state Conversion Surfaces</b>	<b>8</b>
2.1. Principles . . . . .	8
2.1.1. Surface Interactions . . . . .	8
2.1.2. Ionization by Surface Scattering . . . . .	10
2.2. Characterization of Conversion Surfaces . . . . .	11
2.2.1. Angular Scattering Distribution . . . . .	12
2.2.2. ILENA Test Facility . . . . .	15
2.2.3. Polar Scattering . . . . .	18
2.3. Surface Materials under Test . . . . .	22
2.3.1. Aluminum Oxide $\text{Al}_2\text{O}_3$ . . . . .	22
2.3.2. Diamond-like Carbon . . . . .	40
2.3.3. Paper: “Cadmium Telluride as a potential conversion surface” . . . . .	62
2.3.4. Strontium Titanate $\text{SrTiO}_3$ . . . . .	70
2.3.5. Zinc Selenide $\text{ZnSe}$ . . . . .	73
2.3.6. Graphene . . . . .	78
2.4. Summary and Outlook . . . . .	80
<b>3. Development of an Absolute Beam Monitor</b>	<b>83</b>
3.1. Motivation . . . . .	83
3.2. Concept and Prototype Characteristics . . . . .	85
3.2.1. Design Concept . . . . .	85
3.2.2. Measurement Concept . . . . .	95
3.3. Electronics . . . . .	98
3.3.1. Data Acquisition . . . . .	98
3.3.2. Noise and Background Suppression . . . . .	101

3.4. Paper: "Absolute beam monitor: A novel laboratory device for neutral beam calibration" . . . . .	102
3.5. Summary and Outlook . . . . .	115
<b>4. Calibration of Low-energy ENA Instruments</b>	<b>116</b>
4.1. Neutral Beam Production . . . . .	116
4.1.1. MEFISTO Calibration Facility . . . . .	117
4.1.2. Surface Neutralizer . . . . .	121
4.1.3. Beam Profiles . . . . .	126
4.1.4. Neon Flux Calibration . . . . .	128
4.2. Paper: "Calibration beam fluxes of a low-energy neutral atom beam facility" . .	130
<b>5. Conclusion</b>	<b>144</b>
<b>Bibliography</b>	<b>146</b>
<b>A. Appendix</b>	<b>151</b>
A.1. Test facility drawing . . . . .	151
A.2. Neutralizer Quick Start Guide . . . . .	151



# List of Abbreviations

ABM	Absolute Beam Monitor
AFM	Atomic Force Microscopy
AC	Alternating Current
AU	Astronomical Unit
CEM	Channel Electron Multiplier (aka channeltron)
CS	(charge-state) Conversion Surface
CVD	Chemical Vapor Deposition
DC	Direct Current
DLC	Diamond-Like Carbon
ECRIS	Electron-Cyclotron Resonance Ion Source
EM	Engineering Model
ENA	Energetic Neutral Atom
ESA	Electrostatic Analyzer
FWHM	Full-Width at Half Maximum
HV	High Voltage
IBEX	Interstellar Boundary Explorer
IENA	Imager for Low Energetic Neutral Atoms (test facility)
IMAP	Interstellar Mapping and Acceleration Probe
IR	Infrared radiation
ISN	Interstellar Neutrals
(L)ISM	(Local) Interstellar Medium
MCP	Micro-Channel Plate
MEFISTO	Messkammer für Flugzeit-Instrumente und Time-Of-Flight (calibration facility for solar wind instrumentation)

ML	monolayer
NS	Neutralizing Surface
PIID	Plasma-Immersed Ion Deposition (coating technique)
PVD	Physical Vapor Deposition
rms	Root mean squared
RPA	Retarding Potential Analyzer
SS	Start Surface
SW	Solar Wind
SwRI	Southwest Research Institute (San Antonio TX, USA)
TDC	Time-to-Digital Converter card
ToF	Time of Flight
TS	Termination Shock
UHV	Ultra-High Vacuum
UV	Ultraviolet radiation
VOC	Volatile Organic Compounds

# 1. Introduction

---

Space, the whole universe –  
I know no better place  
To find new physics.

Eugene Parker

---

Space is not empty. The dark void between galaxies is not truly empty. Neither is the interstellar space between individual stars in our galaxy, the Milky Way. In fact, interstellar space is filled with a dilute, partly ionized gas termed the *Interstellar Medium* (ISM).

## 1.1. Heliosphere

The Sun, and with it the entire solar system, moves through the surrounding Interstellar Medium at a speed of about 26 km/s. This is not the solar orbital velocity on its orbit around the galactic center (which is roughly 220 km/s), but it is the solar system's relative motion with respect to the Interstellar Medium's rest frame. On its way through the ISM, the Sun clears a gigantic bubble into the ISM, the *heliosphere*, by emission of a steady particle stream, the *Solar Wind*. An illustration of the heliosphere is shown in Fig. 1.1.

**Solar Wind.** The interplanetary space in our solar system is in fact not empty, but is suffused with a dilute medium of light atomic gases, ions and electrons. The dominant constituents of this medium is made up of the Solar Wind (SW), a constant stream of charged particles flowing outwards in all directions radially away from the Sun at supersonic speeds. The existence of a Solar Wind was first predicted by Eugene Parker in 1958 and was soon after confirmed by spacecraft Luna 1 and Mariner 2. The Solar Wind originates from the Sun's corona (the beautiful gleaming crown one can see during a total eclipse), where matter is in a state of almost completely ionized plasma, at temperatures of a few million Kelvin.

The Solar Wind, similar to the Sun's corona, is composed predominantly of protons, electrons and a few percent of alpha particles ( $^4\text{He}^{2+}$ ) at energies from 500 eV – 10 keV. Its density decreases with the square distance from the Sun and is around  $3 - 10 \text{ cm}^{-3}$  at 1 Astronomical Unit (1 AU: Sun-earth distance). The Solar Wind speed varies with solar latitudes and the solar cycle; it is around 400 km/s near the ecliptic and amounts up to 750 km/s at high solar latitudes and over the poles. The SW speed distribution is thus aligned with the dipole solar magnetic field.

Despite the very high temperatures and thermal velocities at the Sun's corona, these are not sufficient to explain the high velocities of Solar Wind particles. Another acceleration mechanism, possibly by magnetic reconnection processes in the solar magnetic field, is involved in accelerating the Solar Wind to supersonic speeds. Furthermore, the Sun's magnetic field lines are frozen-in to the Solar Wind, hence the magnetic field is carried radially outward. In combination with the rotation of the Sun, this creates a global spiral structure of the magnetic field in interplanetary space, the Parker Spiral.

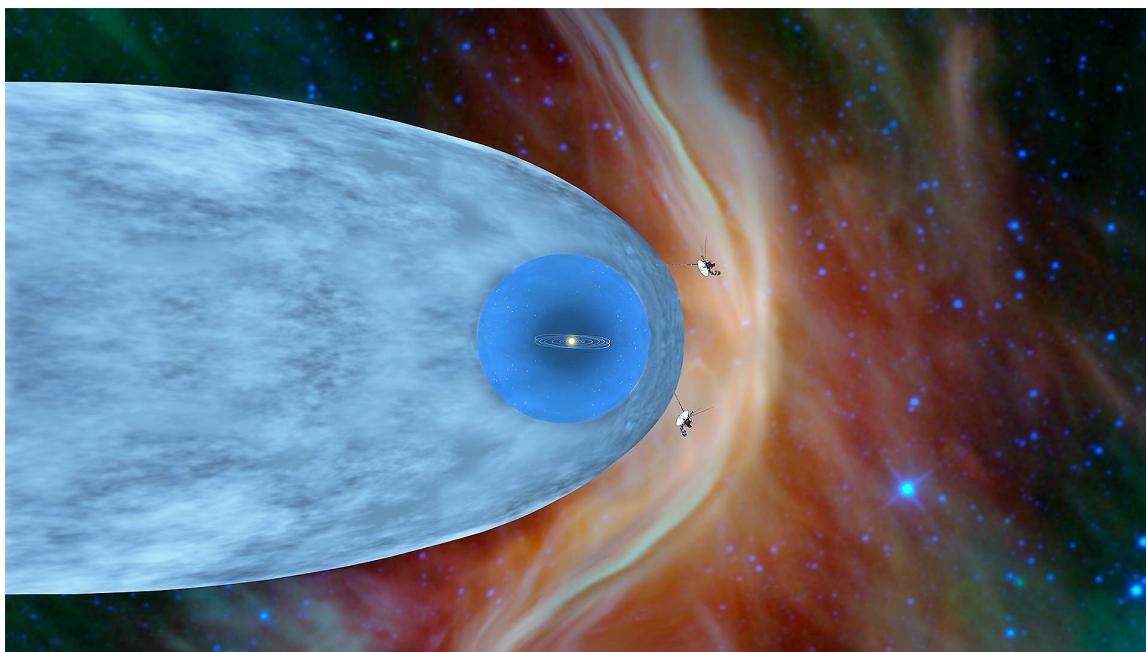


Figure 1.1.: Illustration of the heliosphere. At the center you see the Sun and solar system planets, surrounded by the supersonic Solar Wind (blue) inside the Termination Shock boundary, the heliosheath (fair blue), and the heliopause boundary to the Interstellar Medium (background). The Sun's motion is to the right side (nose), where a bow wave forms in the ISM (light red). Positions of V1 and V2 spacecraft in interstellar space are added. [Image credit: NASA.]

**Heliosphere.** The supersonic Solar Wind extends out through the solar system as far as about 90 AU until the SW speed drops below the sonic point. (For comparison, the outermost planet, Neptune, is 30 AU away from the Sun.) This is where a steady shock front builds up,



the *Termination Shock* (TS). Besides the transition from the upstream supersonic speed to a subsonic plasma flow outside, the downstream Solar Wind is also much denser and warmer after the TS than in front. The Termination Shock has a spheroidal global shape. On the outside, the shocked Solar Wind continues its outward propagation across a region called the *heliosheath*, until it reaches the final boundary region of our solar system towards interstellar space in terms of space plasma, the *heliopause*.

**Heliopause.** At the heliopause, roughly 120 AU from the Sun, the solar wind is stopped by the Local Interstellar Medium (LISM), with which the SW is in pressure balance. The heliopause boundary is marked by a sharp decrease in the flux of solar protons, and an increase in incoming interstellar atoms and ions as well as Galactic Cosmic Rays, which are highly energetic particles or photons originating from distant sources within our galaxy. At the heliopause, the solar magnetic field carried along by the Solar Wind is in contact and mutual interaction with the interstellar magnetic field. Thus, the heliopause marks the boundary of our solar system towards interstellar space.

**Heliosphere structure.** At present, it is not determined what the global shape of the heliosphere looks like. Several heliospheric models exist [19], predicting a spherical-closed, or a croissant-shaped heliosphere with two lobes extending from the solar polar regions, which are bent back in anti-ram direction by SW interactions with the ISM and interstellar magnetic fields and end up in turbulent plasma motion [25]. The currently most popular global heliosphere picture predicts a comet-like shaped heliosphere directed towards the direction of the Sun's motion through the ISM, the *nose*. This is the celestial region where the heliopause is closest in from the Sun. At the nose, the pressure balance and magnetic field interaction at the heliopause cause the slow Solar Wind to be deflected and to stream along this boundary downwards to the tail of the heliosphere. At the same time, the LISM in front of the nose is also perturbed and compressed by the SW pressure, so that a bow wave piles up at the front. At the opposite celestial direction, the heliosphere extends in an elongated heliotail, with few details known from measurements so far, but it is suggested that the heliopause is much further away from the Sun than towards the nose. It is also not clear whether a heliopause boundary also exists in the heliotail, at much larger distance from the Sun, or if the heliotail remains 'open', and the ISM and Solar Wind plasma ultimately mix up with no distinct interaction boundary.

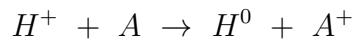
It is confirmed, though, that the heliosphere as a whole is not static at all: in contrary, its size, plasma properties and likely the shape change dynamically over time, e.g., with changing solar activity over a solar cycle and perhaps also due to local conditions in the ISM. The heliosphere is not a specialty of our Sun: astrospheres surrounding other stars have been imaged, in particular the nose region, suggesting that astrospheres are a common feature of stellar plasma interaction with its interstellar surroundings.

**Interstellar Medium.** The ISM is interspersed with an interstellar magnetic field. The ISM is composed of molecular, atomic and ionic gas (99 %) as well as dust ( $\sim 1$  %), cosmic rays

and electromagnetic radiation. The most abundant gaseous ISM compounds are hydrogen and helium (about 9 %), with around 0.1 % of heavier elements. The ISM gas density is in the order of  $0.1 \text{ cm}^{-3}$ .

## 1.2. Energetic Neutral Atoms

Energetic Neutral Atoms (ENAs) are fast electrically neutral single atoms travelling freely through space. Light atomic species like hydrogen, helium and oxygen are very common, but also deuterium, neon, carbon, sulfur, sodium, and other heavier elements can be found depending on their source. ENAs are created from charge exchange interactions of space plasma ions with slow neutral ambient background gas particles. For example, a fast proton picks up an electron from a neutral atom at relative rest:



The neutralized ion largely retains its energy-momentum, constituting now an ENA. Plasma ions and electrons are highly affected by magnetic fields in space: they are accelerated and, due to the Lorentz force, start to gyrate about the magnetic field lines. Thus, they are confined ('trapped') into the magnetic field configuration. ENAs, as opposed to ions, are not affected by electromagnetic forces and thus propagate through space at very large distances, unperturbed by the present magnetic field, just subject to the gravitational potential. Therefore, ENAs can transport information about their source plasma population such as the distribution, density and composition to a remote observer, information that would otherwise not be accessible from a distance. This is what makes ENA detection in space an interesting and important observation technique. ENA can be observed in a wide range of energies, from as low as 10 eV up to 1 MeV.

**ENA sources.** Sources of ENA can be found almost everywhere in space: fast solar wind ions are neutralized in charge-exchange collisions to form heliospheric ENAs, predominantly hydrogen. The plasma population of planetary magnetospheres is another source of ENA, especially hydrogen, helium and oxygen. In Jupiter's magnetosphere, sulfur is also present, which originates from intense volcanic activity on the innermost Galilean moon, Io. Moreover, solar wind interactions with planetary atmospheres or the surface can also produce an ENA population around the planet or moon.

Finally, as the Sun moves through interstellar space, interstellar neutral atoms (ISN) from the Local Interstellar Medium can penetrate the heliopause and travel on hyperbolic free-fall trajectories into the (inner) solar system, where they can be observed as a distinct population of 'ENA'. As they start off all at roughly the same relative velocity, ISN species show a characteristic observed energy depending on their atomic mass and apparent incidence direction. The major ISN component is also hydrogen, accompanied by some fraction of helium, oxygen, deuterium, neon, and further trace species. Particularly, the determination of the D/H abundance ratio in the ISM by energetic neutrals observations is an outstanding scientific question related to Big Bang nucleosynthesis.

**ENA Imaging.** Over the last two decades, ENA imaging has become an important observation method in space plasma and planetary science. Remote detection of ENAs allows to observe and analyze source ion populations which would otherwise not be accessible. Nevertheless, imaging observations of ENAs are still challenging by the fact that the observable ENA fluxes are often very low, and the detection efficiencies decrease below the percentage level at low energies. Furthermore, electrically neutral particles cannot be directly analyzed by ion-optical means, so an efficient ionization technique suited for space applications need be in place in an ENA imaging instrument. At energies below 1 keV, the widest used ionization method to date is via surface scattering at grazing incidence angles. Review papers on ENA imaging were written by Gruntman [16] and Wurz [51].

### 1.3. Space Missions

Much of what is known today about the heliosphere and planetary magnetospheres has been learned from data from spacecraft on (inter-)planetary missions. Here is a selection of important missions that contributed to our knowledge of the heliosphere.

**Voyager.** The two NASA spacecraft Voyager 1 (V1) and Voyager 2 (V2), launched in 1977, were originally built to investigate the giant planets and the outer solar system. In 2004 and 2007, respectively, Voyager 1 and 2 crossed the Termination Shock, and in 2012, V1 was the first human-built object to cross the heliopause and to enter into interstellar space, followed by V2 in 2018. Both spacecraft left the solar system in the direction of the heliosphere's nose. Each probe carries a particle detector, cosmic ray detector, and a magnetometer on board, which are still in operation after 45 years. The data on space plasma and interplanetary magnetic field obtained through V1 and V2 have made great contributions to our understanding of the heliosphere. This makes the Voyager twins two of the most famous spacecraft and of the most successful space missions of all times. V1 is currently (end of 2022) 158.5 AU away from the Sun, which makes it the most distant human-built object ever. Both spacecraft are expected to continue operations for another few years, making their way through interstellar space.

**Ulysses.** The joint ESA/NASA spacecraft Ulysses was launched in 1990 to investigate the solar corona and magnetic field, Solar Wind, plasma waves and cosmic rays. It was sent to Jupiter for a close fly-by that brought the spacecraft on a high-inclination orbit around the Sun, which allowed observations above the Sun's polar regions. Ulysses remained in operation for almost two decades.

Several planetary missions have had a dedicated ENA instrument onboard the spacecraft, for example on the IMAGE mission to study Earth's magnetosphere, the CENA/SARA instrument by ESA on the Indian lunar mission Chandrayaan-1, the ASPERA instrument on ESA's Mars Express and Venus Express, and the LENA instrument onboard BepiColombo, which is currently on its way to Mercury. The JUICE mission by ESA, to be launched in April 2023 to

explore the Jovian system, also has an ENA imaging instrument, JNA, contained in its Particle Environment Package suite.

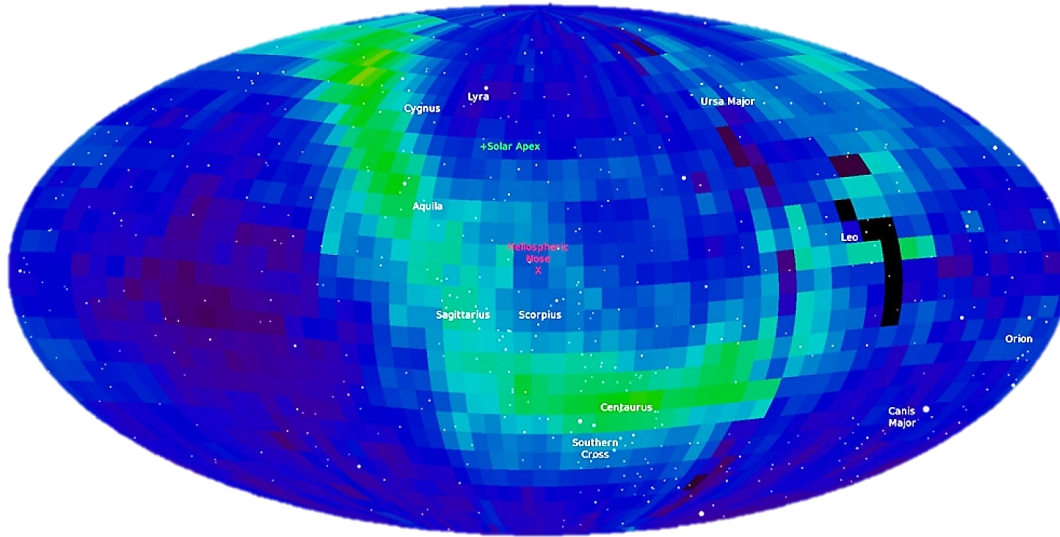


Figure 1.2.: Celestial map of the global heliospheric ENA intensity distribution as observed by IBEX. The heliosphere's IBEX 'ribbon' is clearly visible (green). [Image credit: NASA.]

**IBEX.** The *Interstellar Boundary Explorer* (IBEX) mission by NASA was dedicated to the remote observation of heliospheric ENAs and interstellar neutrals. Launched in 2008, IBEX entered a highly eccentric orbit around Earth, which brings it out of the terrestrial magnetosphere for unperturbed ENA observations. IBEX has two ENA cameras on board, IBEX-Lo and IBEX-Hi, which cover complementary energy ranges. Originally planned to last for two years, IBEX has performed observations over one full solar cycle, and is expected to operate for another few years.

Already until today, IBEX has been a great success, leading to more than 100 research articles. In particular, global maps of the heliospheric ENA distributions at several energy bands were produced with the two IBEX ENA instruments. This has led to the discovery of the IBEX 'ribbon', a narrow band of high ENA intensities across the heliospheric nose region (see Fig. 1.2). This unanticipated feature of our heliosphere is clearly visible at a wide range of ENA energies.

Furthermore, the long mission extension has allowed to study the temporal evolution of the heliosphere over the solar cycle.

**IMAP.** Due to the huge success of IBEX, a successor NASA mission, the Interstellar Mapping and Acceleration Probe (IMAP), is currently under development, with launch scheduled for early 2025. The IMAP spacecraft will be placed at the L1 libration point between the sun and Earth, from where it will observe the global structure of the heliosphere and its interaction

with the interstellar medium in much more detail. For this purpose, a suite of ten scientific instruments are onboard, including solar wind electron and ion detectors, a heliospheric dust detector, a UV-light sensor, a vector magnetometer as well as three dedicated ENA imaging instruments (IMAP-Lo, IMAP-Hi, IMAP-Ultra) for detecting and analyzing ENA at increasing energy ranges. With its scientific instruments arranged around the spacecraft's mantle, IMAP will be re-pointed towards the sun periodically. As the spacecraft is spinning about its sunward-pointing axis, each instrument scans over a great circle perpendicular to the position axis. This allows the instruments to observe the entire sky once every half a year.

**IMAP-Lo.** The low-energy ENA imaging instrument onboard IMAP has been developed at the University of New Hampshire in collaboration with the Southwest Research Institute and the University of Bern. Its development has profited much from flight-heritage knowledge of IBEX-Lo, as its basic instrument concept and structure is very similar. As an additional feature, the IMAP-Lo sensor will be installed on a pivot platform, allowing for a variation of the instrument's observation pointing angle. This will enable IMAP-Lo to keep track of the interstellar neutrals incident into the inner solar system over a larger part of the year. The IMAP-Lo instrument calibration using low-energetic laboratory neutral atom beams will be carried out in 2023 in the MEFISTO calibration and test facility at the University of Bern.

## 1.4. Thesis Outline

The scope of this thesis is the development and calibration of scientific instruments for the detection and analysis of low-energy ENA in space. The laboratory work presented herein aims at improving the calibration capabilities and instrument performance characterization for ENA cameras, particularly in the low-energy range.

Chapter 2 focuses on the experimental characterization of charge-conversion surfaces used for particle ionization inside ENA instruments. In Chapter 3, the development of a novel Absolute Beam Monitor (ABM) laboratory device for the absolute flux calibration of neutral atoms beams is described. The production of low-energetic ENA beams for ENA instrument calibration in a dedicated test facility (MEFISTO) is covered in Chapter 4. The calibration of laboratory neutral atoms beam fluxes by application of the ABM is included here as well.

## 2. Charge-state Conversion Surfaces

---

God has made the bulk  
Surfaces were invented  
by the devil, though

*attributed to Wolfgang Pauli*<sup>1 2</sup>

---

### 2.1. Principles

#### 2.1.1. Surface Interactions

The interaction of energetic particles (be they photons, ions, or neutral atoms) with the surfaces of a bulk material is an interesting and rich field of research by itself: surface science, which combines important aspects of physics as well as chemistry. In reality, as opposed to surfaces in mathematics, the *surface* of a solid body is not infinitely thin but it rather refers to a boundary region between the bulk (solid or liquid) on one side and the void or gas phase on the other side. Focusing on solid materials, this surface region typically comprises a few to few tens of atomic layers. The surface region can and usually will have quite different (mechanical, thermodynamic and electrical) properties than the bulk, precisely because the continuous crystal lattice of the solid ends there. A large variety of phenomena are taking place at surfaces, such as reflection and refraction of light, adsorption of molecules, on-surface catalysis of chemical reactions, adhesion of liquid droplets or other solids on surfaces etc. Not at least the photoelectric effect, first explained by Einstein, is intrinsically a surface phenomenon.

---

<sup>1</sup>He is quoted in “*Fractals, Chaos, Power Laws*” by R. M. Schroeder, 1991, p. 230, as:

“*God made the bulk; surfaces were invented by the devil.*”

<sup>2</sup>A German version of this quote is found in the novel “*Gehen, ging, gegangen*” by J. Erpenbeck:

“*Gott schuf das Volumen, der Teufel die Oberfläche.*”

Many surface analysis techniques (electron and X-ray diffraction, ion scattering, scanning tunnelling microscopy, photo-electron spectroscopy) [40] aim at making use of the particle-surface interactions to probe properties of the surface of the bulk material, such as its atomic and electronic structure. These are typically operated under ultra-high vacuum conditions. Other techniques, such as Atomic Force Microscopy (AFM), were specifically invented and developed to investigate the surface topography by electromagnetic interaction.

On the other hand, particle-surface interaction can also be used to detect and analyze the incident particles, or modify their properties: energetic neutral atoms (ENA) can be charged electrically by surface scattering. In fact, reflecting atoms at a highly polished crystal surface at grazing incidence angle (typically  $< 10^\circ$ ) has become the one well-established detection technique in space research for ENA below about 1 keV [51]. As ENA are electrically neutral, they need to be electrically charged by scattering off the so-called charge-state conversion surfaces (CS) prior to their further mass and energy analysis, and detection by electronic means.

**Ionization.** The basic working principle of surface ionization is as follows: ENA impinge the CS with some kinetic energy  $E_0$  at grazing incidence angle  $\alpha$  relative to the surface plane, then interact with the crystal surface and are reflected off the CS in a direction given by a polar angle  $\theta$  and azimuth angle  $\phi$ . Due to the surface scattering interaction, some fraction of the reflected atoms become positively or negatively charged while the rest of them leave the CS in electrically neutral state.

Given the power, weight and cost constraints on any spaceborne instrument, and the fact that the incidence direction and kinetic energy of the ENA are often of interest, a passive charging method is most economic with the available resources. Thus, traditional techniques used in laboratory ion sources such as electron-impact ionization or field ionization are not suitable. Surface ionization is an alternative which meets the mentioned criteria for space applications. ENA with energies above a few keV can be ionized by letting them pass through a micrometer-thin carbon foil [1, 15]. However, the ENA transmission of such carbon foils drops dramatically below about 1 keV/nuc. Thus this method is essentially ruled out for low-energy ENA detection, while charge-conversion surfaces remain a viable technique in the energy range much below 100 eV [20].

**Neutralization.** Grazing-angle surface scattering can be used for neutralization of an incident ion beam, as there is generally a dominant neutral component in the scattered particle beam. This process was applied in the development of a surface neutralizer to produce a low-energy laboratory ENA beam [48] (see Section 4.1.2).

**Secondary electrons.** And the scattering interaction of atoms or ions with the surface can also lead to the ejection of electrons from the surface material ([5, 17] and refs therein). This so-called *secondary electron emission* is also used to detect and analyze incident particles, e.g., time-of-flight measurement from combined registration of (fast) accelerated electrons and the (slower) atoms. I applied this process in the development of an Absolute Beam Monitor for low-energy laboratory ENA beams (see Chapter 3).

**Sputtering.** Besides electrons, incident atoms can also knock off adsorbed particles from the surface [37, 38, 41]. On typical CS in spaceborne ENA instruments these are mostly H and O components, presumably from an adsorbed water layer on the surface (see below). Sputtered atoms can be neutral as well as positively or negatively ionized. It is generally difficult to distinguish the direct-scattered from the sputtered components in the scattered particle beam (see Section 2.2.2), particularly unless an accurate energy measurement method is available. On the other hand, detection of sputtered negative ions is the primary mechanism how low-energy noble gas ENA can be detected with instruments such as IBEX-Lo or IMAP-Lo, since He and Ne (and Ar) do not form stable negative ions.

### 2.1.2. Ionization by Surface Scattering

A thorough introduction into the topic of low-energy ion interactions with surfaces can be found in Niehus et al. [24].

The detailed physical mechanisms of charge conversion by grazing-angle surface scattering are still not fully understood theoretically. Even though several scattering models exist to describe ion interaction with certain types of crystal surfaces [4, 13, 49], it is difficult to explain the whole set of observations related to atom surface scattering and related charge exchange. For example, it is not clear which surface materials, composition and structure are best suited for negative charge-conversion of atoms. Nor is ultimately determined which ones are the relevant properties of surfaces to (re-)produce efficient negative ionization and narrow angular scattering distributions.

The situation is complicated by the fact that, unlike in actual surface science, realistic conversion surfaces never be clean on atomic level, and are rarely pristine perfect surface lattices: foreign atoms impurities, lattice defects at atomic scales, contamination by adsorbed molecules (e.g., organic compounds) or even dust particles, and an adsorbed water layer are permanently omnipresent in space instrumentation applications.

For single crystals, depending on the material, it is challenging to cut and polish a surface along one primary lattice plane over a range of  $10^8$  atomic rows. Single-crystal silicon wafers are industrially manufactured at ultra-smooth surface level (roughness below 1 nm *rms*). However, pure Si has shown not to be very efficient in ionizing neutral atoms. Therefore a suitable coating by a thin film is often applied unless a single-crystal surface of a different material is used. The thin film deposition generally alters the surface structure and tends to increase surface roughness, though. Coatings of a few tens of nanometers are usually sufficient for scattering and charge conversion of low-energetic ENA, as these do not penetrate more than a few atomic layers into the surface material at the grazing incidence angles.

Second, conversion surfaces cannot be kept under constant vacuum conditions. Even in clean environment, it is possible that some ambient dust deposits on the surface during transport, preparation and installation. It is therefore very important to clean the samples before use, rinsing with alcohol, propanol and dry N<sub>2</sub> gas. Any physical contact of tools or tissues with the surface should be avoided.

Third, during laboratory testing as well as in operation in the spacecraft environment, a residual gas pressure of around  $10^{-7}$  mbar is assumed to persist more or less indefinitely, even



with a very good vacuum system. This leads to the presence of an adsorbed  $\text{H}_2\text{O}$  layer of a few ML which cannot be avoided, since  $\text{H}_2\text{O}$  is a major component of the residual gas at this vacuum level. This is in contrast with the typical ultra-high vacuum (UHV) conditions under which actual surface science laboratory experiments are carried out (about  $10^{-10}$  mbar). Last, the adsorption of volatile organic carbon (VOC) compounds may deteriorate the conversion surface. Riedo et al. [29] have shown that, in combination with ultraviolet (UV) light, these may react chemically with the surface, leading to permanent alterations and likely reduced conversion performance. These considerations are summarized in a contamination control report by A. Galli, J. Gasser, and P. Wurz [9].

## 2.2. Characterization of Conversion Surfaces

One approach of circumventing these hindrances is characterizing experimentally the charge-conversion and scattering properties of different prepared conversion surface samples. In this approach the concrete surface interaction is normally dealt with as a black-box and the CS properties are described by a set of experimental parameters: For applications in ENA imaging space instrumentation, the key properties to judge on the suitability of a sample CS are a high ionization efficiency combined with a narrow angular scattering distribution.

The number of, say, negative (positive) ions in relation to the total number of reflected atoms is the negative (positive) ion yield  $\eta_-$  ( $\eta_+$ ). It generally depends on the CS material and structure, the incident atom species  $m$ , charge state  $q$ , kinetic energy  $E_0$  and incidence angle  $\alpha$ :

$$\eta_- = \eta_-(m, q, E_0, \alpha) .$$

The angular scattering distribution  $p(\phi, \theta)$  of a given CS is a function of ENA species, kinetic energy and incidence angle as well:

$$p(\phi, \theta) = p(\phi, \theta; m, E_0, \alpha) .$$

Where  $\phi$  is the azimuthal scattering angle (tangential to the surface), and  $\theta$  is the polar scattering angle (off the surface plane). Instead of always reporting the full angular scatter distribution, the ion-scattering behavior of a CS material or sample is characterized by reporting the three key parameters: negative ion yield  $\eta$  and the full-width at half maximum (FWHM) of the angular scattering distribution in both polar and azimuthal direction. These are usually measured for a few species of interest at a given incidence angle, within an appropriate energy range.

The situation in scattering on conversion surfaces is summarized as follows:

Typically, just a subset of these parameters are investigated at once, while the rest of them are either kept constant or cannot be measured at the same time. The Imager for Low Energetic Neutral Atoms (ILENA) experiment at the University of Bern is a dedicated test facility that was designed for characterizing the scattering properties of different CS in terms of the negative ion yield and angular scattering distribution resulting from various atom or ion species depending on their incidence angle and kinetic energy [44].

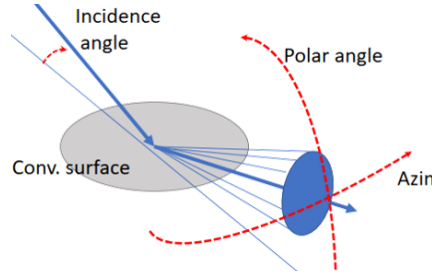


Table 2.1.: Experimental parameters of charge conversion by surface scattering.

Incident atoms:	Surface:	Emergent atoms:
<ul style="list-style-type: none"> <li>• Ion species</li> <li>• Charge state</li> <li>• Kinetic energy</li> <li>• Incidence angle</li> </ul>	<ul style="list-style-type: none"> <li>• Surface material</li> <li>• Crystal structure</li> <li>• Surface roughness</li> <li>(•) Coating thickness</li> <li>(•) contamination</li> </ul>	<ul style="list-style-type: none"> <li>• Yield of (negative) ions</li> <li>• Angular scattering distribution</li> <li>(•) Energy distribution</li> <li>(•) sputtered products</li> </ul>

In the ILENA experiment (Section 2.2.2), one surface sample is characterized using  $H^+$ ,  $O^+$  ion beams at fixed incidence angle (though it can be varied) and a few energy steps, and the negative ion yield and angular scattering distribution are measured while the energy distribution in the scattered particle beam cannot be determined. After all, intrinsic surface properties such as the surface roughness are determined with an independent method (e.g., AFM scanning). While this may seem very limited aspects, it allows experimental characterization of the most relevant CS properties for application in space instrumentation, and under representative conditions. Hence, it also allows a direct comparison of different samples and different surface materials.

### 2.2.1. Angular Scattering Distribution

The quantitative description of angular scattering requires the definition and use of an appropriate spherical coordinate system. It is illustrated in Figure 2.1. As the surface interaction of an ion or atom is a localized process, define first the Cartesian coordinate system  $(x, y, z)$  with respect to the surface plane at the incidence point  $P$ :

$z$ : the surface normal direction  $\vec{z} = \vec{n}$ .

$x$ : the direction of propagation  $\vec{v}$  of the incident particle, projected onto the surface plane:

$$\vec{x} = \frac{\vec{v} - (\vec{v} \cdot \vec{z}) \vec{z}}{|\vec{v} \times \vec{z}|}$$

$y$ : the direction perpendicular to both  $x$  and  $z$ , such that  $(x, y, z)$  is a right-handed normal coordinate system:  $\vec{y} = (\vec{z} \times \vec{x})$

The surface normal  $\vec{n}$  and the incidence direction  $\vec{v}$  span a plane  $\Pi$  that is normal to the surface plane.  $\vec{y}$  lies within the surface plane and is normal to  $\Pi$ .

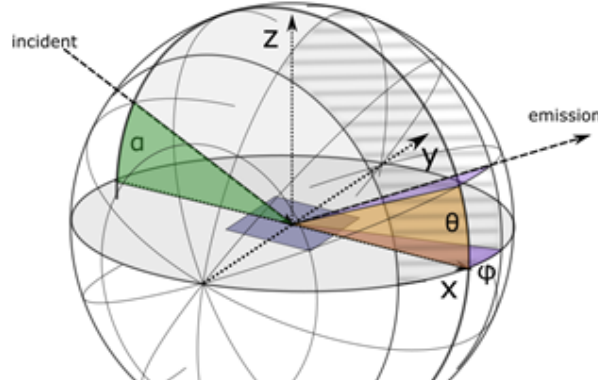


Figure 2.1.: Coordinate system and notation. Trajectory of one example particle is shown, impinging from the left ( $\alpha$ ) and being reflected off the surface (dark square) to the right ( $\theta, \phi$ ). The shaded region on the sphere shows the angular range that can be covered by the ILENA detector.

Based on this, we define the spherical (directional) coordinate system as follows, using azimuth angle  $\phi$  and polar angle  $\theta$ :

The polar angle  $\theta$  gives the elevation from the surface plane along the plane  $\Pi$  spanned by the surface normal and the incidence direction. It runs from 0 (limit case of surface coplanar forward scattering) to  $180^\circ$ . The azimuthal angle  $\phi$  quantifies the deviation of the outgoing particle's flight direction from the plane  $\Pi$  ("sideways scattering"). The polar axis of this spherical coordinate system is thus  $y$ . The particle's incident angle  $\alpha$  is the angle between the incident direction and the surface:

$$\cos(\alpha) = \frac{(\vec{v} \cdot \vec{x})}{|(\vec{n} \times \vec{v})|}$$

The direction going back to where the incident particle came from has thus coordinates  $\theta = \pi - \alpha$ ,  $\phi = 0$ . An ideally specularly scattered atom with incidence angle  $\alpha$  has azimuth angle  $\phi = 0$  and polar angle  $\theta = \alpha$ . Actual scattered particles show a broader angular distribution. This distribution represents both the set of directions of many scattered particles, and – if properly normalized – the scattering direction probability distribution of one particle of given species, energy, and incidence angle.

The angular direction distribution of the scattered ion or atom beam is generally dependent on atomic species, beam energy and incidence angle. The distribution is symmetric in the azimuth angle, while in polar direction the distribution is skewed: it peaks close to specular reflection with a steep slope towards small polar angles and a flat tail towards high-elevation emission angles. As a typical generic approach, the scattering distribution is fitted by independent azimuth and polar distribution functions,

$$p(\phi, \theta) = p_1(\phi) \cdot p_2(\theta)$$

The azimuth distribution is symmetric about the zero-deflection angle, thus can be fitted using

a Gaussian distribution function:

$$p_1(\phi) = A \exp \left\{ -\frac{\phi^2}{2\sigma^2} \right\} \quad (2.1)$$

with amplitude  $A$  usually normalized to one, and FWHM  $\Delta_\phi = (2\sqrt{2\ln(2)})^{-1} \sigma$ .

**Polar angular scatter distribution fit functions.** For the polar distribution, an Exponentially Modified Gaussian (EMG) is often chosen as fit function [23], which is the convolution (\*) of a Normal  $\mathcal{N}(x)$  with an Exponential distribution function with decay parameter  $\tau$ :

$$\begin{aligned} \text{EMG}(x) &= \mathcal{N}(x; \mu, \sigma) * \text{Ex}(x; \tau) \\ &= A' \frac{\sigma}{\tau} \exp \left\{ \frac{1}{2} \left( \frac{\sigma}{\tau} \right)^2 - \frac{x - \mu}{\tau} \right\} \cdot \text{erfc} \left\{ \frac{1}{\sqrt{2}} \left( \frac{\sigma}{\tau} - \frac{x - \mu}{\sigma} \right) \right\} \end{aligned} \quad (2.2)$$

where  $\text{erfc}(x)$  is the complementary error function. For fitting and modeling purposes it is often convenient to rewrite the EMG, normalized to one at peak location  $\theta = \hat{\theta}$ , as

$$\text{EMG}(\theta) = \frac{\exp \{ -(\theta - \hat{\theta})/\tau \}}{\text{erfc}(\psi)} \cdot \text{erfc} \left\{ \psi - H_{-1}(\psi) \frac{\theta - \hat{\theta}}{\tau} \right\}, \quad (2.3)$$

where  $H$  is the first Hermite polynomial,  $\psi$  is an asymmetry parameter, and  $\tau$  scales the distribution width. However, other fit functions have been proposed and applied, such as the Log-normal distribution  $\text{LN}(x)$  [14] ( $\ln(x)$  is the natural logarithm):

$$\text{LN}(x) = \frac{A}{x} \exp \left\{ -\frac{1}{2\sigma^2} (\ln(x) - \mu)^2 \right\} \quad (2.4)$$

We can rewrite the Log-normal in terms of the distribution FWHM  $\Delta_\theta$ , the peak location  $\hat{\theta}$  and the zero intercept  $b$ , with amplitude normalized to  $A = 1$  as

$$\text{LN}(x) = 2^{-q(\theta)^2}, \quad \text{where } q(\theta) \doteq \frac{\ln \left( \frac{\theta - b}{\hat{\theta}} - 1 \right)}{\ln \left( \frac{\Delta_\theta}{2\hat{\theta}} + \sqrt{\left( \frac{\Delta_\theta}{2\hat{\theta}} \right)^2 + 1} \right)} \quad (2.5)$$

Another option for a fit function is the Erlang distribution of the form

$$\text{Erl}(x) = A(x - d)^c e^{-b(x-d)} \quad | \ x > d \quad (2.6)$$

Any and all of the fit functions, EMG, Log-normal and Erlang, were chosen just because they represent the measured angular distributions well, without any underlying physical interpretation or justification. All three polar distributions exhibit the following necessary properties: Normalizable skew distribution, steep flank going to zero at small polar angles, and distribution tail at large polar angles. It becomes clear, though, that the EMG cannot be the true underlying distribution function, as it would predict nonzero probability of negative polar angles, which is physically not possible (atoms cannot scatter off the CS *into* the CS).

The accuracy of these three functions in fitting the polar scatter distributions off CS is checked and compared in Section 2.2.3.

### 2.2.2. ILENA Test Facility

The Imager for Low Energetic Neutral Atoms (ILENA) is a test facility at the University of Bern, dedicated to the experimental testing of charge conversion surface samples regarding their ionization behavior and angular scattering properties of atoms at grazing incidence angle. The ILENA experiment setup has repeatedly been described in great detail elsewhere (see Gasser et al. [11], Wahlström et al. [45] and references therein). Therefore I am going to describe ILENA here only briefly. Some more details can also be found in Section 2 of the test report on  $\text{Al}_2\text{O}_3$ , see Section 2.3.1. A top view image of the ILENA setup is shown in Fig. 2.2. A schematic of the ILENA setup is also shown in Fig. 1 of the IMAP report on DLC surfaces, Section 2.3.2.

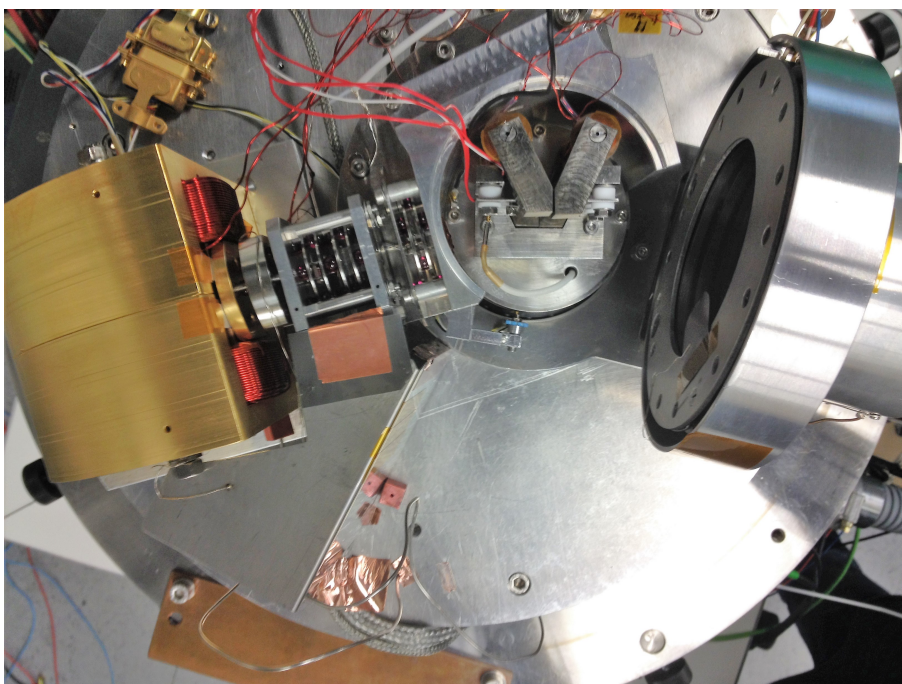


Figure 2.2.: Top view photograph of the ILENA experiment setup. The sector magnet (gold), beam guiding ion optics, sample holder with thermal wiring (red cables) and SEL coils, and the detector are clearly seen. The ion source is located beneath the sector magnet.

**Experiment setup.** A test gas is leaked from a reservoir into the Nier-type electron impact ion source in ILENA. A beam of positive atomic or diatomic ions is accelerated to energies from 100 eV/q to about 2 keV/q, mass-filtered in a 90° sector magnet (SEM, see Fig. 2.2), and directed through a 1 mm pinhole onto the test sample (Fig. 2.3b). The sector magnet mass resolution is  $m/\Delta m \simeq 45$ . The B-field is monitored using a Hall probe. The limiting factors for the energy range are the positive-ionization and extraction efficiency of the ion source at low energies, the required magnetic field precision and stability in the SEM at low

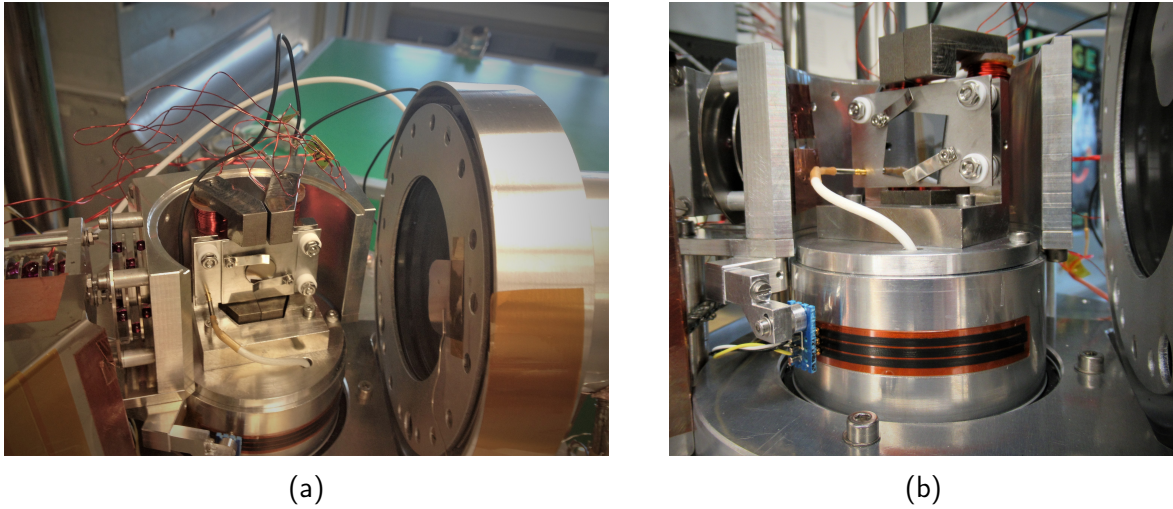


Figure 2.3.: Photographs of the ILENA rotating sample holder with a CS test sample installed. The ion beam comes in from the left side. (a) shows the SEL magnet coils above the sample and the detector case on the right side. (b) shows the resistive stripe goniometer below, and the pinhole to the left of the sample (mirrored on the sample surface).

masses ( $H^+$ ,  $D^+$ ,  $H_2^+$ ) and energies, and the magnetic field strength at high masses ( $O^+$ ,  $Ne^+$ ,  $O_2^+$ ) and energies.

A test sample of typically about  $2 \times 2$  cm size is mounted vertically on a rotatable sample holder, that way the incidence angle can be manually adjusted. A 2D imaging micro-channel plate (MCP) detector is placed opposite to the incident ion beam and can independently be moved horizontally around the sample holder rotation axis as well. The angular positions of sample holder and detector are read out from a resistive strip goniometer (Fig. 2.3b), which has been calibrated using a set of six metal plate templates cut at different angles. A small magnetic field is applied vertically over the sample (SEL), with the magnetic field being parallel to the sample surface, by two magnet coils placed accordingly for deflecting any released secondary electrons back onto the sample (Figs. 2.2 and 2.3a). A Minco heater foil and a PT1000 temperature sensor are attached at the back of one sample holder aluminum plate for sample surface heating.

**Detector.** The ILENA MCP detector consists of a stack of five MCPs mounted in front of a quadratic resistive anode to generate an electron avalanche signal from each impacting particle. 2D imaging information is retrieved in an analog positioning computer from the signal intensities at the four anode corners. The MCP channels are tilted alternately by  $8^\circ$  off the plate normal to maximize detection efficiency. A total bias high voltage of  $-3.2$  kV is applied to the MCP stack. A retarding potential analyzer (RPA) is mounted in front of the MCP detector, which consists of three consecutive grids:

The first and third one at ground potential and the middle one is at positive high voltage (corresponding to 110 % of the ion beam energy) to reject all positive ions. In front of the



first MCP, a secondary grid (at  $U_g = -50$  V) is installed to reject any low-energy electrons released from the RPA grids. The MCP detector can be floated to a negative high voltage to prevent also the negative ions from reaching the MCPs. The electrical potentials inside the detector are shown schematically and qualitatively in Fig. 2.4. The RPA and the MCP detector are electro-statically shielded in a cylindrical metal case (see Fig. 2.3a).

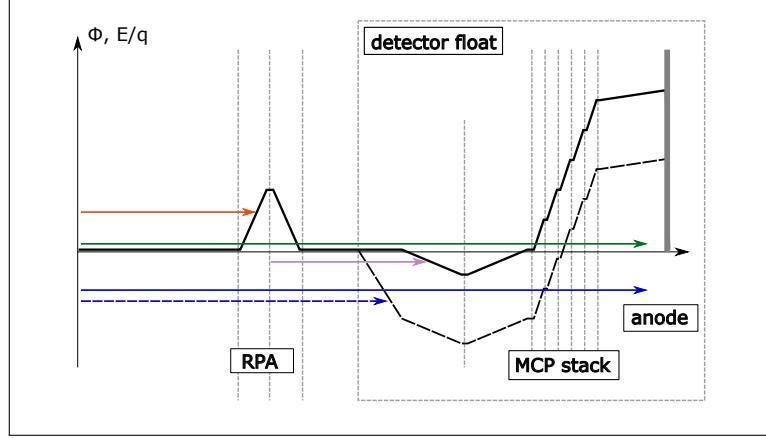


Figure 2.4.: Schematic representation of the detector components and voltages: electrical potential  $\Phi$  (*black*) at Zero and negative float voltage (*dashed*); positive ions (*red*) rejected at the RPA, neutrals (*green*) passing through, electrons (*pink*) rejected at the grid, negative ions (*blue*) passing through if the detector is at Zero float voltage and blocked otherwise (*blue dashed*). The arrows' ordinate represents the particles' respective energy per charge  $E/q$  (except for neutrals).

**Standard Measurement.** A standard ILENA measurement series for sample characterization has been established over the past 20 years: the negative ion yield  $\eta$  is obtained from the ratio of detected negative ions to neutrals ([11], see p.66).

$$\eta = 1 - \left( 1 + \frac{\kappa_0}{\kappa_-} \cdot \left( \frac{N_z - N_h}{N_h} \right) \right)^{-1} \quad (2.7)$$

with  $\kappa_{0,-}$  the detection efficiency for neutrals and negative ions.

This is realized in the experiment by alternately floating the MCP detector to a negative HV (thus rejecting negative ions) and Zero voltage (setting it to ground potential), permitting both neutrals and negative ions to reach the MCP detector. Positive ions are permanently blocked in the RPA. The different detection efficiencies of negative ions and neutrals are species and energy dependent [26, 39] and are accounted for. During the measurement, the ambient conditions (chamber pressure, temperature, filament emission current, ion beam guiding, and sector magnet field) are monitored and held constant.

Moreover, the angular scattering direction distribution of scattered atoms and ions is obtained directly from the 2D image on the detector. It is typically represented by the full-width

at half maximum (FWHM) in both polar and azimuthal angular direction. The limiting factor here is the angular range of about  $21^\circ \times 21^\circ$  (as seen from the sample center) covered by the detector open area. So far, separation and analysis of particle kinetic energies or energy distribution is not possible with the ILENA imaging detector and therefore we could not discern different sputtering populations. However, only a fairly coarse kinetic energy analysis is achievable for the negative ions component by varying the detector float voltage (see Gasser et al. [11]) but is quite involved and requires very stable ambient and beam conditions.

For a standard measurement series, the negative ion yield  $\eta$  and the polar and azimuthal scattering distribution FWHM are measured at an incidence angle of  $8^\circ$  and beam energies 1000, 780, 500, 390 eV/atom (sometimes additionally at 250 eV and 195 eV), mostly for gas species hydrogen and oxygen. Usually, corresponding measurements are performed with helium and neon to obtain experimental proxy values for the negative ion yield contribution due to sputtering. The noble gases of similar atomic mass are used since those do not form stable negative ions. Detection of sputtered negative (H, O) ions off a CS, as opposed to direct scattered negative charge-converted atoms, is also the principal mechanism to detect low-energy He and Ne ENA signals in space.

### 2.2.3. Polar Scattering

The angular scatter distribution off a CS depends on the incidence angle of the scattered atoms. Hereby the most interesting region of the distribution is of naturally around the intensity maximum (or: probability maximum), which is near the specular reflection direction: for moderately wide scatter distributions, the FWHMs in the polar and azimuth angular range can be obtained to parametrize the scattering behavior of the sample surface under test. With the ILENA experiment setup, an angular range of about  $21^\circ \times 21^\circ$  is covered by the imaging detector. However, by varying the detector's angular position, we can record a much wider polar angular range of the scatter distribution.

In the following, the polar angular distribution was measured in a polar range from  $\theta = 0^\circ$  to  $> 60^\circ$  by sequentially shifting the detector by  $10^\circ$  (i.e., half a detector width) between each counts accumulation while the beam and sample position were kept constant. At the end of the sequence, another recording was taken at the original detector position. Comparing the total detected counts in the first and last take allows to keep track of slow changes over time in overall beam intensity and compensate them in the evaluation. The relative difference in total counts in the first and last take (which were taken at the same detector position) was less than 2 %.

The polar distribution was obtained from the 2D scatter distributions by integrating the detected counts in the central 50 % of the detector's azimuth range, i.e., in a belt about  $10^\circ$  wide in azimuth direction (the gray shaded area in Fig. 2.5).

A set of angular distribution measurements over a wider polar range was recorded in that manner for hydrogen, helium, and oxygen scattered off a DLC coated test sample, each: a) at three beam energies and fixed incidence angle  $\alpha = 8^\circ$ , and b) at incidence angles varying from  $2^\circ$  to  $16^\circ$  for 780 eV beam energy.



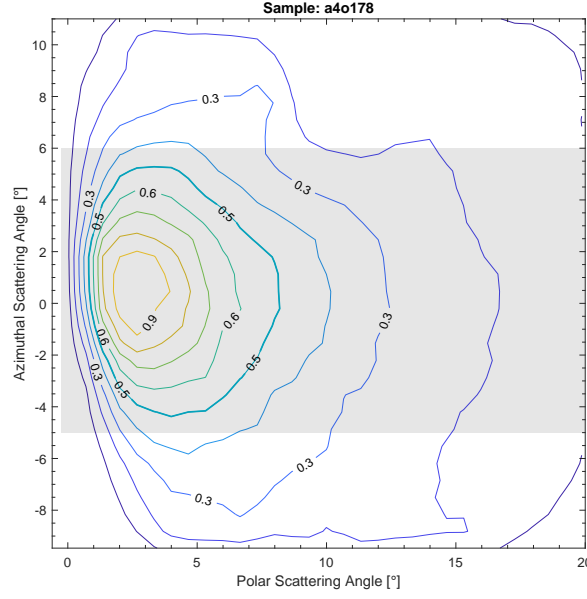


Figure 2.5.: Contour plot of the 2D scatter distribution for 780 eV oxygen scattered off a DLC sample at 5° incidence angle. Counts in the grey area were summed up along the azimuth range to obtain the polar distribution.

**Polar angular fit functions.** In a first step, I used these measured distributions to probe which of the three available fit functions mentioned in Section 2.2.1 is best suited for fitting polar angular scatter distributions: Exponentially Modified Gaussian, Log-Normal, and Erlang distribution. The data were fitted by a four-parameter (peak maximum, peak location, distribution width, and asymmetry) fit function each. The polar distribution of 500 eV hydrogen at 8° incidence angle is shown in Fig. 2.6 as an example, along with the residuals of each fit function. The sum of the residuals squared, as a measure of the goodness of fit, was compared among the three fit functions for each measured polar angular distribution. Throughout the whole data set, the Log-Normal distribution showed the least deviation from the data, with average ratio

$$\begin{aligned} (\Sigma R^2)_{EMG} / (\Sigma R^2)_{LN} &= 1.60 \pm 0.32 \quad \text{and} \\ (\Sigma R^2)_{Erlang} / (\Sigma R^2)_{LN} &= 2.70 \pm 0.37 \end{aligned}$$

We see in Fig. 2.6 that the Log-Normal fit function best approximates the data particularly in the range around the global maximum and in the high-polar angle tail. The same is seen at all energies, species, and incidence angles for which a wide-range polar distribution was recorded. We conclude that all three fit functions are suited to mode the measured polar distributions, of which the Log-Normal shows the least deviation and should thus be preferred. This conclusion is in agreement with Ghielmetti [14].

Therefore, for the rest of this section, the Log-Normal was used as the fit function for polar angular scatter distributions. In Fig. 2.7, fitted polar distributions are compared for varying beam energy at fixed incidence angle. The prompt observation that higher beam energy leads

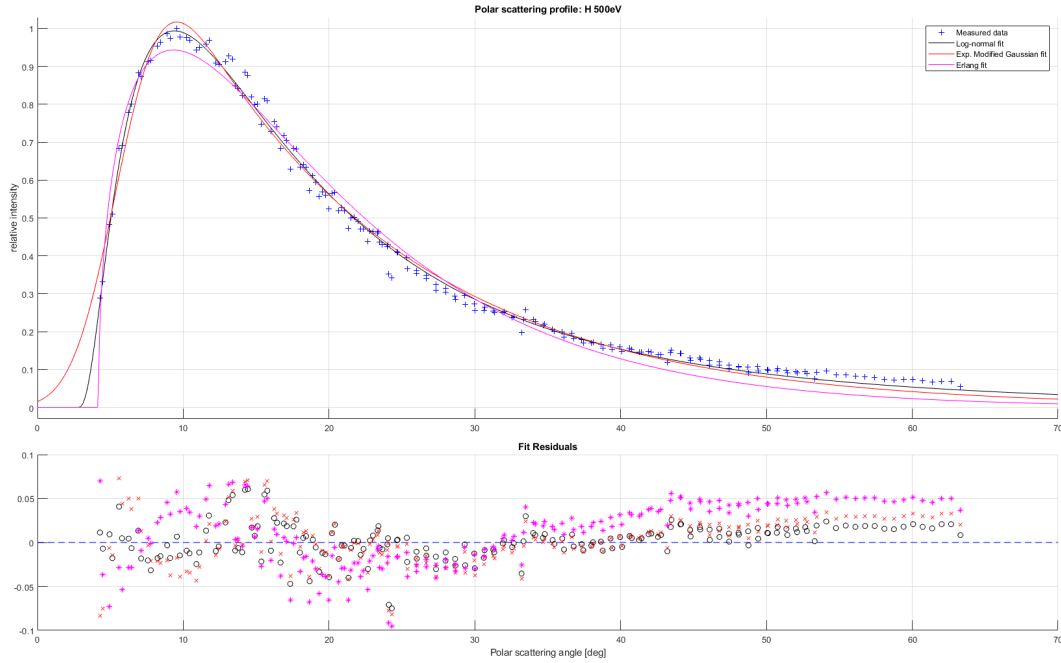


Figure 2.6.: Comparison of three 4-parameter fit functions for the polar angular scatter distribution.

to a broader scattering distribution has long been established and comes with no surprise. Extensive tests on various CS materials (also see Section 2.3) have confirmed it repeatedly. Beyond that, we show here that not only the distribution FWHM increases, but also the peak location shifts to slightly larger polar angles at higher beam energy. Over all, the distribution maximum is located at a polar angle slightly smaller than specular reflection. However, this is usually difficult to verify in the ILENA test facility, as both the sample and detector angle need be precisely adjusted to experimentally confirm this.

In Fig. 2.8, polar scatter fits are shown for 780 eV hydrogen scattered off DLC at varying incidence angles from  $2^\circ$  to  $15^\circ$ . This figure illustrates well the changes in polar scatter width and its shift towards steeper polar angles in dependency of the atoms' incidence angle.

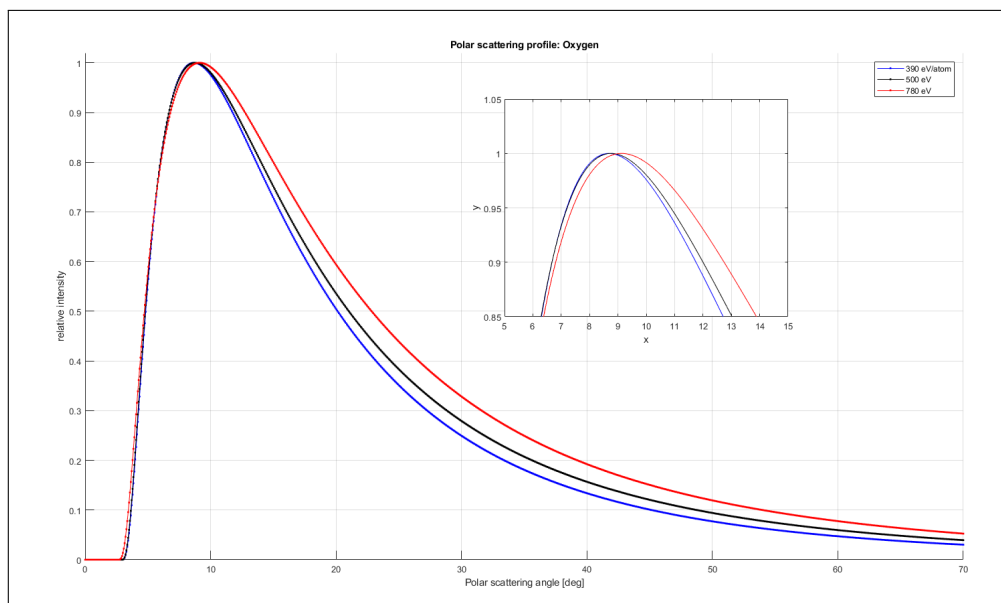


Figure 2.7.: Polar scattering distribution of O on a DLC sample, at fixed incidence angle  $\alpha \simeq 10^\circ$  and different energies 390 eV, 500 eV and 1000 eV.

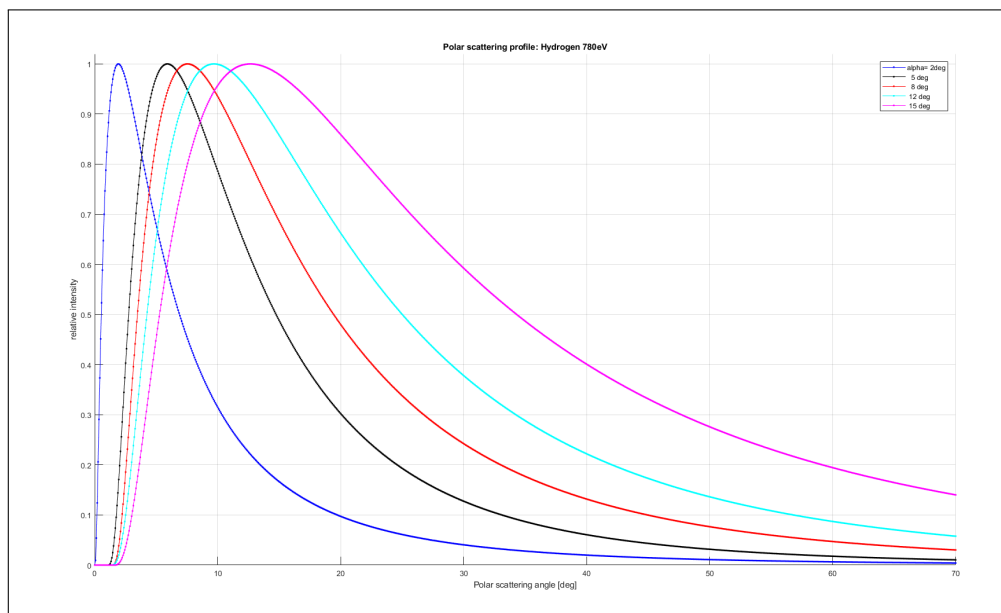


Figure 2.8.: Polar scattering distribution of H on a DLC sample, at fixed beam energy 780 eV, for incidence angles  $2^\circ - 15^\circ$ .

## 2.3. Surface Materials under Test

In this section, I report on experimental results for a range of conversion surface materials.  $\text{Al}_2\text{O}_3$  is currently one well-established CS coating materials in space instrumentation. It has been used in the ENA instrument of MPPE on BepiColombo, and the JNA instrument of PEP on JUICE. Recent test results of an  $\text{Al}_2\text{O}_3$  sample as well as a summary overview of previous results are contained in section 2.3.1. Diamond-like carbon (DLC) coatings are widely used in ENA instruments as well. The results contained in Section 2.3.2 concentrate on tested samples in regard of the IMAP-Lo sensor. In Sections 2.3.3 to 2.3.6 results of a few novel CS materials are presented.

### 2.3.1. Aluminum Oxide $\text{Al}_2\text{O}_3$



Aluminum oxide ( $\text{Al}_2\text{O}_3$ ) coated CS have been studied extensively over the past 15 years ([30, 35, 36], Riedo [28, Section 3.1], Allenbach [2, Section 4.1], Föhn [6, Ch. 3]). The reported negative ion yields (energy range: 200 eV to 1000 eV/atom;  $8^\circ$  incidence angle) are typically about 10-12 % for oxygen (increasing with energy), about 2 % for hydrogen and helium, and about 4 % for neon (due to sputtering).  $\text{Al}_2\text{O}_3$  is thus one of the best performing CS materials suitable for space applications to date.

In consequence, ENA imaging instruments relying on  $\text{Al}_2\text{O}_3$  conversion surfaces have been flown successfully on several planetary space missions such as the ENA instrument as part of the Mercury Plasma Particle Experiment in BepiColombo [31] and the Jovian Neutrals Analyser (JNA) [8, 27] in the Particle Environment Package (PEP) on the Jupiter Icy Moons Explorer, with launch planned in April 2023.

**Report on  $\text{Al}_2\text{O}_3$  samples.** Previous  $\text{Al}_2\text{O}_3$  test samples and facets were coated by the two manufacturers, Thin Film Physics (TFP) and Jenion. In regard of the JNA instrument, another manufacturer was found, namely RhySearch (Buchs, Switzerland). In January 2019, I tested an exemplary sample of  $\text{Al}_2\text{O}_3$  coated Si (25 nm coating thickness) from RhySearch and found results matching the typical values for this coating material. Another two high-quality test samples were then produced at RhySearch and tested in ILENA, too.

The test results are summarized in the following report: *“Sputtering performance measurements of an  $\text{Al}_2\text{O}_3$  conversion surface”* (March 2019) to the attention of the PEP team.

# Sputtering performance measurements of an Al<sub>2</sub>O<sub>3</sub> conversion surface

	Name and function	Date	Signature
<b>Prepared by:</b>	Jonathan Gasser, PhD student	25 March 2019	
<b>Verified by:</b>			
<b>Approved by:</b>	Peter Wurz, PEP Co-PI	26 March 2019	
<b>Issued by:</b>			

## CHANGE RECORD

Version		Date	Changed Paragraphs	Remarks
Issue	Rev			
1	1	25.3.2019	All	New document
1	2	08.10.2022	None	Minor adaptations, no content changed.

## TABLE OF CONTENTS

<b>1</b>	<b>INTRODUCTION.....</b>	<b>4</b>
<b>2</b>	<b>EXPERIMENTAL SETUP.....</b>	<b>4</b>
<b>3</b>	<b>MEASUREMENTS .....</b>	<b>5</b>
3.1	Strategy .....	5
3.2	Processing .....	6
<b>4</b>	<b>RESULTS .....</b>	<b>9</b>
4.1	Angular Scattering Distribution.....	9
4.2	Ionisation Efficiency.....	10
4.3	Former Results.....	11
<b>5</b>	<b>DISCUSSION.....</b>	<b>12</b>
<b>6</b>	<b>LIST OF ACRONYMS .....</b>	<b>12</b>
<b>7</b>	<b>REFERENCES.....</b>	<b>13</b>

## 1 INTRODUCTION

In the past decades, particle scattering on smooth planar surfaces under grazing incidence angles has become a well-established method to change the charge state of atomic ions and neutrals [Jans, 2000]. Namely, the low energy consumption of the method, and the ability to ionise incident atoms of energies down to a few tens of eV make it the method of choice for ion conversion for various spaceborne instruments, such as on Mars Express, Venus Express, Rosetta, IBEX and, more recently, MINPA, BepiColombo, and IMAP (planned). To maximise sensitivity and resolution of the analysing instruments, one major goal is to find conversion surface (CS) materials that simultaneously achieve a narrow angular scattered particle beam and a high yield of negatively charged ions.

Among others, aluminium oxide  $\text{Al}_2\text{O}_3$  has been established as well suited conversion surface material and has been used in neutral particle detectors, recently in BepiColombo<sup>1</sup>. Typically, a thin layer of a few 100 Å of  $\text{Al}_2\text{O}_3$  is vapour deposited on a silicon substrate. The incoming neutral atoms and small molecules hit the CS at grazing incidence angles of typically  $\alpha \leq 15^\circ$  or less, and are scattered into a solid angle around the geometrical reflection direction.

## 2 EXPERIMENTAL SETUP

To characterise and compare the primary scattering properties of a given sample, the negative ion yield  $\eta$  as well as the angular FWHM of the scattered beam in the directions parallel (azimuth angle) and normal (polar angle) to the surface are measured. We performed the desired measurements in the ILENA test facility [Wahlström et al., 2013] using hydrogen (H), helium (He), oxygen (O), and neon (Ne) ion beams of energies in the range 390 eV – 1000 eV under a grazing incidence angle.

The ILENA experiment consists of a Nier-type electron impact ion source, a  $90^\circ$  sector magnet and beam guiding system, a pivotable sample holder, and a movable two-dimensional imaging MCP detector with an angular field-of-view of  $21^\circ \times 21^\circ$  seen from the sample centre. A schematic overview of ILENA is shown in Figure 1.

The setup is contained in a vacuum chamber equipped with a turbo molecular pump and an ion getter pump, which can establish a base pressure in the low to mid  $10^{-8}$  mbar range after baking out the vacuum chamber during at least 24 hours at a temperature of  $80^\circ\text{C}$ . Typically, a test gas is inserted for measurements up to the mid  $10^{-7}$  mbar range, and is held in a dynamical equilibrium.

In the ion source, a beam of positive test gas ions is produced and subsequently accelerated to 100 eV up to 2 keV. The beam is deflected and mass analysed in the sector magnet and then guided through a pinhole of about 1 mm in diameter. The beam line may be adjusted via two perpendicular electrostatic plates before and after the sector magnet, respectively. After the pinhole, the ion beam strikes the sample conversion surface which is mounted on the sample holder. The beam is scattered towards the MCP detector thereafter.

A retarding potential analyser (RPA) consisting of three consecutive grids is mounted in front of the MCP detector. The outer grids are grounded while the middle grid is biased to a positive voltage to reject positive ions. The entire MCP detector may optionally be floated to a high negative potential (HV1) for negative ion rejection. In addition, a low negative voltage grid in front of the first MCP serves to reject secondary electrons created by particles hitting the RPA or floating grids. Possible

<sup>1</sup> See e.g. [Riedo, 2010], chapter 1.



secondary electrons from the CS are effectively returned to the CS by an additional small magnetic field applied over the CS.

The MCP detector itself consists of five consecutive MCP's mounted in front of a quadrilateral resistive anode. A subsequent analogue position computing unit determines the location of each detected particle. The entire detector unit, including the RPA, is shielded electrostatically. It can be rotated about the polar axis at the centre of the sample holder from  $\theta = 0^\circ$  to  $90^\circ$ .

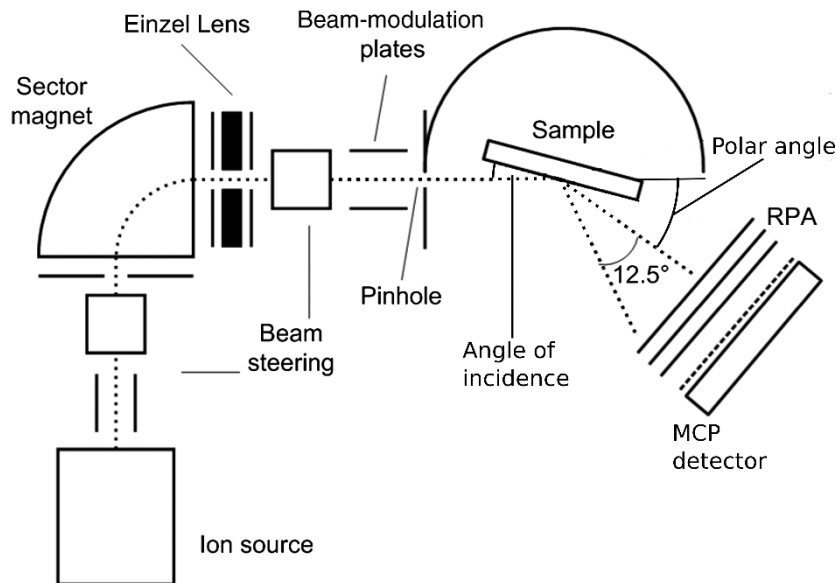


**Figure 1: Schematic ILENA experiment setup, viewed from top. The ion source is placed vertically below the sector magnet (Courtesy of M. Föhn, adapted from [Wahlström et al., 2013]).**

### 3 MEASUREMENTS

#### 3.1 Strategy

The objective of the measurement campaign at hand is to test the scattering properties of an aluminium oxide ( $\text{Al}_2\text{O}_3$ ) conversion surface produced by the company RhySearch<sup>2</sup>. Namely, to be eligible for the use as CS in space instruments or test facilities, it has to be verified that the ionisation efficiency and the angular scattering distribution of this sample for incident H, He, O and Ne is at least as good as it was for previously tested  $\text{Al}_2\text{O}_3$  CS samples of the same structure but from other manufacturers (see e.g. section 3.1 in [Riedo, 2010]). A series of preliminary measurements done with an exemplary RhySearch  $\text{Al}_2\text{O}_3$  test sample, which was performed in January 2019 by Martina Föhn and Jonathan Gasser, showed an overall scattering performance comparable to preceding test results with comparable  $\text{Al}_2\text{O}_3$  samples (cf. section 4.3).

<sup>2</sup> RhySearch innovation and research institution, CH-9471 Buchs SG, Switzerland  
[www.rhysearch.ch](http://www.rhysearch.ch)

Manufacturer:	RhySearch
Surface Material:	aluminium oxide (Al <sub>2</sub> O <sub>3</sub> ) single crystal, 99.9% purity
Supporting Material:	silicon wafer, 20 mm x 20 mm x 1 mm
Coating Thickness:	25 nm
Surface Roughness:	< 1.0 nm (rms)

**Table 1: Overview of test sample properties**

Scattering experiments were done using primary beams of H<sup>+</sup>, He<sup>+</sup>, O<sup>+</sup> and Ne<sup>+</sup> ions at an incidence angle  $\alpha = 8^\circ$  and beam energies of 390 eV, 500 eV, 780 eV, and 1 keV. The pressure in the vacuum chamber was held at  $(4.0 \pm 0.1) \cdot 10^{-7}$  mbar while measuring. The incident particles are neutralised shortly before reaching the CS [Wahlström et al., 2013] and are scattered as neutral atoms and negative ions.

### 3.2 Processing

For each data point, a series of five consecutive measurements is performed, with alternatingly setting HV1 to a voltage above the post-acceleration threshold (meas. no. 1, 3, 5) and to zero (meas. no. 2, 4) to measure neutrals alone and combined neutrals with negative ions, respectively.

Taking into account the detection efficiencies  $\kappa_0$  and  $\kappa_-$  for neutrals and negative ions respectively, the negative ion yield  $\eta$  is then computed according to [Föhn, 2017], section 3.1:

$$\eta = \frac{N_-/\kappa_-}{\widetilde{N}_{tot}} = \frac{1}{1 + \frac{\kappa_-}{\kappa_0} \frac{N_0}{N_{tot} - N_0}}$$

where  $\widetilde{N}_{tot} = N_0/\kappa_0 + N_-/\kappa_-$  is the total number of particles ( $N_{tot} = N_0 + N_-$  is the total number of counts, measured when HV1 = 0),  $N_0$  the number of detected neutrals (measured with HV1 high) and  $N_-$  the number of detected negative ions (not directly measured).

During each measurement series, the relative change of total counts ( $\frac{|N_{i+2} - N_i|}{N_i}$ ) is varies by less than 2%, otherwise the measurement series is repeated.

The nominal  $\eta$  we find here for the noble gases He and Ne is interpreted as sputtering background of surface deposited H and O on the CS (e.g. from water condensation). We use noble gases – which in principle cannot form stable negative ions – of comparable atomic mass to estimate this sputtering background in H and O scattering, respectively:

$$\eta_H = (\eta_{H,meas} - \eta_{He}) \text{ and } \eta_O = (\eta_{O,meas} - \eta_{Ne})$$

28 Furthermore, the production rate of atomic ions in the ion source is quite low for the diatomic gases hydrogen and oxygen. Instead, a primary beam of molecular ions (H<sub>2</sub><sup>+</sup> or O<sub>2</sub><sup>+</sup>) and twice the nominal beam energy is used occasionally to probe the scattering behaviour of H and O at low energies. This is

justified by the observation that positive molecular ions dissociate shortly before hitting the CS, as described in [Wurz et al., 1997], and consequently two individual atoms of about half the molecular beam energy enter the scattering process (cf. [Jans et al., 2001]).

The polar and azimuthal FWHM of the scattered beam are retrieved from contour plots of the detected scattering pattern. For this, the detected raw image is processed as follows:

- Each image is calibrated by the position-dependent detection efficiency of the MCP detector, which was obtained from a long-term ( $t_{\text{int}} = 40'000$  s, due to the relatively low count rate of 20-30 cts/s and for acceptable statistics) measurement without any beam production ('dark') using neutral He at a pressure of  $6.0 \cdot 10^{-7}$  mbar.<sup>3</sup>
- The image is corrected for the locally lower detection efficiency in the region where the scattered particles hit the first MCP at an angle nearly parallel to the microchannel orientation, i.e. about  $8^\circ$  relative to the microchannel plate normal. This causes a spot of reduced count number in the detected image, because particles can pass the first MCP without producing secondary electrons, which reduces the detection efficiency.<sup>4</sup>
- The image is normalised to the peak maximum.
- A contour plot is printed for each of the (HV1 high) scattering patterns, from which the azimuthal and polar FWHM are read out and averaged.

The contour plots for the measurements with 500 eV beam energy are shown in Figure 2 as examples. The indentation in the upper image centre of Figure 2A is due to an imperfect compensation of the MCP hole.

<sup>3</sup> It was checked that within the range ( $1.0 \cdot 10^{-7}$  ...  $9.0 \cdot 10^{-7}$  mbar), the ambient pressure has little influence on the sensitivity distribution of the detection unit.

<sup>4</sup> This does not apply for the 'dark' measurements, since there is no directed beam and particles hit the MCP from random direction

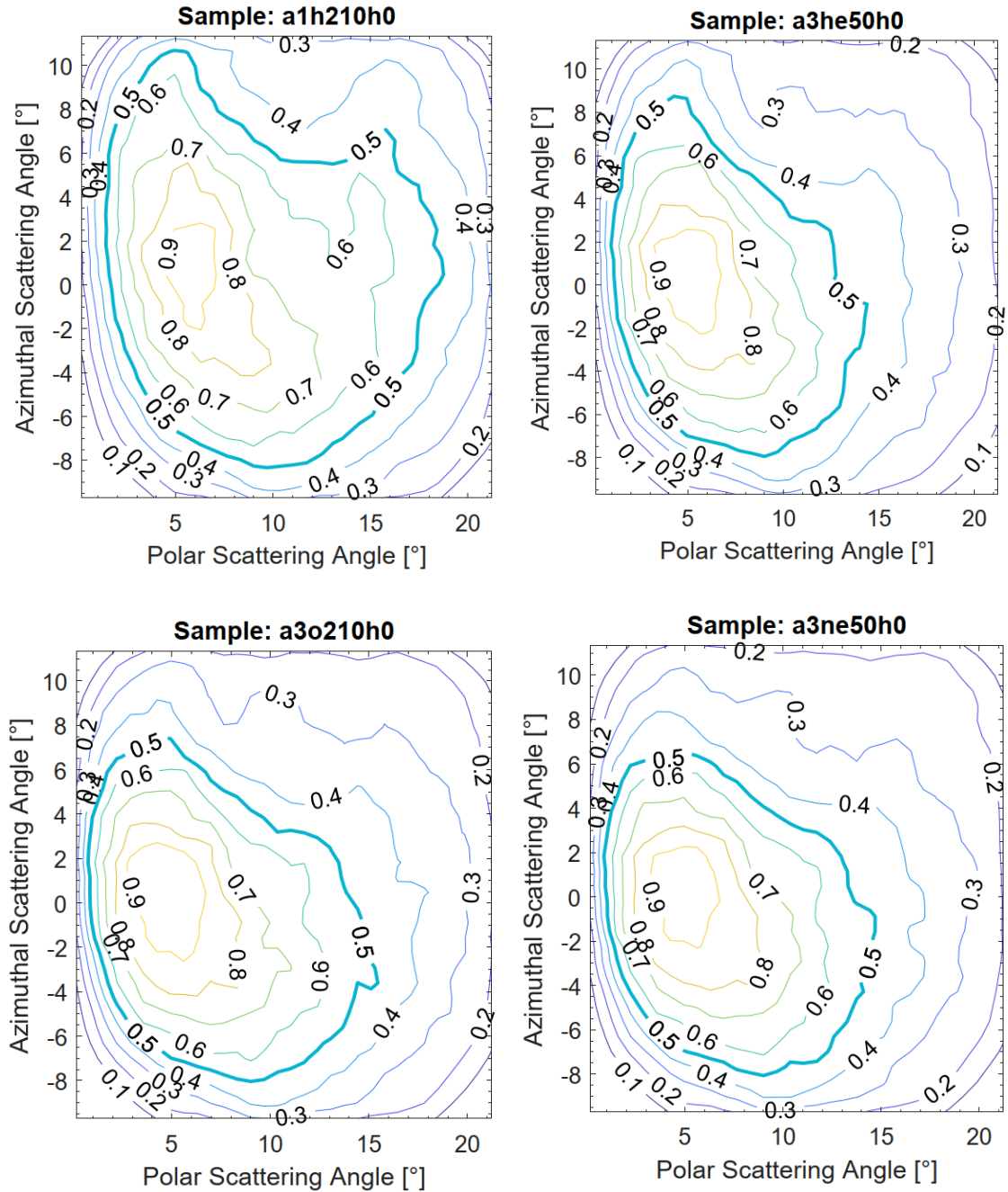


**Figure 2: Contour plots of the scattering distributions for 500 eV beam energy. A) hydrogen, sample a1h210h0. B) helium, sample a3he50h0. C) oxygen, sample a3o210h0. D) neon, sample a3ne50h0. Bold lines: 50% percentile with respect to the scattered beam maximum.**

## 4 RESULTS

In the following, we present the measured results for the angular scattering distribution and negative ion yield of the selected particles when scattering off the  $\text{Al}_2\text{O}_3$  CS manufactured by RhySearch. In addition, a brief summary overview of previously tested comparable  $\text{Al}_2\text{O}_3$  surfaces is presented.

### 4.1 Angular Scattering Distribution

The azimuthal scattering FWHM for the test gases H, He, O and Ne at energies from 390 eV to 1000 eV are shown in Figure 3. Due to some uncertainty in the stability of the experiment conditions, statistical fluctuations and possible readout inaccuracies, an overall standard error of  $\Delta\Phi = \pm 1.0^\circ$  is assigned to the values, and a relative uncertainty in the energy per atom of  $\frac{\Delta E}{E} = 10\%$  is assumed in case the measurements were performed using a molecular primary beam.

The polar scattering FWHM can be determined up to an estimated error of  $\Delta\theta = \pm 0.5^\circ$  for all gases. The results for polar scattering are shown in Figure 4. The beam incidence angle was  $\alpha = 8.0^\circ \pm 0.5^\circ$  for all measurements.

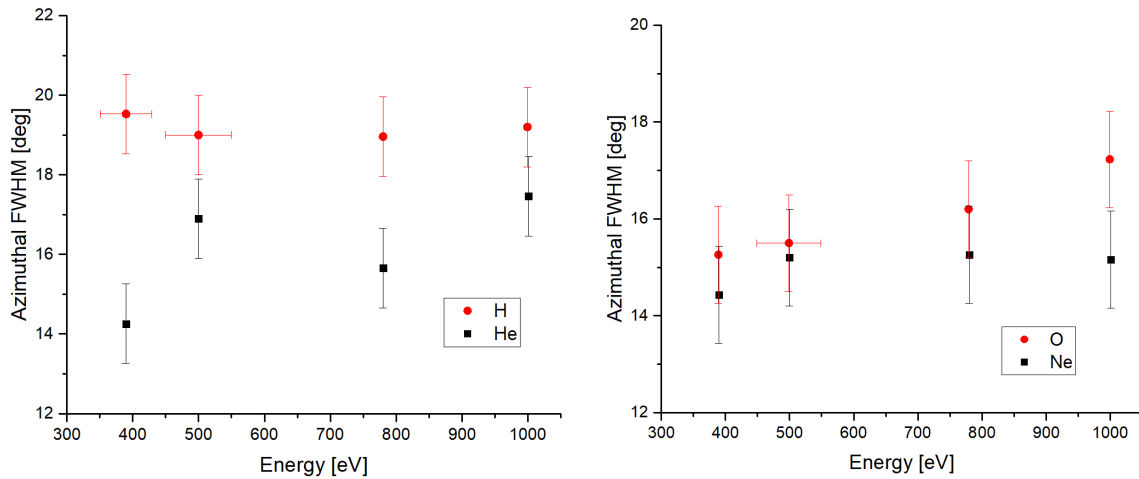


**Figure 3: Azimuthal FWHM of scattered atoms at different primary beam energies.**

**Left: hydrogen and helium. Right: oxygen and neon. Error bars on the energy value indicate measurements with a primary beam of molecular  $\text{H}_2$  and  $\text{O}_2$ , respectively. The incidence angle was  $8^\circ$  with respect to the surface plane.**

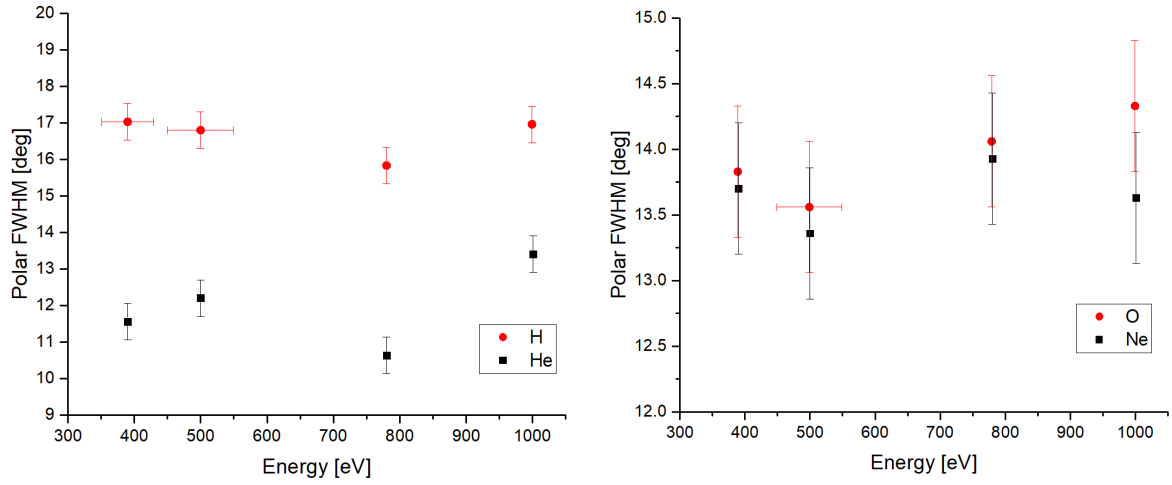


**Figure 4: Polar FWHM of scattered atoms at different primary beam energies, and an incidence angle of 8°.**  
**Left: hydrogen and helium. Right: oxygen and neon.**

## 4.2 Ionisation Efficiency

Moreover, we measured the negative ion yield  $\eta$  for hydrogen, helium, oxygen and neon. For H and O, the nominal ion yield of the respective similar mass noble gas was subtracted as estimated sputtering background. The detailed results are plotted in Figure 5.

For hydrogen, we find values of about  $\eta_H = 2\%$ , whereas for oxygen, the negative ion yield is significantly higher,  $\eta_O = 14\%$ . The noble gases reveal intermediate results of about  $\eta_{He} = 3.5\%$  for helium, and  $\eta_{Ne} = 5.5\%$  for neon.

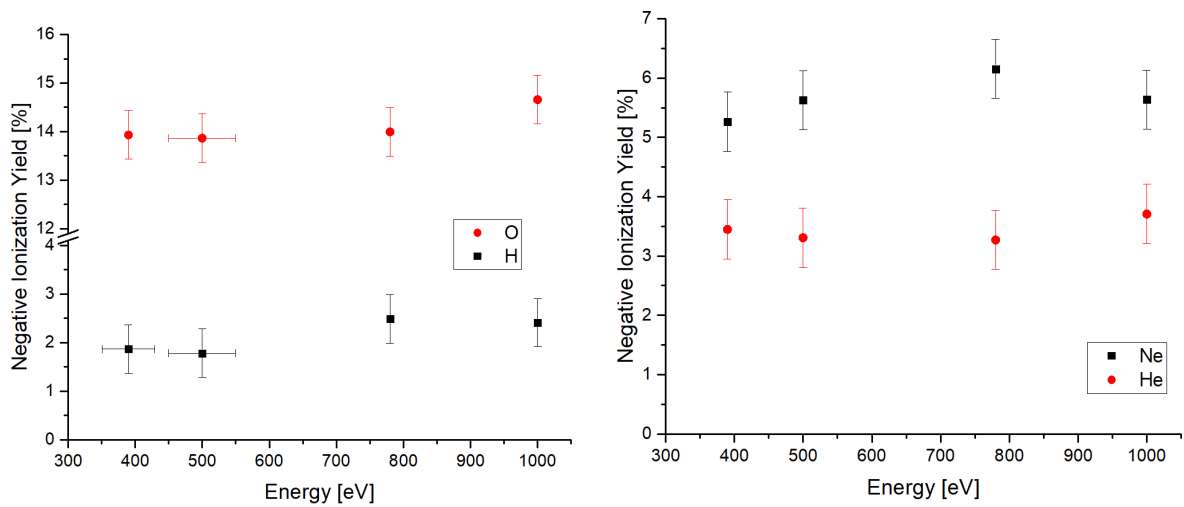


**Figure 5: Negative ion yield for atomic scattering off an  $\text{Al}_2\text{O}_3$  surface at 8° incidence angle and different beam energies.**  
**Left: hydrogen and oxygen; sputtering background was subtracted. Right: helium and neon.**

### 4.3 Former Results

Similar surface tests with principally identical samples were already performed earlier with ILENA. Results that can directly be compared were reported by [Scheer et al., 2009] [Riedo, 2010] [Riedo et al., 2012] [Allenbach, 2016] and [Föhn, 2017].

In Table 2, we list the approximate values of former scattering performance measurements with H, He, O and Ne on a thin film Al<sub>2</sub>O<sub>3</sub> surface. Energies range from 390 eV (250 eV in [Föhn, 2017]) up to 1000 eV, and the incidence angle was held at 8° to the surface. The tested CS were each manufactured either by Jenion Inc., by Thin Film Physics (TFP) or by RhySearch.

Al <sub>2</sub> O <sub>3</sub> sample		Yield [%]				Polar FWHM [deg]				Azimuth FWHM [deg]			
Report	Manufacturer	H	He	O	Ne	H	He	O	Ne	H	He	O	Ne
Wahlström, 2007	(?)	1.5	1	13	1	12	11	11	17...20	20	18	17...20	11
Scheer et al, 2009	Jenion	1...2	--	12...16	--								
Riedo, 2010	TFP	1.5	2	10...12	4	11...15	9...13	7...12	9...13	--	15...20	11...15	13...17
Riedo, 2010	Jenion	1.5	2	9...12	4	11...16	10...13	7...12	9...13	15...22	15...20	11...17	13...18
Riedo et al, 2012	TFP	--	--	9...12	4	--	--	8...13	9...15	--	--	11...17	13...20
Allenbach, 2016	TFP	2	1.7	--	--	7...11	7...9	--	--	10...16	10...13	--	--
Föhn, 2017	TFP	1.5	2	10...12	3	14...12	11	10...15	11...12	--	16...20	13...20	14...18
Föhn, Gasser, 2019*	RhySearch	2	2	10...11	3.5	--	11...13	10...15	11...12	--	17...20	--	16...19
<b>This</b>	<b>RhySearch</b>	<b>2</b>	<b>3.5</b>	<b>14</b>	<b>5.5</b>	<b>17</b>	<b>11...13</b>	<b>14</b>	<b>13</b>	<b>19</b>	<b>14...17</b>	<b>15...17</b>	<b>15</b>

**Table 2: Overview over previous results for negative ion yield and angular FWHM for Al<sub>2</sub>O<sub>3</sub> conversion surfaces.**  
(\*Results not reported yet)

An energy dependency is indicated by dots (...), where higher energies tend to yield both wider FWHM and a higher negative ionisation efficiency.

For the azimuthal FWHM of hydrogen, missing values are in part not due to missing measurements, but also because the detected scattering FWHM was broader than the detection range of about 21°.

## 5 DISCUSSION

We measured the negative ion yield as well as the angular scattering FWHM in polar and azimuthal direction for scattering off an Al<sub>2</sub>O<sub>3</sub> CS test sample manufactured by RhySearch.

For the azimuthal scattering FWHM, we find values in the range of 10° - 18° (cf. Figure 3), while for the polar scattering FWHM (Figure 4), values vary between 14° and 20° depending on the gas type and the incident energy, which is in the range of 390 eV - 1 keV. In general, the results obtained here agree well with previous findings (cf. Table 2) within the given experimental uncertainties.

The negative ion yield  $\eta$  we found for the noble gases He and Ne (cf. Figure 5) is significantly higher than was ever reported before. We interpret this as enhanced sputtering background signal coming from, e.g., water deposited on the CS.

Despite this fact<sup>5</sup>, the ionisation efficiencies for H and O are the same as was reported for previous samples, within error. The slightly higher  $\eta$  for He and Ne is thus not crucial for the performance of converting H and O atoms into negative ions. The polar scattering FWHM we found for H is slightly wider, while the FWHM in azimuthal direction agrees well with the result of Wahlström and [Riedo, 2010]. The scattering FWHM's we find for He, O and Ne are in good agreement with previous results. The wider scattering angles seen with H are mainly for the lower energies, which tend to show narrower scattering patterns, and should therefore not limit the overall performance of this sample.

From the present results, and in comparison with previous results, we conclude that the in hand Al<sub>2</sub>O<sub>3</sub> surface sample, manufactured by RhySearch, is at least equally well suited to serve as active conversion surface in upcoming space science instruments as are the well-established Al<sub>2</sub>O<sub>3</sub> surface samples in use, produced by other manufacturers.

## 6 LIST OF ACRONYMS

CS	Conversion Surface
FWHM	Full-width at half maximum
HV	High Voltage
IBEX	Interstellar Boundary Explorer
ILENA	Imager for Low Energy Neutral Atoms
IMAP	Interstellar Mapping and Acceleration Probe
MCP	Micro-Channel Plate(s)
MINPA	Mars Ion and Neutral Particles Analyser
RPA	Retarding Potential Analyser

Table 3: List of acronyms

<sup>5</sup> Recall that the noble gas yield is used as background signal estimate for H and O measurements



## 7 REFERENCES

- Allenbach, Marc. *Evaluation of Potential Conversion Surfaces for the IMA Mission*. Bern, 2016.
- Föhn, Martina. *Application of Surface Physics for Instruments in Space Science*. Bern, 2017.
- Jans, Sarah et al. „Scattering of atoms and molecules off a barium zirconate surface.“ *Nuclear Instruments and Methods in Physics Research B* 173, 2001: 503-515.
- Jans, Sarah. *Ionisation of Energetic Neutral Atoms for Application in Space Instrumentation*. Bern, 2000.
- Riedo, Andreas. *Optimisation of the Detection-technique for Energetic Neutral Atoms for the BepiColombo Mission*. Bern, 2010.
- Riedo, Andreas, Michael Ruosch, Martin Frenz, Jürgen A. Scheer und Peter Wurz. „On the surface characterisation of an Al<sub>2</sub>O<sub>3</sub> charge state conversion surface using ion scattering and atomic force microscope measurements.“ *Applied Surface Science* 258, 2012: 7292-7298.
- Scheer, Jürgen A. et al. „Conversion Surfaces for Neutral Particle Imaging Detectors.“ *Advances in Space Research* 38, 2006: 664-671.
- Scheer, Jürgen A., Peter Wahlström and Peter Wurz. "Scattering of light Molecules from thin Al<sub>2</sub>O<sub>3</sub> Films." *Nucl. Meth. B* 267, 2009.
- Schletti, Reto. *Anwendung der Oberflächenionisation in Raumforschungsexperimenten*. Bern, 1996.
- Wahlström, Peter. *Optimisation of the Detection-Technique for Energetic Neutral Atoms for the IBEX Mission*. Bern, 2007.
- Wahlström, Peter, Jürgen A. Scheer, Andreas Riedo, Peter Wurz and Martin Wieser. "Test Facility to Study Surface-Interaction Processes for Particle Detection in Space." *Journal of Spacecraft and Rockets*, March 2013.
- Wurz, Peter, Reto Schletti and Matthias Aellig. "Hydrogen and oxygen negative ion production by surface ionisation using diamond surfaces." *Surface Science*, February 1997: 56-66.

**Summary of previous results.** In the following overview figures, a set of published surface characterization results from ILENA are collected and summarized. The source research articles and theses are listed in Table 2.2:

Table 2.2.: List of  $\text{Al}_2\text{O}_3$  samples tested and reported.

Abbrev.:	Reference:	$\text{Al}_2\text{O}_3$ manufacturer, spec.:
Riedo/TFP	Riedo, Master Thesis 2010 [28]	Thin Film Physics; 25 nm /Si
Riedo/Jen	Riedo, Master Thesis 2010	Jenion Inc.; 25 nm /Si
Föhn/TFP	Föhn, Master Thesis 2017 [6]	Thin Film Physics; 25 nm /Si
Allen/TFP	Allenbach, Master 2016 [2]	Thin Film Physics; 25 nm /Si
Scheer/Jen	Scheer+, NIMB 2009 [35]	Jenion Inc.; 25/50/89 nm $\text{Al}_2\text{O}_3$ /Si
Rhy1	(Gasser, PEP Report 2019)	RhySearch, first test sample
Rhy2	Gasser, PEP Report 2019 (p. 25)	RhySearch, quality sample
Wahl07	Wahlström, Master 2007 [43]	Single crystal
Scheer07	Scheer+, NIMB 2007 [36]	500 nm $\text{Al}_2\text{O}_3$ on graphite

The reported negative ion yields are compiled in Fig. 2.10, and best fit linear trends are added. For H and O, two trend lines are drawn that indicate 'optimal' and minimal values to be expected.

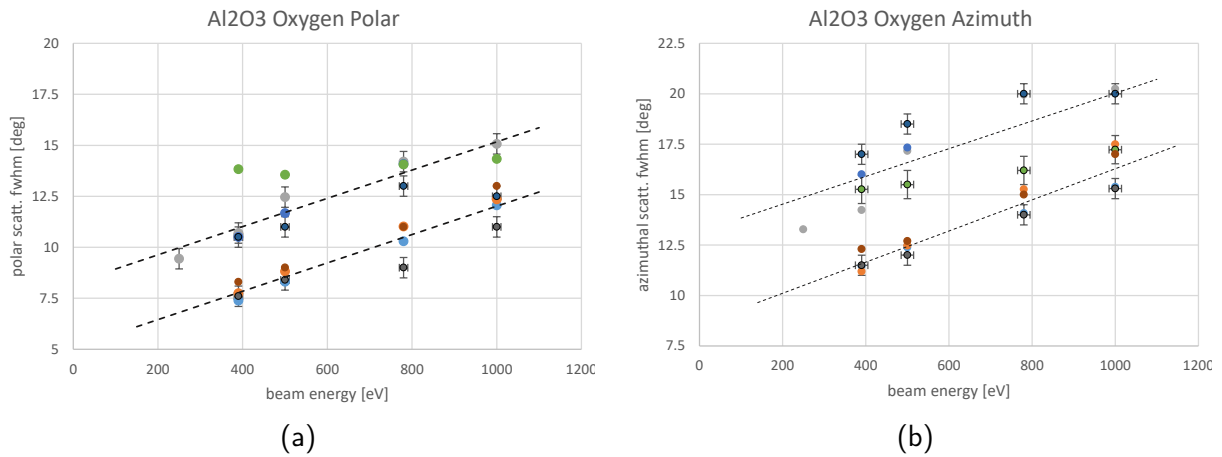


Figure 2.9.: Oxygen polar (a) and azimuthal (b) scattering FWHM off  $\text{Al}_2\text{O}_3$  surfaces ( $\alpha = 8^\circ$ ). An optimal (lower) and less favored trend line are added to the data.

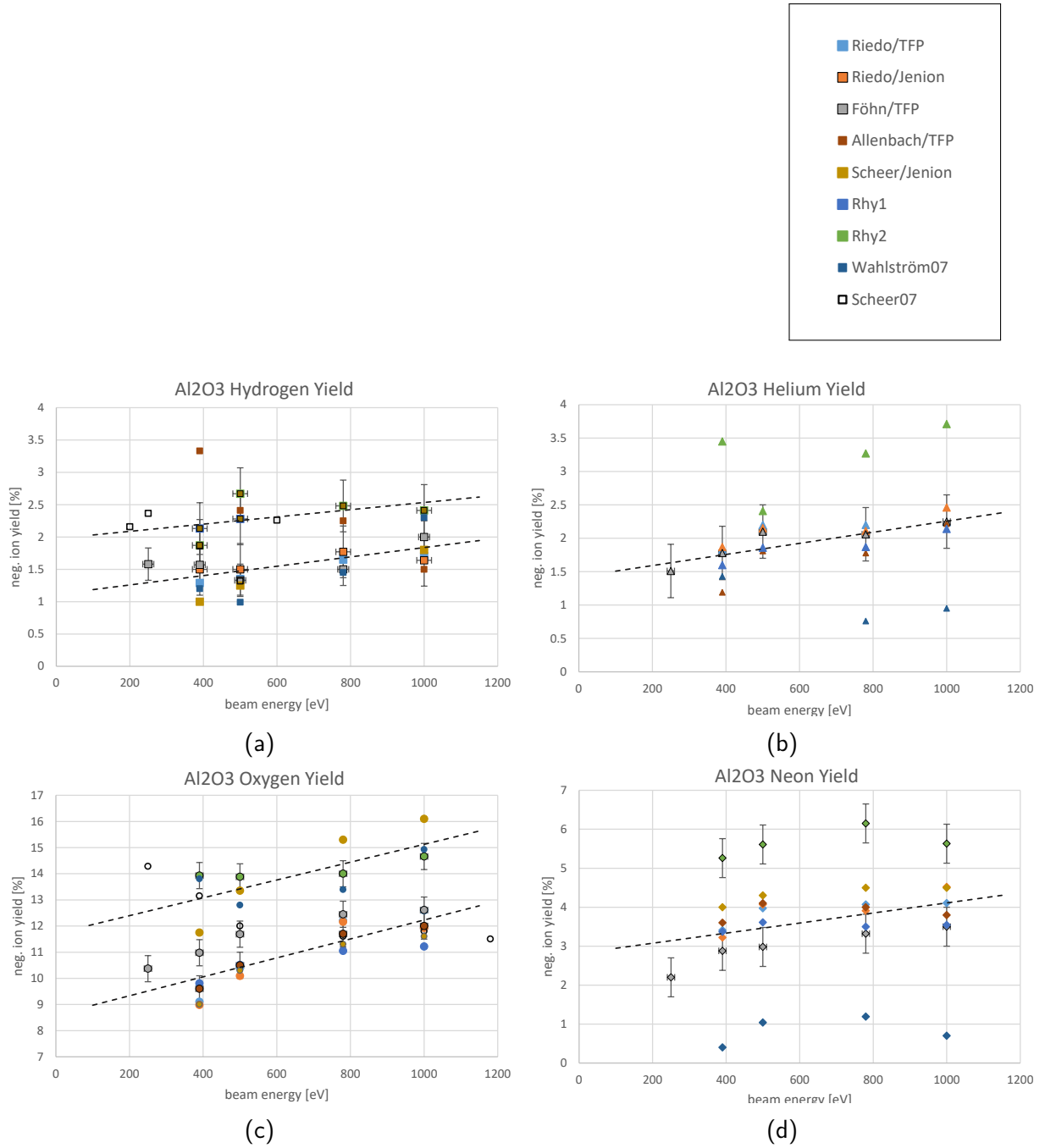


Figure 2.10.: Overview of reported negative ion yields from scattering off Al<sub>2</sub>O<sub>3</sub> surfaces at 8° incidence angle. Typical error bars are indicated only at a few data points for better readability. Dashed lines represent best fits to the available data. (a) hydrogen, (b) helium, (c) oxygen, (d) neon.

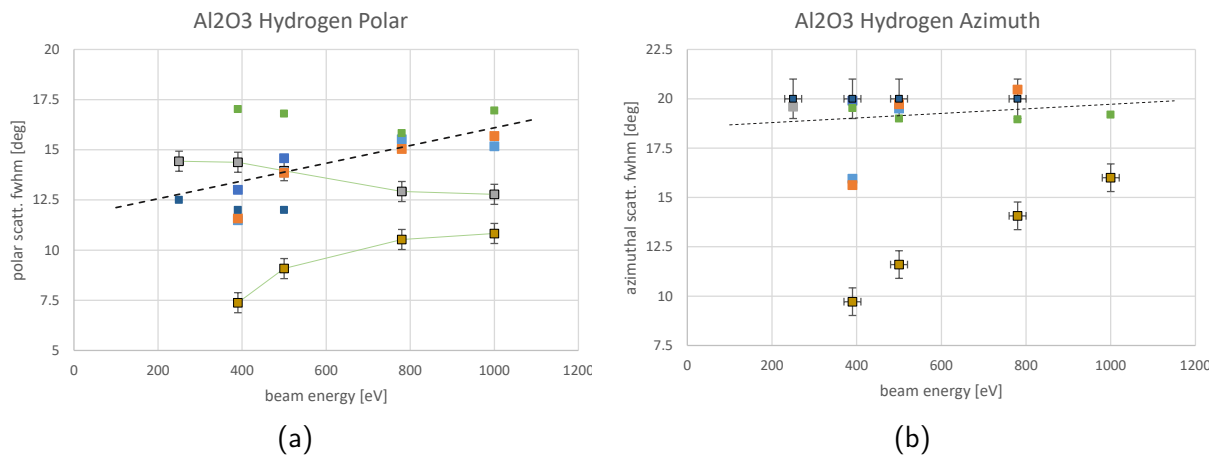


Figure 2.11.: Hydrogen polar (a) and azimuthal (b) scattering FWHM off  $\text{Al}_2\text{O}_3$  surfaces ( $\alpha = 8^\circ$ ). The azimuthal distribution tends to extend beyond the detector range, therefore these values should be taken with a grain of salt.

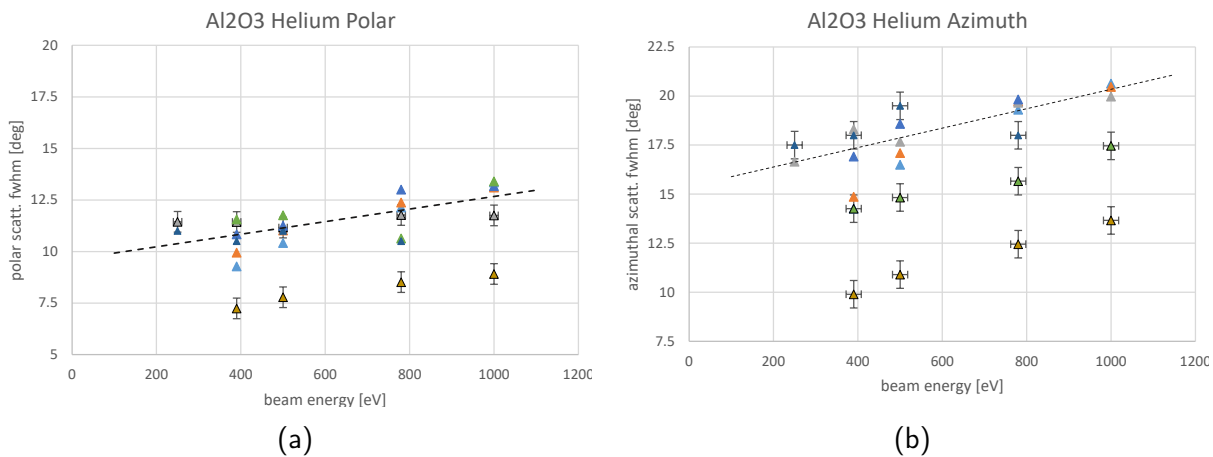


Figure 2.12.: Helium polar (a) and azimuthal (b) scattering FWHM off  $\text{Al}_2\text{O}_3$  surfaces ( $\alpha = 8^\circ$ ).

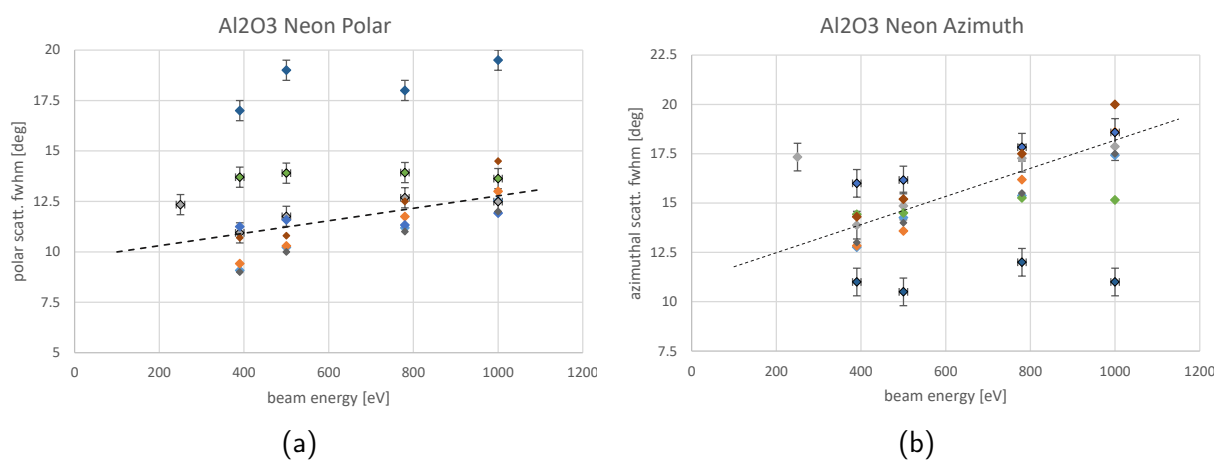


Figure 2.13.: Neon polar (a) and azimuthal (b) scattering FWHM off  $\text{Al}_2\text{O}_3$  surfaces ( $\alpha = 8^\circ$ ).

### 2.3.2. Diamond-like Carbon

Several variants of diamond or diamond-like surfaces were tested: besides the (very expensive!) bulk natural diamond these were, e.g., chemical vapor deposited (CVD) diamond and diamond-like carbon (DLC) coatings, which are sometimes referred to as tetrahedral amorphous carbon (ta-C). These carbon-based crystalline films sometimes differ in their structure, the ratio of amorphous compared to polycrystalline ordering, as well as their composition (i.e., if doped to enhance the electrical conductivity) [3, 22].

A thin film coating of diamond-like carbon (DLC) on a silicon wafer is also a conventional CS material employed in space instrumentation (e.g., Fuselier et al. [7]). In particular, the CS facets in IBEX-Lo are ta-C coated, and so will be the ones for IMAP-Lo. These CS facets are coated via plasma-immersed ion deposition (PIID) [46], produced and delivered for IMAP-Lo by the Southwest Research Institute (SwRI), San Antonio TX. (The CS facets for IBEX-Lo, however, were produced using magnetron sputtering technique.) This results in a very smooth, partly polycrystalline, partly amorphous carbon thin film whose surface bonds are hydrogen terminated afterwards to enhance chemical stability of the surface.

Much effort was undertaken in the IMAP-Lo team to ensure that the quality and testability of the FM CS facets for IMAP-Lo are at the same standard level as they were for IBEX-Lo. A first comparative measurement in ILENA was done by Martina Föhn in late 2017, when she tested an 'old' IBEX test sample (100 nm DLC film on silicon) and a newly manufactured DLC coated sample (about 20 nm film thickness) and showed very comparable results in terms of ionization efficiency and angular scattering.

In 2020, a first set of eight  $2 \times 2$  cm test samples was produced for testing in ILENA, with coating thickness of 20, 40, 80, and 100 nm, respectively. The samples were produced by magnetron sputtering technique at SwRI. Additionally, another four samples were produced at SwRI using the PIID technique, with 40 nm and 100 nm coating thickness. Originally it was foreseen to test several of these samples and investigate them primarily regarding the influence of coating thickness on charge-conversion performance. However, it soon turned out that the surfaces are not good enough to provide a clear result on the coating thickness question, a finding that was later confirmed by AFM scanning results.

Besides that, the IMAP-Lo team put more emphasis on comparing the two production techniques and impact of varying the incidence angle. Thus, it was decided to have just a few samples (*DLC 100A*, *100P*, *40P*) tested in more detail. Sample A was coated by magnetron sputtering, samples P by the PIID technique, and the number gives the approximate coating thickness in [nm]. The three samples, along with the two previous DLC samples tested in 2017, were also AFM scanned to obtain their surface roughness for comparison. The 2020 study aimed at investigating the following six questions:

- How and how much does surface roughness affect the scattering properties?
- What is the influence of the coating thickness on the charge conversion efficiency and on the angular scattering properties?
- How does the incidence angle affect conversion efficiency and scattering properties?

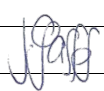
- Is the DLC coating homogeneous over the test samples?
- Are the surface scattering parameters of the test samples comparable or better than those of IBEX-Lo CS?
- Is the PIID technique suitable as well for producing DLC coatings appropriate for IMAP-Lo?

**Report on DLC Samples.** The further details of this measurement series, method and results are summarized in the Engineering Report titled *“Influence of coating thickness and surface roughness on charge conversion performance for DLC conversion surfaces”* from January 2021:

## ENGINEERING REPORT

<b>TITLE:</b> Influence of coating thickness and surface roughness on charge conversion performance for DLC conversion surfaces		<b>EM NO:</b> <b>DATE:</b> <b>REVISED:</b>
<b>AUTHOR(S):</b> Jonathan Gasser Peter Wurz André Galli	<b>PHONE:</b> +41 31 631 36 58 +41 31 631 44 26 +41 31 631 59 16	

### Distribution:

Approvals			Information Only
	Signature	Date	
Jonathan Gasser		30-Jan-2021	
André Galli			
Peter Wurz			

### Reference/Affected Documents:

Title:	Number:	Revision:

### Summary

DLC samples with varying coating thickness, to be used as conversion surfaces in IMAP-Lo, were investigated regarding their charge conversion efficiency and scattering spread. These tests were done in the ILENA facility at UBE. Under the AFM probe, they showed a rougher surface than CS samples tested for IBEX-Lo. Also, the measured angular scattering distribution is considerably wider than for the earlier IBEX-Lo conversion surfaces. The larger angular scatter is expected to result in a reduced throughput in the IMAP-Lo instrument.



## 1. INTRODUCTION

In heliosphere and space plasma research, in situ measurements of energetic neutral atoms (ENA) continue to be a relevant means of investigation. The Interstellar Boundary Explorer mission (IBEX) was the first to produce whole-sky mappings of ENA in a wide energy range<sup>1</sup>. IBEX revealed several unexpected features of the heliosphere, in particular the IBEX ‘Ribbon’. Encouraged by these findings, the successor mission Interstellar Mapping and Acceleration Probe (IMAP), which is currently under development, will improve our understanding of the local interstellar medium (LISM) and its interaction with the solar magnetic field and the heliosphere. The scientific payload also comprises IMAP-Lo, a low-energetic ENA imaging instrument dedicated to detecting interstellar neutrals (ISN) and ENA fluxes from 1000 eV down to 10 eV.

Prior to electrostatic analysis of the incident ENA, IMAP-Lo relies on an efficient method of converting ENA into negative ions. In the past decades, particle scattering on charge conversion surfaces under grazing incidence angles has become method of choice for low-energetic ENA detection in spaceborne applications, such as Mars Express, Venus Express, Rosetta, IBEX and, more recently, MINPA, BepiColombo, and JUICE (under implementation). To maximize sensitivity and resolution of the analysing instruments, one major goal is to find conversion surface (CS) materials that simultaneously achieve a narrow angular scattered particle beam and a high yield of negatively charged ions. CS materials for space applications should be chemically stable and mechanically robust on time scales commensurate with the mission duration, and should be available at affordable cost.

The incoming neutral atoms and small molecules hit the CS at grazing incidence angles of typically  $\alpha \leq 15^\circ$  or less and are scattered into a solid angle around the specular reflection direction. Diamond-like carbon (DLC) has shown to be among the most efficient suitable CS materials. A thin film of 100 nm DLC coated on a Si wafer has been used as the charge conversion surface in IBEX-Lo. Due to its long-established use in space, its good conversion efficiencies and moderate scattering cone width, DLC is the designated CS coating material in IMAP-Lo as well. A maximized negative ionization yield and minimal angular scattering are key properties of the CS with regard to enhancing the instrument throughput. As the latter is correlated with the surface roughness, smooth surfaces at atomic scales (few Å<sub>RMS</sub>) must be ensured. Other design parameters that influence the negative ion yield and the scattering width are the incidence angle  $\alpha$  of the impinging neutral atoms as well as the CS coating thickness. The incidence angle in IMAP-Lo has been set to  $\alpha = 15^\circ$ , as it was in IBEX-Lo.

---

<sup>1</sup> D.J. McComas, F. Allegrini, P. Bochsler, M. Bzowski, M. Collier, H. Fahr, H. Fichtner, H. Funsten, S. Fuselier, G. Gloeckler, M. Gruntman, V. Izmodenov, P. Knappenberger, M. Lee, S. Livi, D. Mitchell, E. Möbius, T. Moore, S. Pope, D. Reisenfeld, E. Roelof, J. Scherrer, N. Schwadron, R. Tyler, M. Wieser, M. Witte, P. Wurz, and G. Zank, "IBEX - The Interstellar Boundary Explorer," Space Science Review 146 (2009) 11-33.

## 2. EXPERIMENTAL SETUP

To investigate the principal scattering properties of a CS sample, the negative ionisation yield  $\eta$  and the angular width of the scattered beam in the directions parallel (azimuth angle) and normal (polar angle) to the surface are measured. We performed these measurements in the ILENA test facility [Wahlström et al., 2013]<sup>2</sup> using hydrogen, helium, oxygen, and neon ion beams in the energy range from 195 eV to 1000 eV under an incidence angle of 8° and 15°, respectively.

The ILENA experiment consists of an electron impact ion source, a 90° sector magnet for selection of the ion species, a beam guiding system, a pivotable sample holder, and a movable two-dimensional multi-channel plate (MCP) imaging detector with an angular field-of-view of 21° x 21° as seen from the CS sample. A schematic of the experiment setup is shown in Figure 1.

The setup is contained in a vacuum chamber equipped with a turbo molecular pump and an ion getter pump, which can establish a base pressure in the low 10<sup>-8</sup> mbar range after baking out the vacuum chamber during at least 24 hours at a temperature of 80°C. Typically, a test gas is inserted for measurements raising the pressure up to the mid 10<sup>-7</sup> mbar range, and is held in a dynamical equilibrium.

A positive ion beam is accelerated to 100 eV – about 3 keV. The ion beam is deflected and mass filtered by the sector magnet and then guided through a pinhole of about 1 mm diameter. The ion

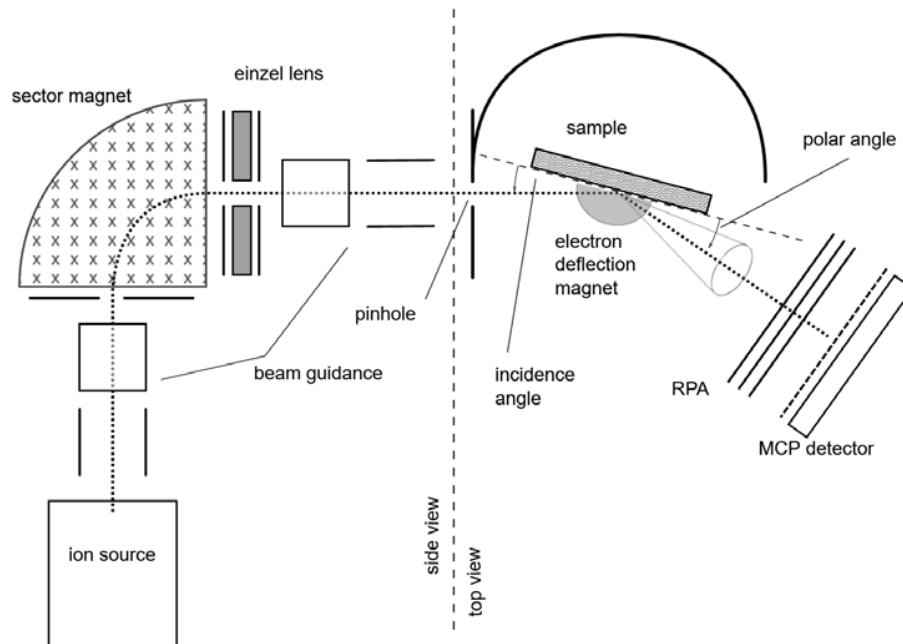


**Figure 1: Schematic of the ILENA experiment setup. The detector covers angular scattering cone of 21° x 21° (adapted from [Gasser et al., 2020]<sup>4</sup>).**

<sup>2</sup> P. Wahlström, M. Wieser, J. Scheer, A. Riedo, and P. Wurz, "Test facility to study surface interaction processes for particle detection in space," *Jou. Spacecr. Rock.* 50(2), (2013), 402-410, doi: 10.2514/1.A32134.

beam is adjusted via two perpendicular electrostatic plates before and after the sector magnet, respectively. After the pinhole, the ions impinge the CS sample and are scattered towards the MCP detector. Possible secondary electrons are effectively returned to the sample by a parallel magnetic field applied over the CS.

A retarding potential analyzer (RPA) consisting of three consecutive grids is mounted in front of the MCP detector. The outer grids are grounded while the middle grid is biased to a positive voltage to reject positive ions. The entire MCP detector may be floated to a high negative potential (HV1) for negative ion rejection. Secondary electrons emerging from the RPA or floating grids are rejected by a low-voltage grid in front of the MCP detector.

The MCP detector itself consists of five consecutive MCP's mounted in front of a quadrilateral resistive anode. A subsequent analog position computing unit determines the location of each detected particle. The entire detector unit is shielded electrostatically and can be rotated about the polar axis from  $\theta = 0^\circ$  to  $90^\circ$ .

### 3. MEASUREMENTS

#### 3.1 Objectives

The objective of this study is the investigation and characterization of a set of diamond-like carbon (DLC) coated test samples with coating thickness varying from 20 nm to 100 nm, and the comparison with previous results from IBEX-Lo test samples. Table 1 shows an overview of the test samples, with DLC samples from a conventional coating process and from a plasma immersion ion deposition (PIID) coating process. The PIID samples were produced by applying plasma immersion ion deposition as an alternative coating technique. All other samples were coated by magnetron sputtering. The surface roughness was determined by atomic force microscopy (AFM) scans at SwRI. For each listed sample, there is an identical spare sample (labelled 20B, 40B, 80B, 100B, 40Q, 100Q).

**Table 1: Overview of available samples. The measured samples are marked in green.**

	conventional DLC coating, H-terminated				PIID coating DLC	
SAMPLE	20A	40A	80A	100A	40P	100P
coating thickness	20 nm	40 nm	80 nm	100 nm	40 nm	100 nm
surface roughness, RMS [nm]	1.25	1.5	0.265	1.44	0.25	0.29

There are five questions addressed within this study:

- Are the test samples homogeneously coated?
- What is the influence of surface roughness on the scattering properties?
- What is the influence of coating thickness on conversion efficiency and scattering properties?
- How does the incidence angle affect conversion efficiency and scattering properties?

- Could the IBEX-Lo CS properties be reproduced in this set of test samples?

To answer these questions, we performed measurements on samples 100A, 100P and 40P. For each tested sample, the negative ionization yield as well as the angular scattering width was measured for incident particle energies from 195 eV to 1000 eV at incidence angles of  $\alpha = 8^\circ$  and  $15^\circ$  at two different locations on the sample, according to the measurement scheme in Table 2:

**Table 2: Measurements overview.**

incident Energy [eV]	Incidence Angle [deg]		
	8°, spot 1	8°, spot 2	15°, spot 2.
195	☑	✗	✗
250	☑	✗	✗
390	☑	☑	☑
500	☑	☑	☑
780	☑	☑	☑
1000	☑	☑	☑

Angular scattering measurements were done using primary beams of  $H^+$ ,  $He^+$ ,  $O^+$ , and  $Ne^+$  ions at an incidence angle  $\alpha = 8^\circ$  and  $15^\circ$  and beam energies of 195 eV to 1000 eV. The pressure in the vacuum chamber was held at  $(4.0 \pm 0.1) \cdot 10^{-7}$  mbar while measuring. The incident ions are neutralised shortly before reaching the CS<sup>3</sup> and are scattered as neutral atoms and negative ions.

### 3.2 Processing

For each data point, a series of five consecutive measurements is performed, with alternatingly setting HV1 to a voltage above the post-acceleration threshold (measurement no. 1, 3, 5) and to zero (meas. no. 2, 4) to measure neutrals alone and combined neutrals with negative ions, respectively. Taking into account the detection efficiencies  $\kappa_0$  and  $\kappa_-$  for neutrals and negative ions respectively, the negative ionisation yield  $\eta$  is then computed according to [Gasser et al., 2020]<sup>4</sup>:

$$\eta = \frac{N_- / \kappa_-}{\widetilde{N}_{tot}} = \frac{1}{1 + \frac{\kappa_-}{\kappa_0} \frac{N_0}{N_{tot} - N_0}}$$

<sup>3</sup> P. Wahlström, M. Wieser, J. Scheer, A. Riedo, and P. Wurz, "Test facility to study surface interaction processes for particle detection in space", *Jou. Spacecr. Rock.* 50(2), (2013), 402-410, doi: 10.2514/1.A32134.

<sup>4</sup> J. Gasser, M. Föhn, A. Galli, A. Romeo, E. Artegiani, and P. Wurz, "Cadmium telluride as a potential conversion surface", *J Appl Phys* **129**, 045303 (2021), doi: 10.1063/5.0033701

During each measurement series, the relative change of total counts ( $|N_{(i+2)} - N_i| / N_i$ ) varies by less than 2%, otherwise the measurement series is repeated.

The ionization yield  $\eta$  we find here for the noble gases He and Ne is interpreted as sputtering background of surface deposited hydrogen and oxygen on the CS (e.g. from water condensation). We use noble gases, which cannot form stable negative ions, of comparable atomic mass to estimate this sputtering background in H and O scattering, respectively:

$$\eta_H = (\eta_{(H, meas)} - \eta_{He}) \text{ and } \eta_O = (\eta_{(O, meas)} - \eta_{Ne})$$

Furthermore, the production rate of atomic ions in the ion source is quite low for the diatomic gases hydrogen and oxygen. Instead, a primary beam of molecular ions ( $H_2^+$  or  $O_2^+$ ) and twice the nominal beam energy is used occasionally to probe the scattering behaviour of H and O at low energies. This is justified by the observation that positive molecular ions dissociate shortly before hitting the CS, as described in [Wurz et al., 1997],<sup>5</sup> and consequently two individual atoms of about half the molecular beam energy enter the scattering process [Jans et al., 2001].<sup>6</sup>

The polar and azimuthal FWHM of the scattered beam are retrieved from contour plots of the detected scattering pattern. For this, the detected raw image is processed as follows:

- Each image is calibrated by the position-dependent detection efficiency of the MCP detector, which was obtained from a long-term ( $t_{int} = 40'000$  s, due to the relatively low count rate of 20–30 cts/s and for acceptable statistics) measurement without any beam production ('dark') using neutral He at a pressure of  $6.0 \cdot 10^{-7}$  mbar.
- The image is corrected for the locally lower detection efficiency in the region where the scattered particles hit the first MCP at an angle nearly parallel to the microchannel orientation, i.e. about  $8^\circ$  relative to the MCP normal. This causes a spot of reduced count number in the detected image, because particles can pass the first MCP without producing secondary electrons, which reduces the detection efficiency.
- The image is normalized to the peak maximum.
- A contour plot is printed for each of the (HV1 high) scattering patterns (see Figure 2), from which the azimuthal and polar FWHM are read out and averaged.

---

<sup>5</sup> P. Wurz, R. Schletti, and M. Aellig, "Hydrogen and oxygen negative ion production by surface ionisation using diamond surfaces", *Surf. Sci.* 373, 56 (1997).

<sup>6</sup> S. Jans, P. Wurz, R. Schletti, K. Brünig, K. Sekar, W. Heiland, J. Quinn, and R. Leuchtner, "Scattering of atoms and molecules off a barium zirconate surface", *Nucl. Instrum. Methods Phys. Res. Sect. B* 173, 503 (2001).

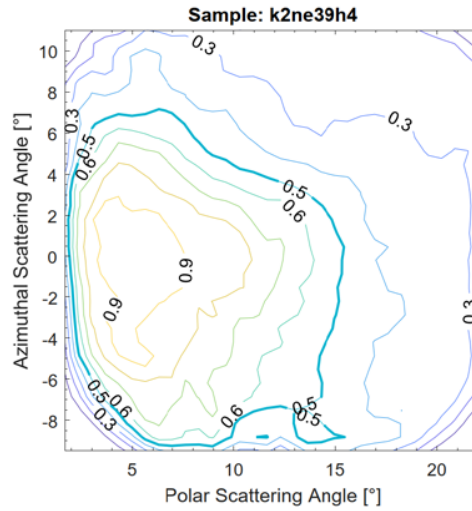


**Figure 2: Example contour plot for scattered neon at 390 eV and 8° incidence angle.**

## 4. RESULTS

In the following, the measurement data of negative ionization yield and angular scattering distribution are presented for neutral H, He, O and Ne atoms scattered off the tested DLC coated CS samples at incidence angles of 8° and 15°.

### 4.1 Negative Ionization Yield

In Figure 3, the negative ionization yield  $\eta$  for hydrogen and oxygen is shown against incident energy per atom from 195 eV to 1000 eV at incidence angles of 8° (left panel) and 15° (right panel) for the three DLC samples tested. Due to some uncertainty in the stability of the experiment conditions, statistical fluctuations and possible readout inaccuracies, an overall standard error of  $\Delta\Phi = \pm 1.0^\circ$  is assigned to the values, and a relative uncertainty in the energy per atom of  $\Delta E/E = 10\%$  is assumed in case the measurements were performed using a molecular primary beam.

The measured ionization yields are about 2% for  $\eta_H$  and 8% to 15% for  $\eta_O$ . Within the measurement uncertainties, we do not see a difference in  $\eta_H$  between the tested samples and with incidence angle.

For O, the negative ion yield is somewhat higher for the 40 nm coated sample, about 0.5% to 1% at  $\alpha = 8^\circ$ , and about 2% at  $\alpha = 15^\circ$ . In all three samples, the negative oxygen ion yield increases with kinetic energy of the incident atom.

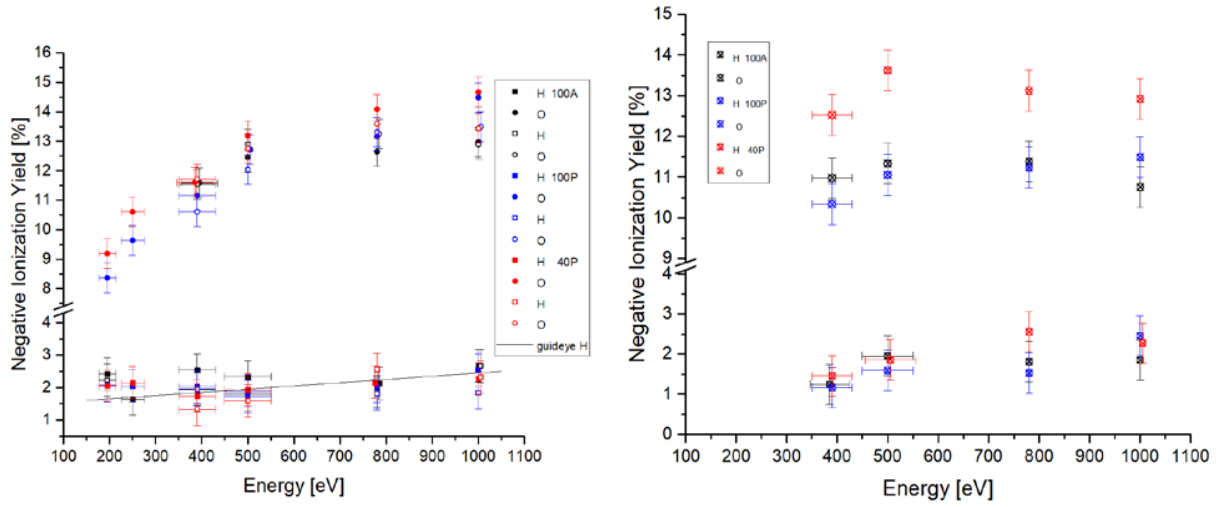


**Figure 3: Hydrogen and oxygen negative ionization yield  $\eta$  at 8° (left) and 15° (right) incidence angle, for samples 100A (black), 100P (blue) and 40P (red).**

The measured negative ion yield  $\eta$  for helium and neon for the three DLC samples are shown in Figure 4. For both species He and Ne, we see an increase in  $\eta$  with increasing energy from 195 eV to 1000 eV:  $\eta_{\text{He}} = 1.5\% - 2.7\%$  and  $\eta_{\text{Ne}} = 3.5\% - 4.5\%$  for  $\alpha = 8^\circ$ . At the larger incidence angle  $\alpha = 15^\circ$  and incident energies from 390 eV to 1000 eV, the negative ion yields for He and Ne are compatible, within the measurement uncertainties, with constant values  $\eta_{\text{He}}(15^\circ) = 3.0\%$  and  $\eta_{\text{Ne}}(15^\circ) = 7.0\%$ . Thus, we see a clear increase in the negative He and Ne ion yield with larger incidence angle:  $\eta_{\text{He}}$  increases by a factor of 1.1 to 1.3 when  $\alpha$  is nearly doubled, while  $\eta_{\text{Ne}}$  increases by a factor of 1.5 to 1.8.

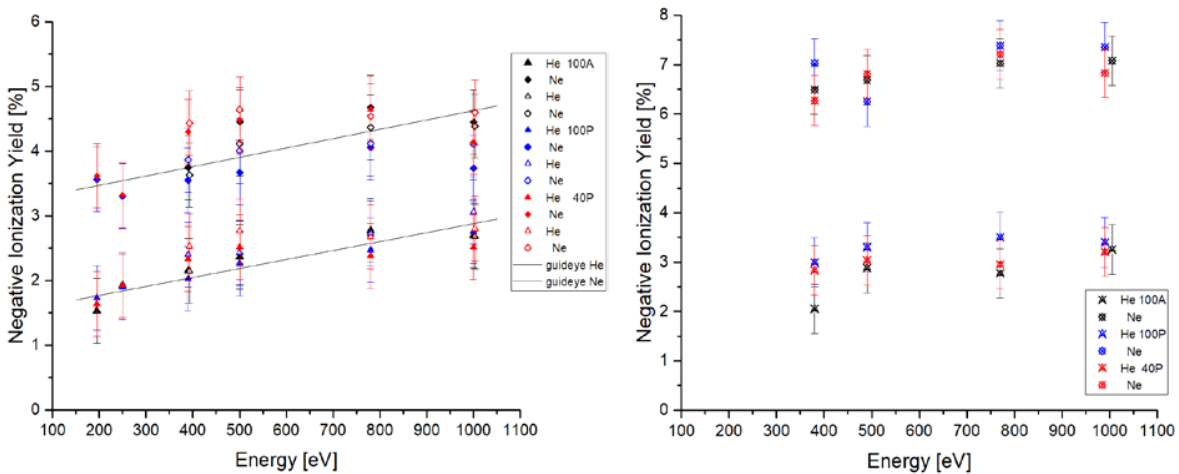


**Figure 4: Negative Ionization Yield  $\eta$  for He and Ne at incidence angle of 8° (left) and 15° (right), for DLC samples 100A (black symbols), 100P (blue) and 40P (red).**

## 4.2 Angular Scattering Distribution

The scattering distribution FWHM in polar and azimuthal directions for the test gases hydrogen, helium, oxygen and neon at energies from 195 eV to 1000 eV are shown in Figures 5, 6, 7 and 8. The angular scattering FWHM can be determined up to an estimated error of  $\Delta\theta = \pm 0.5^\circ$  for all gases. Polar or azimuthal scattering width larger than  $20^\circ$  FWHM were obtained based on a Gaussian extrapolation of the 60%, 70% and 80% contour line width, since the imaging detector size is limited to  $21^\circ \times 21^\circ$ . For the sample 100A (black symbols), all results at  $\alpha = 15^\circ$  could not be estimated since the measured angular scattering distribution was too wide.

The measurement series show consistent angular scattering results between spots 1 (full symbols) and 2 (open symbols) at each CS coating sample within the measurement uncertainty. A significant difference could only be seen across sample 100A for the He polar scatter at lower energy (Fig. 6, left). From this sample, not all data could be determined for H and O due to the large angular scattering exceeding the detector angular range.

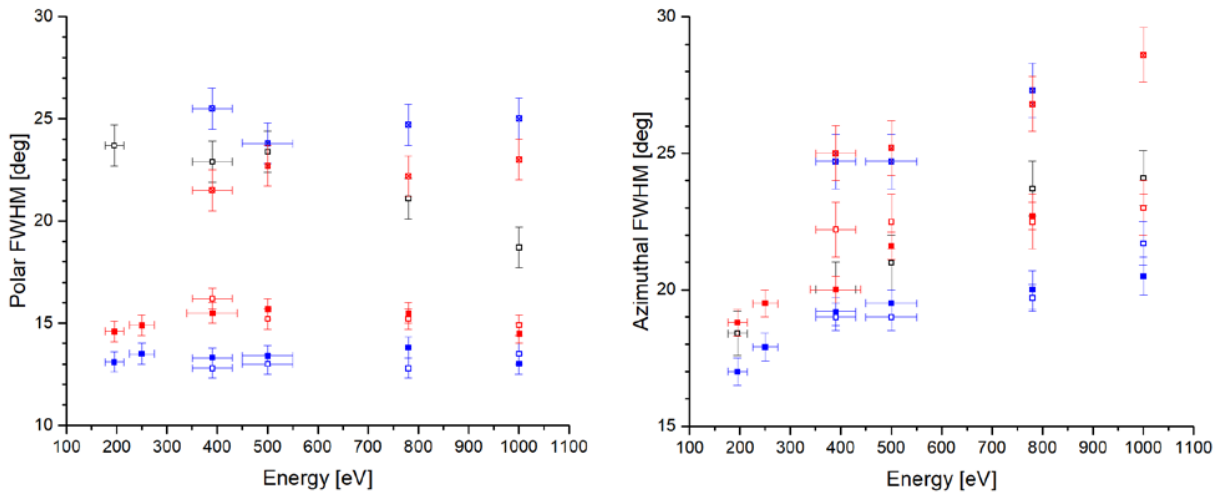


Figure 5: Hydrogen polar (left) and azimuth (right) scattering width. (*Legend: samples 100A (black), 100P (blue), 40P (red). Filled and empty symbols:  $8^\circ$  incidence angle. Crossed symbols:  $15^\circ$  incidence angle. H – squares, He – triangles, O – circles, Ne – diamonds.*)



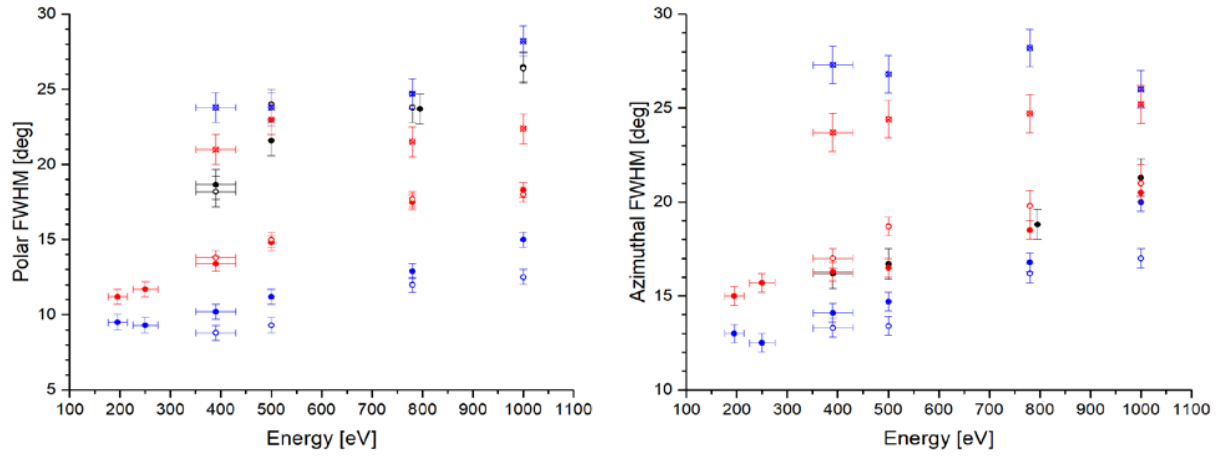


Figure 6: Polar and azimuthal scattering width for oxygen.

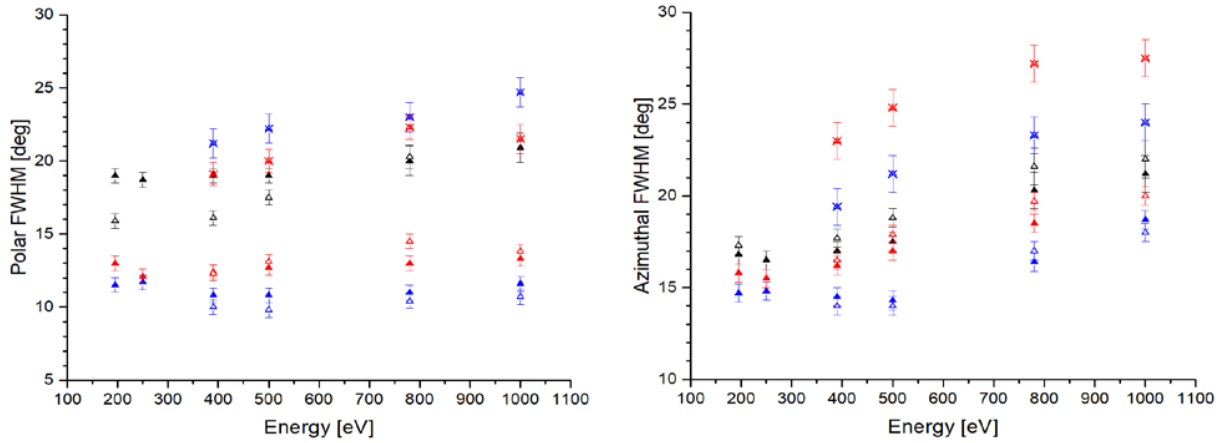


Figure 7: Polar (left) and azimuth (right) scattering width for helium.

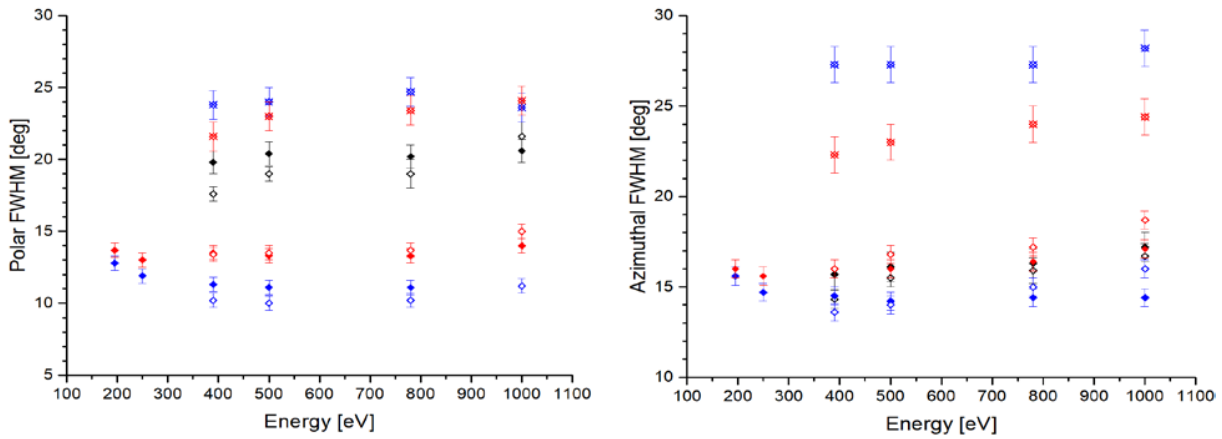


Figure 8: Polar (left) and azimuthal (right) scattering FWHM for Neon.

**Table 3: Angular scattering width of the measured samples at 8° incidence angle.**

	<b>H</b>		<b>O</b>		<b>He</b>		<b>Ne</b>	
<b>Sample</b>	<b>Polar</b>	<b>Azimuthal</b>	<b>Polar</b>	<b>Azimuthal</b>	<b>Polar</b>	<b>Azimuthal</b>	<b>Polar</b>	<b>Azimuthal</b>
<b>100A</b>	23° - 19°	18.5° - 24°	18° - 27°	16° - 20.5°	18° - 21°	17° - 21°	20°	16°
<b>100P</b>	13°	17° - 20.5°	9.5° - 15°	12.5° - 18.5°	11°	14° - 18°	11.5°	14.5°
<b>40P</b>	15°	19° - 23°	11° - 18°	15° - 20.5°	13°	16° - 19.5°	14°	16°

The angular scattering width is larger for an incidence angle of 15° compared to 8° by about 5° up to 15°, depending on the CS sample and scattered species but almost independent of the incident energy. For sample 100A (black symbols), the angular scattering for  $\alpha = 15^\circ$  could not be evaluated as the measured scattering distribution is too wide. For the sample 40P (red symbols), the angular widening is less pronounced (about +7°) than for the sample 100P (blue symbols, about +10° to +15°).

### 4.3 AFM Imaging at UBE

The tested samples were investigated using Atomic Force Microscopy (AFM) at the Department of Chemistry and Biochemistry, University of Bern, regarding the surface roughness and structure. Performing AFM measurements at the nanometer scale is quite involved and results might depend on the AFM performance and operator experience. In Figure 9, AFM images of the samples at three different resolution steps are displayed.

For each sample, at least two AFM scans were performed at five different spots each, to verify the homogeneity of the samples. No significant difference in the structure or roughness was observed, respectively, between the individual spots on each sample.

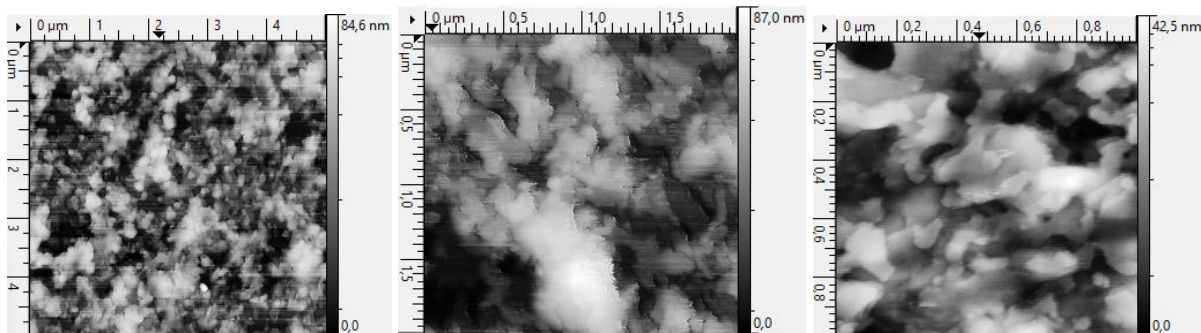


**Figure 9: AFM scans of samples 100A (left), 100P (center) and 40P (right) at scan areas of (5 μm)<sup>2</sup>, (2 μm)<sup>2</sup> and 1 μm<sup>2</sup>, respectively. The structure of the three samples is very similar.**

The two DLC samples tested in 2017 were also AFM scanned for comparison, and images are shown in Figure 10.

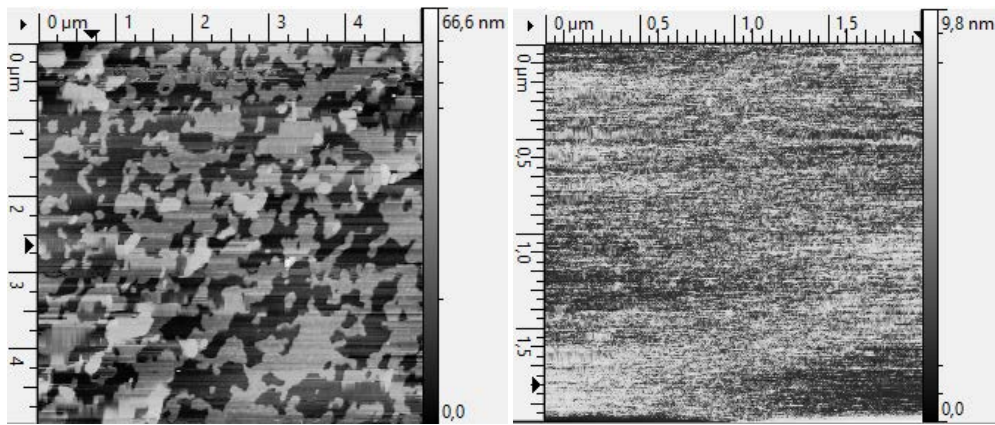


**Figure 10: AFM scans of DLC samples characterized in November 2017. Left: 100 nm coated IBEX spare sample (L125). Right: 20 nm coated "new" test sample.**

**Table 4: AFM measured surface roughness**

Sample:		Roughness			
_01	IMAP DLC 100A	4.57	+-	1.12	nm rms
_02	IMAP DLC 100P	8.20	+-	0.86	nm rms
_03	IMAP DLC 40P	8.85	+-	1.7	nm rms
_04	IBEX DLC "NEW"	0.23	+-	0.068	nm rms
_05	IBEX DLC "OLD"	4.20	+-	0.57	nm rms

#### 4.4 Former Results

The measurement results found here are compared with previous test results of IBEX test samples. Several test samples (particularly, sample L109 data are shown here in Figure 11) for IBEX-Lo were characterized and reported in 2004 by E. Herzberg and J. Scheer. Additionally, M. Föhn did a comparative investigation of a spare IBEX-Lo sample (L125) with a newly coated DLC sample in Nov. 2017.

Typical values (optimal values in case of the 2004 report) of the negative ionization yield are compared to the present results, see Figure 11.

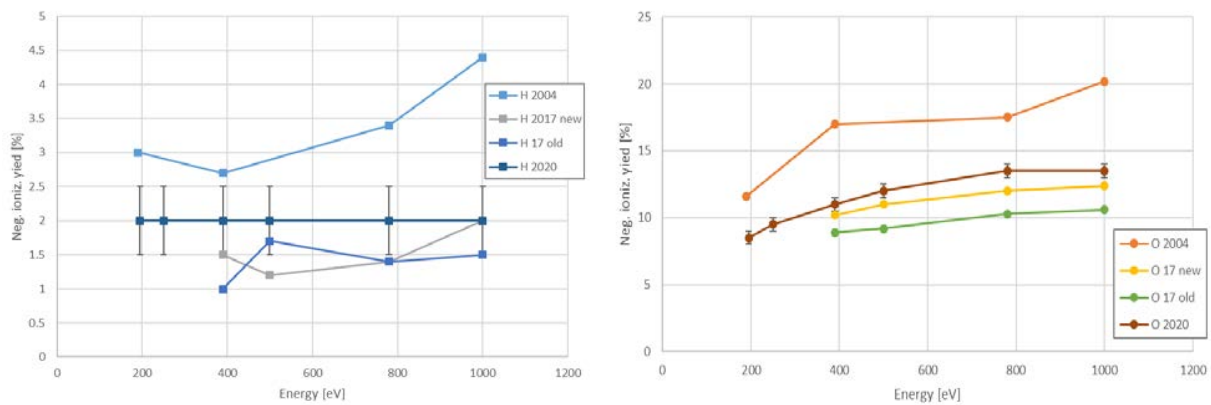


**Figure 11: Typical values of  $\eta$  for H (left) and O (right) at 8° incidence angle on sample 100P, and previous results.**

The negative ionization yield of the present samples 100A, 100P and 40P is comparable to previous DLC samples. For both H and O, the negative ionization is slightly higher than for the samples reported in 2017, but considerably lower than what was found in 2004.

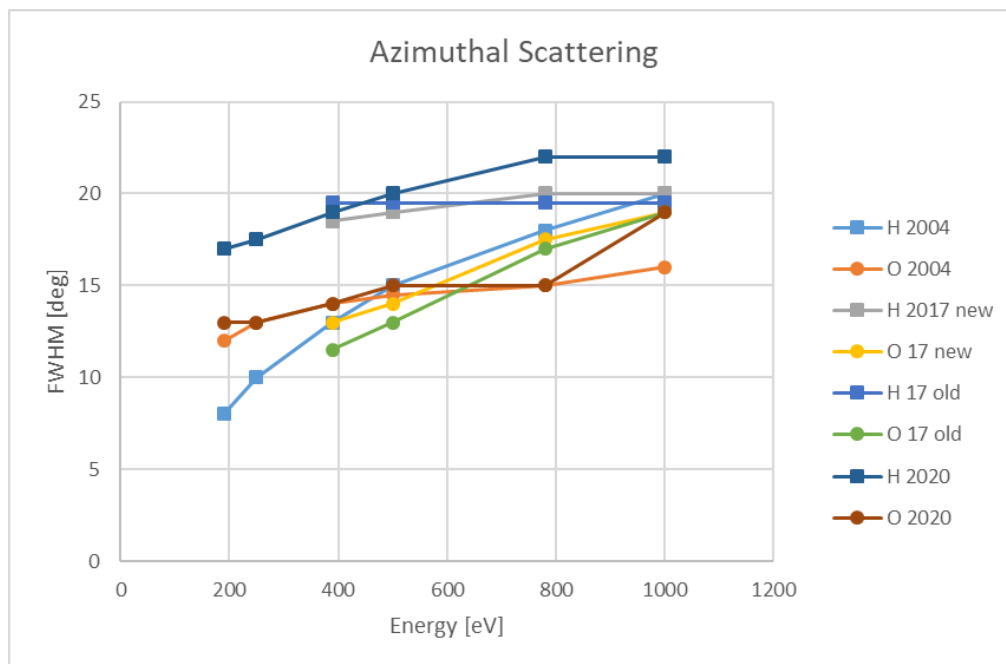


**Figure 12: Azimuth scattering width for H and O at 8° incidence angle.**

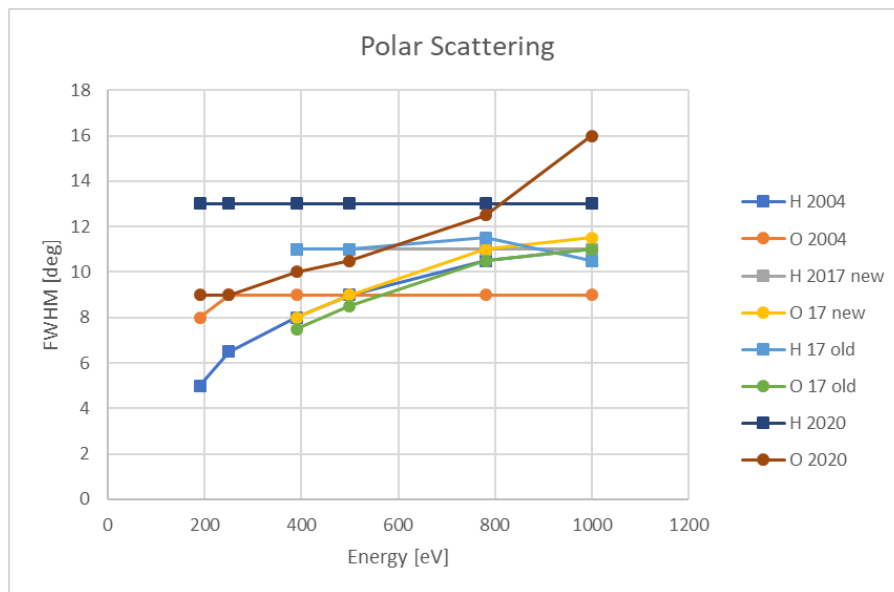


**Figure 13: Polar scattering width for H and O at 8° incidence angle.**

The angular scattering distribution is considerably wider than was reported before, except for the azimuth width for oxygen, which is similar for the newly tested DLC sample 100P as for the older samples L109 (anno 2004), L125 (2017) and the “new” 20nm coated sample (unlabeled, 2017).

## 5. CONCLUSION

We are primarily concerned about the following three points:

1. The new samples have a notably higher surface roughness compared to previous batches (2004 and 2017) as confirmed with independent AFM-measurements.
2. Scattering angles of H and O ions achieved with the new samples are as high or higher than the scattering angles measured with previous samples at most energies (see dark brown and dark blue curves in Figure 12 and Figure 13). This broadened scattering of the conversion surfaces would result in a decrease of IMAP-Lo instrument efficiency.
3. Samples 100P and 40P were produced with the same method, but differ in the coating thickness (100 nm and 40 nm). This has no observable influence on the negative ionization yield. However, the angular scattering distribution tends to increase for all test gases with reduced coating thickness. This apparent tendency remains to be confirmed with samples of lower surface roughness.

Furthermore, we report the following observations:

- All three tested samples show, within the measurement uncertainties, the same results at spots 1 and 2, respectively. This suggests the samples are coated homogeneously with a homogeneous surface structure.
- Comparing samples 100A and 100P, which are both DLC coated with 100 nm thickness, yields no significant difference in the negative ionization yield at 8° incidence angle. However, the higher surface roughness of sample 100A correlates with a broader angular scattering distribution.
- Samples 100P and 40P were produced with the same method, but differ in the coating thickness (100 nm and 40 nm). This has no observable influence on the negative ionization yield. However, the angular scattering distribution tends to increase for all test gases with reduced coating thickness (see Figure 5 and Figure 6).
- In all samples, an increased incidence angle leads to an increased sputtering background, while the negative ionization yield does not vary much. We observe a much broader angular scattering distribution in all samples and test gases at an incidence angle of 15° than at 8°.

**Engineering Report Summary.** Over all, the results for the newly produced ta-C samples reported here show much broader angular scattering for H and O, correlated with (and probably a consequence of) a much higher surface roughness of these tested samples compared to the previous results. In consequence, a wider angular spread of scattered ions would reduce the overall acceptance in the IMAP-Lo ion-optical system, an effect which is certainly not acceptable. The negative ion yield, though, is in general comparable (hence, acceptable for the instrument design) and apparently independent of the coating thickness.

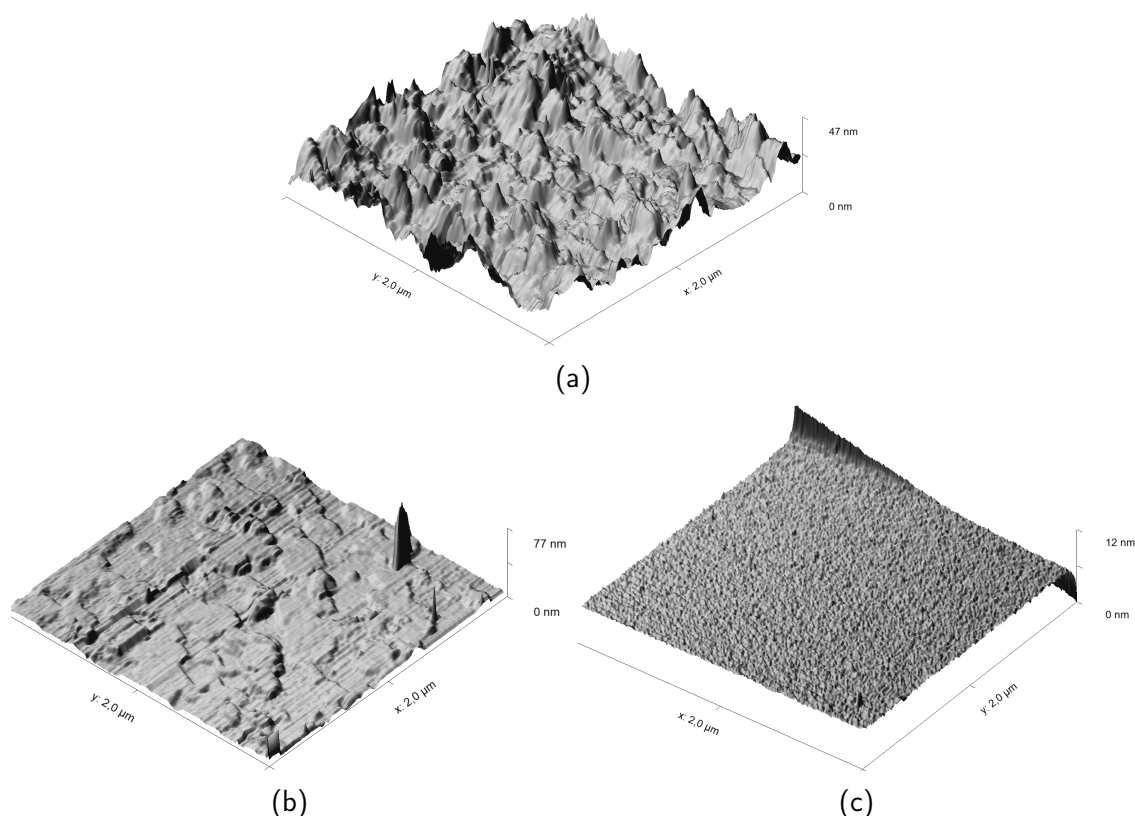


Figure 2.14.: 3D illustrations of AFM surface scans on three DLC samples from the report above. Scanning area was  $(2\mu\text{m})^2$  each. Note the different z-scales. (a) sample *100P*, representative of all samples in Fig. 9 of the report. (b) *OLD* IBEX spare sample (see Engineering Report Fig. 10, left). (c) *NEW* DLC sample from 2017 (Fig. 10, right).

To illustrate this graphically, 3D maps of AFM scans on three samples (one (a) produced and tested in 2020, an 'old' sample from IBEX (b) and (c) a newer DLC sample from 2017) are shown in Fig. 2.14. The differences in surface structure and roughness are well visible in Fig. 2.14: Sample (a) shows a very rough surface at this scale, with height differences of about 40 nm, while on sample (b) we see large flat plateaus with only minor edges, and (c) is flat on the nanometer level with fine-grained structure. The bending on the right edge is a scanning artefact. This shows that the samples produced in 2020 do not meet the surface quality of previous IBEX-Lo samples.

**DLC test samples for IMAP-Lo EM.** In fall 2021, another set of test samples for investigation in ILENA was produced at SwRI. Two possible suppliers of Si wafers for instrument facet production were available: Sil'Tronix<sup>3</sup> and Virginia Semiconductors<sup>4</sup>. A lot of three test samples each, produced from Si wafers from both companies, was shipped to the University of Bern for testing. Out of the six samples, two of each that showed the smoothest surfaces in AFM scans (samples *SW-004*, *SW-006*, *VW-003*, *VW-006*) were tested in ILENA at 8° incidence angle. One aim of this study was to determine which of the Si wafer suppliers is best suited in terms of delivering the smoothest, flat and homogeneous Si wafers for producing the CS facets for the IMAP-Lo flight model. A summary of the results for oxygen are shown in Figures 2.15 and 2.16. The respective results for hydrogen, helium and neon can be found below (Figs. 2.17 to 2.20).

Along with the production of a set of CS facets for the IMAP-Lo Engineering Model (EM), a few test samples were produced again that are representative for the EM CS. Two of these DLC samples (*VW-036*, *VW-039*) were characterized in ILENA in summer 2022. Those results are also contained in Figures 2.15 and 2.16, and are compared with the previously measured test samples. The sample *VW-036* measurement was repeated (open dots) after a too large incidence angle ( $\alpha = 10^\circ$ ) was diagnosed during sample removal. At  $\alpha = 8^\circ$  it showed only minor reduction in the oxygen ionization efficiency but a clearly narrower angular scattering distribution by roughly 2° (see Fig. 2.16a and b).

We see that there is some significant scatter in the data from different samples that is larger than the measurement uncertainty. This can be due to several reasons:

- Differences in the cleanliness of individual samples: even though all samples were cleaned and installed under the same procedure and tested under the same vacuum conditions, impurities and/or the persisting water layer might not always be precisely the same.
- The variations may reflect the homogeneity and/or reproducibility of the CS coatings, or effect of surface structure at atomic level.
- Several systematic uncertainties cannot be excluded: changes in the vacuum conditions from sample to sample (e.g., residual gas pressure), the beam stability, the magnetic field and the incidence angle ( $\sim \pm 0.3^\circ$ ) at installation.
- A number of other factors to be considered beforehand can be excluded from causing the variation in results: the sample position is accurately reproducible, the detector setup is unchanged, the beam size is significantly smaller than the sample, the beam strength is irrelevant as only relative count rates are evaluated, and the change in beam strength over time is checked to be less than 1 %.

In short, we have no clear answer at hand as to why different DLC samples produced in the same manner show differing results. One takeaway here is that the set of samples (and thus all untested samples and CS facets) shows a larger range of ionization efficiency and angular scattering than the uncertainties of an individual sample measured in ILENA.

---

<sup>3</sup>Sil'Tronix Silicon Technologies SA, Archamps (F), [www.sil-tronix-st.com](http://www.sil-tronix-st.com)

<sup>4</sup>Virginia Semiconductor Inc., Fredericksburg VA, USA, [www.virginiasemi.com](http://www.virginiasemi.com)



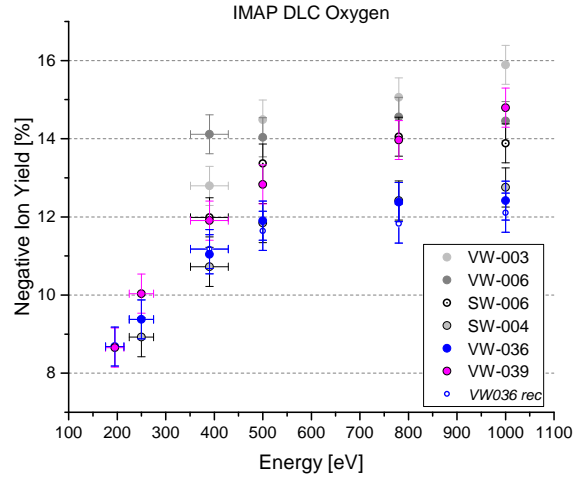


Figure 2.15.: Oxygen negative ion yield  $\eta_O$  from scattering on different DLC test samples at  $\alpha = 8^\circ$ . Repeated results on sample VW-036 (open dots) showed consistent ion yield.

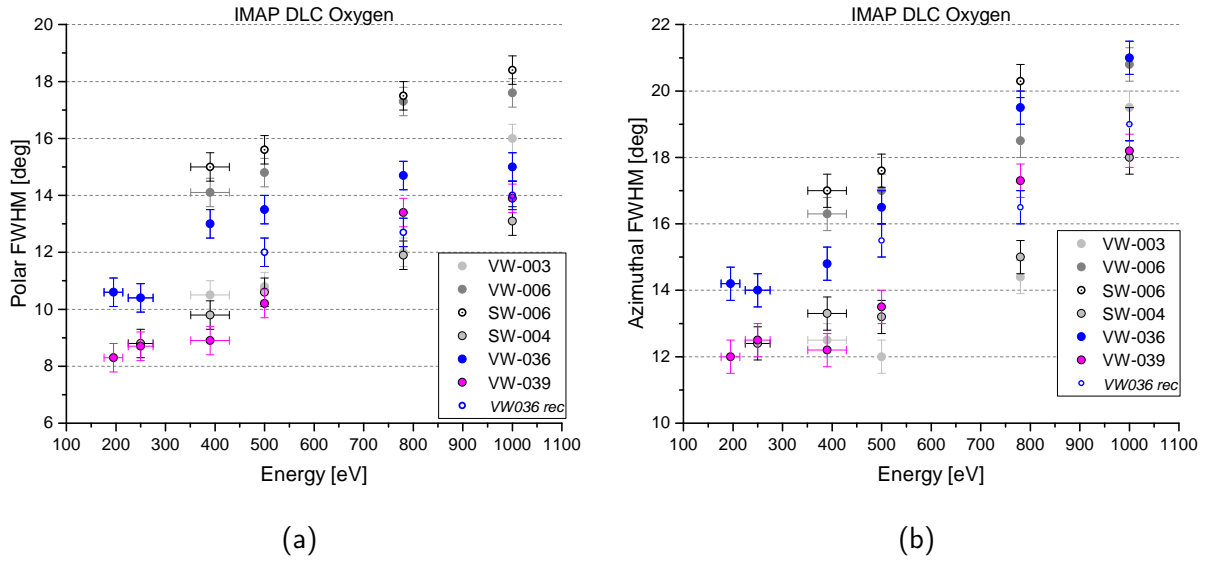


Figure 2.16.: Width of angular scattering distribution for oxygen on different DLC test samples, incidence angle  $\alpha = 8^\circ$ . (a) polar, (b) azimuthal FWHM.

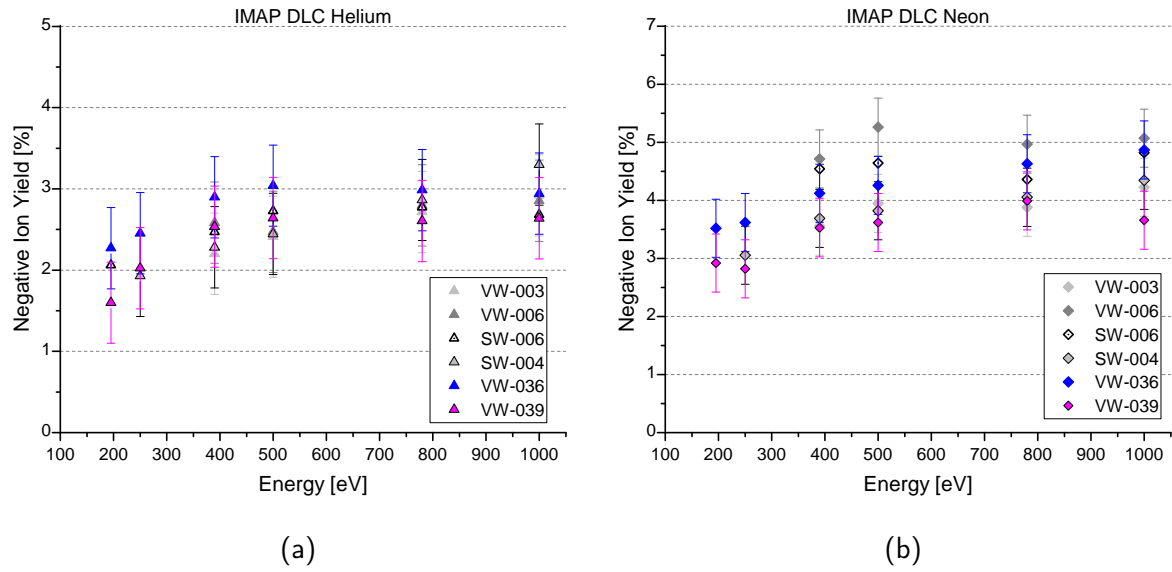


Figure 2.17.: Effective negative ion yield from (a) helium and (b) neon incident on different DLC samples at incidence angle  $\alpha = 8^\circ$ .

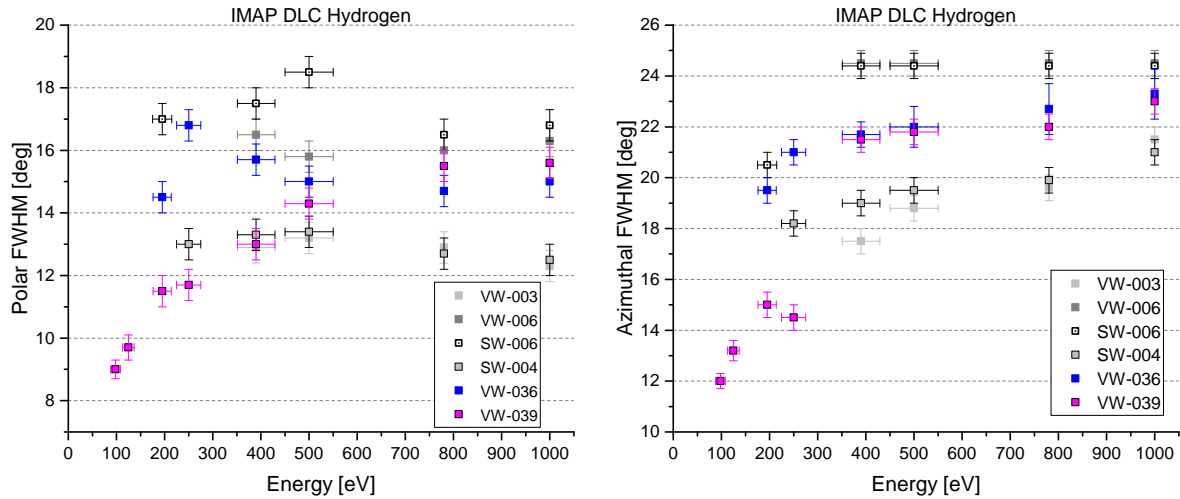


Figure 2.18.: Angular scattering distribution width of hydrogen on DLC test samples.

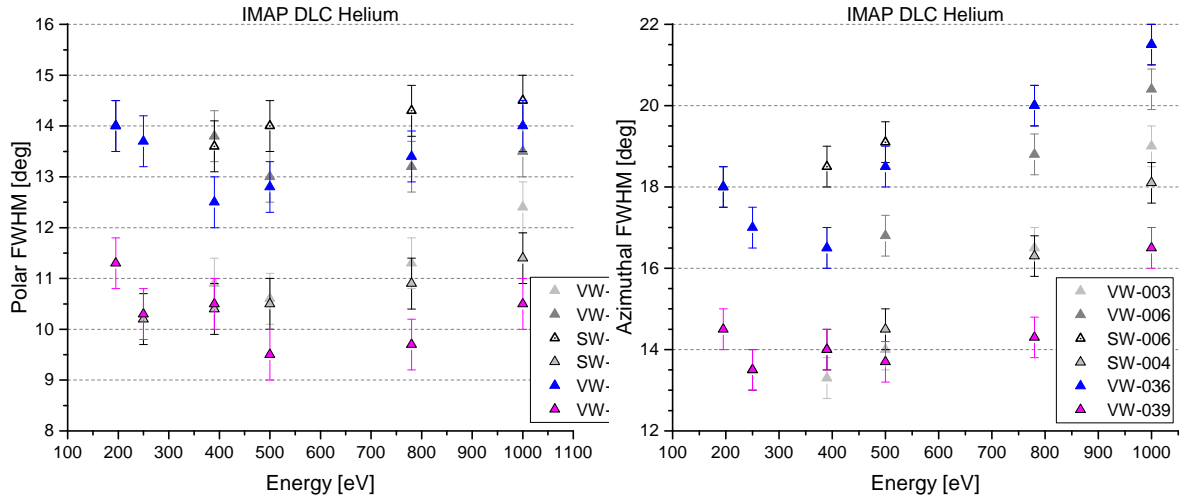


Figure 2.19.: Angular scattering distribution FWHM of helium on DLC test samples.

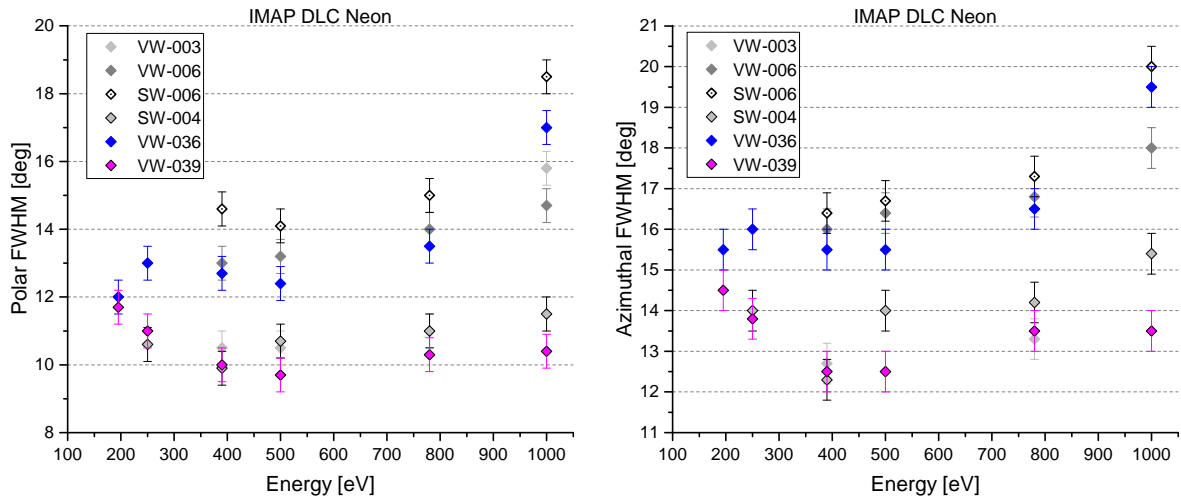


Figure 2.20.: Angular scattering distribution FWHM of neon on DLC test samples.

### 2.3.3. Paper: “Cadmium Telluride as a potential conversion surface”

In the search for new suitable and potentially much more efficient conversion surface materials, cadmium telluride (CdTe) has been selected for testing as one of the first semiconductor CS coating materials. Fortunately, the photovoltaics research group of Alessandro Romeo (LAPS, University of Verona, Italy) have the expertise on thin film solar cells (including CdTe) and have been able to produce test samples by CdTe coating deposition on a Si wafer substrate.

The following article *"Cadmium telluride as a potential conversion surface"* summarizes the considerations for testing CdTe as a CS coating material, the main material properties (section I), the ILENA experiment setup and procedure (Sections II.A and II.C), the CdTe sample preparation and characterization (Section II.B) as well as the measurement results (Sections III and IV).

The negative ionization efficiency of H and O was measured for energies from 195 eV to 1000 eV at 8° incidence angle as well as the angular scattering distribution. Additionally, the coarse energy distribution of scattered ions was recorded for incident  $O_2^+$  ions by retarding potential analysis. That way I could confirm that incident molecular ions are effectively disintegrated into atoms within this energy range. This is in agreement with previous results [18, 52].

On scattering off CdTe the measured negative ion yield  $\eta$  was up to 13 % for O and about 2 % for H, which is comparable to DLC coatings in use. For H, the negative ion yield is also comparable to the one of  $Al_2O_3$ , but for O, somewhat higher negative ion values are reported (up to  $\eta_O = 15$  %). In terms of angular scattering, the distribution widths on CdTe tend to be narrower than on typical DLC or  $Al_2O_3$  samples, with oxygen azimuth FWHM of 10° to 14° and polar FWHM of 10° to 17°. This is despite the rather high measured surface roughness of the CdTe sample. Particular about CdTe is that the ratio of azimuth/polar width is smaller than for most other materials, meaning the angular scatter distribution is narrower in the azimuth and thus more circular. This might be of advantage for ion-optical designs in future ENA instruments that are effective in focusing negative ions in elevation but less tolerant of deviating trajectories in azimuth direction from the CS.

**Perspective.** These first measurements showed that there is potential in CdTe as a CS material, as it results in high negative ion yield. The investigated CdTe coating was rather too rough, resulting in a wide angular scatter. As described in the article, with some effort a smoother CdTe coating can be produced, that might lead to a narrower angular scattering distribution and/or enhanced ionization efficiency. In fact, Elisa Artegiani at the University of Verona has produced a set of two CdTe coated samples, which are available to be tested in ILENA, with reduced surface roughness according to first AFM scans. Evaluation and comparison of those results will hopefully clarify if CdTe is still a competitive alternative CS coating material and whether it should be used as such in an ENA space instrument.

*The following article reprint "Cadmium telluride as a potential conversion surface" is reproduced from J. Appl. Phys. 129, 045303 (2021); doi: 10.1063/5.0033701, with the permission of AIP Publishing.*

# Cadmium telluride as a potential conversion surface

Cite as: J. Appl. Phys. **129**, 045303 (2021); doi: [10.1063/5.0033701](https://doi.org/10.1063/5.0033701)

Submitted: 18 October 2020 · Accepted: 12 January 2021 ·

Published Online: 29 January 2021



Jonathan Gasser,<sup>1,a)</sup> Martina Föhn,<sup>1</sup> André Galli,<sup>1</sup> Elisa Artegiani,<sup>2</sup> Alessandro Romeo,<sup>2</sup>   
and Peter Wurz<sup>1</sup>

## AFFILIATIONS

<sup>1</sup>Physics Institute, Space Research and Planetary Sciences, University of Bern, Sidlerstrasse 5, 3012 Bern, Switzerland

<sup>2</sup>Department of Computer Science, Laboratory for Photovoltaics and Solid State Physics, University of Verona, Strada le Grazie 15, 37134 Verona, Italy

<sup>a)</sup>Author to whom correspondence should be addressed: [jonathan.gasser@space.unibe.ch](mailto:jonathan.gasser@space.unibe.ch)

## ABSTRACT

In instruments for low energetic neutral atom imaging of space plasmas, a charge state conversion surface (CS) is used to convert neutral atoms into ions for detection. We investigated a cadmium telluride (CdTe) coated sample as a novel material candidate regarding its suitability to be used as a CS. We measured the efficiency of converting H and O atoms into negative ions by surface scattering, as well as their angular scattering distribution, for energies from 195 eV to 1 keV at 8° incidence angle. Also, the energy distribution of scattered particles was recorded for incident O<sub>2</sub><sup>+</sup> ions, which confirms that molecules are mainly scattered as single atoms. The mean energy loss per atom was about 45%. The negative ion yield from scattering off CdTe was up to 13% for O and about 2% for H, which is comparable to other CS coatings in use. CdTe shows a nearly circular angular scattering cone of width comparable to established CS materials. We conclude that CdTe is a viable CS coating material for ENA instruments in space applications.

Published under license by AIP Publishing. <https://doi.org/10.1063/5.0033701>

## I. INTRODUCTION

Spaceborne instruments for energetic neutral atoms (ENAs) continue to be a highly relevant tool for interplanetary and interstellar space plasma research. Reviews on scientific techniques and instrumentation for imaging of space plasmas can be found in Gruntman,<sup>13</sup> Williams *et al.*,<sup>38</sup> and Wurz.<sup>40</sup> Several past and present space missions have been equipped with an ENA instrument at low energies, such as IMAGE,<sup>22</sup> Mars and Venus Express,<sup>3,4</sup> Chandrayaan-1,<sup>2,6,16</sup> and BepiColombo.<sup>24</sup> The well-known IBEX mission<sup>9,20</sup> has brought light on, among others, the global heliospheric structure by observing the plasma of the heliospheric interface via ENAs from Earth's orbit. While IBEX is expected to run until at least 2025, its successor mission the Interstellar Mapping and Acceleration Probe (IMAP) is currently under development,<sup>21</sup> with a low-energetic ENA camera being among the scientific instruments. Most recently, the upcoming JUICE mission (Jupiter Icy Moons Explorer)<sup>10</sup> by ESA also includes two ENA instruments for low- and high-energy ENAs in its particle environment package.<sup>5</sup>

All the low-energetic neutrals instruments for space research rely on an efficient method of ionization for the ENAs to electrically analyze the ENAs.<sup>40</sup> To date, in the low-energy range, the most widely used method and so far the only space-proven is via surface conversion: Neutral particles strike a highly polished charge-state conversion surface (CS) at a grazing angle of incidence and thereby pick up an electron while being scattered. An overview of negative ion sources and their application to accelerator physics and plasma research is given in Faircloth and Lawrie.<sup>7</sup>

The underlying physical theory of particle charge conversion upon surface scattering at a grazing incidence angle is still not understood in full detail. Quite a few theoretical models exist for special types of surfaces such as metals or alkali halides.<sup>19,39</sup> Negative ionization happens via resonant electron transfer from the crystal lattice to the incident atom's electron affinity level. Thus, a low work function in the surface material enhances electron transfer to the atom. However, diamond and other insulator surfaces with high work function showed comparably high negative ionization efficiency,<sup>42</sup> which are probably promoted by surface states.

The efficiency of converting neutral atoms into ions and the scattering properties strongly depend on the CS material. A high yield of negative ions and a narrow angular scattering cone both directly alter the instrument efficiency by improving the throughput of downstream ion-optical elements within the instrument. In space ENA imaging instruments, the CS should at least yield about 1% negative ions for the ENA species of interest (predominantly H and O). Even though this seems a low value, the 1% ion yield is required for an acceptable signal to background level, which is a key criterion especially in low-energy ENA instrumentation.<sup>40</sup> Compared, e.g., to electron impact ionization, with efficiencies of about  $10^{-4}$ , this is still respectable for a passive ionization method. Moreover, this ionization method does not require electrical power, which is a big advantage for space instrumentation. In addition, CS materials for space applications should be chemically stable and mechanically robust on long time scales, without possibly hazardous components, show no degeneration or surface charging effects, and should be readily available at affordable cost. Various materials have been considered and investigated over the past decades (cf., Wurz *et al.*<sup>41</sup> and references therein).

Among the highest negative ion yields have been reported for aluminum oxide<sup>26</sup> ( $\text{Al}_2\text{O}_3$ ) and diamond-like carbon<sup>1,23,30,36</sup> (DLC), conversion surfaces, which both have been successfully applied in several space missions, e.g., in BepiColombo<sup>24</sup> and IBEX.<sup>9</sup> Nevertheless, there is interest in finding potential CS materials offering improved conversion efficiencies, less angular scattering, and less energy scattering to achieve even better performance in future space instrumentation.

Cadmium telluride (CdTe) was chosen as a candidate surface material based on the high atomic mass of its two components, Cd and Te, compared to the atoms of interest in space plasma research. In the binary collision model, ion-surface scattering happens via a single ideal collision of the incident atom (mass  $m_1$ , kinetic energy  $E_i$ ) with a surface atom (mass  $m_2$ ) in the crystalline lattice at rest. The incident atom is scattered by the angle  $\theta$  from its initial trajectory, thereby some portion ( $p'_2, E'_2$ ) of the energy-momentum is transferred to the lattice atom. The relative amount of the incident atom's kinetic energy lost in the collision,  $\delta E_i/E_i$ , would then depend on the mass ratio according to

$$\frac{\delta E_i}{E_i} = \frac{E'_2}{E_i} = \frac{m_1}{m_2} \sin^2(\theta) \left( 1 + \frac{1}{4} \left( 1 - \frac{m_1}{m_2} \right)^2 \sin^2(\theta) \right) + \mathcal{O}(\theta^6) \quad (1)$$

for small deflection angles  $\theta$ . If applicable, this suggests that the energy transfer from the incident atom to the surface should be reduced for mass ratios  $m_2/m_1$  much larger than one, as opposed to carbon or oxygen atoms in CS coating materials such as DLC or  $\text{Al}_2\text{O}_3$  ( $m_{\text{C}}/m_{\text{O}} \simeq 0.75$ ,  $m_{\text{O}}/m_{\text{Ne}} \simeq 0.8$ ). For CdTe, the most abundant isotopes are  $^{110}\text{Cd}$ ,  $^{111}\text{Cd}$ ,  $^{112}\text{Cd}$ ,  $^{114}\text{Cd}$ ,  $^{126}\text{Te}$ ,  $^{128}\text{Te}$ , and  $^{130}\text{Te}$ , which yields mass ratios of  $m_{\text{Cd}}/m_{\text{O}} \geq 6.8$  and  $m_{\text{Te}}/m_{\text{O}} \geq 7.8$ .

Moreover, CdTe is a II–IV semiconductor material. It has a crystalline sphalerite structure (F43m), a lattice constant of 6.48 Å, and a direct band gap of 1.56 eV. Its work function is about  $\Phi = 5.7$  eV and the melting point is above 1300 K, and it is nearly insoluble in water. CdTe is widely used as an absorber

material in thin film solar cells.<sup>11,12</sup> Alloyed with Hg or Zn, it makes an efficient infrared (IR), x-ray, or gamma ray detector material.<sup>18,27,33,34</sup> Furthermore, CdTe is used for IR optical windows and lenses. It, therefore, fulfils the aforementioned criteria to be considered a suitable CS material for space applications. Other similar semiconductor materials with the same crystal structure have a larger bandgap and reveal other disadvantages (e.g., ZnTe is flammable, CdSe is toxic and a suspected carcinogen, GaAs oxidizes over time, and ZnSe may react with acids to form toxic  $\text{H}_2\text{Se}$ ). Despite its heavy metal component, the possible harmfulness of CdTe is very moderate and is further evaluated due to its wide application in photovoltaic research and production.

## II. SETUP AND METHODS

### A. ILENA test facility

The measurements were done in the Imager for Low Energetic Neutral Atoms (ILENA) test facility<sup>35</sup> at University of Bern. The ILENA setup consists of an electron impact ion source, a 90° sector magnet for ion species selection, a beam guiding system, a rotatable sample holder, and a movable two-dimensional imaging multi-channel plate (MCP) detector with an angular field-of-view of  $21^\circ \times 21^\circ$  as seen from the sample center. A schematic overview of ILENA is shown in Fig. 1. The experimental setup is contained in a vacuum chamber equipped with a turbo molecular pump and an ion getter pump, which establish a base pressure in the low to mid- $10^{-8}$  mbar range.

In the ion source, positive test gas ions are produced and extracted by a post-acceleration voltage of 100 V–3 kV. The ion beam is then focused and guided into the sector magnet, where the ion species of interest is selected by applying the appropriate magnetic field normal to the ion beam. The ion beam passes through a 1 mm diameter pinhole before it strikes the CS sample under an adjustable grazing incidence angle. In the scattering

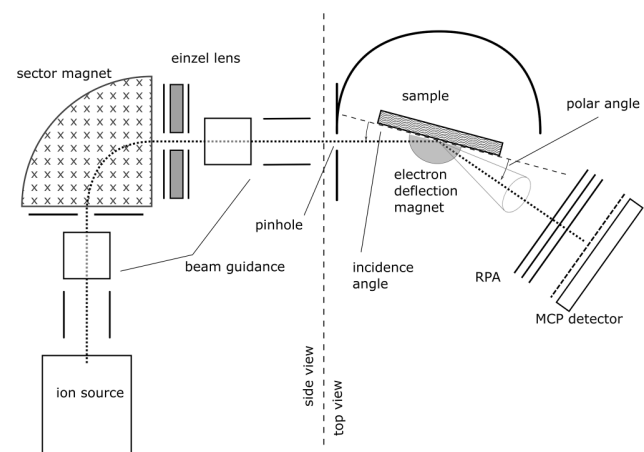


FIG. 1. ILENA measurement setup.

interaction with the CS, a memory loss of the initial charge state of the atom happens,<sup>7,28,37,42</sup> i.e., atoms of different charge state ( $H^+$ ,  $H^0$ ,  $H^-$ ) experience the same scattering and negative ion yield. The interaction can, therefore, be regarded as acting between a neutral atom and the CS. This was also experimentally confirmed in Jans *et al.*<sup>15</sup>

A weak vertical magnetic field is used at the CS to direct released secondary electrons back onto the CS. After charge-exchange interaction with the sample, the particles are scattered toward the MCP detector. A retarding potential analyzer (RPA) prevents positive ions from reaching the detection subsystem; low-energy electrons are rejected likewise by a slight negative potential grid in front of the detector. Therefore, only neutral atoms and negative ions are detected.

The MCP detector itself consists of five consecutive MCPs mounted in front of a quadrilateral resistive anode. A subsequent analog position computing unit determines the location of each detected particle. The entire detector unit, including the RPA, is shielded electrostatically. It can be rotated about the polar axis at the sample holder center from  $\theta = 0^\circ$  to  $90^\circ$ . The entire MCP detector may optionally be floated on a high negative potential to reject negatively charged ions.

## B. Sample preparation and characterization

The CS sample under test consists of a highly polished Si wafer coated with cadmium telluride (CdTe) of about 35 nm thickness, according to parameters during the fabrication process. Two identical trapezoidal Si wafer facets of about  $18 \times 28 \text{ mm}^2$  and 1 mm thickness were prepared for coating. Initial surface roughness was about 0.1 nm rms. The CdTe layer was deposited at the Laboratory for Photovoltaics and Solid State Physics, University of Verona, Italy. CdTe was deposited by thermal evaporation in vacuum with a deposition rate of 0.29 nm/s at a pressure of  $10^{-5}$  mbar. CdTe lumps are put in a graphite crucible and brought to a temperature of around  $700^\circ\text{C}$ , the deposition rate, and the thickness is controlled by a quartz thickness monitor. The process duration was 2 min. The substrate temperature reached  $90^\circ\text{C}$  during the coating process. According to Heisler *et al.*,<sup>14</sup> these conditions might result in a slight Te excess of a few percent compared to the nominal stoichiometric ratio (Cd:Te = 1:1), which is not considered relevant for this application. The surface of one CdTe-coated sample was investigated for its roughness using atomic force microscopy (AFM) at the Department of Chemistry and Biochemistry, University of Bern. We measured the surface roughness from AFM scans at three different locations on the sample: one near the center, another one near the lower left rim, and a third near the upper right rim. The AFM operates at ambient conditions with a FlexAFM scan head and a Tap190AI-G cantilever. Each location was scanned twice, with an imaging resolution of  $256 \times 256$  pixels per  $5 \mu\text{m}$  and  $1 \mu\text{m}$ , respectively.

Figure 2 shows an AFM image of the CdTe surface. It reveals a granular surface structure with about 25 nm grain size. On large scales, the coated surface is homogeneous with only very few small defects. The measured surface roughness was averaged over the total area of three spots, which all showed very similar results for

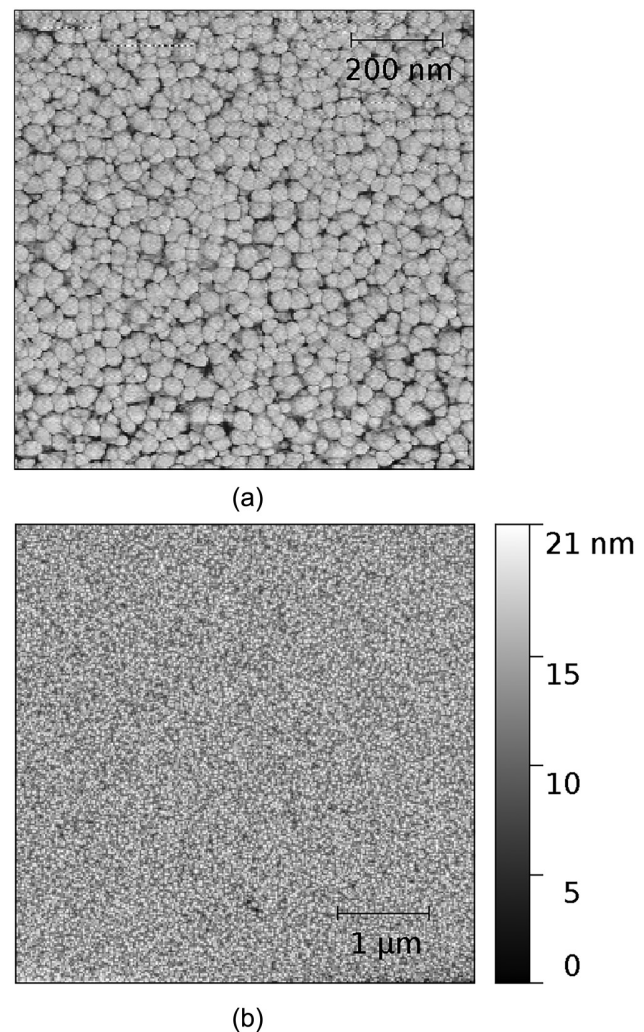


**FIG. 2.** AFM image of the CdTe surface. (a) Phase image that clearly shows the granular structure. The image area is  $1 \mu\text{m}^2$ . (b) Grayscale-coded height profile. The image area is  $5 \mu\text{m}^2$ .

all scanned spots at either imaging resolution. This yields a surface roughness  $\mathcal{R}$  of

$$\mathcal{R} = 2.8 \pm 0.05 \text{ nm}_{\text{rms}}$$

with maximal height differences of about 20 nm peak-to-valley. This is significantly rougher than previous tested samples of different materials, by a factor of 2–3<sup>1,23</sup> to more than a factor of 10.<sup>26,36</sup> Furthermore, we obtained the coating thickness by measuring the height difference at the edge of the coated area, because a margin of about 2 mm remained uncoated. At several places along the coating edge, the surface height was compared



for two points separated about  $600\mu\text{m}$  across the coating edge. The CdTe coating thickness was measured to be  $38.0 \pm 4.0\text{ nm}$  using interferometry.

### C. Measurement procedure

After the sample installation, the vacuum chamber was baked out during 48 h at a temperature of  $T = 80^\circ\text{C}$ . Before starting a measurement, test gas was inserted into the ion source, which increases the pressure in the vacuum chamber, and held in dynamical equilibrium at a pressure of  $(4.0 \pm 0.1) \times 10^{-7}\text{ mbar}$ . The typical base pressure before gas insertion was  $(2.5 \pm 0.5) \times 10^{-8}\text{ mbar}$ .

An ion beam was produced and ion-optical throughput was optimized using the focusing and deflection plates. For each test gas, a series of five consecutive measurements was performed, alternating between floating and the grounded detector subsystem to keep track of long-term system stability (cf., Fig. 3 in Neuland *et al.*<sup>23</sup>). When high-voltage floating the detector, it only accepts neutrals ( $N_h = N_0$ ), while on ground potential, negative ions and neutrals  $N_z = N_- + N_0$  are detected. In each single measurement, at least  $10^6$  counts were collected to guarantee sufficient statistics.

The negative ionization yield  $\eta$  is then computed<sup>8</sup> from the numbers  $\tilde{N}_{(0,-)}$  of neutral atoms and negative ions scattered off the CS,

$$\eta = \frac{\tilde{N}_-}{\tilde{N}_0 + \tilde{N}_-} = 1 - \frac{1}{1 + \alpha \frac{\tilde{N}_-}{\tilde{N}_0}} = 1 - \frac{1}{1 + \alpha \left( \frac{N_z - N_h}{N_h} \right)}, \quad (2)$$

where the parameter  $\alpha = \kappa_0/\kappa_- < 1$  is the ratio of the detection efficiencies of neutrals and negative ions and  $N_{(z,h)}$  are the number of counts detected, respectively, with zero and high negative retarding potential.  $\alpha$  depends on particle species and energy.<sup>25,32</sup> The values used here lie within the range  $0.5 < \alpha < 1$ .

In this setup, a possible measured background emerges from recoil sputtered particles off the CS, especially secondary H and O from a persisting thin water layer adsorbed on the surface of the sample in the present pressure range. We use the noble gases He and Ne, with atomic masses comparable to those of H and O, respectively, as a proxy for the sputtering background, and subtract these values from the measured data. Since noble gases do not form stable negative ions, the total measured negative ion yield is considered to be due to sputtering.

For acceleration voltages below 500 V, the efficiency of forming atomic positive hydrogen and oxygen ions in the ion source was too low to achieve reasonably good statistics. Instead, positive molecular ions ( $\text{H}_2^+$ ,  $\text{O}_2^+$ ) were selected and accelerated to twice the nominal energy. This is justified since the vast majority of molecules break up into single atoms during interaction with the CS at the given energies,<sup>15,17,42</sup> so that the measured negative ion yield is essentially the same as for atomic H or O.

We assign an estimated energy uncertainty of  $\pm 10\%$  to these data points to take into account that the kinetic energy of the molecule may be unevenly partitioned among the separate atoms in the molecule dissociation upon surface scattering from the CS. The respective time-of-flight spectra can be found in Jans *et al.*<sup>15</sup>

Additionally, the angular distribution of scattered atoms is recorded using the 2D-imaging MCP detector. The full-width at half-maximum (FWHM) in azimuthal (tangentially to the surface) and polar (normal to the surface) direction is measured for all species at various incident energies by reading out the extend of the 50% contour line in the angular distributions.

In a third part, we investigated the effective energy distribution of the scattered ion beam by the retarding potential analysis. For this purpose, the countrate was monitored at constant incident energy  $E_i$  while varying the retarding potential in steps of 100 V from  $1.3 E_i/q$  down to 0 V. At high RPA voltage, only the scattered neutral atoms can reach the detector. When lowering the RPA voltage, an increasing amount of negative ions whose energy exceeds the retarding potential will be detected. To close the measurement sequence, data at the highest retarding potential were taken again, and the data were corrected for a slow linear time trend. The energy distribution of scattered negative ions was then computed as the counts difference between adjacent RPA values and is normalized by the constant number of detected neutrals. The energy distribution of scattered neutrals cannot be directly monitored by this method. However, we assume the particle energy distribution does not depend on the charge state, so that the obtained distribution is considered representative for the total set of scattered oxygen ions and atoms.

## III. RESULTS AND DISCUSSION

### A. Negative ionization yield

The negative ionization yield of H and O atoms upon scattering at a CdTe conversion surface was measured for energies from 195 eV to 1000 eV per atom at an incidence angle of  $8^\circ$ . The results are shown in Fig. 3. Background values measured with He and Ne, respectively, at the same energies are subtracted from the H and O data to account for recoil sputtering of surface atoms. For helium, the measured negative ion yield was 1.7% at 195 eV, increasing to 2.9% at 1000 eV. For neon, the measured negative ion yield was 3.1% at 250 eV and 4.3%–4.6% for energies from 390 eV to 1000 eV. The value at 195 eV could not be measured for Ne due to ion source instability at this low energy. Instead, the same value as for 250 eV was subtracted from oxygen at 195 eV as sputtering background.

We find a negative hydrogen ionization yield of 2%–3% for incident energies between 195 eV and 1000 eV, showing only a slight increase over the energy range within the uncertainties. For oxygen, the negative ionization yield is about 8.6% at 195 eV and increases to about 12.8% at 1000 eV.

The results found here for a CdTe-coated CS are comparable to those found previously for other coatings: Allenbach *et al.*<sup>1</sup> found very similar negative ionization yield for B-doped DLC. Neuland *et al.*<sup>23</sup> likewise report  $\eta \simeq 2\%$  for H on metallized DLC, and  $\eta = 10\%$ – $12\%$  for O. Various DLC-coated CS candidates for IBEX were tested by Wahlström *et al.*<sup>36</sup> and slightly higher negative ion yields were found, 11–20% for O, and 2–4% for H. Scheer<sup>30</sup> did a similar investigation using various H-terminated DLC samples that showed comparable results. Negative ion yields for  $\text{Al}_2\text{O}_3$  were in the same range<sup>26</sup> as in this work for oxygen ( $\eta_O = 9\%$  to 13%), but considerably higher for hydrogen ( $\eta_H = 3.5\%$  up to 4.6%).



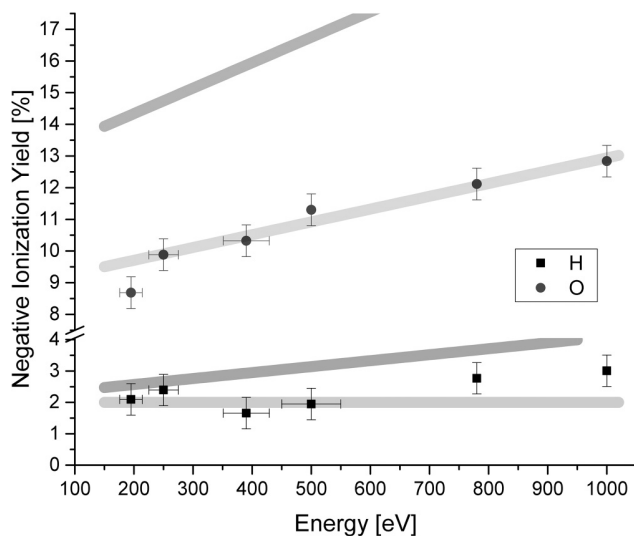


**FIG. 3.** Negative ionization yield of H and O atoms upon scattering at a CdTe conversion surface under  $8^\circ$  incidence angle for different incident energies per atom. Points with indicated energy uncertainty were done using primary molecular ions with twice the energy. Underlying grayscale bars represent the trends found in previous measurements with DLC samples. Dark gray: results from Scheer *et al.*<sup>30</sup> and Wahlström *et al.*,<sup>36</sup> light gray: results from Neuland *et al.*<sup>23</sup> and Allenbach *et al.*<sup>1</sup>

## B. Angular scattering distribution

The angular scattering FWHM of H, He, O, and Ne was measured in azimuthal and polar directions for energies from 195 eV to 1000 eV per atom upon scattering on a CdTe-coated CS at an incidence angle of  $8^\circ$ . The results are displayed in Figs. 4 and 5. Hydrogen shows the broadest scattering distribution of more than  $14^\circ$  azimuthal and  $16^\circ$  polar FWHM, while the other species show angular FWHM of  $10^\circ$ – $15^\circ$  in both directions. Values above  $20^\circ$  were on or beyond the detector edge and were obtained using a Gaussian fit in the azimuth direction and a log-normal in the polar direction using a least-squares fit. We estimate a 10% uncertainty in the incident energy per atom for measurements done using molecular primary ions, as explained in Sec. II C.

The angular scattering width increases with particle energy in both angular directions, except for He and Ne at the lowest measured energy. This trend is in accordance with our expectations from previous results with DLC,<sup>1,23,36</sup> and  $\text{Al}_2\text{O}_3$ -coated CS samples.<sup>26,29</sup> While the azimuthal scattering width is usually broader than the polar width by typically about 30%, we see here that for the CdTe-coated CS the azimuthal and polar widths differ by less than 10% for all particle species and energies. The azimuthal widths found here are within the range of angular scattering reported for other coatings. The polar widths are slightly higher compared to the results in Allenbach *et al.*,<sup>1</sup> Neuland *et al.*,<sup>23</sup> Riedo *et al.*,<sup>26</sup> and Wahlström *et al.*<sup>36</sup>

For the application in ENA instruments, a narrow angular scattering cone is strongly favored, as it directly improves the

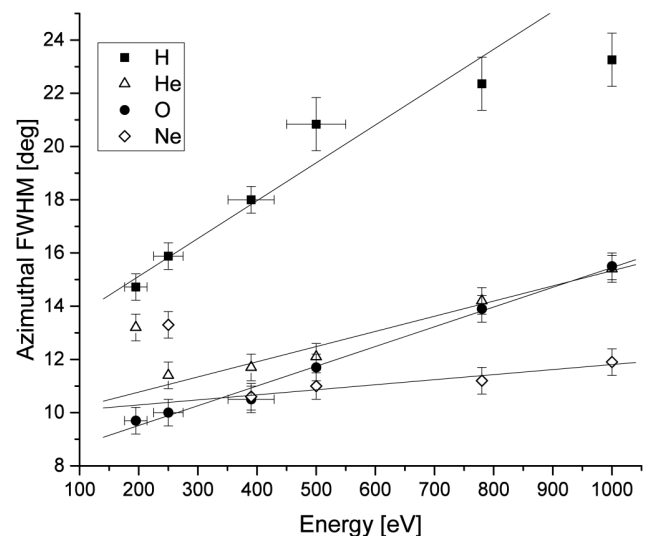


**FIG. 4.** Azimuthal FWHM of scattered atoms off the CdTe surface at different incident energies at  $8^\circ$  incidence angle. Linear fit lines are shown to guide the eye.

possible instrument throughput of the downstream ion optics. The tested CS sample showed a tolerable but rather high surface roughness in comparison with previous candidates. Moreover, it showed a particular granular structure under the AFM scan rather than a homogeneously smooth surface. While Wahlström *et al.*<sup>36</sup> see no

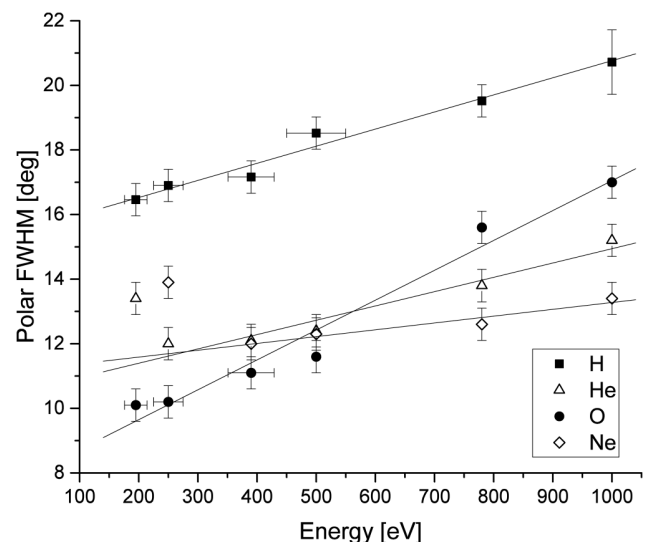


**FIG. 5.** Polar FWHM of scattered atoms off the CdTe surface at different incident energies at  $8^\circ$  incidence angle. Linear fit lines are shown to guide the eye.

influence of surface roughness on angular scattering, Riedo *et al.*<sup>26</sup> relate broader angular scattering to changes in the surface structure at few Å smooth surfaces, even if the surface roughness increased only insignificantly. This effect will be even larger at rougher surfaces, and angular scattering is expected to be reduced by a smoother coating. This, in turn, depends on the coating process and the underlying Si wafer roughness.

### C. Energy distribution

The energy distribution of the scattered particles was investigated using the retarding potential method. A primary  $\text{O}_2^+$  ion beam of  $E_i = 1000 \text{ eV/q}$  (500 eV per atom) was directed onto the CdTe-coated sample. The fraction of negative ions was then monitored while varying the RPA potential from 1300 V down to 0 V. In Fig. 6, the differential of scattered oxygen ions, normalized to the number of scattered neutral particles, is plotted against the retarding potential.

We observe all negative ions scattered off the CdTe CS at energies below 600 eV. Above ion energies of 500 eV/q, the data are in accordance with zero scattered particles. Small fluctuations are due to statistical variability in the experiment. The RPA measurement shows that all incident molecular ions break up into atoms in the scattering interaction. This agrees with the results found in Wurz *et al.*<sup>42</sup> and Jans *et al.*,<sup>15</sup> where a time-of-flight analysis was used. Otherwise, we should see some fraction of scattered ions still carrying an energy of 500–1000 eV with only some fraction of their energy lost in the scattering process.

The data point around 50 eV is likely dominated by a low-energy component, which originates from ions sputtered off the CS

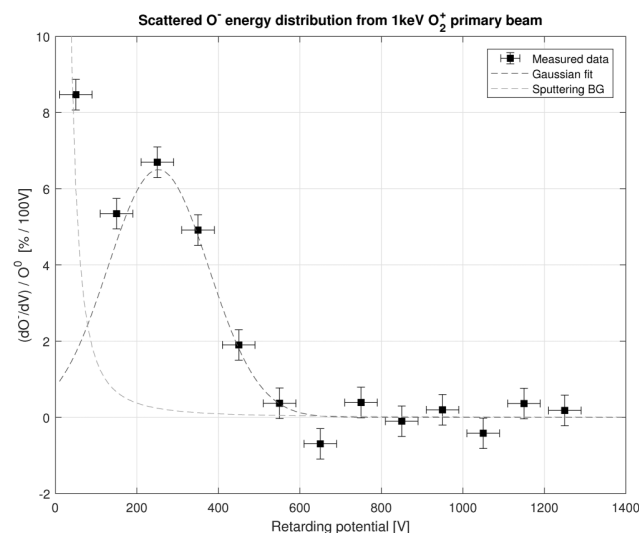


**FIG. 6.** Energy distribution of scattered  $\text{O}^-$  ions off the CdTe CS as percentage of total scattered neutral oxygen. The primary  $\text{O}_2^+$  ions were accelerated to 1000 eV and were scattered under  $8^\circ$  incidence angle. The low-energetic sputtering background and a Gaussian fit to the scattered  $\text{O}^-$  energy distribution are indicated.

rather than direct scattered  $\text{O}^-$  ions. This Sigmund–Thompson sputtering background<sup>31</sup> drops off as  $\propto E^{-2}$ , as indicated in Fig. 6.

The mean energy of scattered  $\text{O}^-$  ions is about  $\langle E \rangle = 273 \pm 30 \text{ eV}$ . This corresponds to a mean energy loss of about  $\langle dE/E_i \rangle = 45\%$  for O atoms from primary molecules in the scattering process, which is well in agreement with the energy loss at the IBEX-Lo CS (cf., Fig. 18 in Fuselier *et al.*<sup>9</sup>), where the reported values are  $(45 \pm 15)\%$  for  $\text{O}^-$  ions at about 500 eV.

A similar energy distribution was obtained using primary  $\text{H}_2^+$  ions with an energy of 1500 eV, however with a much smaller fraction of scattered negative ions (up to 1%/100 V) and thus much larger relative uncertainties.

### IV. CONCLUSION

A CdTe-coated Si wafer sample was investigated in the ILENA test facility<sup>35</sup> at University of Bern for its suitability as potential conversion surface in future ENA detection instruments in space research. One key characteristic of a CS is the smoothness on atomic scales. The surface roughness of the CdTe sample under test was investigated by AFM microscopy and was found to be  $R = 2.8 \text{ nm rms}$ , which is near the upper limit for suitable CS as seen from the measurements of angular scatter. Moreover, the granular structure is of concern for the angular and energy scatter. Improvements in the smoothness and homogeneity of the coating are possible in the fabrication process. By chemical (nitro phosphoric or bromine methanol etching) or physical (plasma) etching, it is possible to further reduce the surface roughness. Alternatively, epitaxially grown coating might lead to smoother surfaces.

The scattering properties of the CdTe CS, i.e., the negative ionization yield and the angular scattering width, were measured in the ILENA test facility for various energies at  $8^\circ$  incidence angle. Moreover, the energy distribution of scattered O was recorded. This shows that incident molecular ions are effectively split upon scattering and are scattered as individual atoms. The mean energy loss of about 45% turns out to be higher than previously expected. Our hypothesis that a CS material consisting of heavier atoms compared to C or O could significantly reduce the scattering energy loss could not be confirmed with the present CdTe coating. However, the results are comparable to other CS surfaces in use.

Over all, scattering results for CdTe are comparable to other established CS materials for space applications. Scattered negative ionization yields should exceed at least the 1% threshold for H to get further consideration as a CS.<sup>42</sup> This threshold requirement is readily fulfilled with CdTe. Given that an even smoother coating with CdTe is feasible, it should be possible to reduce angular scattering. In conclusion, we find that CdTe is indeed a possible alternative CS coating material for use in future ENA instruments.

### ACKNOWLEDGMENTS

We warmly thank Dr. Vitali Grozovski at DCB, University of Bern, for his great support with AFM microscopy. This work was supported by the Swiss National Science Foundation.

## DATA AVAILABILITY

The data that support the findings of this study are available from the corresponding author upon reasonable request.

## REFERENCES

- <sup>1</sup>M. Allenbach, M. Neuland, A. Riedo, and P. Wurz, *Appl. Surf. Sci.* **427**, 427 (2017).
- <sup>2</sup>S. Barabash, A. Bhardwaj, M. Wieser, R. Sridharan, T. Kurian, S. Varier, E. Vijayakumar, V. Abhirami, K. Raghavendra, S. Mohankumar, M. Dhanya, S. Thampi, K. Asamura, H. Andersson, Y. Futaana, M. Holmström, R. Lundin, J. Svensson, S. Karlsson, and P. Wurz, *Curr. Sci.* **96**, 526 (2009); available at <http://repository.ias.ac.in/64228/>
- <sup>3</sup>S. Barabash, R. Lundin, H. Andersson, K. Brinkfeldt, A. Grigoriev, H. Gunell, M. Holmström, M. Yamauchi, K. Asamura, P. Bochsler, P. Wurz, R. Cerulli-Irelli, A. Mura, A. Milillo, M. Maggi, S. Orsini, A. Coates, D. Linder, D. Kataria, and J. Thocaven, *Space Sci. Rev.* **126**, 113 (2006).
- <sup>4</sup>S. Barabash, P. Wurz, P. Brandt, M. Wieser, M. Holmström, Y. Futaana, K. Brinkfeldt, M. Holmström, R. Lundin, M. Yamauchi, K. Asamura, W. Baumjohann, T. Zhang, A. Coates, D. Linder, D. Kataria, C. Curtis, K. Hsieh, B. Sandel, A. Fedorov, and P. Bochsler, *Planet. Space Sci.* **55**, 1772 (2007).
- <sup>5</sup>S. Barabash, P. Wurz, P. Brandt, M. Wieser, M. Holmström, Y. Futaana, G. Stenberg Wieser, H. Nilsson, A. Eriksson, M. Tulej, A. Vorburger, N. Thomas, C. Paranicas, D. Mitchell, G. Ho, B. Mauk, D. Haggerty, J. Westlake, M. Fränz, and D. Grodent, *Proc. Eur. Planet. Sci. Congr.* **8**, EPSC2013 (2013); available at <https://meetingorganizer.copernicus.org/EPSC2013/EPSC2013-709.pdf>
- <sup>6</sup>A. Bhardwaj, S. Barabash, Y. Futaana, Y. Kazama, K. Asamura, D. McCann, R. Sridharan, M. Holmström, P. Wurz, and R. Lundin, *J. Earth Syst. Sci.* **114**, 749 (2005).
- <sup>7</sup>D. Faircloth and S. Lawrie, *New J. Phys.* **20**, 025007 (2018).
- <sup>8</sup>M. Föhn, "Application of surface physics for instruments in space science," master thesis (University of Bern, 2017).
- <sup>9</sup>S. Fuselier, P. Bochsler, D. Chornay, G. Clark, G. Crew, G. Dunn, T. Friedmann, H. Funsten, A. Ghielmetti, J. Googins, M. Granoff, J. Hamilton, J. Hanley, D. Heirtzler, E. Hertzberg, D. Isaac, B. King, U. Knauss, and S. Zaffke, *Space Sci. Rev.* **146**, 117 (2009).
- <sup>10</sup>Y. Futaana, S. Barabash, X.-D. Wang, M. Wieser, G. S. Wieser, P. Wurz, N. Krupp, and P. Brandt, *Planet. Space Sci.* **108**, 41 (2015).
- <sup>11</sup>M. Gloeckler, I. Sankin, and Z. Zhao, *IEEE J. Photovoltaics* **3**, 1389 (2013).
- <sup>12</sup>M. Green, E. Dunlop, J. Hohl-Ebinger, M. Yoshita, N. Kopidakis, and X. Hao, *Prog. Photovoltaics Res. Appl.* **28**, 629 (2020).
- <sup>13</sup>M. Gruntman, *Rev. Sci. Instrum.* **68**, 3617 (1997).
- <sup>14</sup>C. Heisler, M. Brückner, F. Lind, C. Kraft, U. Reislöhner, C. Ronning, and W. Wesch, *J. Appl. Phys.* **113**, 224504 (2013).
- <sup>15</sup>S. Jans, P. Wurz, R. Schletti, K. Brünig, K. Sekar, W. Heiland, J. Quinn, and R. Leuchner, *Nucl. Instrum. Methods Phys. Res. Sect. B* **173**, 503 (2001).
- <sup>16</sup>Y. Kazama, S. Barabash, M. Wieser, K. Asamura, and P. Wurz, *AIP Conf. Proc.* **1144**, 109 (2009).
- <sup>17</sup>A. Kleyn, *J. Phys. Condens. Matter* **4**, 8375 (1992).
- <sup>18</sup>W. Lei, J. Antoszewski, and L. Faraone, *Appl. Phys. Rev.* **2**, 041303 (2015).
- <sup>19</sup>J. Los and J. Geerlings, *Phys. Rep.* **190**, 133 (1990).
- <sup>20</sup>D. McComas, F. Allegrini, P. Bochsler, M. Bzowski, M. Collier, H. Fahr, H. Fichtner, P. Frisch, H. Funsten, S. Fuselier, G. Gloeckler, M. Gruntman, V. Izmodenov, P. Knappenberger, M. Lee, S. Livi, D. Mitchell, E. Moebius, T. Moore, S. Pope, D. Reisenfeld, E. Roelof, J. Scherrer, N. Schwadron, R. Tyler, M. Wieser, P. Wurz, and G. Zank, *Space Sci. Rev.* **146**, 11 (2009).
- <sup>21</sup>D. McComas, E. Christian, N. Schwadron, N. Fox, J. Westlake, F. Allegrini, D. Baker, D. Biesecker, M. Bzowski, G. Clark, C. Cohen, I. Cohen, M. Dayeh, R. Decker, G. de Nolfo, M. Desai, R. Ebert, H. Elliott, H. Fahr, and E. Zirnstein, *Space Sci. Rev.* **214**, 116 (2018).
- <sup>22</sup>T. Moore, D. Chornay, M. Collier, F. Herrero, J. Johnson, M. Johnson, J. Keller, J. Laudadio, J. Lobell, K. Ogilvie, P. Rozmarynowski, S. Fuselier, A. Ghielmetti, E. Hertzberg, D. Hamilton, R. Lundgren, P. Wilson, P. Walpole, T. Stephen, B. Peko, B. van Zyl, P. Wurz, J. Quinn, and G. Wilson, *Space Sci. Rev.* **91**, 155 (2000).
- <sup>23</sup>M. Neuland, A. Riedo, J. Scheer, and P. Wurz, *Appl. Surf. Sci.* **313**, 293 (2014).
- <sup>24</sup>S. Orsini, S. Livi, K. Torkar, S. Barabash, A. Milillo, P. Wurz, A. Di Lellis, and E. Kallio; the SERENA team, *Planet. Space Sci.* **58**, 166 (2008).
- <sup>25</sup>B. Peko and T. Stephen, *Nucl. Instrum. Methods Phys. Res. Sect. B* **171**, 597 (2000).
- <sup>26</sup>A. Riedo, M. Ruosch, M. Frenz, J. Scheer, and P. Wurz, *Appl. Surf. Sci.* **258**, 7292 (2012).
- <sup>27</sup>U. Roy, G. Camarda, Y. Cui, R. Gul, A. Hossain, G. Yang, J. Zázvorka, V. Dedic, J. Franc, and R. James, *Sci. Rep.* **9**, 1620 (2019).
- <sup>28</sup>J. Scheer, W. Brünig, T. Fröhlich, P. Wurz, and W. Heiland, *Nucl. Instrum. Methods Phys. Res. Sect. B* **157**, 208 (1999).
- <sup>29</sup>J. Scheer, P. Wahlström, and P. Wurz, *Nucl. Instrum. Methods Phys. Res. B* **267**, 2571 (2009).
- <sup>30</sup>J. Scheer, M. Wieser, P. Wurz, P. Bochsler, E. Hertzberg, S. Fuselier, F. Koeck, R. Nemanich, and M. Schleberger, *Adv. Space Res.* **38**, 664 (2006).
- <sup>31</sup>P. Sigmund, *Phys. Rev.* **184**, 383 (1969).
- <sup>32</sup>T. M. Stephen and B. L. Peko, *Rev. Sci. Instrum.* **71**, 1355 (2000).
- <sup>33</sup>T. Takahashi and S. Watanabe, *Nucl. Sci. IEEE Trans.* **48**, 950 (2001).
- <sup>34</sup>S. Velicu, G. Badano, Y. Selamet, C. Grein, J. Faurie, D. Rafol, and R. Ashokan, *J. Electron. Mater.* **30**, 711 (2001).
- <sup>35</sup>P. Wahlström, J. Scheer, A. Riedo, P. Wurz, and M. Wieser, *J. Spacecr. Rockets* **50**, 402 (2013).
- <sup>36</sup>P. Wahlström, J. Scheer, P. Wurz, E. Hertzberg, and S. Fuselier, *J. Appl. Phys.* **104**, 034503 (2008).
- <sup>37</sup>M. Wieser, P. Wurz, K. Brünig, and W. Heiland, *Nucl. Instrum. Methods Phys. Res. Sect. B* **192**, 370 (2002).
- <sup>38</sup>D. Williams, E. Roelof, and D. Mitchell, *Rev. Geophys.* **30**, 183, (1992).
- <sup>39</sup>H. Winter, *Phys. Rep. Rev. Sect. Phys. Lett.* **367**, 387 (2002).
- <sup>40</sup>P. Wurz, *The Outer Heliosphere: Beyond the Planets* (Copernicus Gesellschaft e.V., Katlenburg-Lindau, 2000), p. 251.
- <sup>41</sup>P. Wurz, J. Scheer, and M. Wieser, *J. Surf. Sci. Nanotechnol.* **4**, 394 (2006).
- <sup>42</sup>P. Wurz, R. Schletti, and M. Aellig, *Surf. Sci.* **373**, 56 (1997).

### 2.3.4. Strontium Titanate $\text{SrTiO}_3$

At the turn of the millennium, scattering experiments were done at our institute on barium zirconate ( $\text{BaZrO}_3$ ) coated samples [18]. These samples showed very high ionization efficiencies, with yields up to 35 % for O and 5 % for H, along with very moderate angular scattering. Unfortunately, the manufacturer of those coatings was no longer available and no other supplier could be found since.  $\text{BaZrO}_3$  is an oxidic ceramic with cubic crystal structure, a lattice constant of  $a = 4.26 \text{ \AA}$  and an electronic band gap of 3.04 eV. It is potentially due to these electronic properties, along with a sufficiently smooth surface topography, that leads to this outstanding ionization efficiency of  $\text{BaZrO}_3$ . We were thus looking for some alternative material(s) with similar structure and properties, hoping that they would turn out to ionize scattered atoms similarly well, and be readily available. As the first other ceramic CS material candidate I tested strontium titanate ( $\text{SrTiO}_3$ ). It is likewise a ceramic material with cubic crystal lattice ( $a = 3.95 \text{ \AA}$ ), but the band gap is considerably lower (1.77 eV).

**Sample preparation and characterization.** An  $\text{SrTiO}_3$  sample was already available in the group stock. It is a  $10 \times 10 \text{ mm}$   $\text{SrTiO}_3$  single crystal. Due to its relatively small size, it had to be attached to a 1 mm aluminum carrier plate which could then be mounted on the sample holder in ILENA. The  $\text{SrTiO}_3$  sample was glued on the Al carrier using a silver epoxy resin (Ag-EP), which also maintains electrical conductivity (see Fig. 2.21).



Figure 2.21.: Microscopic image of the  $\text{SrTiO}_3$  sample glued on an aluminum carrier plate, taken after ILENA measurements at the department of chemistry and biochemistry (DCB), University of Bern. *Sample:* polished square with edge size 10 mm, surrounded by Ag-EP residuals (black).

The  $\text{SrTiO}_3$  sample was investigated by microscopy, AFM, and interferometry to check the surface quality. Already in the microscope images (Fig. 2.21) one sees many pollution dots and grains all over on the sample surface despite the sample was thoroughly cleaned before



installation in ILENA. Overall, these dots cover a relatively small area, but can nevertheless degrade the angular scattering off the surface. Interferometry and AFM show that the prominent contaminating grains are typically 50 – 200 nm high. AFM reveals pollution at smaller scales as well, as can be seen in Fig. 2.22.

The sample was AFM scanned at four different spots across the sample (edge – center – edge). From averaging all measurements I obtained a surface roughness of  $\mathcal{R}_{rms} = 2.16 \pm 0.28$  nm. The scanned area was  $(10 \mu\text{m})^2$  at each investigated location. This result indicates that the surface roughness of this sample is of the same order of magnitude as for other sample surfaces tested for charge conversion. The rather large relative uncertainty of 13 % is likely owing to inhomogeneity between different scanned locations across the sample.

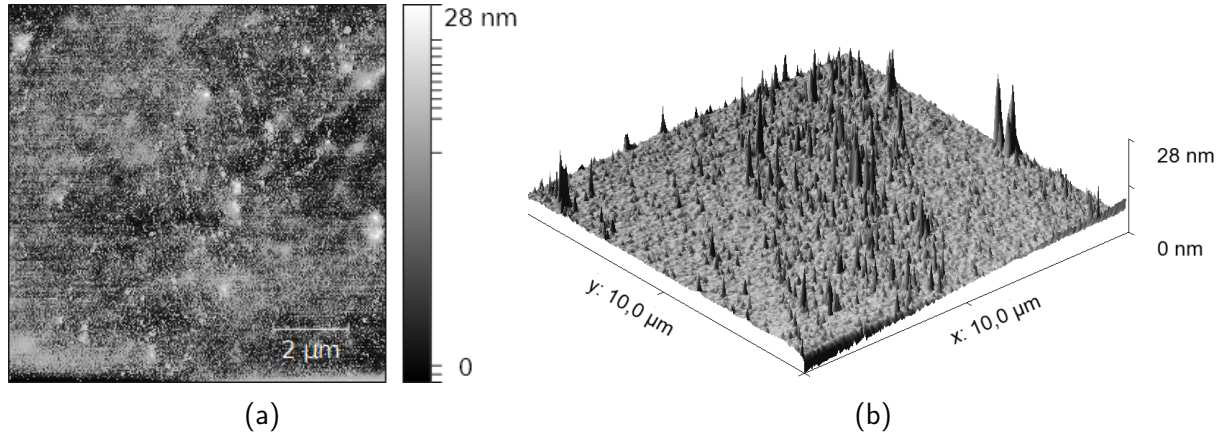


Figure 2.22.: (a) AFM image of the  $\text{SrTiO}_3$  surface. (b) 3D representation of the same surface section. One clearly distinguishes a relatively flat and homogeneous base surface with much rougher grains distributed over it.

**Scattering properties.** The  $\text{SrTiO}_3$  sample was installed in the ILENA test facility, where ion beams of kinetic energies from 390 eV to 1000 eV/atom were directed onto the surface at the standard measurement procedure. The ILENA setup and experiment procedure is described in Section 2.2.2 and elsewhere [11, 45] in great detail.

The measured negative ion yield resulting from scattering at the  $\text{SrTiO}_3$  surface is shown in Figure 2.23. For H we obtained about 1.5 % to 3.0 % negative ions, and for O the yield was roughly  $\eta_O = 9$  % to 12 %. He and Ne show almost constant values of 2.5 % and 4.0 %, respectively. As the noble gases do not form negative ions [51], these contributions probably come from sputtering other atoms (H, O) off the CS, dominantly from a thin adsorbed water layer omnipresent at this pressure level. In Figure 2.24 the FWHMs of the angular scattering distribution in polar and azimuth direction are plotted as function of the incident atoms' kinetic energy. For H the azimuth FWHM exceeded by far the detector limits at all tested energies, thus no meaningful analysis was possible. All FWHM values larger than  $20^\circ$  were extrapolated based on the 60 % contour line assuming a Gaussian distribution.

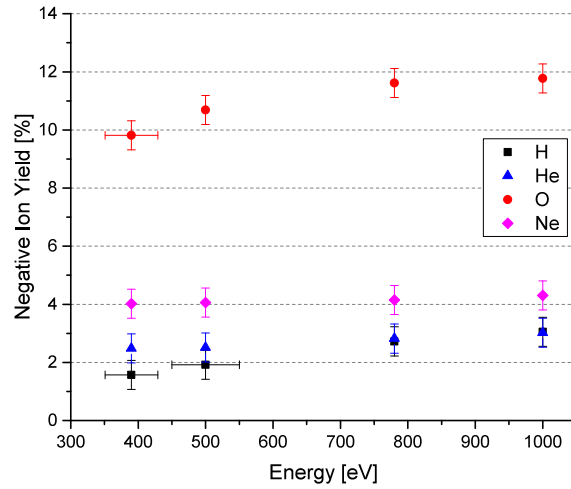


Figure 2.23.: Negative ion yield of four gas species scattered on a  $\text{SrTiO}_3$  surface at  $8^\circ$  incidence angle. The contribution due to sputtering was subtracted from H and O data. Data points with indicated energy error bars were done using a molecular primary ion beam.

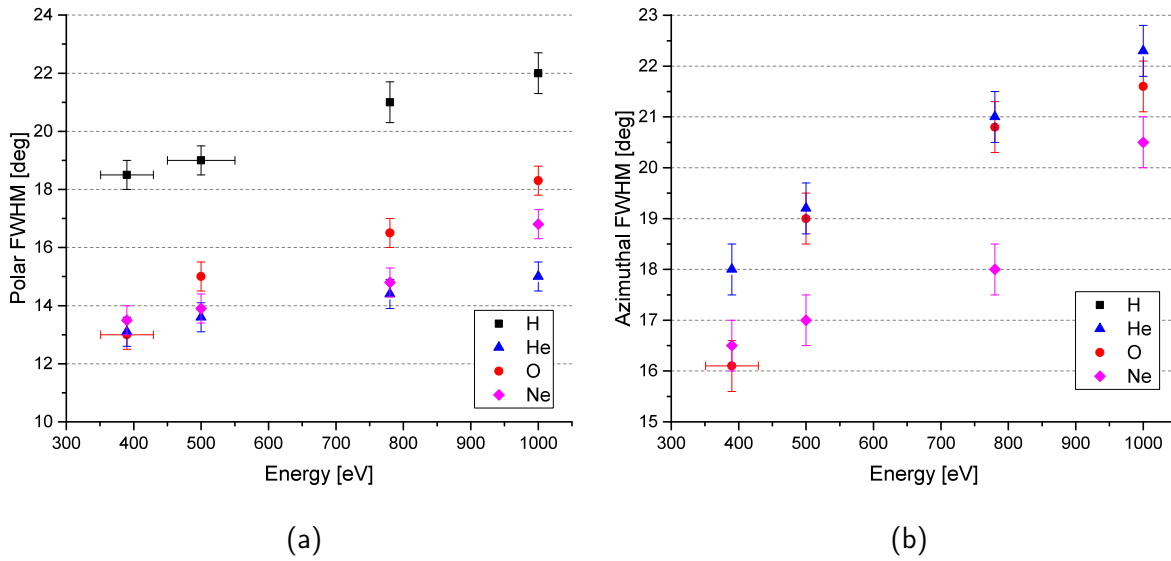


Figure 2.24.: Width of the angular scattering distribution from scattering off a  $\text{SrTiO}_3$  surface at  $8^\circ$  incidence angle. Values exceeding  $20^\circ$  were obtained by extrapolation. The azimuth FWHM for H exceeded by far the detector limits.

**Discussion** The values for H and He ionization efficiencies found here are comparable to typical values found for other CS coating materials such as  $\text{Al}_2\text{O}_3$  or DLC. The situation is different with Ne and O: the negative ion yield for Ne is often found to be around 5.0 % to 6.5 % in the energy range investigated here. For O, the negative ion yield is typically in the range 11 % to 15 % for DLC samples (see Section 2.3.2), and 13 % to 15 % on  $\text{Al}_2\text{O}_3$  samples

as reported in Section 2.3.1. Compared to these numbers the oxygen ionization efficiency of this  $\text{SrTiO}_3$  sample is considerably lower by about 2 % to 4 % percentage points.

Comparing the angular scattering with other samples results, we notice that the distribution widths found here are generally much wider than on typical  $\text{Al}_2\text{O}_3$  or DLC samples. For example, the polar and azimuth FWHM for  $\text{Al}_2\text{O}_3$  coated CS were  $14^\circ$  and  $15^\circ - 17^\circ$ , respectively; thus up to  $4^\circ$  narrower (see Fig. 2.24). Typical oxygen scattering FWHMs for DLC surfaces are  $9^\circ - 17^\circ$  in polar direction and  $13^\circ - 19^\circ$  in azimuthal direction, which is about  $3^\circ$  to  $5^\circ$  narrower than for this  $\text{SrTiO}_3$  sample. For the other species the comparison is similar: all show a significantly wider angular distribution for all energies.

Note that the AFM and interferometric investigation of the  $\text{SrTiO}_3$  sample revealed considerable particulate contamination on the surface, possibly contamination that degraded the performance of the coating and broadened the scattered beam width. Therefore it might be worth testing  $\text{SrTiO}_3$  again after thorough cleaning of the surface or eventually re-polishing it. Unfortunately, it was not possible to run another test series in ILENA after this finding to recheck (the sample was tested in Jan. – Feb. 2020). Later on I assigned lower priority to it, mainly because the ionization efficiency is also very moderate compared to other coatings already in use. Overall, I conclude from these first results that  $\text{SrTiO}_3$  is way less promising as a coating material candidate than expected, though I would not yet completely exclude it due to the aforementioned issues with the sample quality.

**Perspective** As mentioned,  $\text{SrTiO}_3$  should be tested again after re-polishing. Should it show a similar result than before, this raises the question what is the particular difference between  $\text{SrTiO}_3$  and  $\text{BaZrO}_3$  in terms of material properties that causes this remarkable dissimilarity in their charge conversion and scattering property? And more broadly, what implication does this put on the broader search for new highly efficient conversion surface materials?

### 2.3.5. Zinc Selenide $\text{ZnSe}$

Besides  $\text{SrTiO}_3$ , I was searching for other semiconductor materials for subsequent testing in ILENA. One other sample readily at hand was zinc selenide ( $\text{ZnSe}$ ).  $\text{ZnSe}$  is a II-IV-semiconductor with a band gap of 2.42 eV. It shows a cubic sphalerite crystal structure<sup>5</sup> with lattice constant  $a = 5.67 \text{ \AA}$ , and naturally occurs as a rare mineral called *stilleite*. Microcrystalline  $\text{ZnSe}$  is a yellowish transparent solid material that is often used for infrared (IR, at wavelengths  $\lambda = 0.5 - 20 \text{ }\mu\text{m}$ ) optics windows and lenses, and it is thin film deposited by physical vapor deposition (PVD) to produce highly reflective surfaces. Thus, in principle, this material is readily available. It is chemically stable under vacuum conditions; only when in contact with acids, it forms toxic hydrogen selenide.

Here we have the additional feature that all constituents of the surface material have atomic masses  $m_{surf}$  higher than 20 amu (Ne). Concretely, stable Se isotopes are between  $^{76}\text{Se}$  and  $^{82}\text{Se}$ , where  $^{80}\text{Se}$  is the most abundant (50 %), and stable zinc isotopes have masses from 64 to 70 amu, with  $^{64}\text{Zn}$  the most abundant one (about 50 %). This means  $m_{scatt} < m_{surf}$ ,

---

<sup>5</sup>There exists a hexagonal wurtzite structure modification of  $\text{ZnSe}$ .

the scattered atoms are lighter by at least a factor 3 to 4. Based on a simple binary collision scattering model, this implies a smaller momentum transfer from the incident atom to the surface and thus a smaller relative loss of kinetic energy.

The ZnSe sample at hand is a 10 mm diameter disk. To ease installation in ILENA the ZnSe sample was glued on an aluminum plate with silver-epoxy glue, just like the  $\text{SrTiO}_3$  sample. This process changed the sample's color from the characteristic bright indian yellow to a dark rosy-brownish hue (see Fig. 2.25).

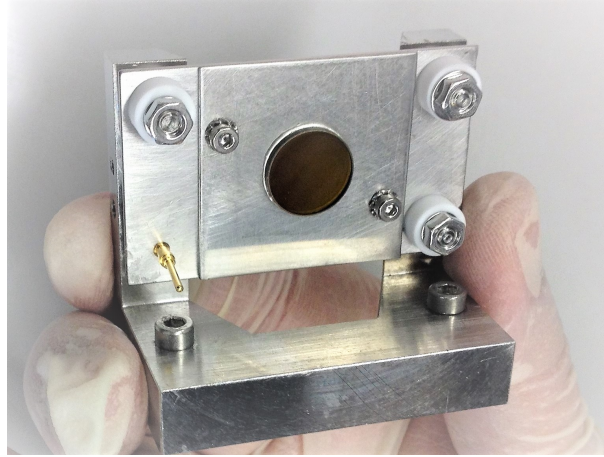


Figure 2.25.: The ZnSe disk glued on an aluminum plate and mounted on the ILENA sample holder.

Table 2.3.: Approximate angular scattering FWHMs on ZnSe in energy range 200 eV to 1000 eV.

Species:	Polar ( $8^\circ$ ):	Polar ( $5^\circ$ ):	Azimuth ( $8^\circ$ ):	Azimuth ( $5^\circ$ ):
H	$18.5^\circ - 21^\circ$	$15^\circ - 17^\circ$	$19^\circ - 25^\circ$	$18^\circ - 24^\circ$
He	$14.5^\circ - 18^\circ$	$13^\circ - 14^\circ$	$15^\circ - 18^\circ$	$15.5^\circ - 19^\circ$
O	$12.5^\circ - 21^\circ$	$10.5^\circ - 16.5^\circ$	$16^\circ - 21^\circ$	$12.5^\circ - 18.5^\circ$
Ne	$15^\circ - 19^\circ$	$13^\circ - 13.5^\circ$	$17.5^\circ - 19.5^\circ$	$14.5^\circ - 15.5^\circ$

**Results.** The negative ion yield and angular scattering widths were measured for H, He, O, and Ne beams scattered off the ZnSe sample surface at energies between 195 eV and 1000 eV. Two sets of measurements were done at  $8^\circ$  incidence angle, and another series at smaller incidence angle  $\alpha = 5^\circ$ . The results of the negative ion yield are shown in Fig. 2.26: At  $\alpha = 8^\circ$ , the negative ion yield ranges from about 8.5 % to 12.5 % for O, and is in the 1 % – 2.5 % range for H. For He and Ne, the sputter negative ion yield shows an almost flat



dependence on energy, in the range of  $\eta_{He} = 2\% - 2.5\%$  and  $\eta_{Ne} = 3\% - 4\%$ , respectively. In general, you see in Fig. 2.26a that the two series of measurements are well consistent within the measurement uncertainties.

In the first measurement series (full symbols) the data points of Ne at 390, 500 and 1000 eV exceeded 5 %, i.e., over 1 % higher than measured values for the other energies and the corresponding values for Ne in the second series. The polar angular width of the same Ne data points also shows significantly lower values (see Fig. 2.27); not the ones in azimuth direction, though. From this I suspect the experiment conditions might not have been stable or different, casting into doubt the validity of these three data points. Subtracting these from the directly measured (scattered and sputtered) O negative ion yield would result in equally lowered values of  $\eta_O$ . Thus, I excluded these values from  $\eta_{Ne}$  in series 1 at  $\alpha = 8^\circ$ , and used the corresponding Ne values from series 2 for sputter subtraction in  $\eta_O$  at 390, 500 and 1000 eV for reference.

Comparing the negative ion yield at  $8^\circ$  and  $5^\circ$  incidence angle, we notice that the negative ion yield for oxygen,  $\eta_O$ , is roughly the same at low energies, but it is up to 1 % higher at energies above 300 eV for the shallower incidence angle  $\alpha = 5^\circ$ . Along with that, the sputter contribution (Ne data points) is generally larger by 0.6 % to 1.9 % at  $8^\circ$  than at  $5^\circ$ , with the difference decreasing at higher beam energy. This indicates that a larger incidence angle leads to more sputtering here, at cost of direct scattering. It explains the difference seen in  $\eta_O$  between  $\alpha = 8^\circ$  and  $5^\circ$ ; the combined sputtered and scattered negative ion yields for O are roughly the same.

Looking at the angular scattering width in polar (Fig. 2.27) and azimuth direction (Fig. 2.28), we see a clear linear trend to larger polar and azimuth FWHM with higher ion energies for all species. In polar direction, we observe for oxygen the steepest energy dependence of the FWHM, ranging from  $13^\circ$  to  $21^\circ$  at  $\alpha = 8^\circ$  and from  $10.8^\circ$  to  $16.4^\circ$  at  $\alpha = 5^\circ$ . The remaining values at the lowest and highest energy are listed in Table 2.3.

The results in Figures 2.27 and 2.28 and Table 2.3 indicate that the angular scatter distribution is consequently wider at the larger incidence angle, and that the polar FWHM is always narrower than the azimuth FWHM at the same energy, incidence angle and species. Note that in the second measurement series, I could not reasonably evaluate the angular scatter width of hydrogen, as the half-max was outside the angular range of the detector at all energies.

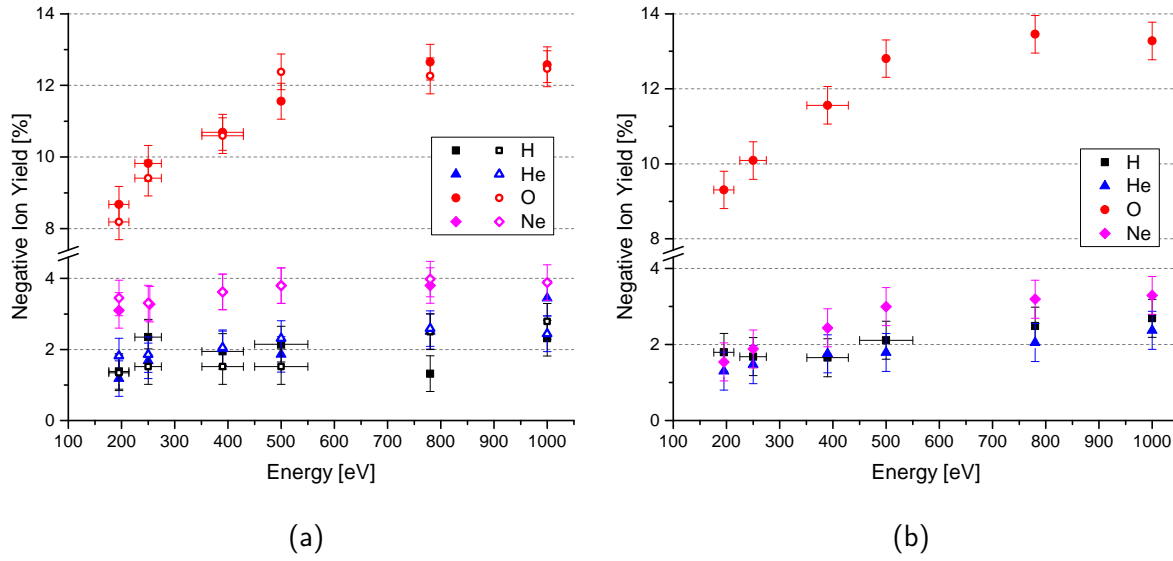


Figure 2.26.: Negative ion yield of H, He, O, Ne upon scattering off a ZnSe surface. The sputter contribution was subtracted from the H and O data. (a) Incidence angle  $\alpha = 8^\circ$ . Two sets of measurements with full and open symbols are displayed. (b) incidence angle  $\alpha = 5^\circ$ .

**Comparison.** When we compare the negative ion yield of this ZnSe sample with typical values of other CS materials at  $\alpha = 8^\circ$ , we see that  $\eta_H$ ,  $\eta_{He}$ ,  $\eta_{Ne}$  are within the range of 1.5 % to 3 % and 3 % to 4 %, respectively, about the same as for  $\text{Al}_2\text{O}_3$ . For oxygen, on the other hand, the negative ion yield for ZnSe is generally significantly lower than it typically is on DLC or  $\text{Al}_2\text{O}_3$  samples (which are typically about 11 % to 15 %). Moreover, the angular scatter distributions here are much broader for all species (FWHM by at least  $3^\circ$ ) than the ones usually seen from DLC or  $\text{Al}_2\text{O}_3$  at the same incidence angle. Also for the CdTe sample (see Gasser et al. [11], Figs. 4 and 5) I obtained significantly narrower scatter distributions than here for ZnSe. In competition with  $\text{SrTiO}_3$  (see Section 2.3.4), which is not among the most efficient materials tested either, ZnSe shows slightly better ionization efficiency for oxygen (about +0.5 %), but roughly the same efficiency for H, He and Ne. On the other hand, the angular scattering is wider for ZnSe.

Based on these first measurements presented here and compared to  $\text{Al}_2\text{O}_3$ , DLC, and CdTe, one concludes that ZnSe is likely not among the most efficient CS materials available. However, recall that the ZnSe sample under test was a solid disk designed to be used as an IR optical window. Such optical elements are typically polished at the micrometer- or even sub-micrometer level. The surfaces may still appear rough at the atomic (Å) level, which is the relevant dimension for surface scattering processes, leading to broader angular scattering. This could be circumvented by re-polishing or by depositing a ZnSe coating on an atomically flat surface, e.g., ZnSe coating of a silicon wafer. Unfortunately, most of the few companies with PVD capacity and atomic-level polishing capabilities reject to work with Se components to avoid contamination of their production facilities and its toxic potential.

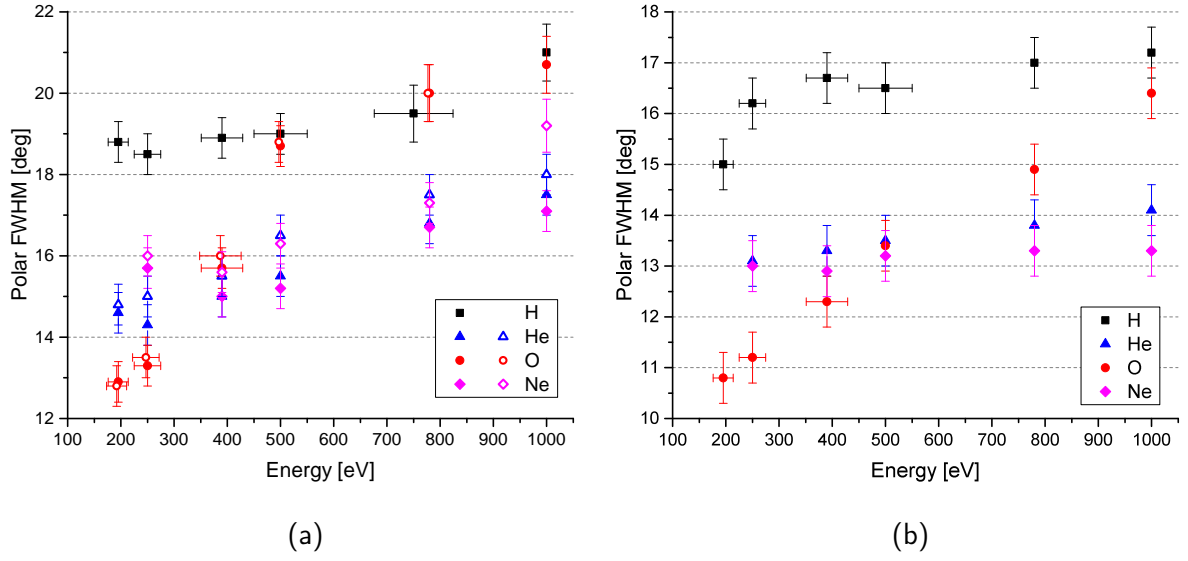


Figure 2.27.: Polar angular scatter distribution width off a ZnSe surface. (a) Incidence angle  $\alpha = 8^\circ$ . Two sets of measurements are presented (full/open symbols), except for hydrogen. (b) incidence angle  $\alpha = 5^\circ$ .

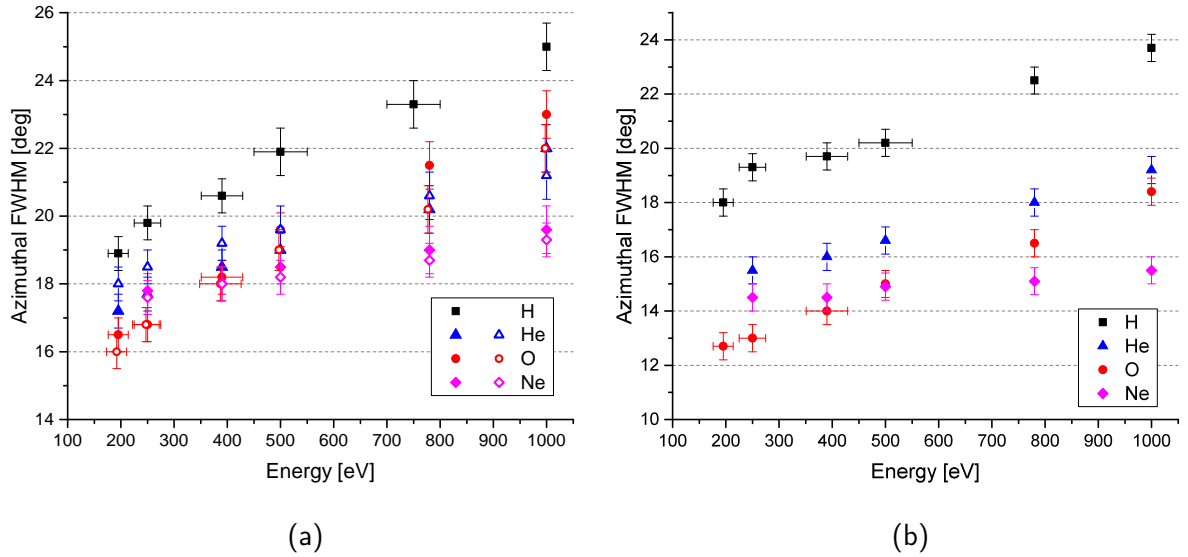


Figure 2.28.: Angular scatter width in azimuth direction off a ZnSe surface. (a) Incidence angle  $\alpha = 8^\circ$ . Two sets of measurements are shown, except for hydrogen. (b) incidence angle  $\alpha = 5^\circ$ .

Furthermore, due to the low electrical conductivity of undoped ZnSe (about  $10^{12} \Omega \text{ cm}$ ), the bulk sample may suffer from considerable surface charging under ion irradiation. This likely deteriorates the charge conversion and it affects the angular scatter, because the charged surface deflects the incident ions in ILENA such that they impact at a smaller incidence angle.

### 2.3.6. Graphene

In the past, various forms of carbon crystalline surfaces were tested as possible CS. Natural diamond was not expected to be a suitable ionizing material in theory (due to it being an insulator) before it was tested experimentally and actually showed very promising results [32, 53]. Further investigation on bulk diamond-like carbon materials revealed that surface charging can happen. However, doping the diamond crystals with, e.g., boron will reduce this effect [3]. Different types of DLC coatings have been tested in detail and proved suitable as CS for space applications, so this material has become one of the standard CS used today. This development encouraged us to examine yet another potentially suitable carbon material: *graphene*.

Graphene is a modification of carbon that forms a 2-dimensional structure, one monolayer (ML) of a flat hexagonal grid of C atoms each bound to three neighboring atoms. An every-day material very similar to graphene is graphite (which pencil tips are made of), which consists of many stacked C layers. Only in the early 2000s, Andrej K. Geim and Konstantin S. Novoselov successfully isolated graphene monolayers by successively stripping apart graphite particles on a scotch tape. In 2010, Geim and Novoselov were awarded the Nobel prize in physics “for groundbreaking experiments regarding the two-dimensional material graphene”.<sup>6</sup>

Graphene shows several extraordinary properties: it is the thinnest existing 2D material, it is extremely stiff and also the strongest known material with a tensile strength of 130 GPa, and it is among the least transparent materials given its extremely thin layer (it absorbs 2.3 % of visible light per monolayer), and many more. Most importantly, however, graphene shows almost no electrical resistance along the grid plane, which is related to the fact that graphene consists of a flat fence of hexagonal C rings, which have de-localized electron orbitals. Thus, the valence and conduction bands in graphene intersect at singular Dirac points, which has interesting and astonishing consequences on the quantum behavior of electrons in graphene, such as quasi-massless propagation.

Moreover, graphene is the starting product for various C nanostructures such as nanoribbons, carbon nanotubes (CNT) and fullerenes. Each of these open its own field of research and applications in physics, chemistry and surface science. Besides its popularity, it is primarily this high electrical surface conductivity along with the intrinsic flatness and stability that drew my attention to graphene as a possible CS coating.

**Sample and first results.** The tested sample consists of a  $10 \times 10$  mm polished Si wafer with 1 ML of graphene<sup>7</sup> deposited on its surface (graphene flakes size  $\sim 10 \mu\text{m}$ ,  $\geq 95$  % coverage). It was fixed at two corners on an Al plate using Cu tape to facilitate mounting on the sample holder. The sample holder clamps would only touch on the Al and not on the graphene deposited on silicon (gr/Si) sample.

The negative ion yield from scattering off this graphene sample surface is shown in Fig. 2.29 for an incidence angle of  $\alpha = 8^\circ$ . For O, the yield  $\eta_O$  is between 9 % and 14 % within the standard energy range. H and He show values around  $\eta = 2 - 3$  %, and the Ne sputtering

---

<sup>6</sup>Geim had also been awarded the Ig Nobel prize in 2000 “for using magnets to levitate a frog”. This makes him the first and so far the only Ig Nobel and Nobel laureate.

<sup>7</sup>from Graphenea Inc., San Sebastian, Spain, <https://www.graphenea.com>

negative ion yield is slightly larger than 4 %. The polar and azimuth angular scatter widths are shown in Fig. 2.30 a and b, respectively. Hydrogen experiences the broadest angular distribution with a polar FWHM from  $15^\circ$  to  $18.5^\circ$  and an azimuth FWHM from  $16.7^\circ$  at 195 eV to  $21.6^\circ$  at 1 keV. For the other gases the polar FWHM is in the range of  $12^\circ$  to  $14.5^\circ$ , and the azimuth FWHM within  $13^\circ - 17^\circ$  for O and  $14.5^\circ - 19^\circ$  for He. Data points for Ne below 300 eV have not been measured for this sample.

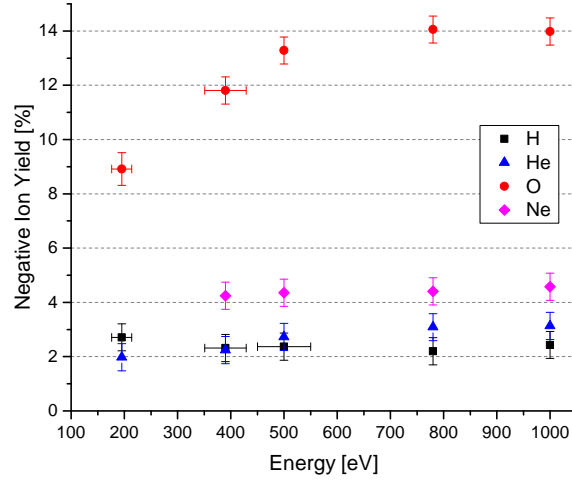


Figure 2.29.: H, He, O, and Ne negative ion yield from graphene (1 ML on Si) surface scattering at  $\alpha = 8^\circ$  incidence angle. The value for Ne at 195 eV has not been measured; an estimated 4 % was subtracted from the respective O data point to account for the sputter contribution (estimation is based on the available Ne data points).

**Comparison.** In comparison with the tested  $\text{SrTiO}_3$  and ZnSe samples (see Sections 2.3.4 and 2.3.5),  $\eta_O$  is about 2 % and 1.5 % higher on graphene, respectively.  $\eta_H$  is also slightly higher especially at low energies, while the sputtering  $\eta_{He}$  and  $\eta_{Ne}$  are comparable among the three samples. Thus, the negative O ion yield excess seen on graphene is not just owing to less sputtering, but indeed altered direct-scattering charge conversion. Note that the scattering width as well is significantly (if not drastically) smaller on graphene than on the  $\text{SrTiO}_3$  and ZnSe sample: by roughly  $4^\circ$  azimuth and polar FWHM for most species, the polar FWHM of He and Ne is  $0.5^\circ - 3^\circ$  narrower on graphene.

Comparison with the samples that have shown indication of charge conversion performance lower than state-of-the-art surfaces is not very convincing. Let us contrast the graphene result with DLC samples for IMAP-Lo: the graphene negative ion yield for H, He, and Ne is in the typical range of the set of DLC samples. For oxygen, just a few DLC samples (40Q, VW-003) showed clearly higher negative ion yield, but the gr/Si sample can compete well with most other tested DLC samples (Section 2.3.2) in terms of the oxygen negative ion yield. In particular, the EM flight samples for IMAP-Lo show about the same oxygen ionization efficiency (VW-039), and about 2 % lesser efficiency (VW-036:  $\eta_O \simeq 12\%$  at energies above 450 eV) than the gr/Si sample.

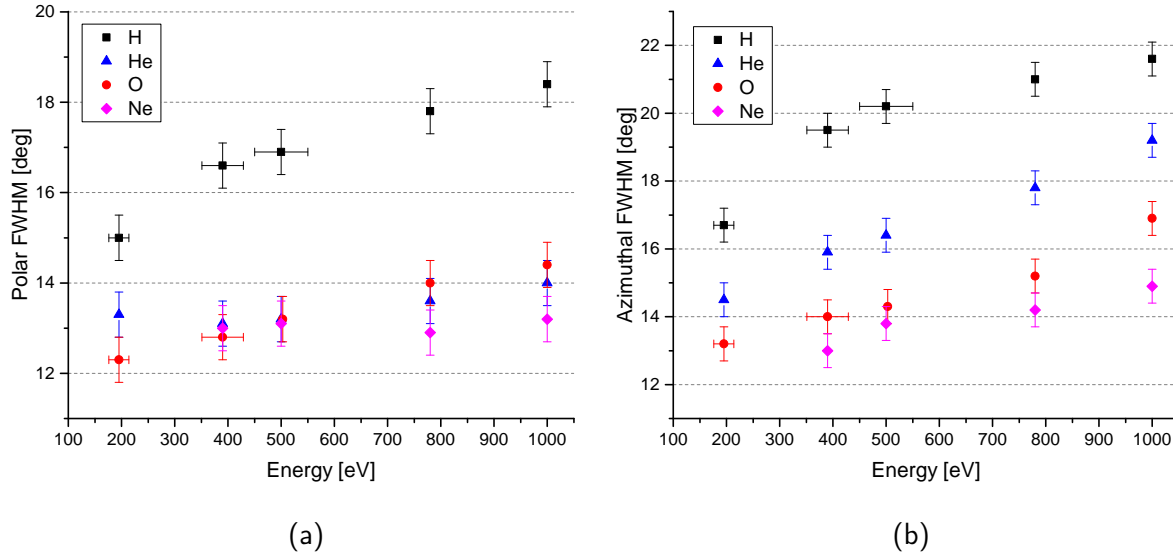


Figure 2.30.: (a) Polar and (b) azimuth angular scatter distribution FWHM for four species at standard energies scattered off 1 ML gr/Si at an incidence angle  $\alpha = 8^\circ$ .

The oxygen polar scatter FWHM on gr/Si is significantly broader than the best DLC samples (*VW-003*, *SW-004*, *VW-039*) by about  $1^\circ$  at 1 keV and up to  $4^\circ$  at the lowest energy. The azimuthal FWHM is comparable to the one of samples *SW-004*, *VW-039*, which are the narrowest scattering DLC samples. For hydrogen, the polar scattering FWHM of gr/Si is about  $3^\circ$  broader compared to optimal DLC samples, but the azimuthal FWHM is similar to the narrowest samples (*VW-003*, *SW-004*). The same comparison applies to the He and Ne scattering FWHMs. Overall, the ratio of polar/azimuthal FWHM ratio is larger for gr/Si than for DLC samples. One concludes that scattering on graphene appears to produce less elliptical angular distributions. This would be rather unfavorable in case of the IMAP-Lo sensor, but for other instrument designs this might be an advantage. The O negative ion yield is up to 2 % higher on gr/Si than on CdTe. There the azimuthal FWHM is roughly  $2^\circ$  narrower for H and O, but the polar FWHM is about  $2^\circ$  wider on CdTe than on gr/Si. The He and Ne angular scattering distributions are significantly narrower on CdTe as well.

## 2.4. Summary and Outlook

Several different types of materials had been investigated in the past as charge-conversion surface (coating or bulk) materials: alkali halide salts (LiF, KBr) and magnesia (MgO), mainly because they form very simple cubic crystals, to insulators like diamond and  $\text{Al}_2\text{O}_3$ , which actually turned out to be among the most efficient CS coatings for space applications to date.

More recently, also ceramic materials and other semiconductors have been considered and investigated, which showed at least partially very promising results: based on the convincing charge conversion performance of  $\text{BaZrO}_3$  [18], which material to date is not available, I tested a  $\text{SrTiO}_3$  sample, with the results presented in Section 2.3.4. From the semiconductor division

I investigated ZnSe and CdTe coatings, the latter of which should clearly be considered an alternative to the well-established  $\text{Al}_2\text{O}_3$  and DLC CS surfaces on future spaceborne ENA instruments. Some further experimental investigation of CdTe coated samples is certainly in place, to ensure reproducible samples quality and the shown conversion performance.

Table 2.4 provides a brief summarizing overview of the tested CS materials: negative ion yield, polar and azimuth scatter FWHM values are listed for 780 eV oxygen at  $8^\circ$  incidence angle.

Table 2.4.: Overview of the measured ionization efficiency and angular scatter of 780 eV oxygen, for different CS materials reported in this Section 2.3.

Material	Negative ion yield	Polar scatter FWHM	Azimuth scatter FWHM
$\text{Al}_2\text{O}_3$	14 %	$14^\circ \pm 1.5^\circ$	$16^\circ \pm 1.5^\circ$
DLC	12 % – 15 %	$12^\circ - 16^\circ$	$16^\circ - 18^\circ$
CdTe	12 %	$15^\circ \pm 0.5^\circ$	$13.5^\circ \pm 0.5^\circ$
$\text{SrTiO}_3$	11.5 %	$16.5^\circ \pm 0.5^\circ$	$21^\circ \pm 1^\circ$
ZnSe	12 %	$20^\circ \pm 1^\circ$	$21^\circ \pm 1^\circ$
graphene	14 %	$14^\circ \pm 0.5^\circ$	$14^\circ \pm 0.5^\circ$

The search for new possible alternatives to the established conversion surface materials does certainly not end at the samples already tested. There are a set of other semiconductor materials similar to CdTe, which might be suitable for testing as CS and characterization in future, listed in Table 2.5. Most of these materials crystallize in zincblende structure. ZnS and ZnTe eventually might not be long-term chemically inert as they tend to react with  $\text{O}_2$  or  $\text{H}_2\text{O}$ . None of them has yet been tested as a charge-CS material.

Besides extending the range of surface materials under consideration, the search for novel high-efficiency CS for space instruments would certainly also benefit from improvements on the ILENA test facility itself: The current experiment setup has been in operation for more than two decades now, and has proven – within its designed limitations – consistent and reliable test results. However, certain components are reaching their end-of-life and should soon be replaced by more modern counterparts. This certainly concerns the entire MCP detector, signal readout, and data processing system including the operation software, for which a major experiment refurbishment will be appropriate.

Further design changes could be considered to improve on the experiment stability and capabilities, or the measurement efficiency. Here are a few approaches and ideas:

- implementation of a feedback-loop on the SEM current control to improve on the B-field stability
- a mechanically more robust way of adjusting the sample angular position

Table 2.5.: List of semiconductor materials for testing as CS candidates.

Material:	Chemical formula:	Relevant properties and current applications:
Zinc telluride	ZnTe	II-IV semiconductor, 2.26 eV band gap, <i>water soluble</i> blue light-emitting diodes, solar cells, laser optics
Cadmium-zinc telluride	CdZnTe	II-IV semiconductor, tunable band gap (by Zn:Cd ratio)
Cadmoselite	CdSe	II-IV semiconductor, 1.74 eV band gap, wurtzite structure IR windows, quantum nanoparticles
Gallium arsenide	GaAs	III-V semiconductor, 1.42 eV band gap transistors, solar cells
Indium antimonide	InSb	III-IV semiconductor, 0.17 eV narrow band gap, IR detectors, IR astronomy
Zincblende	ZnS	II-IV semiconductor, 3.54 eV band gap, <i>oxidizable</i>
Germanium	Ge	Carbon-type element, semiconductor with 0.67 eV indirect band gap

- some design modification to enable detector vertical position changes: This would allow to scan an extended azimuth range of the scattered beam.
- implementation of a chamber cooling system to reduce the chamber base pressure and extend the duration of stable SEM operation.
- A possible alternative detector system could separate positive, negative and neutral particles in the scattered beam by an electrical field normal to the flight path and guide them into accordingly polarized detector units (e.g., CEMs). This would allow more direct measurement of (simultaneous) positive and negative ion yield at the expense of imaging capability. Hence, it ought rather be a temporal exchange replacement of the imaging detector.



### 3. Development of an Absolute Beam Monitor

---

Look up at the stars and not down at your feet.  
Try to make sense of what you see  
And wonder about what makes the universe exist.  
Be curious.

Stephen Hawking

---

#### 3.1. Motivation

The reliable detection and quantitative analysis of ENA below a few 100 eV in space has always been challenging: the reason for this lies in the nature of low-energetic ENA – their defining properties, electrical neutrality and low kinetic energy (typically also combined with low atomic mass), are responsible for comparably low detection efficiencies. Moreover, one has to cope with typically low fluxes of the ENA sources ( $1 \dots 100$  counts/cm/sr/s/eV) [10]. Therefore, scientific instruments for the detection of low-energetic neutral atoms in space require thorough laboratory calibration procedure in a dedicated test facility. The sensor and overall instrument calibration relies on a well-known and calibrated ENA beam source, against which the instrument response to ENAs can be calibrated. Relatively large uncertainties in the knowledge and characterization of the ENA beam source will directly transfer to the instrument calibration accuracy.

The MEFISTO facility at the University of Bern was originally designed for solar wind simulations and instrument calibration [21]. It is equipped with a powerful plasma ion source, an ion-optical extraction and beam guiding system, and a large vacuum chamber for instrument installation, testing and calibration. Atomic ion beams of energies from 3 keV/q up to

100 keV/q can be produced from any test gas. An overview of the MEFISTO facility is also provided in Section 4.1.1.

Furthermore, a dedicated beam neutralizing stage based on surface neutralization [47] was developed at this institute. The *surface neutralizer* can be mounted in front of the ion beam-entrance to the main test chamber to convert the 3 keV ion beam into a neutralized beam of variable kinetic energy from 3 keV/nuc down to 10 eV. Its functionality, properties and operation are described in detail in Section 4.1.2. The neutralizer was already in operation when the neutral beam calibration campaigns for IBEX-Lo were carried out in MEFISTO in 2007. However, the working principle of a surface neutralizer introduces considerable uncertainties on the neutral beam intensity, angular divergence and energy relative to the primary ion beam due to the fact that ions are first decelerated electrostatically, then deflected by an electrostatic analyzer (ESA) before being effectively neutralized by surface scattering. The henceforth not very precisely determined neutral beam source introduced considerable uncertainty on the overall instrument Geometric Factor (GF), depending on energy bin and species. This uncertainty could partially be resolved by in-flight cross-calibration with the IBEX-Hi instrument, and led to repeated debating among the scientific community concerning data analysis and results interpretation.

Angular scatter distributions were discussed in Chapter 2, especially in Section 2.2.1. In the surface interaction, incident atoms transfer some fraction of their kinetic energy to the surface lattice. The fraction of energy transferred to the surface probably amounts to about 5 % to 15 % depending on the initial energy, incidence angle and species.

More importantly, the surface neutralization process also introduces uncertainty on the neutral beam intensity in this energy range, as the conversion efficiency and overall device throughput are not known beforehand and the neutral beam in the chamber cannot easily be measured directly without having to take into account the low-energy neutrals detection efficiency of a detector to be used, which is species, charge state and energy dependent. Knowledge of such a detection efficiency, on the other hand, strongly relies on estimates based on extrapolation [26, 39] from higher energy range, other species, and/or comparable ion detection.

In short, a device was missing that is capable of determining the neutral beam flux independently of its detection efficiency, and that could serve as a primary standard for the neutral atom calibration of further suitable particle detectors such as MCP or CEM.

The principal goal of this PhD thesis work has thus been to develop, test and bring into operation a low-energy neutral atoms beam calibration device, *Absolute Beam Monitor* (ABM). This chapter describes and summarizes the development of the ABM device. Section 3.2 gives an overview of the design concepts, the measurement principle, as well as of the individual parts of the ABM. Section 3.3.1 describes the ABM data acquisition. The development summary, proof of concept and first results have been published in the scientific article “*Absolute beam monitor: A novel laboratory device for neutral beam calibration*” published in the *Review of Scientific Instruments* [12] (Section 3.4).

## 3.2. Concept and Prototype Characteristics

### 3.2.1. Design Concept

The basic concept for developing a low-energy ENA absolute beam monitor was to have the neutral beam scattered at a CS, then count the electrons released from the surface as start signals, the reflected atoms as stop signals, the coincidence events and time difference between start and stop. With a given entrance aperture, we obtain the ENA flux from the combined start, stop, and coincidence count rates (see Section 3.2.2). In addition, the individual start-stop flight times are accumulated into a ToF spectrum. Given the atomic species of the beam, the ToF spectrum is transformed into a post-scattering energy distribution spectrum. From this we obtain the mean kinetic energy within some uncertainty, and by comparing the kinetic energy of the primary ion beam,  $E_{ion}$ , the relative energy loss in the scattering interaction can be determined.

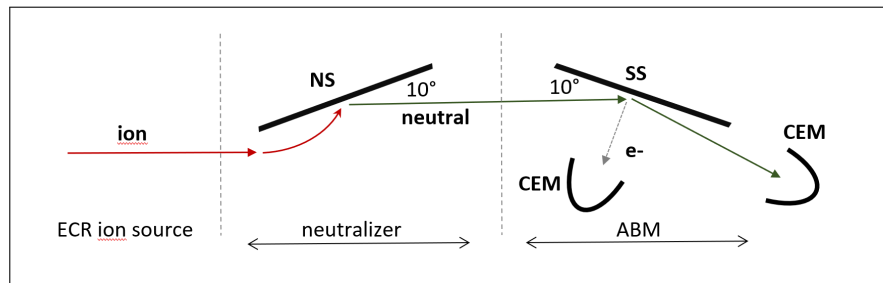


Figure 3.1.: Schematic of the basic measurement concept for the ABM.

Moreover, the following set of requirements shall be met by an ABM prototype design:

1. A closed shape, with no open HV electrodes into the chamber
2. Limited size, perhaps to be installed next to a flight (spare) instrument under test
3. Well-defined entrance aperture and field-of-view, avoid stray particle entrance
4. Same conversion surface and incidence angle as in the neutralizer
5. Ion-optical configuration to separate start electrons from neutrals and ions

Therefore, the design of an Absolute Beam Monitor device was driven by the following baseline concept:

- A neutral atom beam should be reflected at a charge-conversion surface under grazing incidence angle and thereby release secondary electrons from the surface.
- The electrons would then be collected in one channeltron to produce a start signal.
- The reflected atoms, regardless of their charge state, would drift toward another channeltron and produce a stop signal.

- Both start and stop signals would be transmitted out of the vacuum chamber and fed into a pre-amplifier each. Then coincidence counters electronics would produce a coincident signal whenever a stop pulse follows a start pulse shortly after.
- Noise and background suppression was anticipated to be crucial for accurate measurements, therefore - and to avoid open high-voltage electrodes in the test chamber - the system has to be enclosed from all sides with grounded metal shields.
- The ion-optics simulation software SIMION is to be used to run test simulations and iterative improvements of early design drafts.

The individual requirements are described in more detail in the following, as well as how they were implemented.

**Start surface.** It became clear very early on that the incidence angle in the ABM has to be equal to the one in the neutralizer, hence  $\alpha = 10^\circ$ , and that the start surface should be a tungsten (W) single crystal identical to the neutralizer CS. The reasoning behind this is explained in the paragraph *Beam energy measurement* on p. 96. As the ABM design was set up with the base plate parallel to the CS, this implies that the device has to be in  $10^\circ$  tilted position when installed in the test chamber. I incorporate this in the design of the mounting stand (see Fig. 2 in the paper on the Absolute Beam Monitor, p. 106).

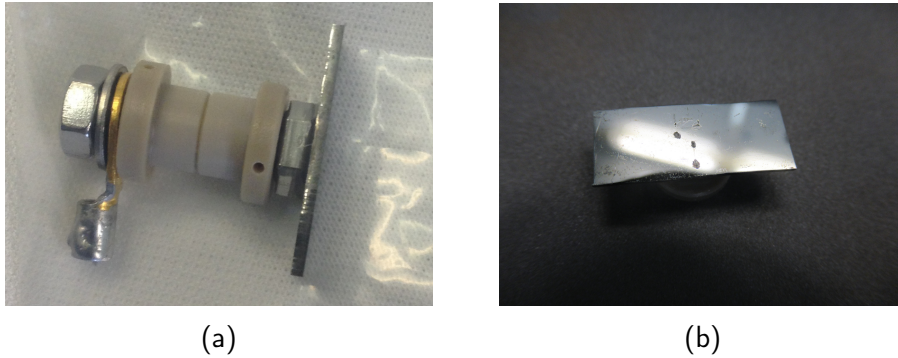


Figure 3.2.: ABM version 1 tungsten start surface (a) assembly on screw with insulating bushings and cable lug, (b) mounted on the inner side of the top plate.

Surface scattering at grazing incidence angle implies the footprint of the incident atomic beam will be elongated in the projected beam direction and unaffected in the perpendicular (“sideways”) direction. Of course, the surface scattering process induces considerable angular broadening in the scattered beam direction, as discussed in detail in Chapter 2. This does not affect the region on the CS where the beam falls on, though. For a circular beam with diameter  $d$  and directional delta distribution, the elliptical footprint on the CS will have length  $\delta s = d / \sin(\alpha) = 5.76 d$  in projected beam direction. This consideration puts in place a limitation for both the size of the entrance aperture and the achievable ToF (energy) resolution. As we will see in Section 3.2.2, the CS length  $\delta s$  adds to the ToF peak width. A larger entrance aperture increases the required CS length and, hence, the energy uncertainty.

Tungsten single crystals with polished surface are generally costly. Thus, not yet knowing whether the targeted measurement concept would work out as expected, I implemented as CS a  $8 \times 20$  mm tungsten plate already at hand, with some minor creases in the surface, in the version 1 ABM prototype. In a later step, the CS was replaced by a newly fabricated  $10 \times 20$  mm W (100) surface (see paragraph *Refurbishment* on p. 92). The 4 mm diameter entrance aperture (see below) is sized to allow the maximal CS coverage of the incident neutral beam, but not beyond its edges. The tungsten plate was soldered onto a M8 hexagonal head cap screw and fixed in the top plate with an insulating bushing. A low DC voltage is applied via a cable lug attached on the outside to electrically bias the CS.

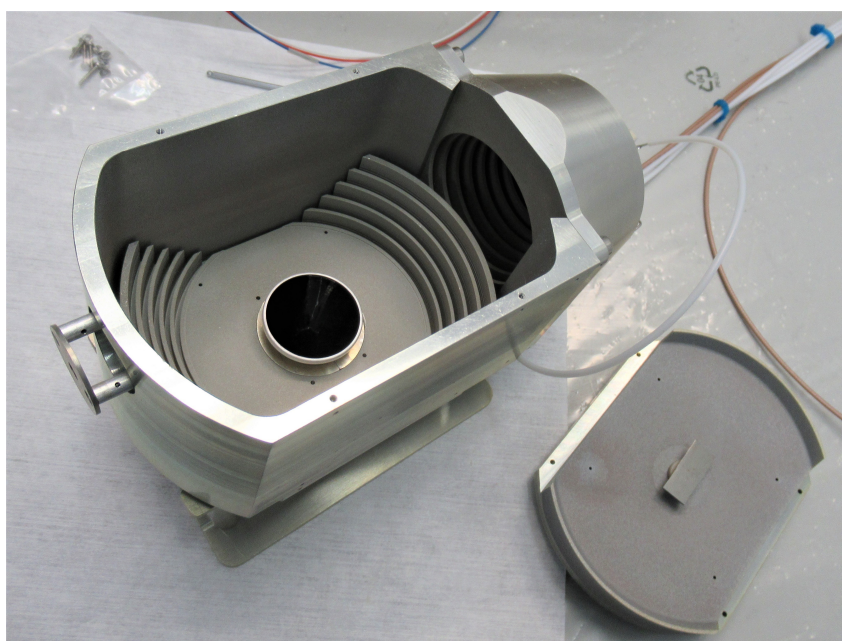


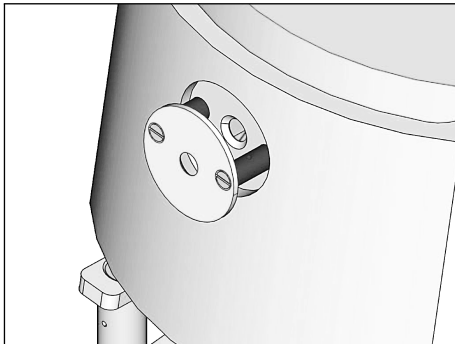
Figure 3.3.: Top view of inside of first version ABM, with top plate removed. The SS is at the center of the top plate (lower right), the start CEM is visible at the center of the ABM, and the stop CEM at its right back (not visible), with the white signal cable attached to it.

**Box shape.** A closed box was required to contain the electrical fields and to prevent ambient gas molecules, electrons and photons from entering the detection volume and interacting with the electrodes and walls as best possible. The basic prototype shape started from a cylinder, with the CS mounted in front of the center of one lid and the start CEM fed through the opposite lid. An entrance hole was integrated in the cylinder mantle where the neutral beam enters and strike the CS. On the mantle side opposite to the entrance, a rectangular opening was removed, as this would be the direction towards the stop CEM. There the cylinder was extended by a conical structure with a baffle structure, the target cone, to suppress particles on undesirable trajectories with symmetry axis radially towards the cylinder center. At the tapering at its far end, the stop CEM was placed. Finally, the cylinder was slimmed down at

either side of the entrance hole to reduce the volume required for the device in the vacuum chamber. According to the ion-optical simulations, this had no considerable or critical effect on the interior electrical fields.

The interior shape of the cylinder was optimized to ion-optical benefits: the top plate behind the CS was curved concave to support confining electrons and pushing them towards the opposite CEM. Likewise, the bottom plate around the start CEM was extended by a conical shape at the edges, also to focus emitted electrons to the center. Several serrations were carved into the interior surface of the bottom plate and the target cone to absorb back-scattered particles.

The final ABM box design consists of just four parts (plus a mounting stand to facilitate installation on the hexapod table in the vacuum chamber): the mantle as the basic structure containing the entrance aperture, a top plate with the CS fixed to it, a bottom plate with a circular hole where the start CEM is placed, and attached to the mantle the target cone with the stop CEM. The CEMs are attached to the bottom plate and target cone, respectively, on CEM holders made from PEEK. The bottom plate comes with two semicircular inlets to almost close up the hole behind the CEM funnel. A small gap of a few mm remains between the enclosure and the top and bottom plates, respectively, which ensures sufficient venting but inhibits a direct path for atoms and photons into the ABM. All the inner walls of the first version ABM were sandblasted for roughening to suppress residual gas molecules. Acktar black coating was applied later (see paragraph *Refurbishment* on p. 92) to enhance this absorption.



(a) computer-aided design drawing.



(b) photograph.

Figure 3.4.: Images of the ABM entrance aperture. The knife edge of the inner aperture is on the wrong side. This was corrected later.

**Entrance aperture.** The ABM entrance was designed from the beginning as a double aperture to collimate the entering beam to the nominal direction, i.e., to define the field-of-view and block stray particles. A circular pocket of 20 mm diameter was cut from the outside into the otherwise 4 mm thick wall at the correct position for the entrance aperture to match the required  $10^\circ$  incidence angle. The remaining wall is 1 mm thick there. At the center, a circular hole of 4 mm diameter was drilled and burred off at  $45^\circ$  to give a sharp edge. The second aperture, a circular metal disk (20 mm outer diameter, 1 mm thick) is mounted on

two standoffs 10 mm in front of the aperture hole. It also contains a 4 mm circular hole and is displaced from the center of the inner aperture by 1.5 mm to account for the  $10^\circ$  incidence angle.

The following considerations led to the aperture size of 4 mm diameter: In principle, a large entrance aperture is favorable, because it automatically increases the neutrals rate into the ABM at a given ENA flux from the neutralizer and, hence, reduces the required accumulation time. However, only atoms that hit the CS can possibly be counted and therefore the reasonable aperture size is limited by the size of the surface plate. Additionally, as the neutral beam is not necessarily homogeneous in intensity [47], a large aperture tends to capture more inhomogeneity, which introduces additional uncertainty to the measurement. With a smaller aperture, it is more likely feasible to perform a neutral beam profiling, for example (even though the ABM was not specifically designed for this).

Moreover, with smaller aperture size it is easier to constrain the directional range of the incident neutral beam. The reason for having the holes edges cut at  $45^\circ$  is to avoid any cylindrical inner surface where particles can be deflected but still enter the device. It is best practice to have the smallest gap at the outer edge, as shown schematically in Fig. 3.5. Unfortunately, the aperture hole edge was on the inner side, and needed correction in the form of a 0.1 mm thin metal plate placed in the incision on the outer edge of the entrance aperture. This may not be the optimal solution, but effectively, the ABM now comes with an almost-threelfold aperture.

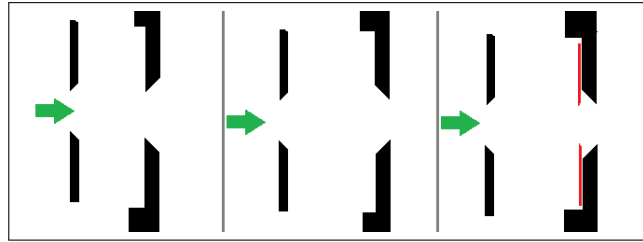


Figure 3.5.: Schematic of the entrance blend with  $45^\circ$  cut edges. The neutral beam (green arrow) comes in from the left, passes the hole in a circular disk and goes through the entrance aperture. *Left*: situation as should be: the sharp edges are on the outer side. *Center*: original situation in the version 1 ABM: sharp edge of the entrance hole is on the inner side. *Right*: hands-on correction with added 0.1 mm thin circular plate.

**Start CEM, stop CEM.** For both the start and stop detector, CEMs model KBL25RS/90 from Sjuts<sup>1</sup> were used. This model from a standard series features a  $90^\circ$  opening angle circular funnel of 25 mm diameter. The CEM opening is coated with a black high-resistivity electron-donating material. The CEMs require about 2.0 – 2.5 kV bias voltage to produce electrical pulses at a gain of  $10^7 \dots 10^8$  depending on bias voltage and ageing. They nominally produce 10 ns short negative voltage pulses of about 100 mV amplitude. From this CEM series, the

<sup>1</sup>Dr. Sjuts Optotechnik GmbH, Goettingen, Germany, <https://www.sjuts.com>



rather large funnel opening was chosen for the stop CEM to maximize the covered angular range as seen from the CS at the given distance and hence the registration probability of scattered particles. For the start CEM the same consideration applies, and it makes sense for the initial prototype to have twice the same CEM model, so just one spare piece for both is sufficient. One argument in favor of a small start CEM funnel (at least 5 mm diameter) would have been to reduce the dark counts, and instead rely on improved secondary electron collection through the electrical potential.

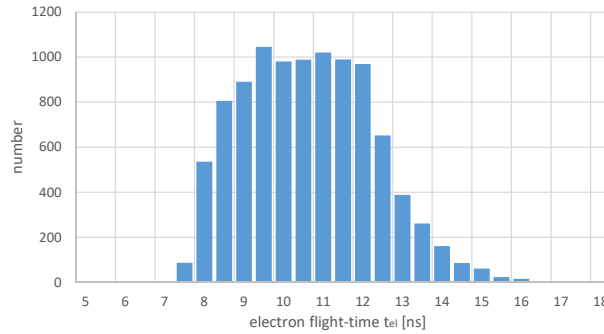


Figure 3.6.: Simulated distribution of the flight-time distribution of secondary electrons in the ABM from the SS to the start CEM.

**Voltages** The ion-optical design of the ABM is relatively simple. The entire enclosure was set to ground potential. The apertures of the two CEMs are on high voltage, as is described in the following. Other than that, only the CS is set to a low positive potential. Combined with the positive high voltage at the start CEM, this makes the inner walls at ground electron-repelling and serves to confine the secondary electrons inside the volume, respectively, pull them towards the start CEM (see Fig. 3.7).

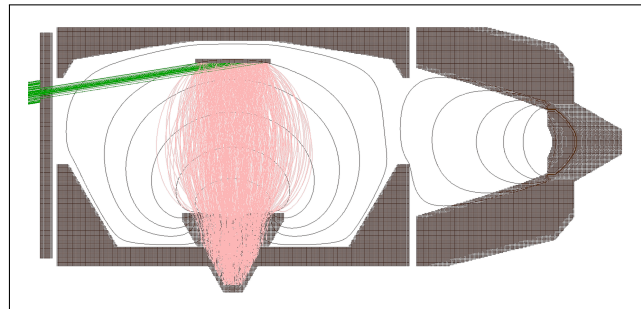


Figure 3.7.: 2D cut through the ABM ion-optical simulation model in SIMION. Electric equipotential lines (grey), incident neutrals (green) through the entrance aperture, and trajectories (pink) of secondary electrons released off the SS and accelerated towards the start CEM are shown.

The start CEM is to detect secondary electrons released from the tungsten surface. Its funnel is thus set to a positive high voltage HV0 of a few 100 eV to attract the (negatively



charged) electrons. As CEM operate by producing an electron avalanche toward the anode for sufficient signal gain, the output end needs be set to an even higher voltage ( $HV0 + HV1$ ). This is realized by electrically floating one voltage supply to the CEM front voltage  $HV0$ . The floating supply provides the start CEM's bias voltage  $HV1$ . A Zener diode was implemented in the circuitry between the back end and the anode to establish a voltage difference of 100 V (Fig. 4a in the ABM paper [12], see p. 107). The signal line was electrically decoupled from HV by a capacitor of  $C = 1$  nF, with only fast AC signals can pass through.

When it comes to the stop CEM, the voltage applied to the front end is not strongly constrained. Positive and negative ions are either attracted towards or rejected from the stop CEM with its funnel at negative or positive HV, respectively, while neutral atoms are not affected. Leaving the stop CEM funnel at ground potential would allow both positive and negative ions to reach it. The actually realized design comes with a negative front potential at the stop CEM, thus allows for attracting positive ions while rejecting negative ions.

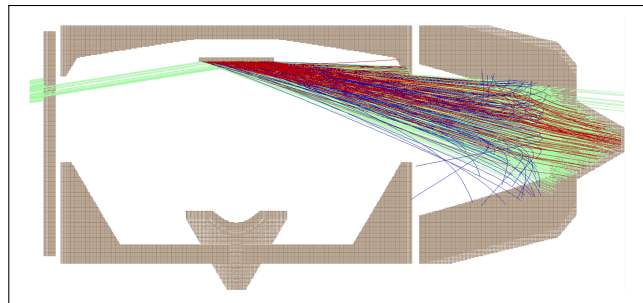


Figure 3.8.: SIMION ABM model vertical 2D projection. Incident neutrals (green) from the left, as well as neutrals (green), negative (blue) and positive ions (red) scattered off the SS are shown. Negative ions are rejected from the stop CEM, while positive ions are attracted.

This ion-optical concept supports collecting the electrons from the start surface into the start CEM and compensates for slightly distorted trajectories of positive ions in the vicinity of the tungsten plate, as they are pushed to one side by the positive HV applied at the start CEM. This is achieved at the expense of not collecting any negative ions at the stop CEM, though.

In principle, another floated HV supply lying on negative voltage could provide the bias voltage for the stop CEM as well. This would allow for tuning the electrical potential at the funnel independently from its bias voltage. It would require another DC separating capacitor at the anode, though. SIMION simulations showed that we can reduce the complexity by setting the stop CEM output and anode to ground potential. The voltage applied at the stop CEM funnel is thus the negative bias voltage by design. This concept reduces the number of 'free' parameters and of needed HV supplies and feedthroughs by one.

**Refurbishment.** After first test series of the ABM prototype with the neutral beam source, a set of measures was incorporated to improve the ABM device:

- A new polished tungsten single crystal surface was ordered from MaTeck<sup>2</sup> and installed in the ABM.
- All the inner walls were coated with Acktar Vacuum Black<sup>3</sup>, a surface coating with a dendritic micro-structure and thus a very large effective surface area (see Fig. 3.9). This enhances absorption of residual gas molecules and any stray particles, hence helps to reduce background counts.
- Capacitors of  $C = 10$  nF were installed in parallel circuit to the CEMs to prevent them from paralysis or sensitivity reduction due to large count rates.
- The entrance aperture was revised as described in paragraph *Entrance aperture* on page 88.
- Additionally, a start surface heater was designed and implemented (see paragraph *Start surface heating*).
- The ABM device obtained its *chic* Bernese emblem on both flanks.



Figure 3.9.: Part of the refurbished ABM: The Acktar blackened top plate with fully assembled new tungsten plate and SS heater.

---

<sup>2</sup>MaTeck Material Technologie & Kristalle GmbH, Juelich, Germany, <https://www.mateck.com/>

<sup>3</sup>Acktar Ltd., Kiryat-Gat, Israel, <https://www.acktar.com>

**Start surface heating.** Along with replacing the start surface tungsten plate, I designed and implemented a surface heater to heat up the SS locally to about 80°C. It became necessary to reduce adsorbed H<sub>2</sub>O contamination from the start surface and hence reduce backgrounds and increase the overall ABM efficiency. The heating power consumed when keeping the tungsten plate at  $T_s = 80^\circ\text{C} = 353\text{ K}$  can be estimated using Stefan-Boltzmann law for Black body radiation:

$$P(T) = \sigma_B A T^4 \quad (3.1)$$

where the Stefan-Boltzmann constant  $\sigma_B = 5.67 \cdot 10^{-8} \text{ W m}^{-2} \text{ K}^{-4}$  and  $A$  is the surface area. For a total area of  $0.4 \text{ cm}^2$  ( $20 \times 10 \text{ mm}$  front and back, the sides and mounting screw disregarded) it yields an estimated electrical power of about  $P = 0.35 \text{ W}$ . A heater with about  $1 \text{ W}$  power should hence be sufficient. The very tight spacing behind and around the SS, combined with the requirement that the front surface must remain absolutely clean rendered this quite challenging, though. Several concepts were considered:

- Kapton resistive heating foil, to be attached at the back of the tungsten plate
- Indirect heating from the outside via the thermal conducting mounting screw
- A resistive wire heater at the back of the tungsten plate

Finally, the resistive wire at the back of the SS was implemented, because the heating should be as local as possible, and it was difficult to find heating foil patches small enough to fit the  $\sim 1 \text{ cm}^2$  free area at the back side of the tungsten plate (for obvious reasons, heating foils cannot be cut into pieces).

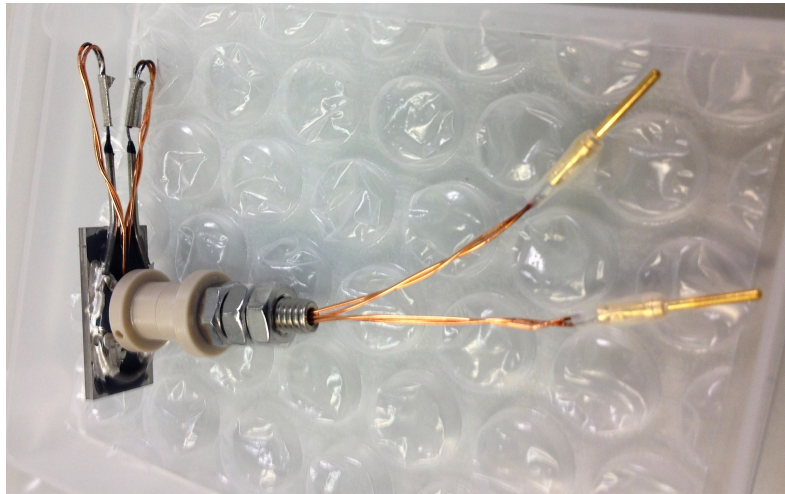


Figure 3.10.: The new SS tungsten plate with integrated resistive heater. Electrical wires are fed through the mounting screw to the outside.

A resistive wire with matching resistivity, small enough bending radius and electrically insulating but thermally conductive sheathing could be found. It was soldered on the tungsten plate back side. Electrical wiring from the outside was another issue as I wanted to avoid

drilling extra holes in the top plate. Instead, a bore was drilled into the mounting screw and two lacquered copper wires were fed through, bringing the resistive wire electrical connections to the outside. A photograph of the assembled tungsten plate and heater is shown in Fig. 3.10.

This heater installation concept comes along without temperature sensor, thus with no real-time temperature measurement. This is only a small drawback owing to spacing limitations, but precise control of the temperature is not that important in this case. Instead, the SS heater was calibrated in vacuum by recording the equilibrium surface temperature as a function of the heating voltage.

For this calibration, the ABM box (without the tilted mounting device and CEMs but with the mounted SS) was installed in the ILENA vacuum chamber, which offers just enough free space at the back of the experiment to perform this test. A PT100 temperature sensor was attached on the tungsten plate. The chamber was pumped down to the mid  $10^{-8}$  mbar pressure range. A low heating voltage was applied and subsequently increased. At each step, I waited until the temperature reached equilibrium. The heating current, voltage, and temperature were recorded and are shown in Fig. 3.11. For a surface temperature of  $80^\circ\text{C}$ , a heater voltage of about 1.05 V is needed, which amounts to about 1.0 W heating power ( $R_h = 1.12\ \Omega$ ,  $I_h = 0.94\ \text{A}$ ). When the temperature reached  $100^\circ\text{C}$ , the heating was switched off and the temporal evolution of the surface temperature (cool-down characteristics) was monitored. As shown in Fig. 3.12 the temperature follows an exponential decrease, approaching room temperature, with a time constant of  $\tau = 280\ \text{s}$ .

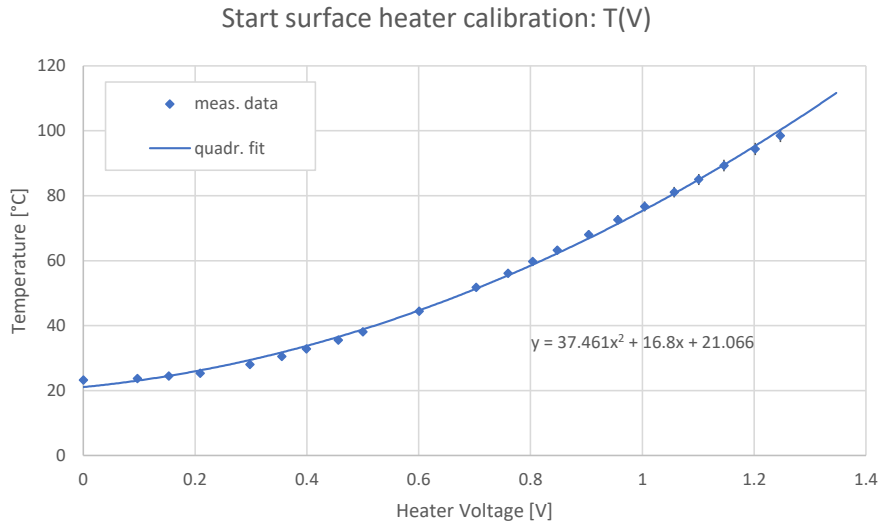


Figure 3.11.: Calibration of the ABM SS heater. The equilibrium temperature is shown as a function of heater voltage.

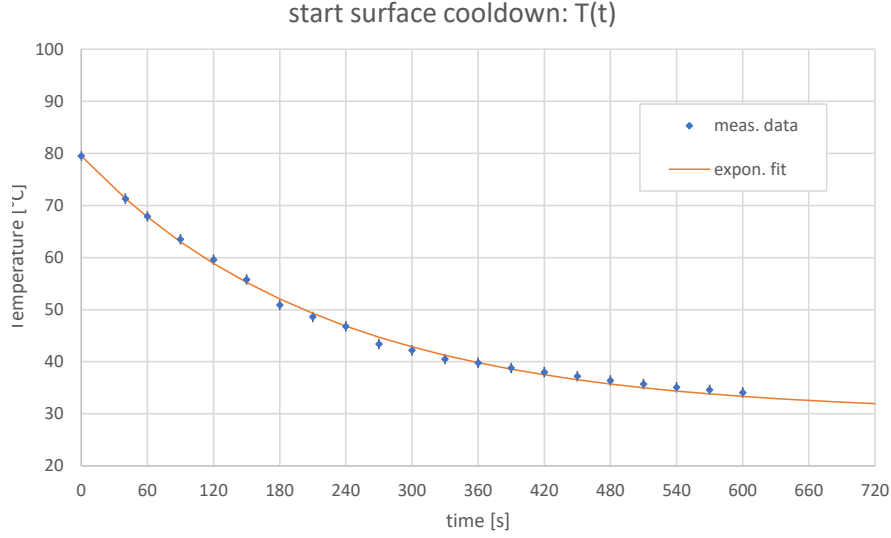


Figure 3.12.: Temperature characteristics of the ABM start surface after switching off the surface heater.

### 3.2.2. Measurement Concept

The ABM was developed to measure the absolute flux of neutral atoms. This is determined by the start, stop, and coincidence count rates and the aperture cross-section, as explained below. In addition, the ABM measures the coarse neutral beam energy, which is obtained from ToF spectra of the coincidence events. Both sub-measurements are carried out in parallel, by separate electronics.

**Particle count rates, ENA flux measurement.** From the three count rates  $r_e$ ,  $r_i$ ,  $r_c$  (where  $e$ ,  $i$ ,  $c$  stand for (start) *electrons*, (stop) *ions* including scattered neutrals, and *coincidences*) we can infer the incident neutrals rate  $F_n$  provided that we have noise-free conditions:

$$F_n = \frac{r_e r_i}{r_c} \quad (3.2)$$

This is true as any incident neutral (given the appropriate geometric restrictions) will have some probability  $\eta_e$  to trigger a start signal, and some other probability<sup>4</sup>  $\eta_i$  to trigger a stop signal. Under the assumption that start and stop signals are detected independently, the probability that an incident neutral atom causes a coincidence signal is  $\eta_c = \eta_e \eta_i$ , and we arrive at Eq. (3.2):

$$\frac{r_e r_i}{r_c} = \frac{(\eta_e F_n)(\eta_i F_n)}{\eta_c F_n} = \frac{\eta_e \eta_i F_n^2}{\eta_e \eta_i F_n} = F_n. \quad (3.3)$$

Here, “*independent*” means that the stop detection probability  $\eta_e$  remains the same whether or not a secondary electron was released from the SS and detected as start signal. This

<sup>4</sup>In the paper [12], the detection probabilities are denoted  $\mu_x$  instead, in accordance with the referenced literature.

cannot be directly verified experimentally, as it is impossible to suppress secondary electron release at the SS to compare on/off stop signal rates at constant neutrals influx. Still, it is a reasonable and justified assumption as the released electron carries away just a small fraction of the energy-momentum, thus does not significantly affect the angular directional distribution of the scattered atom and, in consequence, its probability to make it into the stop CEM.

The secondary electrons are accelerated towards the start CEM by the electrical potential difference only *after* release. The electrons do not primarily come from the impacting neutrals, but from the large reservoir of the metal's electron gas combined with the (few) valence electron(s) of the incident neutral atom. Thus, the process of secondary electron release does not affect the charge state distribution of the scattered atoms either. The signal generation in the start CEM itself does not affect the stop signal generation, so long as the two signal lines are well separated and shielded against electronic noise.

From the incident neutral atoms rate we obtain the actual ENA flux  $f_n$  [atoms/cm<sup>2</sup>/s] by division by the effective entrance aperture cross-section:  $f_n = F_n/\sigma_{ap}$ . The further details are explained in Section II.A of the ABM paper (see Section 3.4, p. 104).

**Beam energy measurement.** The time difference  $\Delta t$  between start and the stop signals is used to determine the kinetic energy of scattered particles:

$$E_{kin} = \frac{m_0}{2} \langle s \rangle^2 (t_{el} + \Delta t)^{-2} \quad (3.4)$$

where  $m_0$  is the atom mass,  $\langle s \rangle$  the effective mean flight distance, and  $t_{el}$  the median start electron flight time from SIMION simulation, see Fig. 3.6.

From this, we can determine the relative loss of kinetic energy of the scattered particles. “Loss” here means the energy(-momentum) is transferred to the surface and thus lost for the atom. This is really important to know when we aim at adjusting the neutral beam energy specifically to the requested energy bins of an ENA imaging instrument under test. It allows to compensate for the energy loss in the scattering process in the neutralizer by increasing the primary ion beam energy inversely proportionally, i.e., a 10 % energy loss at the NS necessitate increasing the ion beam energy by a factor of  $1/(1 - 0.1) = 1.111$  for compensation.

For this to work, the ABM SS should provide the same scattering conditions as the neutralizing W surface, i.e., a highly polished single crystal tungsten surface has to be used as the SS, with an incidence angle fixed at 10° (as it is in the neutralizer). Only this way can we reasonably assume the atoms scattered in the neutralizer NS and in the ABM SS experienced twice the same mean energy loss.

The mean relative energy loss  $\Lambda$  at each surface interaction is determined as

$$E_{neutr} \doteq E_{ion} - \Delta E_{NS} = (1 - \Lambda) E_{ion} \quad (3.5)$$

$$\langle E \rangle_{tof} = (1 - \Lambda) E_{neutr} = (1 - \Lambda)^2 E_{ion} \quad (3.6)$$

$$\Rightarrow \Lambda \doteq \frac{\Delta E_{NS}}{E_{ion}} = 1 - \sqrt{\frac{\langle E \rangle_{tof}}{E_{ion}}} \quad (3.7)$$

see Eq. (10) in the ABM paper, Section 3.4 below. Here,  $E_{neutr}$  is the nominal neutral beam energy, which is itself a mean value of the ENA energy per atom distribution in the beam exiting the neutralizer.

From an acquired ToF spectrum  $n(\Delta t)$  with discrete ToF bins  $\Delta t_j$ , we obtain the corresponding energy spectrum by applying Eq. (3.4) and rescaling the spectrum by

$$n(E_j) = \frac{dt(E)}{dE} n(\Delta t_j) = \sqrt{\frac{m_0}{(2E_j)^3}} \langle s \rangle n(\Delta t_j), \quad (3.8)$$

$$\text{where } E_j = \frac{m_0}{2} \langle s \rangle^2 (t_{el} + \Delta t_j)^{-2} \quad (3.9)$$

to account for the fact that equally sized bins in the time domain turn into energy bins of bin size increasing with energy.

A single ToF spectrum is typically accumulated over several minutes to hours, depending on the beam intensity, which is a strong function of the beam energy. It is expected to show one prominent peak at a flight time roughly determined by the atomic species (mass) and primary ion beam energy. There are several factors possibly contributing to the width of the ToF peaks:

- The thermal energy distribution (temperature) of the primary ion beam. It remains constant when decelerating the beam, thus will have a larger contribution at low beam energies. But it is also limited by the neutralizer ESA.
- The intrinsic energy distribution of the neutral beam into the ABM due to scattering off the neutralizer tungsten surface.
- The variation of individual flight distances  $\delta s$  inside the ABM from different scattering locations on the SS due to the finite start surface length and relatively short distance to the stop CEM, as well as varying impinging points on the stop CEM funnel.
- The variation of energy loss at surface scattering in the ABM.
- Variation in the electron flight time to produce start signals.

The recorded peaks are the result of a convolution of these individual contributions. For the energy distribution of particles just from scattering off a polished surface, see e.g. [33].

### 3.3. Electronics

In the following, the most important aspects of the ABM signal processing electronics are described, complementary to the description in the article on the ABM [12], Section 3.4. The negative low voltage signal pulses from each CEM would be amplified individually and then fed into electronics counters (see Fig. 4b in [12], on p. 107). A coincidence counting logic is required to generate coincidence signals from the two individual signal lines. Additionally, the time difference between coincident start and stop pulses need be registered.

#### 3.3.1. Data Acquisition

**Amplifiers.** In a first trial, a FAST linear direct amplifier was used on the start signal line, and a PAD05 pre-amplifier/discriminator on the stop signal. The FAST amplifier passes on negative voltage signals with arbitrary (input) peak forms, so that the counter threshold voltage needed be set at negative values. Moreover, due to the strong fluctuation of signal amplitudes and peak form, and peak broadening over the coaxial cable, the 'start' time varied strongly, so that no reliable ToF measurement was possible. The PAD05 amplifier discriminates small negative voltage pulses to short (7 ns . . . 22 ns) positive rectangular pulses when the negative voltage threshold is crossed.

It was soon clear that two identical discriminating pre-amplifiers must be in place to allow for valid time-difference recording: the amplifiers were replaced by two amplifiers of the newer model PAD06DS.

**Coincidence logic.** In the original design concept an integrated circuit unit was foreseen for providing the coincidence signal pulses, taking as input the individual start and stop signals. Unfortunately, however, this circuitry has not progressed beyond the planning phase and was never put into realization.

Instead, coincidence signal counting has been realized using the gated operation mode of the Keithley 775A counter, in combination with a gate-and-delay generator Stanford DG535. In this operation mode, the counter signal input B is used as a gating signal for counts accumulation on input A, i.e., stop pulses fed into input A are counted only if input B is at high level (above the set voltage threshold). The DG535 is then used to generate a long (100 ns . . . 10  $\mu$ s) gate window from each start signal.

Figure 3.13 shows a diagram of the originally planned coincidence logic: an input start signal pulse triggers opening a coincidence window to 'high' level. If a stop signal pulse comes in during the open gate window, a coincidence pulse is generated and the gate window is set to 'low'. After that, a second stop pulse will be ignored (single stop count). If no stop signal occurs after set gate time (dotted line), the gate window is set to 'low' as well. After closing the gate window plus a few ns short dead time, a next start pulse opens the gate window again.

The actually implemented setup with the gate generator does not fully incorporate this logic: after the first stop pulse occurs, the gate window remains open, allowing for multi stop



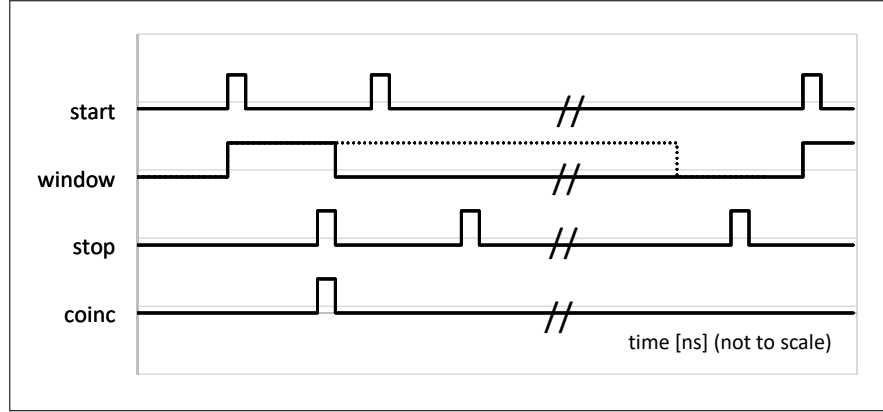


Figure 3.13.: Schematic time sequence of start and stop signals, generated gate window and output coincidence pulses.

counts. As long as the gate window is open, additional start pulses do not re-initiate the gate window, therefore they do not prolong the gate time.

At moderate and low count rates this difference will have no impact on the detected count signals. Only when start and/or stop count rates exceed about  $10^5$  counts/s for a gate window of  $1 \mu\text{s}$  this might affect the registered coincidence count rate and, thus, the flux measurement:

- Possibly ignoring some start pulses during an active gate window would reduce the number of coincidence events registered.
- Accepting more than one stop pulse during the same gate window would enhance the coincidence count rate.
- At about the same start or stop count rates, we should also consider the coincidence count rate being altered by simultaneous signals, that is, two atoms impacting the SS at the very same time, one of them generating a secondary electron start signal and the other being registered in the stop CEM to generate a stop pulse.

Principally, such improper coincidence events cannot be distinguished from single interactions. But it happens just rarely ( $< 10^{-3}$ ) except at very high count rates and atomic masses (as heavier species require longer coincidence windows). The estimated probability  $p$  for this to happen is

$$p(\text{improper coinc}) \simeq \frac{n_{\text{start}} \Delta t_g}{t_{\text{int}}} \left( 1 - \frac{(n_{\text{start}} - 1) \Delta t_g}{t_{\text{int}}} \right), \quad (3.10)$$

where  $n_{\text{start}}$  is the number of start counts,  $t_{\text{int}}$  the total integration time, and  $\Delta t_g$  the coincidence gate time.

The three counters are connected via IEEE-488 interface (also known as General Purpose Interface Bus (GPIB)) to a GPIB controller, which is connected to the computer via ethernet. Initial configurations, trigger threshold and other settings, data acquisition, reset, and data

readout all happen automatically via GPIB and ethernet. I implemented the necessary commands and connections for communication, as well as the data storage on the computer, in a dedicated Python script.

**ToF measurement.** The ABM data acquisition was conceptualized in such a way that the two sub-measurements – count rates and ToF spectra – be recorded in parallel but by separate electronics. That way each sub-measurement can be initiated and terminated independently, a common acquisition trigger is not necessary. A FAST TDC card with corresponding software was used for the ToF spectrum acquisition. Figure 3.14 shows the graphical user interface of the ToF acquisition software. The spectrum ToF range, resolution, trigger thresholds and other settings are set from dropdown menu. During accumulation, the current ToF spectrum is displayed on the screen. The CEM circuitry and electronic signal processing scheme are shown in Fig. 4 in Gasser et al. [12]. The actually used electronics equipment is described in Section II.C on page 107.

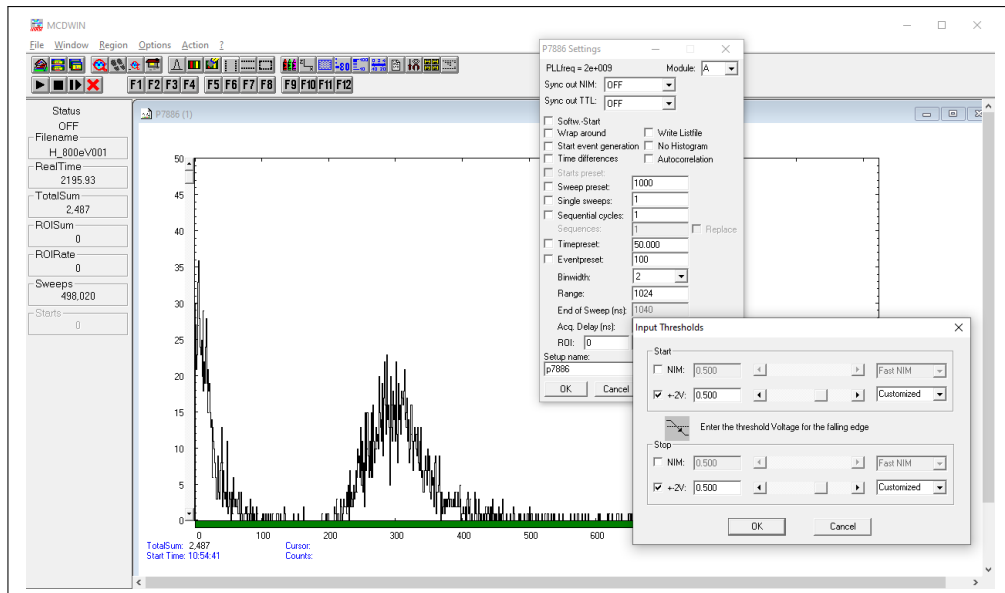


Figure 3.14.: MS Windows control panel of the MCDWIN ToF acquisition software. Data acquisition settings are entered in the options menu.

### 3.3.2. Noise and Background Suppression

In general, the acquisition of a clear, undisturbed signal from the source of interest (here, the ENA beam from the neutralizer) can be compromised by additional unwanted signal counts, a) noise and b) background. I distinguish these two types by their (presumed) causes: *background* counts originate from real physical detected particles in the ABM (example: ambient rest gas molecules). They would likely be present even in a perfect test facility well separated from any other electronic apparatus and on immaculate device installation. The background count rate does not vary greatly with time. *Noise* signals, on the other hand, occur due to some interfering external action unrelated to the test environment (examples: induced electronic pulses, loose connections, fast voltage alterations in a DC supply, . . . )

During the repeated test runs with the ABM in the laboratory, we identified and reduced the following different sources and causes of noise and background signals:

- At the beginning, opening and closing the laboratory main door erratically caused a series of noise signals on one or all of the signal lines.
- Switching on or off the air conditioning caused arbitrary noise start signals.
- Switching on or off the air humidifier caused several tens to hundreds of noise start and coincidence counts. This was clearly seen especially in long-term signal accumulation at low beam energies (with accordingly low count rates), as the auto-controlled humidifier sets in every 10 minutes for a few minutes.
- Mechanical vibrations or shaking of the experiment table could cause some noise signals. All of the above noise sources could be suppressed by an improved electrical grounding and signal shielding scheme, and with re-installation of the ABM into the vacuum test chamber.
- Furthermore, hexapod motions can also cause few noise signals. This goes along with a short-time local pressure increase in the chamber, likely from desorption of volatiles and water off the moving motors. This does not impact ABM measurements as the hexapod is typically not moving during counts accumulation.
- The hot cathode pressure gauge at the back side inside the main vacuum chamber also caused constant start and stop count rates, but no identifiable coincidence counts. The hot cathode filament was turned off during the measurements after identifying this background source. The cathode gauge was thereafter shielded from direct sight to the ABM and the neutralizer.

### 3.4. Paper: “Absolute beam monitor: A novel laboratory device for neutral beam calibration”

The following research article “*Absolute beam monitor: A novel laboratory device for neutral beam calibration*” reports on the successful development of an Absolute Beam Monitor for laboratory low-energy neutral atom beams and summarizes its working principle, design and testing in the laboratory environment. Section I gives a brief general overview over recent ENA instrumentation for space applications, low-energy neutral atoms calibration infrastructure and reasoning why such a device is indeed very useful.

The ABM measurement principle and technical implementation are summarized in Sections II.A and II.B, respectively. Section II.C describes where and how the ABM has been tested and is applied in the laboratory calibration facility. Section III gives an overview of the proof-of-concept test results, device characteristics, and first calibration measurements, and briefly highlights how a neutral beam source is calibrated by application of this Absolute Beam Monitor.

A few typos in formulae (4) and (5) have been discovered after publication. Therefore, we published an erratum on this article, which is appended below (p. 114).

*The following article reprint “Absolute Beam Monitor: a novel laboratory device for neutral beam calibration” is reproduced from Rev. Sci. Instrum. **93**, 093302 (2022); doi: 10.1063/5.0092065, with the permission of AIP Publishing.*

*The following article reprint “Erratum: ‘Absolute Beam Monitor: a novel laboratory device for neutral beam calibration’ ” is reproduced from Rev. Sci. Instrum. **93**, 129902 (2022); doi: 10.1063/5.0133907, with the permission of AIP Publishing.*

# Absolute beam monitor: A novel laboratory device for neutral beam calibration

Cite as: Rev. Sci. Instrum. 93, 093302 (2022); doi: 10.1063/5.0092065

Submitted: 20 March 2022 • Accepted: 10 August 2022 •

Published Online: 13 September 2022



Jonathan Gasser,<sup>a)</sup> André Galli, and Peter Wurz

## AFFILIATIONS

Physics Institute, Space Research and Planetary Sciences, University of Bern, Sidlerstrasse 5, 3012 Bern, Switzerland

<sup>a)</sup> Author to whom correspondence should be addressed: [jonathan.gasser@unibe.ch](mailto:jonathan.gasser@unibe.ch)

## ABSTRACT

Instruments recording Energetic Neutral Atoms (ENAs) for space applications require thorough laboratory calibration in a dedicated test facility providing a neutral atom beam. Accurate knowledge of the neutral beam intensity and energy is central for the laboratory calibration procedure. However, until recently, the quantification of the neutral atom beam intensity in the low-energy range below a few 100 eV was based on relative measurements with standard detectors of approximately known detection efficiencies for neutral atoms. We report on the design and development of a novel calibration device dedicated to determining the ENA beam flux in an absolute manner in the energy range from 3 keV down to about 10 eV. This is realized by applying ENA scattering at a surface and coincident detection of scattered particles and created secondary electrons. Moreover, the neutral beam energy is determined by a time-of-flight measurement. The applied measurement principle relies on very low background signals. The observed background count rates are in the range  $10^{-2}$  s for the individual channels and about  $10^{-5}$  s for coincidence events. The background is, thus, at least two, typically four, orders of magnitude lower than the signal rate for neutral atom beams in the foreseen energy range. We demonstrate a concrete application using the absolute flux calibration of a laboratory neutralization stage.

© 2022 Author(s). All article content, except where otherwise noted, is licensed under a Creative Commons Attribution (CC BY) license (<http://creativecommons.org/licenses/by/4.0/>). <https://doi.org/10.1063/5.0092065>

## I. INTRODUCTION

*In situ* and remote detection and analysis of energetic neutral atoms (ENAs) has become an important method in space and planetary science.<sup>1</sup> Several past and upcoming space missions are equipped with a low-energy ENA imaging instrument, such as IBEX-Lo<sup>2,3</sup> on the very successful and still active Interstellar Boundary Explorer (IBEX) mission by NASA<sup>4</sup> and its successor Interstellar Mapping and Acceleration Probe (IMAP),<sup>5</sup> with launch scheduled for February 2025. The scientific instruments onboard these spacecraft are dedicated to investigate in great detail the heliosphere and its interaction with the Local Interstellar Medium. IBEX provided many new insights into the structure and physical processes of the outer heliosphere, in particular, the discovery of the ENA ribbon and characterization of the globally distributed ENA flux. Annual all-sky ENA maps and interstellar neutral atom observations have been acquired over one full solar cycle,<sup>6</sup> and references therein.<sup>7–9</sup> The active science phase of IBEX is expected to continue until 2025, allowing for overlap between the IBEX and IMAP

missions. Cross-calibration measurements will be performed in flight between IBEX-Lo and IMAP-Lo, once the latter begins science operations.

ENA observations are particularly interesting in heliospheric science because neutral atoms, as opposed to electrons and ions, travel on ballistic trajectories and are not affected by solar wind plasma and magnetic fields. They, thus, provide a pristine source of information about conditions present at their origin, such as density, composition, bulk speed, and energy distribution of the Local Interstellar Medium. In addition, ENA instruments also allow for the remote sensing of planetary atmospheres.

ENA instruments for planetary exploration include IMAGE/LENA,<sup>10</sup> ASPERA-3 on Mars Express<sup>11</sup> and ASPERA-4 on Venus Express,<sup>12</sup> CENA/SARA<sup>13</sup> on the lunar mission Chandrayaan-1, SERENA/ELENA and ENA as part of the Mercury Plasma/Particle Experiment on BepiColombo<sup>14,15</sup> launched in October 2018 heading for Mercury, Mars Ion and Neutral Particle Analyzer (MINPA)<sup>16</sup> on the Chinese Mars mission (Tianwen-1), and the Jovian Neutral Analyser (JNA)<sup>17,18</sup> as part of the Particle

Environment Package on the upcoming JUICE (Jupiter Icy Moons Explorer) mission<sup>19</sup> to be launched in 2023.

Low-energy ENA instruments below a few 100 eV generally rely on an efficient and reliable particle ionization method to allow for electrostatic analysis and post-acceleration in support of detection efficiency.<sup>1</sup> The most widely used technique for space applications in this energy range is charge-conversion via on-surface scattering at grazing incidence angles.<sup>1</sup> However, the underlying physical processes involved in the atom-surface interactions are not yet understood in full detail. Instead, a number of well-suited conversion surface materials have been characterized experimentally,<sup>20</sup> and references therein.<sup>21,22</sup>

For this reason, besides the general specification necessities imposed by the harsh space environment, ENA detection instruments require proper calibration against a neutral atom beam source. For full instrument calibration, substituting the ENA beam by an ion beam is not feasible because low-energy ions, as opposed to neutral atoms, are affected by electric fields inside the instrument under test.

At the University of Bern, we have a dedicated laboratory test facility<sup>23</sup> available for preflight calibration of ENA instruments for space research. The MEFISTO facility is equipped with an electron cyclotron resonance ion source (ECRIS) suitable for producing a positive ion beam from any atomic species. Calibration of the IMAP-Lo instrument will be carried out there. For the IMAP-Lo calibration campaign, calibrated ENA beams from hydrogen, oxygen, helium, and also deuterium, neon, and other light elements are of foremost interest.

In the low-energy range, a neutral beam is obtained from a collimated ion beam via surface neutralization using the neutralizer.<sup>24</sup> This neutralization process introduces angular divergence and some kinetic energy loss upon scattering from the neutralization surface. After beam neutralization in the laboratory, beam characterization by means of particle detection devices such as multichannel-plate detectors and channeltrons is limited by the knowledge of the absolute detection efficiency of these detection devices for atoms at these energies. Until recently, energy loss and neutral beam intensity were estimated based on relative measurements and theoretical considerations, as it was not possible to experimentally determine neutral beam fluxes and energies directly.<sup>24</sup>

The rising demand for an accurate method to determine the ENA flux of a neutral atom beam source urged us to develop the Absolute Beam Monitor (ABM), in particular, in regard of the upcoming IMAP-Lo calibration campaigns. The ABM is a laboratory device used to determine the particle flux of a neutral atom beam in the energy range from 3 keV down to 10 eV. Using coincidence events in this device allows for absolute flux measurements in a manner independent of any implicit detection efficiency assumption. It will, therefore, be used as primary standard for the laboratory ENA beam source calibration. The ABM is so far the only device to measure absolute neutral beam intensities in the energy range below 1 keV.

The general approach for measuring the absolute flux of neutral atom beams using coincidence events has already been used.<sup>25</sup> This instrument uses the neutral beam transmission through a thin foil. Given that the atoms have to pass solid matter, a thin foil, there exists a minimum value of energy the atoms need to possess for their registration. This minimum energy given by the successful

transmission through the foil is around 500–1000 eV/nuc,<sup>1,26</sup> increasing with foil thickness. The energy threshold for H detection using thin carbon foils of 1  $\mu\text{g}/\text{cm}^2$  is about 500 eV, and it increases with atomic mass  $m$ ; as for fixed energy, the nuclear stopping in the foil is approximately proportional to  $m^{27}$  and the angular scatter increases with the mass as well.<sup>28</sup> For IMAP-Lo, the required mass range spans from 1 to 32 (hydrogen to sulfur) in the energy range from 10 eV to 2 keV; thus, the foil-based approach cannot be used.

## II. METHODS

In the following, we describe the ABM design and implementation as well as the basic physical principle it is built on.

### A. Measurement principle

The detection and analysis of low-energy ENAs require prior particle ionization. The most reliable ionization process used in space science at energies below about 1 keV is via on-surface interaction at grazing incidence angles.<sup>29</sup> The grazing incidence surface scattering process is also applied to obtain an ENA beam from a primary ion beam.<sup>24</sup> In the scattering interaction, secondary electrons are ejected from the surface, which can be detected separately.

The ABM measurement principle relies on coincident detection of a neutral atom scattered off a conversion surface and the simultaneous release of a secondary electron during this scattering process. The absolute neutral atom flux  $f_n$  entering the ABM is determined by the number of counts  $N$  for the detected neutral atoms within a time interval  $t_{\text{int}}$ , the detection efficiency  $\epsilon_n$  for neutral atoms, and the cross section  $\sigma_{ap}$  of the ABM aperture,

$$f_n = \frac{N}{\epsilon_n \sigma_{ap} t_{\text{int}}} = \frac{n}{\epsilon_n \sigma_{ap}}. \quad (1)$$

The measured neutral atom rate,  $n$ , is obtained by the simultaneous detection of three count rates: a start count rate  $r_e$  generated by secondary electrons released from the start surface (SS) upon impact of a neutral atom, a stop count rate  $r_i$  of the scattered neutral atoms hitting the stop detector, and a coincidence rate  $r_c$  between these two signals. Each incident neutral atom has an *a priori* unknown probability  $\eta_e$  for ejecting a secondary electron from the SS and an unknown probability  $\eta_i$  of being itself detected subsequently by the stop detector. The probability of generating a coincidence count is, thus,  $\eta_c = \eta_e \cdot \eta_i$ . The start, stop, and coincidence count rates ( $r_e, r_i, r_c$ ) to be observed from the incoming neutral atoms  $F_n = f_n \sigma_{ap}$ , through the entrance aperture with the cross section  $\sigma_{ap}$ , respectively, will then be

$$\begin{aligned} r_e &= \mu_e F_n + r_{e,0}, \\ r_i &= \mu_i F_n + r_{i,0}, \\ r_c &= \mu_c F_n + r_{c,0} = \mu_e \mu_i F_n + r_{c,0}. \end{aligned} \quad (2)$$

With the requirement that the backgrounds on the three rates ( $r_{e,0}, r_{i,0}, r_{c,0}$ ) are negligible, we obtain

$$\begin{aligned}\mu_e &= \frac{r_c}{r_i} = \frac{\mu_e \mu_i F_n}{\mu_i F_n}, \\ \mu_i &= \frac{r_c}{r_e} = \frac{\mu_e \mu_i F_n}{\mu_e F_n},\end{aligned}\quad (3)$$

and we get the detection efficiency  $\varepsilon_n = \mu_e \mu_i$  for neutral atoms. This formalism is well known and has been used in plasma and particle instruments for many years.<sup>30,31</sup> The neutral atom flux  $f_n$  can be obtained directly from the observed count rates as

$$f_n = \frac{(r_e - r_{e,0}) \cdot (r_i - r_{i,0})}{(r_c - r_{c,0})}. \quad (4)$$

This method requires very low detector background count rates; otherwise, the background rate in the start rate  $r_{e,0}$ , the stop rate  $r_{i,0}$ , and the coincidence rate  $r_{c,0}$  will interfere with the derivation of the neutral atom flux. Therefore, we have to keep the background rates very low compared to the respective count rates to apply Eq. (4) to derive the true particle flux  $f_n$ . We carefully record the background count rates separately, see below, and subtract them from the measured count rates in the data evaluation.

By multiplying the rates with the integration time, we can rewrite Eq. (4) by the actual counts collected:

$$f_n = \frac{(c_e + c_{e,0}) \cdot (c_i + c_{i,0})}{(c_c + c_{c,0})}. \quad (5)$$

We assume that the individual counts registered in a time interval are Poisson distributed. The statistical uncertainty of the mean count rate for a single accumulation measurement is, thus,

$$\frac{\delta f_n}{f_n} = \frac{\delta c_e}{c_e} + \frac{\delta c_i}{c_i} + \frac{\delta c_c}{c_c} = \frac{1}{\sqrt{c_e}} + \frac{1}{\sqrt{c_i}} + \frac{1}{\sqrt{c_c}}. \quad (6)$$

The dominant contribution to the statistical uncertainty is due to coincidence counts, as these always give the lowest count rates. At lower beam energies, where the neutral atom flux is typically much reduced, this puts a condition on the required accumulation time: To achieve a relative uncertainty of 10% or better in Eq. (6), the integration time should be long enough to record at least 100 coincidence counts.

From all recorded coincidence events, we measure the time difference  $\Delta t$  between the start pulse and the stop pulse in parallel to the individual counters. Combined with the known mean flight distance  $s$  of scattered atoms from the SS center to the stop detector and the atom species (known from the primary ion beam), we infer the kinetic energy as

$$E_{kin} = \frac{m_0}{2} \langle s \rangle^2 (t_{el} + \Delta t)^{-2}. \quad (7)$$

Here, we also take into account the electron flight time  $t_{el}$  from the SS to the start detector, which is about 11 ns according to the electro-optical simulation.

Neutral atoms can impinge over almost the full length of the SS, which causes an uncertainty  $\delta s$  in the flight distance after generating a start signal. With  $\langle s \rangle = 101$  mm and  $\delta s = \pm 10$  mm, this contributes a relative uncertainty of  $\frac{\delta E}{E} \cong 10\%$  to the energy distribution measured in the time-of-flight (ToF) spectra.

## B. Technical design

The ion-optical properties and the geometry were designed using numerical simulations with the SIMION® software package from Scientific Instrument Services. A schematic overview of the simulation model is shown in Fig. 1.

The ABM consists of a near-cylindrically shaped box of about  $14 \times 7 \times 7$  cm<sup>3</sup> size. The structure is an assembly of a concave top plate and an opposite bottom plate with a conical rim, enveloped by a cylindrical mantle with flattened planar sides. A circular entrance hole of 5 mm diameter is located at the front side of the envelope, the entrance aperture, through which the ENAs enter the ABM. An additional circular aperture of 5 mm diameter is mounted 9 mm in front of the entrance aperture to restrict the allowed angular directions of incoming neutral atoms. At the backside, a passage in the mantle is left open and a conical tube (target cone) is firmly attached. Serrations in the bottom plate and target cone serve to collect the scattered particles off the SS. All inner surfaces, except for the SS and the channel electron multipliers (CEMs), are coated with Acktar Vacuum Black (Acktar Ltd., Kiryat-Gat, Israel) to enhance absorption of photons, electrons, and scattered atoms by its large effective surface area.

The whole ABM is tilted by about 10° with respect to the neutral beam direction, so that the ENA beam entering through the entrance aperture hits the SS at a grazing incidence angle of  $\alpha = 10^\circ \pm 0.5^\circ$ . This shallow incidence angle is a compromise between reducing the angular scattering on the SS by a more grazing incidence on one hand and capturing the full incident ENA beam on a relatively short SS not to broaden the ToF peak on the other hand. Moreover, the same incidence angle was applied in the surface neutralizer (see below). The SS stands off from the top plate and is oriented along the projected neutral beam direction to cover the full neutral beam passing through the entrance hole.

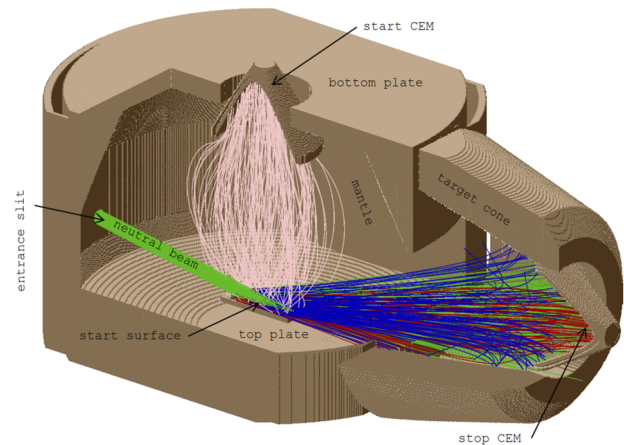


**FIG. 1.** Schematic ABM simulation model in SIMION. Part of the structure is cut away to present the ABM interior. Simulated particle trajectories are shown as colored lines: neutral atoms (green), electrons (pink), positive ions (red), and negative ions (blue) ions. The ABM device is operated such that the neutral atoms enter horizontally through the entrance aperture on the left.



A first channel electron multiplier (start CEM) of 25 mm diameter is placed opposite the SS. Its entrance is held at a positive electrostatic potential (HV0) to attract all secondary electrons emitted from the SS. A second CEM (stop CEM) is placed at the open end of the target cone to accept and detect the scattered neutral atoms.

The entire enclosure (mantle, top and bottom plates, target cone) is at ground potential. The SS at a low positive voltage and the start CEM at +HV0 confine the secondary electrons in the center region of the volume. Scattered charge-converted ions and neutral atoms are directed, simply by their scattering direction distribution, toward the stop CEM with aperture at a high negative potential (HV2). Negative ions are, thus, rejected and effectively absorbed at the inner device walls, while positive ions are attracted toward the stop CEM.

The start surface is, of course, the central element of the entire device. It consists of a  $20 \times 10 \times 1.0 \text{ mm}^3$  highly polished tungsten (W) single crystal plate (MaTeCK GmbH, Jülich, Germany) with (100) surface orientation. Tungsten was chosen as SS to have the same surface interaction as in the neutralizer, to support the validity of Eq. (10) (see below) for the relative loss of particle energy. In the neutralizer design,<sup>24</sup> W was used as neutralizing surface for three reasons: First, metal single crystals serve well to neutralize scattered particles; second, W isotopes have high atomic masses of 182–186 amu, which aids in reducing the energy transfer in a binary collision with low-mass atomic ions;<sup>20,32</sup> and third, W single crystal surfaces are readily available and chemically stable. The SS plate is soldered at its backside onto a screw, which is fed through the top plate but electrically insulated from it. A bias low voltage is applied on the mounting screw from the outside. The SS is equipped with an electrically insulated resistive wire heater at its backside that allows heating the SS to remove adsorbed water layers from it.

The start CEM aperture cone is inserted through a circular hole in the bottom plate; its electrical connections and signal line are placed under the box. Two semicircular inserts close up the hole for electrostatic shielding. The stop CEM holder is mounted at the back of the target cone. The entire device is mounted on a  $10^\circ$  tilted aluminum support that ensures proper geometry for the incidence of the neutral atom beam, proper electrical ground, and firm and flexible installation in the vacuum chamber. Figure 2 shows a photograph of the assembled ABM device.

### C. Laboratory setup

The ABM has been tested and mounted in the MEFISTO test facility.<sup>23</sup> MEFISTO consists of a large vacuum chamber equipped with a microwave-heated electron cyclotron resonance ion source providing a focused positive ion beam of any desired species at energy 3 keV/q. The ion beam is neutralized using the surface neutralizer, which has been moved into the ion beam path.<sup>24</sup> Inside the neutralizer, the incoming ions are scattered at a  $10^\circ$  grazing incidence angle from a polished W surface and, thereby, almost completely neutralized. The neutralizer can be floated to high voltage up to 3 kV, which decelerates the incoming ion beam to the desired final ion energy in the range 10–3000 eV for neutralization. A  $20^\circ$  electrostatic analyzer, with ions of defined energy, is installed in front of the neutralization surface to deflect the ion beam so that

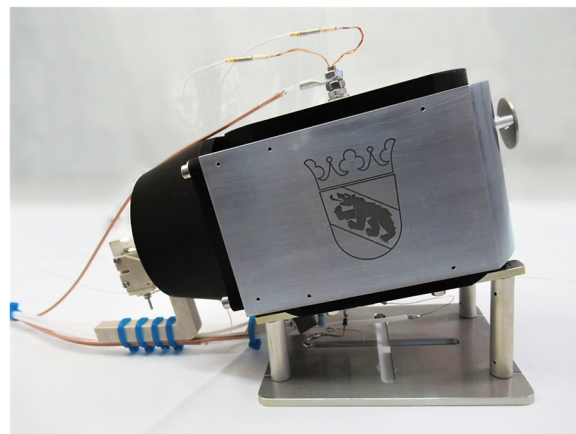


**FIG. 2.** The fully assembled absolute beam monitor version 2. The entrance aperture with the additional standoff aperture is to the right. At the top is the SS mounting screw with the SS voltage connection and the heater connections. Electrical connections for the CEMs come from the left underneath the ABM. The dimension of the base plate is  $100 \times 80 \text{ mm}^2$ .

the outgoing neutral beam is parallel to the incoming ion beam. The neutralization process induces an estimated 15% reduction in beam energy and the deceleration induces an energy-dependent transmission. The neutral beam flux into the test chamber, thus, varies with ion beam energy, ion intensity, and species.

During testing, the ABM is mounted on a four-axis movable and pivotable hexapod table so that the ABM can be placed in the optimal position at the center of the neutral beam in front of the neutralizer exit at a distance of about 10 cm (see Fig. 3). The entire test setup incorporates, thus, a collinear and retarded ion beam passing through an ESA onto a neutralizing W surface. The resulting

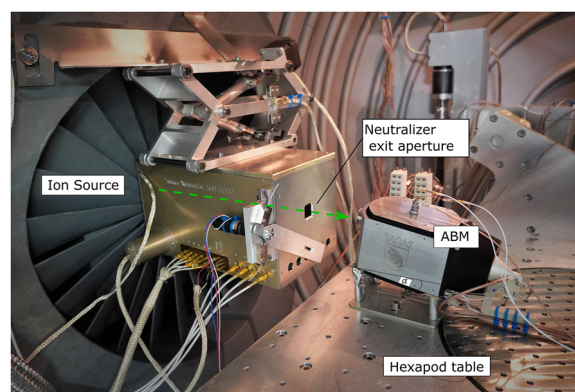


**FIG. 3.** The ABM mounted on the hexapod table in the MEFISTO vacuum chamber, placed at the exit of the surface neutralizer. At the front, toward the neutralizer, there is the entrance aperture and the aluminum shielding to protect the start CEM under the ABM box. The ion beam enters the neutralizer from behind the baffled shroud on the left-hand side. The neutral beam axis (green) and ABM tilt angle are indicated. Scale: The screw hole spacing on the hexapod table is  $40 \times 40 \text{ mm}^2$ .



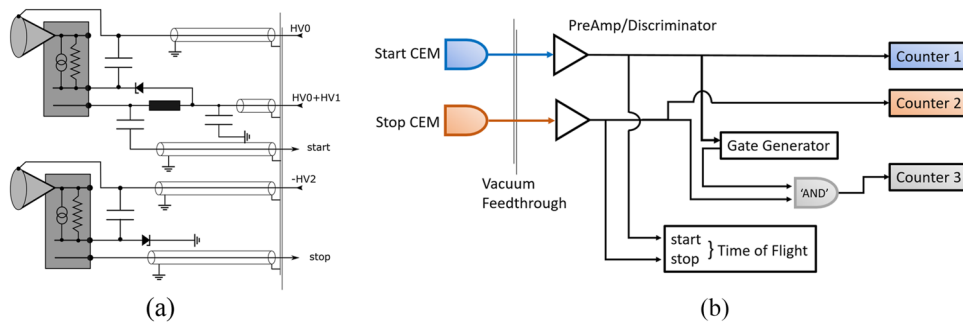


**FIG. 4.** (a) Electronic circuitry of the start (top) and stop CEM (bottom). Gray boxes represent the CEMs with electrical front, back, and anode contacts. The CEM apertures are held at high voltage +HV0 and −HV2, respectively. (b) Electronic signal processing setup in the laboratory. The preamplifiers transform the negative signal pulses from the CEMs to clean rectangular positive pulses. The gate generator provides the time window for coincidence events. ToF spectrum acquisition is done using a separate TDC card.

neutral atom beam is collimated at the neutralizer exit and passes on into the ABM where the neutral atoms strike another W surface to initiate detection.

Secondary electrons or scattered ions and neutral atoms from the ABM SS are collected in the CEMs (Sjuts Optotechnik GmbH, Germany, model KBL25RS/90) with 25 mm diameter apertures. The negative signal pulses from the start and stop CEM are routed through the vacuum chamber flange and fed into a preamplifier and discriminator (Winkelkemper Ing., Hattingen, Germany, model PAD06DS), which converts the CEM signals into 12 ns short +1.5 V rectangular pulses for further processing. The preamp dead time was set to 20 ns. The electronic configuration is shown in Fig. 4.

The discrete start pulses are recorded by the electronic Counter 1 (model: HP 53132A), as shown in Fig. 4(b). The signal also triggers the gate generator (model: Stanford DG535) that outputs a coincidence window signal of adjustable duration. The discrete stop pulses are registered alike in Counter 2 (model: Keithley 776) and in Counter 3 (model: Keithley 775A) during active gate window signal to accumulate the coincidence counts. A signal delay through the gate generator is matched by accordingly longer stop signal line. Compared to a conventional coincidence counting system, the expected flight time of a particle covers a large range; thus, we allow for a long coincidence gate window in the range 100 ns to 10  $\mu$ s, depending on species and beam energy. For each start event, several stop counts could be accepted as coincidence events.

In addition, the time intervals between start and stop pulses for coincidence events were recorded using a fast time-to-digital converter (TDC) card (FAST ComTec GmbH, Oberhaching, Germany, model p7886) with up to 2 GHz (0.5 ns) time resolution. The hardware is installed directly on the main board and operated with commercial software. The TDC acquisition features an end-of-sweep dead time of about 20 ns. All start and stop signal lines and counter and preamplifier thresholds were matched to ensure a maximal shift of <0.1 ns in time difference owing to the setup.

### III. PERFORMANCE CHARACTERIZATION

Several tests were undertaken in support of performance and concept verification.

#### A. Background rates

The background count rate refers to the number of detected signal pulses per time with the beam source and surface neutralizer shut down but the ABM fully working. Background counts may result from ambient ions or electrons from the pressure gauges hitting one of the CEMs or from spontaneous pulses from radioactive decay of materials used in the CEMs. Moreover, electronic noise may be picked up on the signal transmission lines. The ambient gas pressure in the test chamber was in the low to mid  $10^{-8}$  mbar range. In Fig. 5, the measured background count rates are displayed over time. These were usually acquired over several hours. The start background rate is in the order of 1 min, the stop background rate is about 0.3 min, and the coincidence background rate is typically below 0.001 min (i.e., below  $10^{-5}$  s $^{-1}$ ). The exponential fits to the data provided in Fig. 5 show a decrease in background counts over time for the start and stop signals, whereas the coincidence background count rate remains constant over time within the uncertainties given due to the very low counting statistics.

For the most part of the foreseen energy range, the background count rate of each channel is at least two orders below the measured actual signal count rate. Only for the very low-energy neutral atom beams (below about 50 eV), it might become relevant to subtract the background count rate for proper data evaluation.

#### B. Poisson distribution

The detection of individual secondary electrons is independent, but for a constant neutral atom beam flux, the detection probability is constant in time. Likewise, for the detection of scattered atoms. Therefore, the number of detected start or stop counts  $n$  per unit time interval  $\Delta t$  should follow a Poisson distribution with expectation value  $\langle N \rangle$ ,

$$p(n, \Delta t) = \frac{\langle N \rangle^n}{n!} e^{-\langle N \rangle}. \quad (8)$$

This can best be tested in a measurement at low beam energies, where the mean start or stop count rates are just a few counts per time interval, i.e., typically about 5 counts/min. A constant ion beam intensity is required to establish time independence of the detection probability. Figure 6(a) shows start and stop counts over time of a measurement sequence with a 50 eV hydrogen neutral atom beam having low count rates, and Fig. 6(b) shows the histogram for a

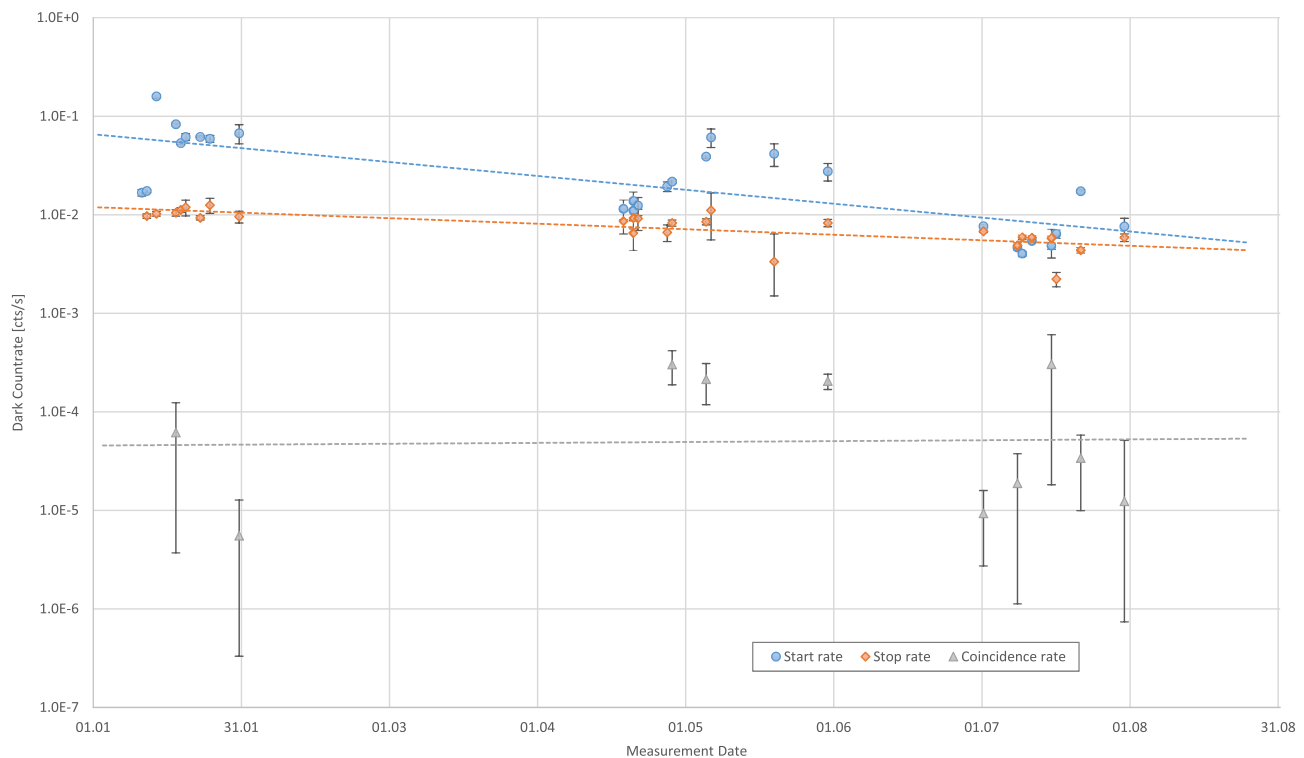


**FIG. 5.** Measured ABM background count rates for start, stop, and coincidence over time shown with statistical errors. The typical acquisition time per data point is several hours. Zero coincidence background counts were recorded where the respective data points are missing. Weighted exponential fit curves are added for each channel.

60 s time interval of these counts along with the Poisson distribution corresponding to the mean count rate. Figure 6(c) shows the respective start, stop, and coincidence count distributions at a beam energy of 80 eV giving higher count rates. The measured distributions are in good agreement with Poisson distributions, confirming that individual atoms or secondary electrons are indeed recorded independently.

This holds true as long as the mean start or stop count rate is small compared to the inverse of the preamplifier dead time,  $n \ll \tau_d^{-1} \equiv (10 \text{ ns})^{-1} = 10^8 \text{ s}^{-1}$ . At the highest ENA energies, where we encounter the highest count rates, the start count rate remained below  $10^7 \text{ s}^{-1}$ , most times below  $10^6 \text{ s}^{-1}$ .

### C. Background and voltage setting

A typical measurement sequence of a neutral hydrogen atom beam at an ion energy of 100 eV/q, during optimization of the measurement parameters, is shown in Fig. 7. Counts were collected for 60 s accumulation time and these data points were stored continuously. The total measurement time is close to 5 h. The number of measured neutral atoms per time unit is calculated from the respective start, stop, and coincidence counts. Several manipulations were done on the CEM voltages (HV1, HV2) and the offset voltage (HV0) during this sequence to optimize the operation of the ABM. Times of these changes are indicated by dashed lines in Fig. 7, with the details given in Table I.

These adjustments on the CEM voltages have a large impact on the start, stop, and coincidence count rates. In particular, increasing the start CEM voltage HV1 by 150 V in total from minute 1 to minute 120 increases the start count rate by about three orders of magnitude until a plateau is reached and similarly for the coincidence events. However, the deduced neutral atom rate is only lower by a factor 3 before compared to after minute 90, when the HV1 voltage reached the nominal level. The large scatter in intensity of neutral atoms during the first hour is a direct consequence of the extremely low start rate and, thus, the extremely low coincidence rate. Increasing HV1 further (around minute 240) leaves the obtained neutral atom rate constant. Furthermore, adjusting the offset voltage HV0 within a range of a few 100 V (after minute 240) does not affect the resulting neutral atom rate despite changes in the individual count rates. Consequently, the offset voltage can be used to minimize the relative statistical variation of the neutral atom rate, by maximizing the coincidence count rate. In summary, once a sufficiently high voltage is applied to the CEMs, their actual value is less critical, and a stable and reliable neutral flux can be derived from these measurements. Changing the preamplifier threshold voltages (minutes 44, 120, 210) does in general also affect the individual start, stop, and coincidence count rates but not the derived neutrals rate.

At minutes 105, 175, and 218, the primary hydrogen ion beam was blocked intentionally by the ion beam scanner for several minutes. This reduced the start and stop counts by four orders of

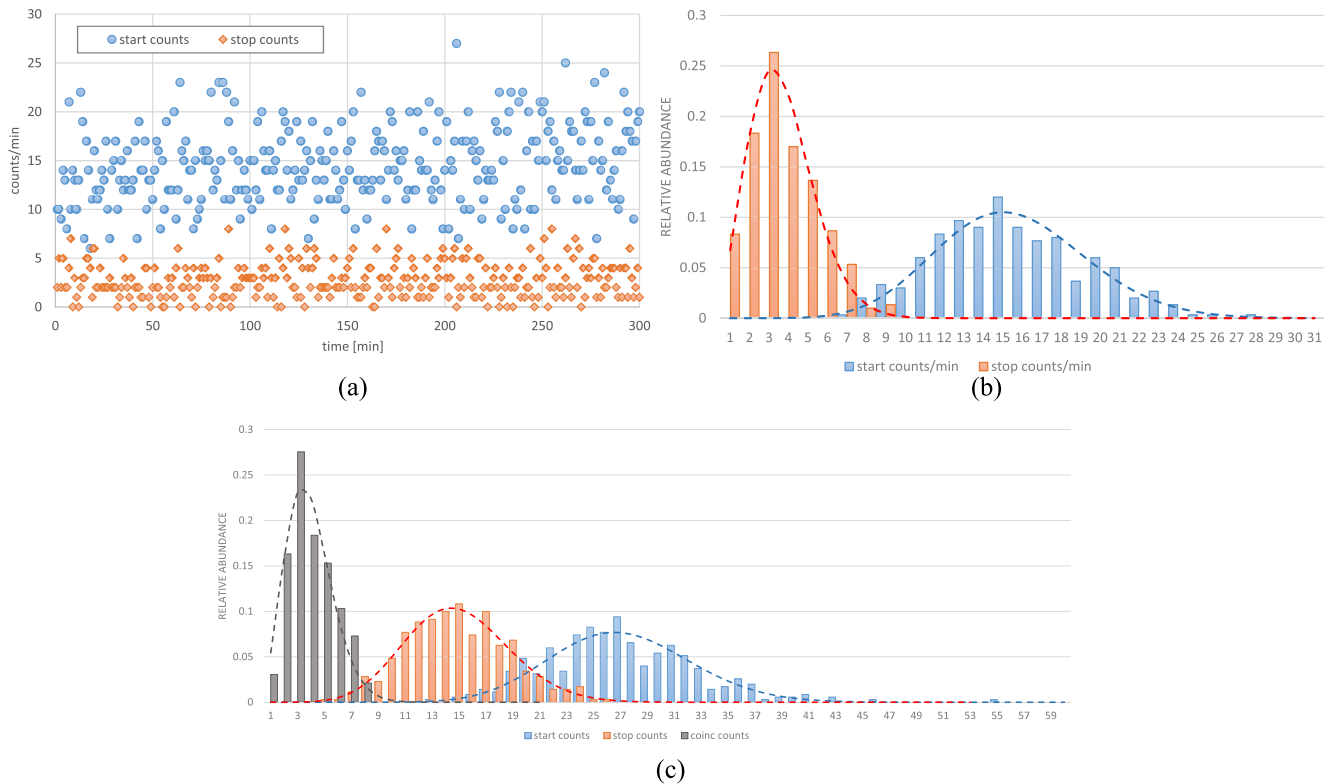


**FIG. 6.** (a) Example time sequence of start and stop counts for H at 50 eV. (b) Corresponding occurrence distribution (histograms) and predicted Poisson distributions (dashed lines). Expectation values are  $\langle N \rangle = 14.5$  and  $\langle N \rangle = 2.7$  for start and stop counts, respectively. (c) Start, stop, and coincidence distributions at slightly higher count rate for 80 eV hydrogen. The dashed lines show predicted Poisson distributions for  $\langle N \rangle = 2.91$ , 14.9, and 27.07 counts/min, respectively.

magnitude to their respective background rates, giving a signal to background ratio of about  $10^4$  for the start rate, as well as for the stop rate. The mean start and stop count rates are indicated, respectively, for each ion beam interrupt period by empty symbols with statistical error bars. No coincidence events were detected during the ion beam interrupts, which is expected given the low coincidence background rate of about  $10^{-4} \text{ s}^{-1}$  presented in Fig. 5. The ion beam interruptions demonstrate the low background during a real measurement situation, in agreement with the background determinations done during the preparation (Fig. 5), which are a requirement for the capability of absolute neutral flux measurements with the ABM.

#### D. Time-of-flight measurement

The TDC card used for the ToF measurements provides time resolution of up to 0.5 ns. The data acquisition speed is, thus, considerably higher than the physical ToF resolution of the ABM, and we obtain a well-resolved peak in the ToF spectra given large enough coincidence events statistics. Acquisition of ToF spectra of variable length (512 ... 8192 bins) and bin size ( $2^{x-1} \text{ ns}$ ,  $x \in \mathbb{N}$ ) can be adjusted to neutral beam species (H, O, He) and estimated energy.

The recorded ToF spectra are subsequently transformed into kinetic energy spectra according to Eq. (7) and need be rescaled by

the factor to compensate for the varying bin width in the energy spectrum,

$$n(E) = \frac{dt}{dE} \cdot n(t) = \frac{\langle s \rangle}{2} \sqrt{\frac{m_0}{2E^3}} n(t), \quad (9)$$

where  $\langle s \rangle$  is the mean flight distance and  $t$  the individual flight time. Any constant background contribution in the ToF spectrum transforms into a power-law background proportional to  $E^{-3/2}$ . We subtract this background, if present, by fitting the nonpeak domain in the energy spectrum by the mentioned power law to obtain the cleaned energy peak.

Note that in this setup, the detected ENA undergoes two surface scattering interactions from the ion beam entering the neutralizer to the ABM's stop CEM, first at the beam-neutralizing surface, then in the ABM. We take advantage of the fact that the SS in the ABM and in the neutralizer are highly polished single crystal W surfaces at  $10^\circ$  incidence angle each. Thus, the relative energy loss will be roughly the same, and we obtain the relative energy loss in each surface interaction as

$$\frac{\Delta E_{NS}}{E_{ion}} = \left( 1 - \sqrt{\frac{\langle E \rangle_{tof}}{E_{ion}}} \right). \quad (10)$$

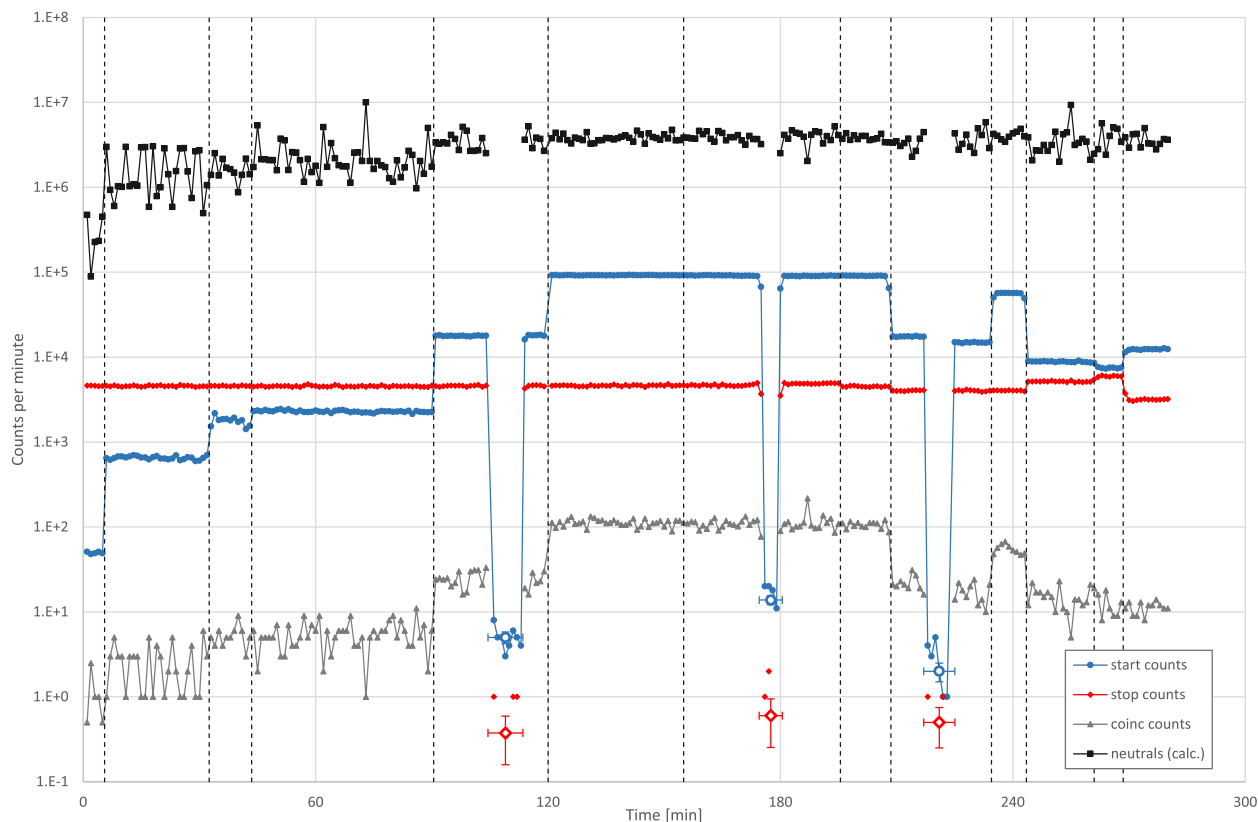


**FIG. 7.** Example measurement sequence with a 100 eV neutral hydrogen beam. The total measurement time is 280 min. Vertical dashed lines represent times of manipulations on the voltage configuration. At minutes 105, 175, and 218, the hydrogen beam was blocked for several minutes.

**TABLE I.** Sequence of the voltage setting during the measurement campaign presented in Fig. 7, taken with the ABM on 5 July 2021.

Minute	Changes
00	HV1 = 2.25 kV, HV2 = -2.35 kV, HV0 = 600 V, $\Delta t_{coinc} = 2.0 \mu s$
06	HV1 = 2.31 kV
33	HV1 = 2.36 kV
44	HV1 = 2.41 kV, adjust the start preAmp threshold to higher level
90	HV1 = 2.45 kV
105–113	Ion beam interrupted by ion beam scanner (Faraday cup)
120	Start preAmp threshold adjust to lower level (as was at start)
155	Shorter gate window: $\Delta t_{coinc} = 1.5 \mu s$
170	Stop preAmp threshold adjust to lower level
175–180	Ion beam interrupted by Faraday cup
195	Reduced stop CEM voltage: HV2 = -2.30 kV
210	Altered both preAmp thresholds
218–225	Ion beam interrupted by Faraday cup
235	HV1 = 2.49 kV (increased)
244	HV1 = 2.45 kV, HV0 = 500 V (lowered)
261	HV0 = 430 V (lowered)
270	HV0 = 700 V (increased)

The ion beam energy is obtained directly from the difference between neutralizer float voltage and ion-source post-acceleration voltage and from the neutralizer ESA voltage.

Figure 8(a) shows an example ToF spectrum of hydrogen and Fig. 8(b) the resulting energy spectrum. The energy peak is fitted with a Gaussian, and the mean energy  $\langle E \rangle$ , the peak width, and standard error are read out. The energy peak width is a convolution of several contributions: the variation in flight distance  $\delta s$  from different scattering locations on the SS mentioned earlier and impinging points on the stop CEM funnel, an estimated  $\pm 2$  ns variation in start electron flight time to produce start signals, the energy spread resulting from scattering from the SS, and the actual energy spread in the neutral atom beam.

As the stop CEM is at negative high voltage, positive ions scattered off the SS are accelerated toward the stop CEM and, thus, show a lower ToF than the neutral atoms. At high energies, ions provide only a minor contribution to the ToF peak and cannot be separated from the neutral peak: The ToF difference between ions and neutral atoms in the ABM is smaller than the peak width. At low energies, ions have a considerably lower ToF than the neutral atoms and may make up a larger fraction of the stop signals due to their higher detection efficiency. Having sufficient statistics, one can separate the peaks of ions and neutral atoms. In this case, only the neutral peak has been used for ToF evaluation. At intermediate energies, where the contribution of ions to the ToF peak is not negligible and cannot be uniquely separated, this may introduce some systematic uncertainty in broadening the ToF peak.

With higher atomic mass and/or lower beam energy, the peak in ToF spectrum shifts to larger flight time. By comparison of the ABM measured mean energy of neutral atoms to the primary ion energy, the energy loss during the scattering interaction with a tungsten surface is inferred. From the spectrum shown in Fig. 8, we get a mean energy of  $\langle E \rangle = 862$  eV and a peak FWHM of 533 eV. Relating this mean energy to the primary ion beam energy of 1300 eV

using Eq. (10), we obtain a mean energy loss per surface interaction of about 18% in this case.

### E. Neutral atom beam calibration

As described above, until recently, the ENA flux from the surface neutralizer in the energy range of 10 eV–1 keV had to rely on the known detection efficiency for neutral atoms of the used detector, which was an MCP-based imaging detector, and allowed for a calibration with neutral atoms with 30% accuracy.<sup>2</sup> This detection efficiency was derived in earlier work on MCP detectors in a different laboratory.<sup>33</sup> One key purpose of the ABM is to determine the incoming neutral atom rate independent of the prior knowledge of the detection efficiencies of the detector using the described start–stop–coincidence method. Combined with the well-defined entrance aperture, it amounts to determining the ENA beam flux  $f_n$  (part  $\text{cm}^{-2} \text{s}^{-1}$ ) as a function of primary ion beam energy  $E_q$ . In the neutralizer, the current on the neutralizer surface  $I_{ncs}$  from the impinging positive ions is measured. This current mostly reflects the primary ion current, with contributions from secondary electron emission by the ion impact, and a small fraction of scattered negative ions. The  $I_{ncs}$  is permanently recorded during the neutralizer operation with a highly sensitive pico-amperemeter.

The ENA flux generated in the neutralizer from an ion beam at a given species and beam energy is proportional to the measured current at the neutralizer surface,<sup>24</sup> which is proportional to the ion flux hitting the tungsten surface. The proportionality is a combination of neutralization efficiency (close to 100%), a geometric factor based on angular scattering distribution at the neutralizer surface and exit aperture of the neutralizer, and possibly others. Of course, this proportionality factor may vary with ion species due to different reflection and scattering properties upon scattering from the neutralizer surface, different secondary electron yields, and different charge-conversion efficiencies. The ion beam geometry and

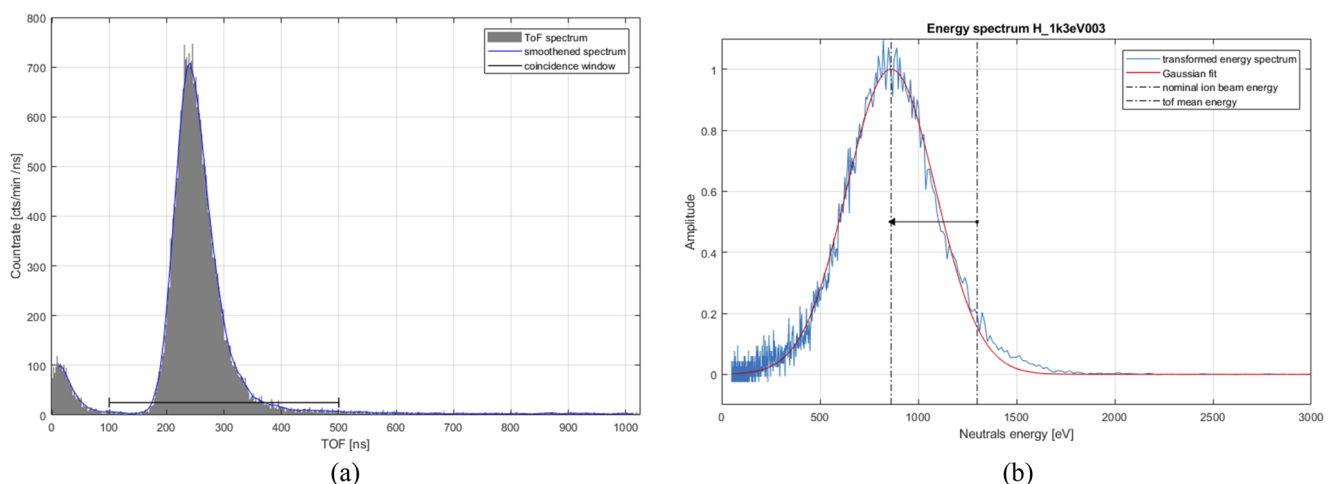


**FIG. 8.** (a) Recorded ToF spectrum from 1.3 keV hydrogen beam, with a moving average added in blue and the typical coincidence window in black. (b) The energy distribution derived from the ToF spectrum for scattered ENA beam in the ABM. Dash-dotted lines show the mean neutral beam energy (862 eV) and the primary ion beam energy (1.3 keV) as well as the mean energy loss (arrow).

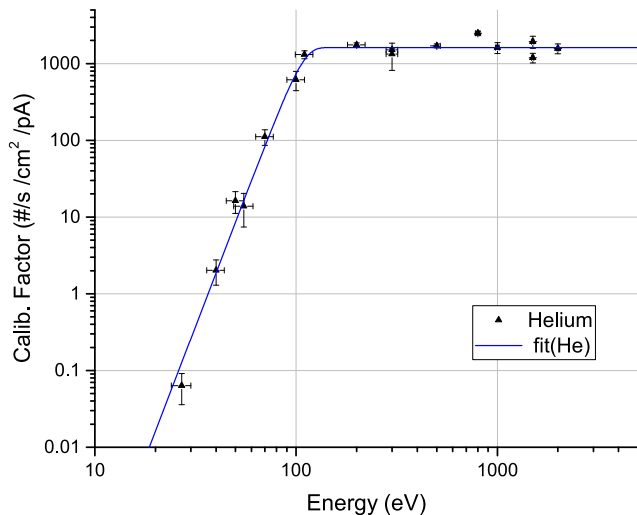


**FIG. 9.** Neutralizer calibration for helium from 3 keV down to 30 eV primary ion energy. The calibration factor is the neutral beam flux per neutralizer surface current (pA), and it is plotted as function of primary ion beam energy. Measured data are fitted with a Weibull function.

angular spread vary with ion beam energy, which, in turn, changes the neutral atom transmission through the neutralizer exit.

By relating the neutral atom flux measured by the ABM to the simultaneously measured neutralizer surface current, we obtain an absolute calibration of the surface neutralizer. For each ENA species of interest, we derive the calibration factor  $CF(E_q) = F_n/I_{ncs}$  that relates the measured current to the emitted neutral atom flux as function of the ion beam energy  $E_q$ .

One example of neutralizer calibration function is shown for He in Fig. 9. An empirical fit is added to the measured data using a three-parameter Weibull cumulative distribution function Eq. (11),

$$f(x) = a \exp(-(bx)^d), \quad (11)$$

with the parameters  $a = 1617$ ,  $b = 9.32 \times 10^{-3}$ ,  $d = 6.85$ . The Weibull function was chosen without physical meaning, but it allows good fits for a wide range of the calibration function  $f$  value at energies  $x$ . Similar neutral beam calibration measurements are prepared for IMAP for a number of species of interest, including hydrogen, deuterium, helium, and oxygen neutral atom beams down to lower beam energy limits of 10 eV (H) to 30 eV (D), for which results will be reported in a later publication.

#### IV. SUMMARY

With the absolute beam monitor, we have developed a new laboratory device that is capable of recording the neutral atom flux from an ENA beam source in the 10 eV–3 keV energy range in an absolute manner. The ABM measurement principle is based on a coincidence technique using surface scattering on a polished W surface and by recording the resulting start, stop, and coincidence signals simultaneously. In addition, the device provides a coarse measurement of the neutral atom beam energy using a simple ToF configuration.

Individual signal counts are Poisson distributed in each channel. The observed background count rates are about four orders of magnitude lower than the actual signal rates.

In the low to mid energy range, the accumulation time required to get sufficient counts can range from minutes to hours because of the low efficiencies for creating a start, stop, and coincidence signal at these low energies. Therefore, operating the ABM in parallel with a scientific ENA instrument under test is difficult. Instead, the ABM serves as an independent primary calibration standard for calibrating the beam surface neutralizer, which records a simultaneous current signal related to the neutral atom flux.

#### ACKNOWLEDGMENTS

This work was supported by the Swiss National Science Foundation.

#### AUTHOR DECLARATIONS

##### Conflict of Interest

The authors have no conflicts to disclose.

#### Author Contributions

**Jonathan Gasser:** Conceptualization (equal); Data curation (lead); Investigation (lead); Methodology (equal); Visualization (lead); Writing – original draft (lead); Writing – review & editing (equal). **André Galli:** Conceptualization (equal); Investigation (supporting); Methodology (equal); Supervision (supporting); Writing – original draft (supporting); Writing – review & editing (supporting). **Peter Wurz:** Conceptualization (equal); Funding acquisition (lead); Investigation (supporting); Methodology (equal); Project administration (lead); Resources (lead); Supervision (lead); Writing – original draft (supporting); Writing – review & editing (equal).

#### DATA AVAILABILITY

The data that support the findings of this study are available from the corresponding author upon reasonable request.

#### REFERENCES

- <sup>1</sup>P. Wurz, “Detection of energetic neutral particles,” *The Outer Heliosphere: Beyond the Planets* (Copernicus Gesellschaft e.V., Katlenburg-Lindau, Germany, 2000), pp. 251–288.
- <sup>2</sup>S. Fuselier, P. Bochsler, D. Chornay, G. Clark, G. Crew, G. Dunn, S. Ellis, T. Friedmann, H. Funsten, A. Ghielmetti, J. Googins, M. Granoff, J. Hamilton, J. Hanley, D. Heitzler, E. Hertzberg, D. Isaac, B. King, U. Knauss, F. Kudirka, H. Kucharek, J. Lobell, S. Longworth, D. McComas, E. Möbius, A. Moore, T. Moore, R. Nemanich, P. Nolin, M. O’Neal, D. Piazza, S. Pope, P. Rosmarynowski, L. Saul, J. A. Scheer, C. Schlemm, J. Scherrer, C. Tillier, S. Turco, J. Tyler, M. Vosbury, M. Wieser, P. Wurz, and S. Zaffke, The IBEX-Lo Sensor, *Space Science Reviews* **146**, 117–147 (2009).
- <sup>3</sup>A. Galli, P. Wurz, S. Fuselier, D. McComas, M. Bzowski, J. M. Sokol, M. A. Kubiak, and E. Möbius, “Imaging the heliosphere using neutral atoms from solar wind energy down to 15 eV,” *Astrophys. J.* **796**, 9–27 (2014).
- <sup>4</sup>D. J. McComas, F. Allegrini, P. Bochsler, M. Bzowski, M. Collier, H. Fahr, H. Fichtner, P. Frisch, H. O. Funsten, S. A. Fuselier, G. Gloeckler, M. Gruntman, V.



- Izmodenov, P. Knappenberger, M. Lee, S. Livi, D. Mitchell, E. Möbius, T. Moore, S. Pope, D. Reisenfeld, E. Roelof, J. Scherrer, N. Schwadron, R. Tyler, M. Wieser, M. Witte, P. Wurz, and G. Zank, "IBEX — Interstellar Boundary Explorer," *Space Sci. Rev.* **146**, 11–33 (2009).
- <sup>5</sup>D. J. McComas, E. R. Christian, N. A. Schwadron, N. Fox, J. Westlake, F. Allegrini, D. N. Baker, D. Biesecker, M. Bzowski, G. Clark, C. M. S. Cohen, I. Cohen, M. A. Dayeh, R. Decker, G. A. de Nolfo, M. I. Desai, R. W. Ebert, H. A. Elliott, H. Fahr, and E. Zirnstein, "Interstellar Mapping and Acceleration Probe (IMAP): A new NASA mission," *Space Sci. Rev.* **214**, 116 (2018).
- <sup>6</sup>A. Galli, I. I. Baliukin, M. Bzowski, V. V. Izmodenov, M. Kornbleuth, H. Kucharek, E. Möbius, M. Opher, D. Reisenfeld, N. A. Schwadron, and P. Swaczyna, "The heliosphere and Local Interstellar Medium from neutral atom observations at energies below 10 keV," *Space Sci. Rev.* **218**, 31 (2022).
- <sup>7</sup>A. Galli, P. Wurz, N. A. Schwadron, K. Fairchild, D. Heirtzler, E. Möbius, H. Kucharek, R. Winslow, M. Bzowski, M. A. Kubiak, I. Kowalska-Leszczynska, S. A. Fuselier, J. M. Sokol, P. Swaczyna, and D. J. McComas, "One solar cycle of heliosphere observations with the Interstellar Boundary Explorer: Energetic neutral hydrogen atoms observed with IBEX-Lo from 10 eV to 2 keV," *Astrophys. J., Suppl. Ser.* **261**(2), 18 (2022).
- <sup>8</sup>D. J. McComas, M. Bzowski, M. A. Dayeh, R. DeMajistre, H. O. Funsten, P. H. Janzen, I. Kowalska-Leszczynska, M. A. Kubiak, N. A. Schwadron, J. M. Sokol, J. R. Szalay, M. Tokumaru, and E. J. Zirnstein, "Solar cycle of imaging the global heliosphere: Interstellar Boundary Explorer (IBEX) observations from 2009–2019," *Astrophys. J., Suppl. Ser.* **248**, 26 (2020).
- <sup>9</sup>P. Swaczyna, M. A. Kubiak, M. Bzowski, J. Bower, S. A. Fuselier, A. Galli, D. Heirtzler, D. J. McComas, E. Möbius, F. Rahmani, and N. A. Schwadron, "Very Local Interstellar Medium revealed by complete solar cycle of interstellar neutral helium observations with IBEX," *Astrophys. J., Suppl. Ser.* **259**, 42 (2022).
- <sup>10</sup>T. E. Moore, D. J. Chornay, M. R. Collier, F. A. Herrero, J. Johnson, M. A. Johnson, J. W. Keller, J. F. Laudadio, J. F. Lobell, K. W. Ogilvie, P. Rozmarynowski, S. A. Fuselier, A. G. Ghielmetti, E. Hertzberg, D. C. Hamilton, R. Lundgren, P. Wilson, P. Walpole, T. M. Stephen, B. L. Peko, B. van Zyl, P. Wurz, J. M. Quinn, and G. R. Wilson, "The low-energy neutral atom imager for IMAGE," *Space Sci. Rev.* **91**, 155–195 (2000).
- <sup>11</sup>S. Barabash, R. Lundin, H. Andersson, K. Brinkfeldt, A. Grigoriev, H. Gunell, M. Holmström, M. Yamauchi, K. Asamura, P. Bochsler, P. Wurz, R. Cerulli-Irelli, A. Mura, A. Milillo, M. Maggi, S. Orsini, A. J. Coates, D. R. Linder, D. O. Kataria, and J. Thocaven, "The analyzer of space plasmas and energetic atoms (ASPERA-3) for the Mars Express mission," *Space Sci. Rev.* **126**, 113–164 (2006).
- <sup>12</sup>S. Barabash, J.-A. Sauvaud, H. Gunell, H. Andersson, A. Grigoriev, K. Brinkfeldt, M. Holmström, R. Lundin, M. Yamauchi, K. Asamura, W. Baumjohann, T. L. Zhang, A. J. Coates, D. R. Linder, D. O. Kataria, C. C. Curtis, K. C. Hsieh, B. R. Sandel, A. Fedorov, and P. Bochsler, "The analyser of space plasmas and energetic atoms (ASPERA-4) for the Venus Express mission," *Planet. Space Sci.* **55**, 1772–1792 (2007).
- <sup>13</sup>S. Barabash, A. Bhardwaj, M. Wieser, R. Sridharan, T. Kurian, S. Varier, E. Vijayakumar, V. Abhirami, K. Raghavendra, S. Mohankumar, M. Dhanya, S. Thampi, K. Asamura, H. Andersson, Y. Futaana, M. Holmström, R. Lundin, J. Svensson, S. Karlsson, and P. Wurz, "Investigation of the solar wind-Moon interaction onboard Chandrayaan-1 mission with the SARA experiment," *Curr. Sci.* **96**(4), 526–532 (2009); available at <https://www.jstor.org/stable/24105464>.
- <sup>14</sup>S. Orsini, A. Di Lellis, A. Milillo, E. De Angelis, A. Mura, S. Selci, I. Dandouras, P. Cerulli-Irelli, R. Leoni, V. Mangano, S. Massetti, F. Mattioli, R. Orfei, C. Austin, J. Medale, N. Vertoli, and D. Giulio, "Low energy high angular resolution neutral atom detection by means of micro-shuttering techniques: The BepiColombo SERENA/ELENA sensor," *AIP Conf. Proc.* **1144**, 91 (2008).
- <sup>15</sup>S. Orsini, S. Livi, K. Torkar, S. Barabash, A. Milillo, P. Wurz, A. Di Lellis, E. Kallio, and SERENA Team, "SERENA: A suite of four instruments (ELENA, STROFIO, PICAM and MIPA) on board BepiColombo-MPO for particle detection in the Hermean environment," *Planet. Space Sci.* **58**, 166–181 (2008).
- <sup>16</sup>L. Kong, A. Zhang, Z. Tian, X. Zheng, W. Wang, B. Liu, P. Wurz, D. Piazza, A. Etter, B. Su, Y. An, J. Ding, W. Li, Y. Liu, L. Li, Y. Li, X. Tan, and Y. Sun, "Mars ion and neutral particle analyzer (MINPA) for Chinese Mars exploration mission (Tianwen-1): Design and ground calibration," *Earth Planet. Phys.* **4**, 1–12 (2020).
- <sup>17</sup>Y. Futaana, M. Wieser, and S. Barabash, "Low energy energetic neutral atom imaging in the Jovian system," in *2013 EGU General Assembly* (2013), no. 12291.
- <sup>18</sup>Y. Kazama, S. Barabash, M. Wieser, K. Asamura, and P. Wurz, "Development of an LENA instrument for planetary missions by numerical simulations," *Planet. Space Sci.* **55**, 1518–1529 (2007).
- <sup>19</sup>S. Barabash, P. Wurz, P. Brandt, M. Wieser, M. Holmström, Y. Futaana, G. Stenberg Wieser, H. Nilsson, A. Eriksson, M. Tulej, A. Vorburger, N. Thomas, C. Parancas, D. Mitchell, G. Ho, B. Mauk, D. Haggerty, J. Westlake, M. Fränz, and D. Grodent, "Particle environment package (PEP)," in *Proceedings of the European Planetary Science Congress EPSC2013* (2013), Vol. 8, no. 709.
- <sup>20</sup>J. Gasser, M. Föhn, A. Galli, E. Artegiani, A. Romeo, and P. Wurz, "Cadmium telluride as a potential conversion surface," *J. Appl. Phys.* **129**, 045303 (2021).
- <sup>21</sup>J. Scheer, W. Brünig, T. Fröhlich, P. Wurz, and W. Heiland, "Scattering of small molecules from a diamond surface," *Nucl. Instrum. Methods Phys. Res., Sect. B* **157**(1), 208–213 (1999).
- <sup>22</sup>P. Wurz, R. Schletti, and M. R. Aellig, "Hydrogen and oxygen negative ion production by surface ionization using diamond surfaces," *Surf. Sci.* **373**(1), 56–66 (1997).
- <sup>23</sup>A. Marti, R. Schletti, P. Wurz, and P. Bochsler, "Calibration facility for solar wind plasma instrumentation," *Rev. Sci. Instrum.* **72**, 1354 (2001).
- <sup>24</sup>M. Wieser and P. Wurz, "Production of a 10 eV–1000 eV neutral particle beam using surface neutralization," *Meas. Sci. Technol.* **16**, 2511–2516 (2005).
- <sup>25</sup>H. O. Funsten, R. W. Harper, and D. J. McComas, "Absolute detection efficiency of space-based ion mass spectrometers and neutral atom imagers," *Rev. Sci. Instrum.* **76**, 053301 (2005).
- <sup>26</sup>M. A. Gruntman and V. A. Morozov, "H atom detection and energy analysis by use of thin foils and TOF technique," *J. Phys. E: Sci. Instrum.* **15**(12), 1356 (1982).
- <sup>27</sup>G. Betz and K. Wien, "Energy and angular distributions of sputtered particles," *Int. J. Mass Spectrom. Ion Processes* **140**(1), 1–110 (1994).
- <sup>28</sup>G. Högberg, H. Nordén, and H. Berry, "Angular distributions of ions scattered in thin carbon foils," *Nucl. Instrum. Methods* **90**, 283–288 (1970).
- <sup>29</sup>P. Wurz, J. Scheer, and M. Wieser, "Particle scattering off surfaces: Application in space science," *e-J. Surf. Sci. Nanotechnol.* **4**, 394–400 (2006).
- <sup>30</sup>W. A. de Zeeuw, H. W. van der Ven, J. M. M. de Wit, and A. J. H. Donné, "An electrostatic time-of-flight analyzer for simultaneous energy and mass determination of neutral particles," *Rev. Sci. Instrum.* **62**(1), 110–117 (1991).
- <sup>31</sup>P. Wurz, A. Balogh, V. Coffey, B. Dichter, W. Kasprzak, A. Lazarus, W. Lennartsson, and J. McFadden, "Calibration techniques," in *Calibration of particle instruments in Space Physics* (ed. M. Wüest, D.S. Evans, and R. von Steiger), ESA Communications, ISSI Scientific Report, SR-007 (2007), Chap. 3, pp. 117–276.
- <sup>32</sup>H. Niehus, W. Heiland, and E. Taglauer, "Low-energy ion scattering at surfaces," *Surf. Sci. Rep.* **17**(4–5), 213–303 (1993).
- <sup>33</sup>T. M. Stephen and B. L. Peko, "Absolute calibration of a multichannel plate detector for low energy O, O<sup>−</sup>, and O<sup>+</sup>," *Rev. Sci. Instrum.* **71**(3), 1355–1359 (2000).

# Erratum: “Absolute beam monitor: A novel laboratory device for neutral beam calibration” [Rev. Sci. Instrum. 93, 093302 (2022)]

Cite as: Rev. Sci. Instrum. 93, 129902 (2022); doi: 10.1063/5.0133907

Submitted: 7 November 2022 • Accepted: 14 November 2022 •

Published Online: 6 December 2022



Jonathan Gasser,<sup>a)</sup> André Galli, and Peter Wurz

## AFFILIATIONS

Physics Institute, Space Research and Planetary Sciences, University of Bern, Sidlerstrasse 5, 3012 Bern, Switzerland

<sup>a)</sup> Author to whom correspondence should be addressed: [Jonathan.gasser@unibe.ch](mailto:Jonathan.gasser@unibe.ch)

<https://doi.org/10.1063/5.0133907>

In Sec. II A of the paper,<sup>1</sup> we used ambiguous nomenclature for the detection efficiencies in the text preceding Eq. (2) and after Eq. (3). The text should read as follows:

“Each incident neutral atom has an *a priori* unknown probability  $\mu_e$  for ejecting a secondary electron from the SS and an unknown probability  $\mu_i$  of being itself detected subsequently by the stop detector. The probability of generating a coincidence count is thus,  $\mu_c = \mu_e \cdot \mu_i$ .”

The start, stop, and coincidence count rates ( $r_e$ ,  $r_i$ ,  $r_c$ ), respectively, to be observed from the incoming neutral atoms at the rate  $F_n = f_n \sigma_{ap}$  through the entrance aperture with the cross section  $\sigma_{ap}$  will then be [as given in Eq. (2)]. With the requirement that the background rates ( $r_{e,0}$ ,  $r_{i,0}$ ,  $r_{c,0}$ ) of the three count rates are negligible, we obtain [Eq. (3)] and the coincidence detection efficiency for neutral atoms is  $\varepsilon_n = \mu_c = \mu_e \mu_i$ .<sup>2</sup>

Furthermore, there is an error in Eqs. (4) and (5). The corrected equations are

$$f_n = \frac{(r_e - r_{e,0})(r_i - r_{i,0})}{\sigma_{ap} \cdot (r_c - r_{c,0})}, \quad (4)$$

$$f_n = \frac{(c_e - c_{e,0})(c_i - c_{i,0})}{(c_c - c_{c,0})\sigma_{ap} t_{int}}, \quad (5)$$

where  $t_{int}$  is the total integration time.

## REFERENCE

<sup>1</sup>J. Gasser, A. Galli, and P. Wurz, “Absolute beam monitor: A novel laboratory device for neutral beam calibration,” *Rev. Sci. Instrum.* **93**, 093302 (2022).



### 3.5. Summary and Outlook

The current ABM was designed from scratch specifically to measure the absolute particle flux of a low-energetic laboratory ENA beam. The realized measurement concept has been tested and proven in the specific laboratory setup as shown in Section 3.4. Several improvements on the ABM device, including measures for background suppression, have been implemented. The ABM has been applied in the calibration and characterization of the surface neutralizer in the MEFISTO test facility (see Ch. 4). Over and above the existing ABM, the following considerations and design ideas may lead the direction towards a future ABM version 2:

**Next ABM design steps.** When it comes to the design of a version two Absolute Beam Monitor, there are several changes for improvements that should be considered and tested in a SIMION simulation model: The direct line-of-sight path from the entrance aperture to the stop CEM is open in the actual ABM design, but the double disk in front of the entrance and a correct ABM alignment to the beam prevent entering ENA from direct hitting the stop CEM past the start surface. It might still be beneficial to block these direct trajectories also internally, e.g., by splitting the volume beneath the SS by a metal wall across the general beam direction. Of course, this will have effects on the overall electrical field configuration, and it remains to be verified that the design concept still holds valid.

This will also necessitate moving the start CEM location with respect to the SS. One option would be to place it near the entrance aperture, which has at least two consequences: for one, start electrons will have to be attracted 'back' towards the entrance by a negative electrical potential (as is) at the start CEM. Therefore, the start CEM, SS, and stop CEM would be in a more collinear configuration, which may reduce the deflection of converted positive and negative ions. Secondly, placing the start CEM near the entrance aperture likely demands a suited aperture at the front side as well as some mounting structure similar to the existing one under the ABM. Additional shielding of the HV and signal lines against the approaching neutrals beam might be required to prevent induced signal background.

**Electronics.** In the actual electronics setup, proper adjustment of signal lines, termination and threshold voltages is crucial for reliable and reproducible counts measurements, particularly for the coincidence counts recording. The signal delay through the gate generator and into the coincidence counter input B needs to be matched with an appropriately longer stop signal line into input A of the coincidence counter. Moreover, as explained in 3.3.1, in this configuration the gate window remains open for a fixed adjustable gate time, therefore multiple stop counts can be recorded as coincident to a single start count.

For these reasons, having a dedicated integrated circuit at hand that fully incorporates the coincidence measurement scheme shown in Fig. 3.13 will signify a beneficial improvement of coincidence counts precision. In a first variant, the coincidence circuit can just replace and improve the combined gate generator and coincidence counter, by combining start and stop signal input and a discretely adjustable gate time to produce the coincidence count pulses as output. In a further step, the accumulation of all three count rates over a given integration time period and digital count numbers output could be included directly in this circuit as well.

## 4. Calibration of Low-energy ENA Instruments

---

However difficult life may seem  
There is always something  
You can do and succeed at.

Stephen Hawking

---

ENA imaging of space plasmas has become an important observation technique in space science and is applied to observe a wide range of ENA sources [16]: neutralized solar wind and heliospheric ENA, interstellar neutral atoms originating from the Local Interstellar Medium, as well as planetary ENA sources such as magnetospheres, planetary surface sputtered products, ENA from volcanic activity, icy water plumes ejecta, or ENA from atmospheric escaping.

ENA detection instruments for space applications crucially rely on thorough laboratory instrument calibration [51] in order to determine the instrument sensitivity, particle throughput, field-of-view and geometric factor for the relevant ENA species in the desired energy range.

For low-energy ENA in the order of 10 – 1000 eV, reliable instrument calibrations need to be carried out using a neutral atoms beam source that cannot be substituted by an equivalent ion beam: at these energies, ion trajectories inside (and possibly in front of) the instrument under test are disturbed subject to the sensor's electrical field configuration and electromagnetic fringe fields. Therefore, it is in general not given that calibrations of the entire ENA instrument using ions would provide realistic and representative instrument characteristics in terms of ENA detection and analysis.

### 4.1. Neutral Beam Production

In the laboratory environment, an energetic neutral atoms beam is generally produced by neutralizing a beam of atomic ions from an ion source. A brief overview of laboratory beam neutralization for instrument calibration can be found in Wurz et al. [54], Chapter 3.8 (pp. 252ff).

The advantage thereof is that an ion beam can be accelerated or decelerated, mass-filtered, focused and directional adjusted relatively easily by conventional ion-optical means. At high beam energies above a few keV/q, ion beam neutralization can happen in collisional charge-exchange interactions with residual gas molecules in a gas cell [42], by capture of electrons emitted from a filament or from passing the ion beam through a plasma. Photo-detachment of an electron from negative ions is another method to produce a laboratory ENA beam, it is however limited to elements which form stable negative ions.

For low-energy ion beams (below a few keV/q), these neutralization techniques become inefficient as the beam transmission decreases rapidly with lower energy. Instead, ion beam neutralization via surface interaction is applied: ions are reflected off an atomically flat polished crystal surface at grazing incidence angle. The reflected beam is dominated by neutral atoms [18, 33, 34, 53], but also contains some fraction of positive and negative ions. These must therefore be deflected away from the beam line downstream to obtain a truly neutral atoms beam. Surface neutralization of ion beams is applied to produce laboratory ENA beams in the energy range from 10 eV to a few keV [47]. At even lower energies, we are in the range of thermal speed of the gas, and neutral atom or molecule beams can be produced from passing a thermalized test gas from a reservoir through a pinhole into the test chamber [50] Ch. 3.7, without introducing an ion beam in the first place.

In the following, the ENA instrumentation calibration facility and specifically the beam neutralization stage are described.

#### 4.1.1. MEFISTO Calibration Facility

The MEFISTO<sup>1</sup> test facility at the University of Bern [21] consists of a powerful electron-cyclotron resonance ion source (ECRIS), an ion-optical system for ion beam extraction and adjustment, and a large (about 1.20 m diameter, about 1.50 m depth) vacuum test chamber. A schematic of the ECRIS and ion-optical beam guiding system is shown in Fig. 4.1.

The gas in the ECRIS is ionized via microwave-induced resonant electron excitation to produce and maintain a plasma. The necessary energy is injected and resonance is generated inside the source using a 2.45 GHz microwave spiral antenna. The plasma is magnetically trapped by 18 permanent magnets arranged in three hexagons around the source, with appropriate magnetic field orientation. Virtually any gas or vapor from a liquid can be inserted into the ion source, and by using an oven crucible even solids can be vaporized and used to produce a plasma from in the ion source. The ECRIS is held at an electric potential of  $U_0 = +3$  kV, thus an ion beam of 3 keV/q is extracted from the plasma toward the puller electrode and into the ion-optical beam-guiding system (see Fig. 4.1). The ion beam is focused at an ion-optical Einzel lens, direction-adjusted vertically and horizontally by a pair of electrostatic deflection plates, and led through a Wien filter to select the desired ion mass  $m/q$ .

---

<sup>1</sup>MEFISTO is the acronym for German “**ME**sskammer für **FlugzeitInStrumente** und **T**ime-**O**f-flight” (Calibration Facility for Solar Wind Instrumentation)

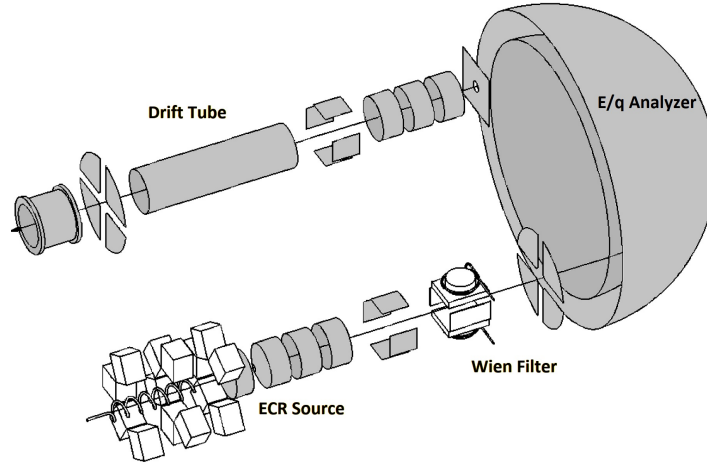


Figure 4.1.: Schematic of the Mefisto ion source and ion-optical extraction system.  
(adapted from Marti et al. [21])

**Wien filter.** A Wien filter consists of a pair of crossed homogeneous electrical  $\vec{E}$  and magnetic  $\vec{B}$  fields, mutually perpendicular with the beam line (i.e., the ion velocity vector  $\vec{v}$ ):  $\vec{B} \perp \vec{E} \perp \vec{v}$ . The ion-deflecting Coulomb force  $\vec{F}_C = q \vec{E}$  and Lorentz force  $\vec{F}_L = q (\vec{v} \times \vec{B})$  counteract anti-parallel and cancel for ions which satisfy:

$$\frac{m}{q} = \frac{2U_0 |B|^2}{|E|^2} \quad (4.1)$$

This defines the ion mass passing the Wien filter unaffectedly. Hence, generally, a Wien filter cannot resolve a degeneracy between mass and charge state, e.g.,  $S^{2+}$  cannot be separated from  $O^+$  ions,  $Ar^{2+}$  from  $Ne^+$  ions, or  $He^{2+}$  from  $D^+$  ions.

The electron plasma in the ECRIS is heated up to  $\sim 10^6$  K through the microwave resonances. The injected power is about 100 W. However, as the plasma ions are thermally decoupled from the electrons, they remain at much lower temperatures and molecular ions are therefore not completely dissociated.

**Beam Guiding.** In addition, at this point there's a degeneracy in the beam between  $m/q$  and the ion energy, which is however resolved after passing the beam through a  $180^\circ$  spherical electrostatic analyzer (ESA). The ESA constrains the ion beam energy  $E/q$  (hence acts as an energy filter) and prevents the test chamber from direct line of sight to the plasma. The entire ECRIS and beam-guiding system is shown schematically in Fig. 4.1.

The beam is then adjusted and focused in a second Einzel lens and deflection plates before it is guided through a drift tube and a ceramic insulator tube into the main vacuum chamber. To support the beam guiding optimization, a four-fold sector aperture after the Wien filter and at the subsystem exit are used to display the ratio of beam-induced current on the plates. Another aperture is placed at the ESA exit for the same purpose.

The entire ECRIS and beam guiding system are contained on an insulated stage (viz. the insulating teflon bushing at the beam exit in Fig. 4.1) in a Faraday cage. The inner stage can

be floated on HV up to +100 kV or down to negative HV about -3 kV, which allows to cover a wide range of beam energies representative for example for laboratory solar wind simulations.

The entire ECRIS vacuum system is separated from the test vacuum chamber by a gate slider, and both vacuum subsystems are pumped independently by separate turbo-molecular pumps each, and a cryopump attached at the vacuum chamber. A beam scanner can be moved into the ion beam between the gate slider and the test chamber. It consists of a Faraday cup and is used to directly measure the ion beam current, typically a few tenths to few tens of nanoamperes. The ion-optical system of the ECRIS is optimized with respect to the ion current measured in the beam scanner. Combined with the Wien filter in the source, it can also be used to record an ion beam mass spectrum.

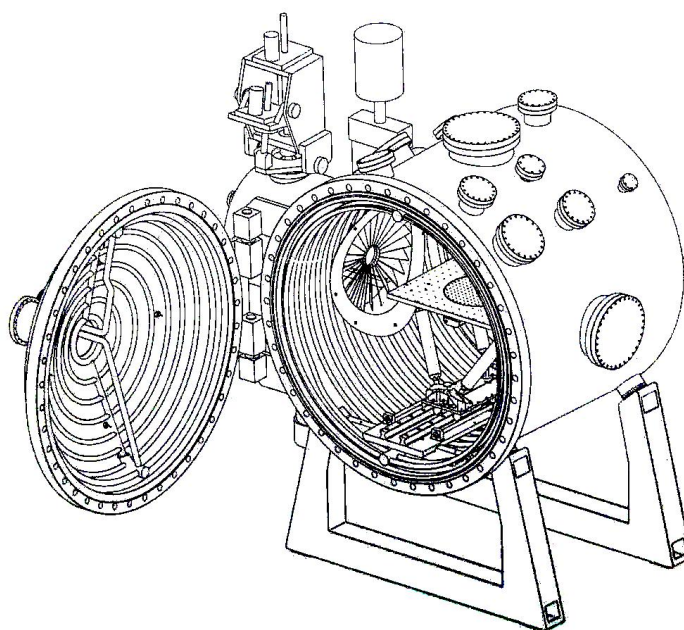


Figure 4.2.: 3D sketch of the MEFISTO vacuum test chamber, including the hexapod table. The ion beam enters from the left side (ECRIS subsystem not shown), through the baffled shroud in the chamber. On the top left you see the beam-scanner motion unit. [Image credit: Space Research division, University of Bern.]

**Vacuum Chamber.** The Mefisto test chamber itself is a large cylindrical vacuum chamber about 1.20 m in diameter and about 1.40 m deep. A 3D visualization of the MEFISTO test chamber is shown in Fig. 4.2, and Fig. 4.3 shows the front view photograph of the chamber. It comes with an integrated heating and bakeout system (tubing along the chamber walls), several feedthrough flanges for flexible experiment setup, two optical windows plus the usual pressure and temperature sensors. With the attached turbo-molecular pump and cryogenic pump, a high vacuum in the  $10^{-8}$  mbar pressure range is achieved. The ECRIS system and beam scanner are attached to the left side as seen from the chamber door, and are separated by a circular baffled shroud (see Figs. 4.2 and 4.3). The core and center of the test chamber

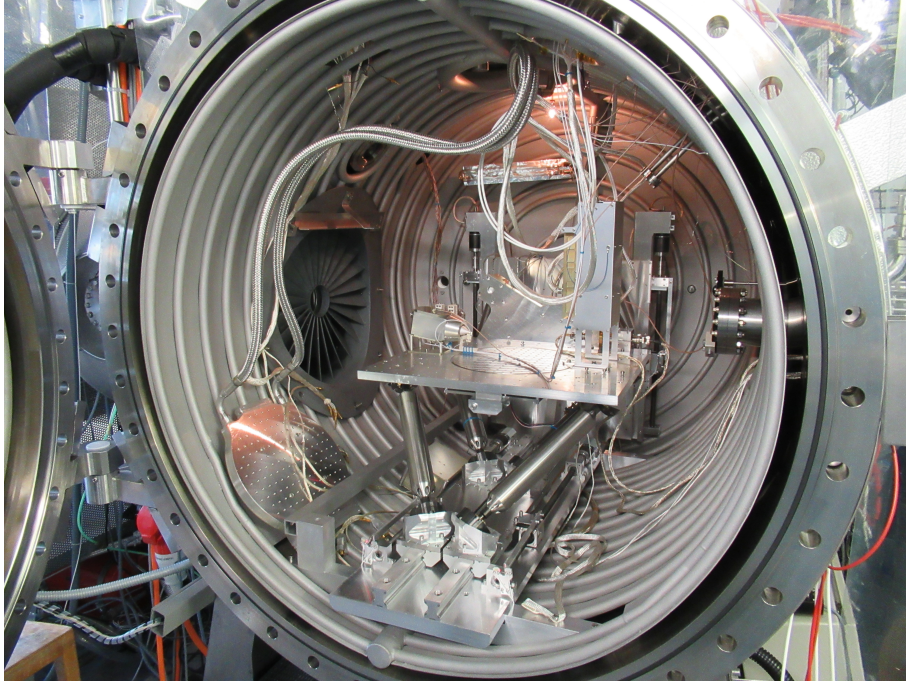


Figure 4.3.: Photograph of the MEFISTO vacuum chamber with the first version ABM and another instrument mounted on the hexapod table, the ion beam entrance shroud and the Huber cooling plate (with  $N_2$  tubes attached) to the left. The surface neutralizer is not yet installed here.

is the movable hexapod experiment table (see below). Additionally, a thermal Huber plate, which can be heated up to  $150^\circ\text{C}$  and cooled down using a liquid nitrogen cycle, allows for active temperature regulation of an instrument under test.

**Beam Neutralizer.** To produce a neutral atoms beam, the surface neutralizer device [47] can be installed into the test chamber in front of the baffled beam entrance. The neutralizer mounting is fixed above the beam entrance and features a two-axis stepper-motor driven positioning system, the YZ-stage. It allows to properly position the neutralizer beam entrance into the ion beam. The neutralizer is described and characterized in more detail in Section 4.1.2.

**Hexapod Table.** The Mefisto vacuum chamber is equipped with a movable square hexapod table where experiments and test instrumentation can be mounted on (see Fig. 4.3). The hexapod table allows for three-axis motion ( $X, Y, Z$ ), plus it can be pivoted about the horizontal axis normal to the beam direction ( $Y$ ) by an angle of about  $\beta = \pm 15^\circ$ . In addition, a circular inner zone, the Theta-stage, can be rotated about the table normal axis by  $\Theta > 360^\circ$  (in principle unlimited) in each direction.

In case an instrument under test such as IBEX-Lo or IMAP-Lo need be revolved about its sensor axis (e.g., parallel to the beam direction), an additional Alpha-stage is available for installation that allows for this rotation.



The hexapod table is held in position through six struts ('legs') in total – thus the name – which are attached by spherical ball joints to allow the struts sufficient angular motion.

The struts are mounted on slides at variable position on two horizontal and two vertical rails as follows: Two struts are mounted at fixed distance on one of the horizontal rails each, and the two remaining struts connect from the back of the table to one vertical rail each. The hexapod motion degrees of freedom are realized by moving the slides which the struts are mounted on along the rails. This happens by means of four precision stepper motors and a position sensor each.

### 4.1.2. Surface Neutralizer

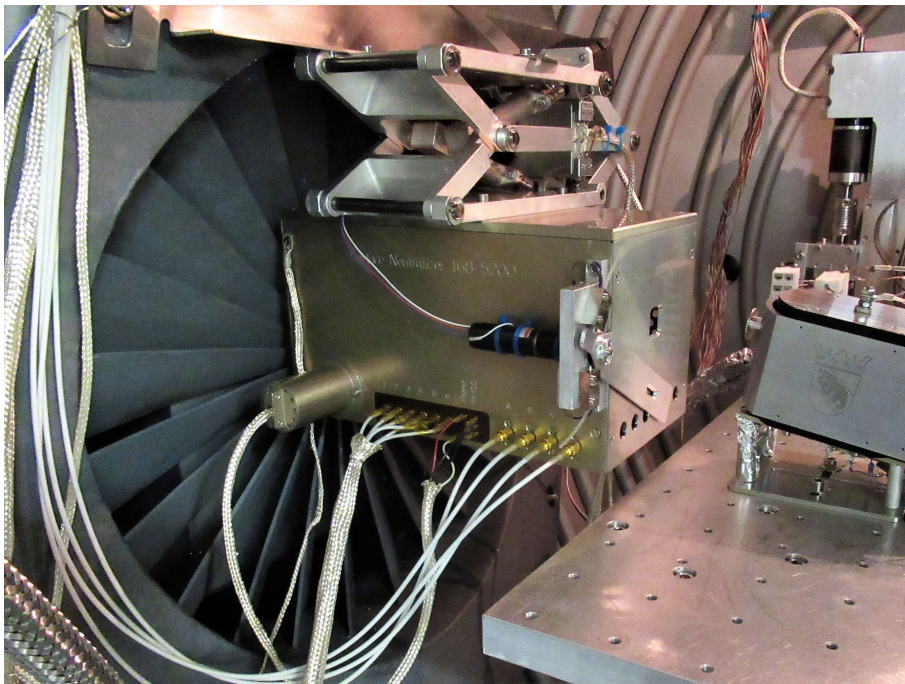


Figure 4.4.: The neutralizer, installed in the MEFISTO vacuum chamber in front of the ion-beam baffled shroud. At the top, you see the positioning YZ-stage. The ion beam to be neutralized passes through the neutralizer from left to right and exits the square aperture at the front side. To the right you see the ABM installed on the hexapod table.

**Overview.** The surface neutralizer (henceforth simply '*the neutralizer*') is a box-shaped device that was developed at the University of Bern by Wieser and Wurz [47] to convert an ion beam into a neutral atoms beam. For this purpose the neutralizer is installed in a vacuum chamber into the ion beam line. Fig. 4.4 shows a photograph of the neutralizer installed in the MEFISTO test chamber. The neutralizer can be moved horizontally and vertically via an

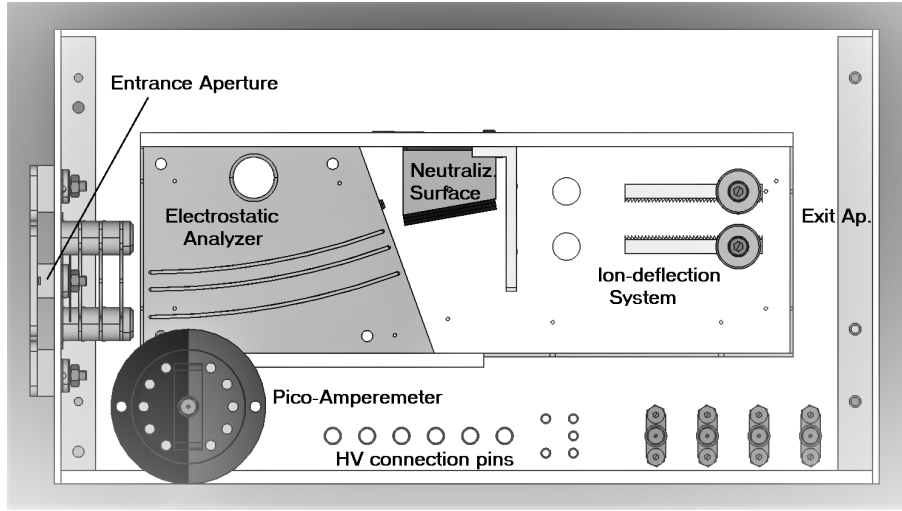


Figure 4.5.: Schematic of the neutralizer device [47]. The entrance aperture, ESA, neutralizer surface, ion-deflection plates and position of the exit aperture are labeled.

adjustable mounting bracket consisting of two axis stepper motors (the YZ-stage, see Fig. 4.4), which is mounted on the neutralizer top.<sup>2</sup>

A schematic of the assembled surface neutralizer is shown in Fig. 4.5. The surface neutralizer consists of an inner and outer housing. The ion beam enters from the left to the inner box, then passes a  $20^\circ$  cylindrical electrostatic analyzer (ESA) and hits a polished single crystal tungsten surface at  $10^\circ$  incidence angle, whereupon the beam is effectively neutralized. The neutralized atoms beam passes by a pair of ion deflection plates held at  $U_{defl} = \pm 200$  V towards the exit aperture to deflect any surviving ions from the neutral beam path.

While the outer housing is at ground potential, the inner housing is operated at positive float HV  $U_{float}$  to decelerate the ion beam before the ESA. The outer back side of the neutralizer housing consists of a perforated metal sheet to guarantee sufficient venting and electromagnetic shielding. The exit aperture of the inner housing is very wide horizontally and about 10 mm high. The outer exit aperture is  $16 \times 16 \text{ mm}^2$  in size. An additional visor can be moved in front of the exit aperture, which further narrows the vertical extent of the neutral beam (see Fig. 4.4).

**Ion-beam Entrance.** The entrance aperture is 12.5 mm wide and 3 mm high. In front of the entrance, there are four plates (A, B, C, D) mounted insulated from the outer housing (see Fig. 4.6), which allow to measure the induced ion beam current on each of the plates on an external high sensitivity amperemeter. With the help of the YZ-stage, this allows to position the neutralizer properly into the optimized ion beam.

At the beam entrance, between the outer and the inner housing, there is a set of three equidistant face plates connected by high resistivity resistors ( $R = 20 \text{ M}\Omega$ ,  $\Delta U = 1/4 U_{float}$  each) to guarantee a constant gradient in electrostatic potential for ion beam retarding.

<sup>2</sup>That is why it is unofficially called ‘birdhouse’ or ‘nesting box’.



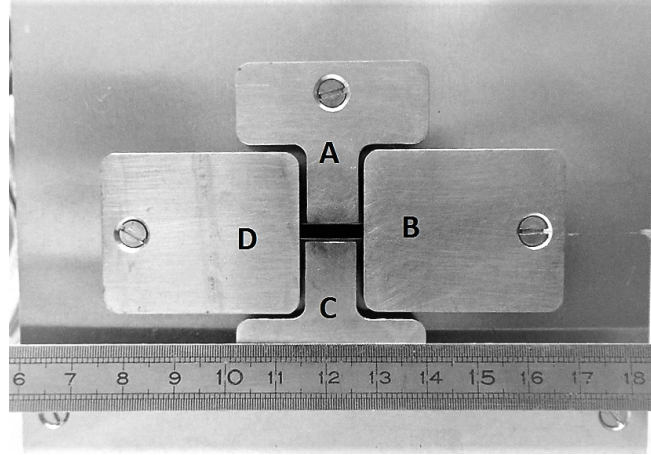


Figure 4.6.: The neutralizer ion-beam entrance aperture and plates for neutralizer position adjustment.

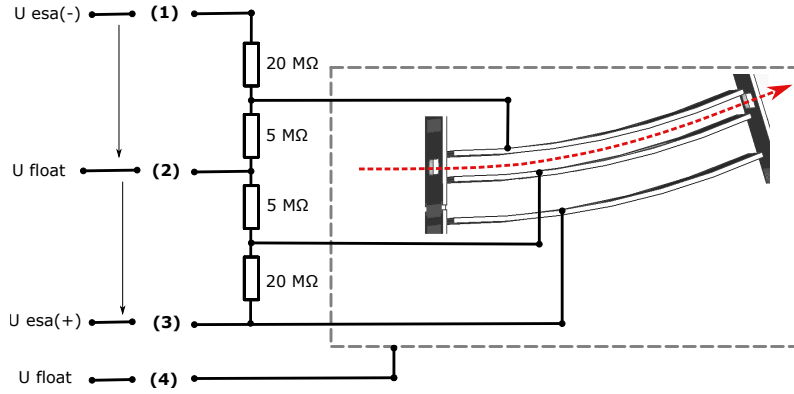


Figure 4.7.: Circuitry of the neutralizer ESA on pins (1) to (4). Ion-deflection voltages on pins (5) and (6) is not shown here.

**Electrostatic Analyzer.** The neutralizer ESA is a  $20^\circ$  cylindrical static analyser at nominal beam path radius  $r_0 = 200$  mm and plate distance  $\Delta r = 4$  mm. It has wide (in horizontal direction) but just 3 mm high entrance and exit apertures that help limit the energy spread of the ion beam passing through. The outer ESA plate is partially grided to allow remaining high-energy ions and neutral atoms to be removed outward from the nominal path. A third (outermost) electrode is installed to stabilize the homogeneous radial electric field.

A sketch of the high voltages applied to the neutralizer is shown in Fig. 4.7. From the external power supply, ESA voltages of up to  $\pm 300$  V are applied symmetric to the float voltage, thus  $ESA_+ = U_{float} + U_{ESA}$  (outer electrode),  $ESA_- = U_{float} - U_{ESA}$ . Internally, there is a 1:5 voltage divider ( $20\text{ M}\Omega$  and  $5\text{ M}\Omega$ ) such that the electric potentials on the ESA electrodes are just

$$U_{\pm} = U_{float} \pm \frac{1}{5} U_{ESA} \quad .$$

The ESA analyzer constant  $k$  is the ratio of ion energy on the nominal path and the voltage  $\Delta U_{ESA}$  between the inner and outer ESA electrodes, and is given by

$$k \doteq \frac{r_0}{2\Delta r} = 25 \quad (4.2)$$

$$= \frac{E_{ion}}{e \Delta U_{ESA}} = \frac{U_{ECR} - U_{float}}{U_+ - U_-} = \frac{U_{ECR} - U_{float}}{\frac{2}{5} U_{ESA}}, \quad (4.3)$$

where  $U_{ECR}$  is the ion source extraction voltage. For experimental operation purposes, it is more practical to work with an effective analyzer constant  $k_{eff}$ , which relates the float voltage to the ESA voltage at the power supply:

$$k_{eff} = \frac{U_{ECR} - U_{float}}{U_{ESA}} \simeq 10 \quad (4.4)$$

**ESA Resolution** In the neutralizer ESA, ions do not feel a horizontal force, as the horizontal component of the electrical field is neglectable in a cylindrical ESA. Thus, ion trajectories in the ESA depend on their entrance energy, direction, and z-coordinate. As the ESA starts off parallel to the beam direction and the beam itself is very well aligned, assume the beam entrance angle to be  $\varepsilon = 0^\circ$ . The potential in a cylindrical analyzer varies with radius as

$$U(r) = U_0 \ln(r/r_0) \quad (4.5)$$

On the central (nominal) trajectory through the ESA, ions are affected by the centripetal force

$$F_z = \frac{mv_0^2}{r_0} = e|\vec{E}| \simeq e \frac{\Delta U}{\Delta r} = \frac{\Delta E}{\Delta r}. \quad (4.6)$$

With  $E_0 = \frac{m}{2}v_0^2$  it follows that the energy shift needed on a circular orbit parallel to the nominal trajectory, for small radial variations, is

$$\frac{\delta E}{E_0} \simeq \frac{2\delta r}{r_0}. \quad (4.7)$$

This determines the relative energy passband for those ions that exit the ESA at nominal angle  $20^\circ$  to the horizontal. However, it is also possible to pass the ESA for higher-energy ions that enter at radii  $r < r_0$ , thus leaving at shallower angle and larger radius. Likewise, lower-energy ions ( $E < E_0$ ) entering at larger radii and being bent inward will also pass at exit angles larger than  $20^\circ$ .

**Neutralizer Surface.** After the ESA, ions are effectively neutralized upon striking a polished single crystal tungsten surface at nominal grazing incidence angle  $\alpha = 10^\circ$ . This neutralizing surface (NS) is mounted on a  $10^\circ$  tilted copper block at the top plate of the inner housing (Fig. 4.5).

A pico-amperemeter is connected to the tungsten NS plate. It allows to permanently monitor the neutralizer surface current  $I_{ncs}$  during operation. The pico-amperemeter itself is

HV-shielded installed inside the vacuum chamber and connected to the neutralizer (isolated pin at the lower left in Fig. 4.5). Electrically isolating the entire pico-amperemeter is necessary, because the neutralizer surface, like the entire inner housing, is held at float HV.

In effect, the tungsten surface serves as an extended neutral atom source, which neutral atoms and surviving ions are scattered off. Ions are then deflected vertically in the electric field between the deflection plates, while neutrals propagate freely in their respective scattering direction which is mostly towards the neutralizer exit. The neutral beam, however, is much broader than the initial ion beam due to the angular scattering at the surface. Its angular extent is basically limited by a window through a thin metal foil right after the tungsten surface, and by the exit apertures of the inner and outer housing.

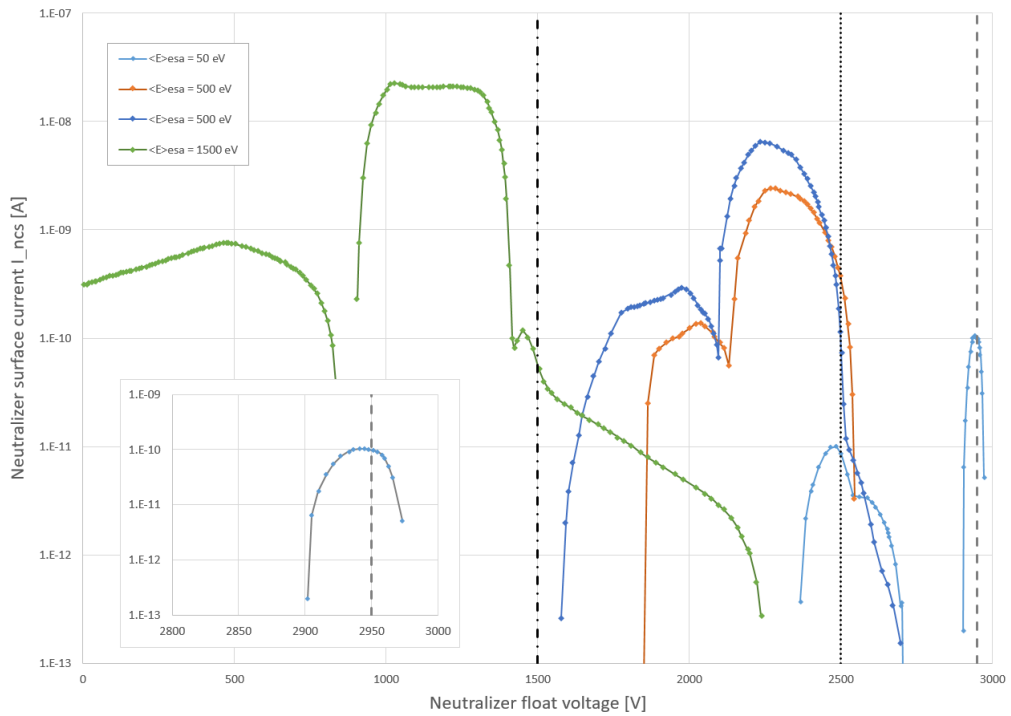


Figure 4.8.: Neutralizer ESA transmission as function of the float voltage for energies  $E_{ESA} = 50$  eV, 500 eV, and 1.5 keV. At the higher beam energies, the float voltage of optimal transmission strongly deviates from the nominal values (dashed, dotted, and dash-dotted line).

**Voltage Adjustment.** The energy of the ion beam at the NS is set by the float voltage  $U_{float}$  and the ESA voltage  $U_{ESA}$ , according to Eq. (4.4). Voltage adjustment is done by optimizing the NS current at the pico-amperemeter with respect to  $U_{float}$  while keeping the ESA voltage fixed at  $U_{ESA} = E_{ion}/(e \cdot k_{eff})$ . However, sometimes the float voltage at optimum NS current strongly deviates from the expected voltage value based on the set ESA voltage. Figure 4.8 illustrates this situation: the neutralizer surface current, representative of the ESA

transmission, was monitored when varying the float voltage while  $U_{ESA}$  was kept at values 5 V, 50 V twice, and 500 V, respectively. This corresponds to beam energies 50 eV, 500 eV, and 1.5 keV. This can be owing to several causes:

- The neutralizer was installed at an angle to the nominal ion beam line.
- The extraction voltage of the source was changed, altering the ion beam energy.
- The ion beam guiding system was optimized such that the ion beam leaves at a vertical angle. Then the beam enters the neutralizer ESA at a significant angle to the nominal trajectory.
- The neutralizer was not properly positioned into the ion beam, causing a similar effect.

In this case, the precise beam energy is difficult to determine, because the ESA's energy analyzing capability cannot be relied on in this configuration. We learn from this observation that a proper beam and neutralizer alignment is essential for accurate beam-energy determination.

### 4.1.3. Beam Profiles

**Neutral beam Scans.** Even though the ABM has not been developed for this purpose, in principle it can be used as well – in combination with the hexapod motion table – to measure the neutral beam profile in front of the neutralizer exit aperture. To do so, the ABM entrance aperture has to be moved stepwise through the neutral beam. At each position step, the neutral atoms rate into the ABM is obtained from start, stop, and coincidence counts accumulated within one minute. It is clear, though, that the ABM is not very well suited to obtain accurate and detailed measurements of the two-dimensional beam cross-section, for the following reasons:

- The ABM is a single-pixel instrument; thus, its spatial resolution is very limited and given by the aperture cross-section.
- The ABM is not (and is not meant to be) an imaging instrument. Therefore, to obtain a 1D-beam profile, we have to scan through the beam at one step after the other. This requires very stable ion and neutral beam conditions over a rather long measurement time.
- To keep the total measurement time of one beam scan with the ABM at a practicable level, and still obtain sufficient coincidence count statistics, such beam scans can reasonably only be obtained at comparably high neutral beam intensities, hence, at beam energies above roughly 1 keV.

In general, a 2D imaging particle detector such as an MCP detector is much better suited to measure the neutral beam cross-section. However, coarse vertical and horizontal profiles of the neutral atoms beam can be obtained that can be used to estimate the beam widths.

In Fig. 4.9, two horizontal beam scans through a neutral helium beam produced from a 3 keV primary He ion beam are shown as an example. One was recorded at about 5 cm in front of the neutralizer exit aperture, and the other at a larger distance of about 11 cm to the neutralizer exit. The measured flux in both He beam scans was normalized with the same factor, so that the ratio of intensities remains conserved.

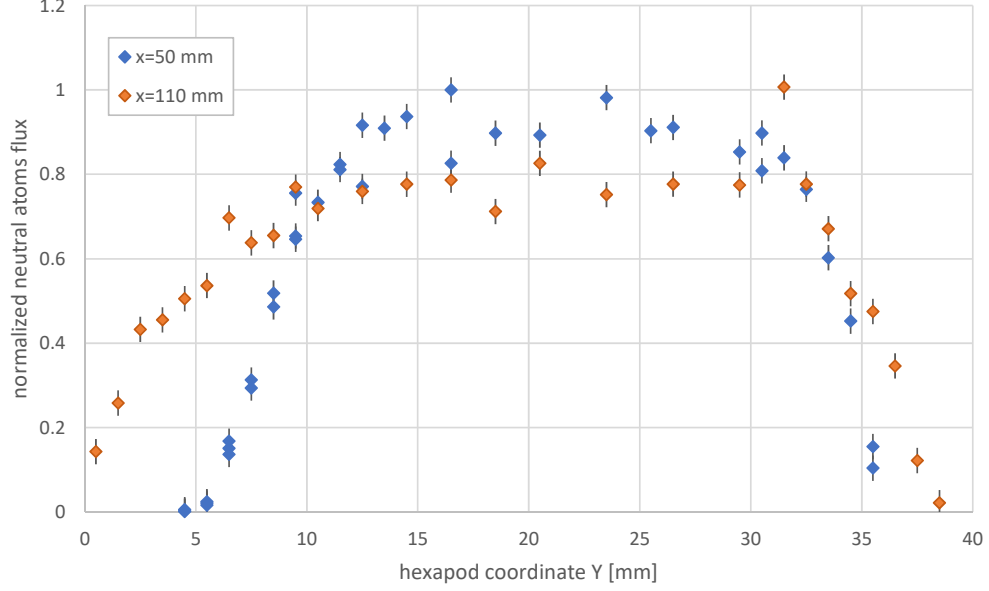


Figure 4.9.: Beam profile of a 3 keV neutral He beam at distances  $x = 50$  mm and 110 mm in front of the neutralizer.

Table 4.1.: Helium beam profile dimensions.

aperture distance:	beam width (FWHM):	rel. intensity:
$d = 50$ mm	$25 \pm 1.5$ mm	$0.93 \pm 0.03$
$d = 110$ mm	$32.5 \pm 1.5$ mm	$0.78 \pm 0.03$
<i>ratio:</i>	1.25	0.84

Neutral atoms propagate freely on straight trajectories. From basic considerations, the Gauss theorem and the proportionality theorem, we expect the the neutrals beam flux to drop roughly as  $f_n \propto d^{-2}$  with distance to the beam's origin, which is at the tungsten plate in the neutralizer. The NS is about 12 cm behind the neutralizer exit aperture. Taking this into account, the observed intensity reduction by about 16 % is still much small than expected. However, as the NS is a spatially extended source, rather than a point source for ENA, this adds another free parameter to the model, and having the horizontal beam profile at hand at just

two distances might not be sufficient constraint to determine the actual distance dependency of the neutral beam flux.

From the horizontal FWHMs obtained from the two beam profiles, and knowing the the exit aperture at distance  $x = 0$  is 16 mm wide, we can estimate the horizontal beam opening. The opening half-angle for 3 keV He is about  $4.0 \pm 0.5^\circ$ .

In another recent measurement, a neutral hydrogen beam (from 2 keV primary  $H^+$  energy) was scanned in horizontal and vertical direction with the ABM on the hexapod. The obtained beam profiles through the center of the ENA beam are shown in Fig. 4.10. The horizontal

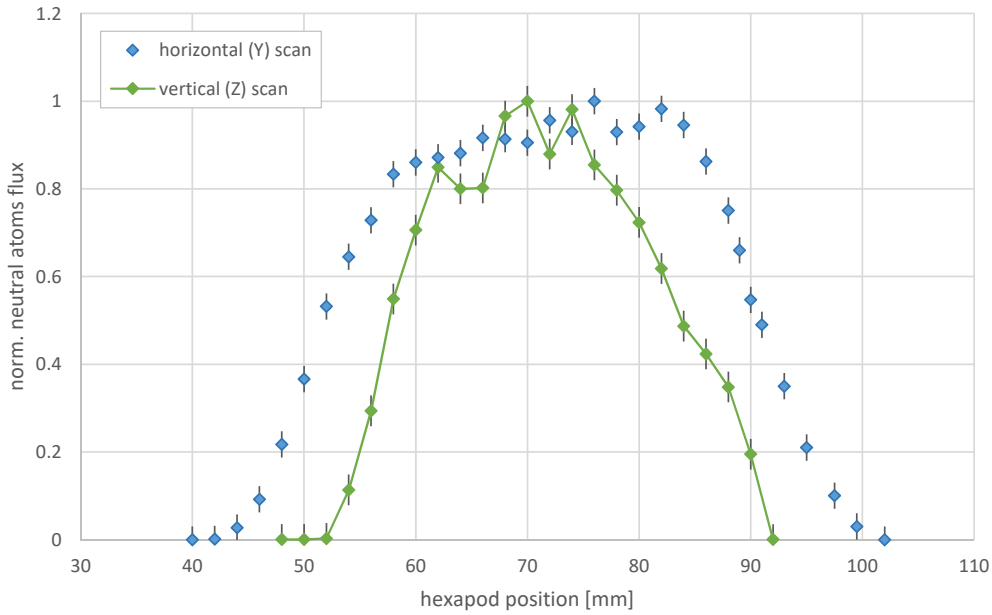


Figure 4.10.: Horizontal and vertical profiles of a neutral hydrogen beam at 2 keV primary ion beam energy. The connection lines are shown at the vertical profile for better readability.

beam FWHM is about 39 mm, while the vertical extent is about 27 mm FWHM. Thus, from these data, the neutral H beam is a factor of  $\sqrt{2}$  wider in horizontal than in vertical cross-section. This is in agreement with the result from a 2D MCP beam image recorded in the neutralizer calibration in preparation for the IBEX-Lo calibration campaigns.

#### 4.1.4. Neon Flux Calibration

Using the ABM, calibration measurements were also performed for a neutral neon beam. Three neon measurement campaigns were done in MEFISTO in April and May 2021, and in September 2022. The measurement procedure is described in the paper manuscript, “*Calibration beam fluxes of a low-energy neutral atom beam facility*”, in Section 4.2.

The resulting Calibration Factor, which is the neutral atoms flux per surface current on the NS, is shown in Figure 4.11 as a function of the Ne ion energy. As we see, the data from

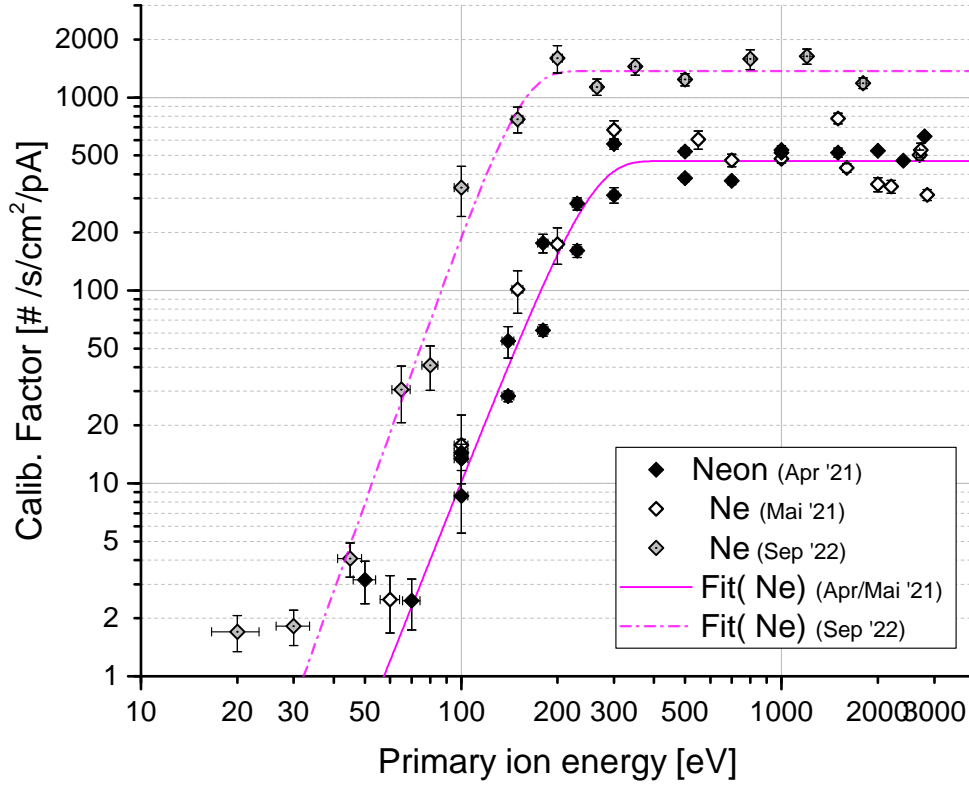


Figure 4.11.: Neon neutral beam flux calibration results from three separate campaigns. A Weibull fit has been added each to the data from the 2021 campaigns and the data set from September 2022, respectively.

April and May 2021 are in agreement within the overall scatter of the data points. However, the same results could not be fully reproduced with the data from Ne measurements in 2022. On one hand, the *Sep '22* data set shows the same overall characteristics; the CF is at a constant plateau at high beam energies above a characteristic roll-over energy, below which there is a power-law dependency of the CF on beam energy. the exponent of this power law in the low-energy regime also agrees within the measurement uncertainty. However, the entire measurement data distribution in September 2022 shows a shift to lower energies by a constant factor of 2, and the measured CF values are about a factor of 2.5 larger than the ones obtained previously.

At this point it is not yet clear what happened that causes this apparent discrepancy, even though several possible causes have been checked:

- Several possible mistakes in the data evaluation procedure have been ruled out, such as to how the neutrals rate into the ABM and beam flux are calculated from count rates.
- The beam energy was determined according to the same routine.
- Positioning of the ABM with respect to the neutralizer, and beam optimization strategy

Other factors could not be checked and ruled out yet, such as erroneous functioning in one of the electronics counters. Moreover, one of the CEMs in the ABM had to be replaced prior to the calibration campaign in September. It is possible that the individual CEM characteristics have an impact on the measurements. However, a different CEM sensitivity would influence the counts statistics of individual counts channels, but not the measured neutrals flux [12]. And it is unclear how this could lead to the observed energy shift of the calibration curve in Fig. 4.11. A significantly higher background count rate was not observed in the recent measurement.

Finally, a series of high-voltage shutdowns happened in the laboratory in September, which might have caused some damage to one of the devices due to discharges.

In consequence, the calibration measurement has to be repeated again to confirm which of the results is reproducible and thus reliable.

### 4.2. Paper: “Calibration beam fluxes of a low-energy neutral atom beam facility”

The primary application of the newly developed Absolute Beam Monitor (Chapter 3) is the calibration of the surface neutralizer in MEFISTO by absolute measurement of the neutral atoms flux. The calibration factor CF, as defined and explained in Gasser et al. [12] (see pp. 111f), is the ENA beam flux from the neutralizer per neutralizer surface current. In the MEFISTO test facility, the CF was obtained from simultaneous accumulation of the neutrals rate by the ABM and monitoring the surface current in the neutralizer at various beam energies. The energy dependency of the CF was thus measured for several species of primary interest, namely hydrogen, oxygen, helium, deuterium, neon, and sulfur.

In addition, the relative reduction in beam energy due to the surface interaction in the neutralizer was quantified for species H, D, He, O and Ne at a wide range of energies. This was done by comparison of the neutral atoms kinetic energy obtained from ABM ToF spectra with the ion beam energy obtained from the electrical potential difference between the ion source and the neutralizing surface.

The calibration results are described and summarized in the following research paper manuscript, “*Calibration beam fluxes of a low-energy neutral atom beam facility*”, submitted to the journal *Review of Scientific Instruments*. This work primarily builds up on references [21], [47] and [12].



# Calibration beam fluxes of a low-energy neutral atom beam facility

Jonathan Gasser, André Galli, and Peter Wurz

*University of Bern, Physics Institute, Space Research and Planetary Sciences,*

*Sidlerstrasse 5, 3012 Bern, Switzerland*

## Abstract

Scientific detection and imaging instruments for low-energetic ENA onboard spacecraft require thorough pre-flight laboratory calibration against a well-characterized neutral atom beam source. To achieve this requirement, a dedicated test facility is available at the University of Bern, which is equipped with a powerful plasma ion source and an ion beam neutralization stage. Using surface neutralization, low-energy neutral atom beams of any desired gas species in the energy range from 3 keV down as low as 10 eV can be produced. As the efficiency of the neutralization stage is species and energy dependent, the neutralizer itself needs to be calibrated against an independent reference.

We report on the calibration and characterization of this neutral atom beam source using our recently developed Absolute Beam Monitor (ABM) as a primary calibration standard. The ABM measures the absolute ENA flux independent of neutral species in the energy range from 10 eV to 3 keV. We obtain calibration factors of a few  $100 \text{ cm}^{-2}\text{s}^{-1}\text{pA}^{-1}$  depending on species at beam energies above about 100 eV, and a power law decrease for energies below 100 eV. Furthermore, the rough energy loss of neutralized ions in the surface neutralizer is determined in the ABM from a time-of-flight measurement. The relative energy loss increases with ENA energy from low levels near zero up to 20 % – 35 % at 3 keV, depending on atomic species.

Having calibrated our neutral beam source allows for an accurate calibration of ENA space instruments.

## 1. Introduction

Remote observation of plasma populations using energetic neutral atoms (ENA) onboard a spacecraft is an established observation technique in space and planetary science [20]. This is owed to the production mechanism of an ENA in space: an energetic ion exchanges its charge with an ambient neutral atom. In interplanetary space, when particle-particle collisions are negligible, the resulting ENA is no longer affected by electric or magnetic fields so that the newly created ENA leaves its region of origin with the energy, velocity, and direction of the parent ion. Imaging ENA thus allows to study entire plasma regions in space, e.g., planetary magnetospheres or the heliosphere, from a remote vantage point [4].

Specifically, the Interstellar Boundary Explorer (IBEX) mission by NASA [13] remotely explores interactions between the solar wind and the interstellar medium at the heliopause using two ENA imaging instruments, IBEX-Lo [5] and IBEX-Hi [3]. All-sky mapping of heliospheric ENA (mainly hydrogen and oxygen, but also helium and deuterium) at a wide range of energy bands has led to a much deeper

understanding of the general physical properties of our heliosphere. For instance, it has led to the discovery of the unanticipated ‘IBEX ribbon’ [12, 16, 17] of the heliosphere. After 15 years of successful operation of IBEX covering more than one full solar cycle, solar cycle effects in the heliosphere can be studied [6]. The successor Interstellar Mapping and Acceleration Probe (IMAP) [14] mission is scheduled for launch in early 2025. It will further extend our understanding of the heliosphere and its interactions with the interstellar medium. Three ENA instruments covering complementary energy ranges are included in IMAP’s suite of ten scientific instruments to analyze heliospheric ENA and interstellar neutral atoms (ISN). ENA imaging and analysis instruments have also been flown successfully on several other planetary missions (see [8] and references therein).

Scientific instruments for ENA detection and analysis must include an efficient ionization method, suitable for application in a space instrument, of the incident neutral atoms prior to their mass and energy analysis by ion-optical means [20]. ENA above an energy threshold of about 1 keV can be ionized by stripping off an electron in letting them pass through a micrometer-thin carbon foil [1]. This ionization technique is applied, among others, in the IBEX-Hi instrument [3].

At lower energies, particle transmission through the foil strongly decreases, so an alternative ionization method must be applied. To date, the widest applied ionization method for low-energy ENA that is also suitable for space applications is via grazing-incidence angle surface scattering [20]. Among the most efficient and widest applied charge-conversion surface (CS) materials in space instrumentation are aluminum oxide ( $\text{Al}_2\text{O}_3$ ) [15] and diamond-like carbon (DLC) materials [18, 21]; however, several other materials have been characterized experimentally and shown suitable as well (see [7] and references therein).

The applied ionization method, negative ionization via surface scattering, inherently introduces some angular spread of the ionized atoms as well as a reduction in their kinetic energy due to the surface interaction. Both effects depend on atomic species, incidence angle and ENA energy. This may affect the overall instrument throughput and analysis. Like other instruments, low-energy ENA instruments rely on thorough laboratory calibration against a well-characterized neutral atom beam source. Substituting the ENA beam by an ion beam would greatly simplify the calibration preparations and procedure, as ion beams can be prepared and characterized much easier by standard means. However, this is not feasible for low-energy ENA instrument calibration, as low-energy ions are affected by electric fields inside the ENA instrument.

## 2. Laboratory Setup

An overview of the experimental setup is shown in Figure 1, and is briefly described in the following. The entire experiment setup is described in more detail in Gasser et al. (2022) [8].

The MEFISTO calibration facility [11] at the University of Bern is used for laboratory calibrations of scientific ion and ENA imaging space flight instrumentation. Originally designed and built for solar wind experiments, the large MEFISTO vacuum test chamber is equipped with a powerful microwave-heated plasma ion source [2, 9, 10] and subsequent ion-optical system to produce a collimated beam of positive ions from any desired gas species and guide it into the main vacuum chamber (Figure 1, left). The calibration campaign of the IBEX-Lo instrument was carried out in MEFISTO [5], and the IMAP-Lo instrument will be calibrated here as well. The IMAP-Lo calibration campaign will include H, He, O, Ne, and D calibrated ENA beams in the energy range of 10 eV to 1 keV.

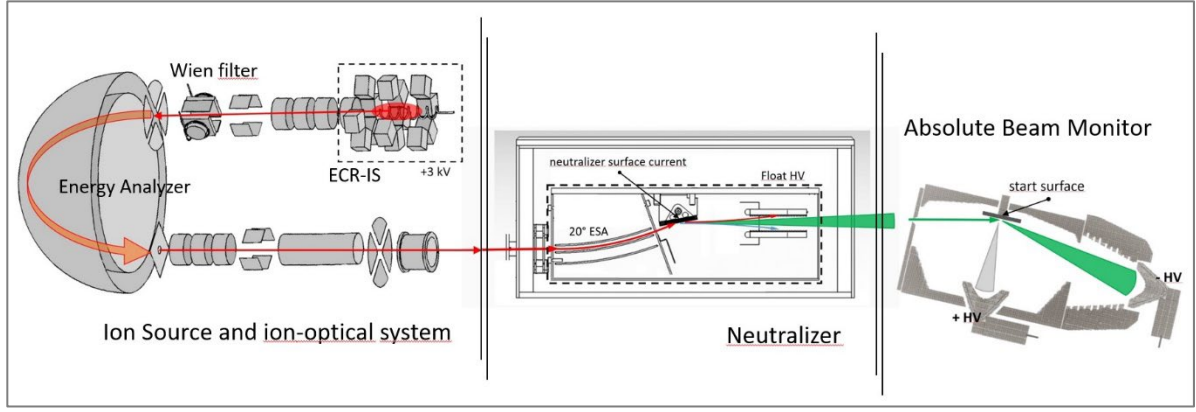


Figure 1: Scheme of the experiment setup of the MEFISTO calibration facility: on the left the plasma ion source and ion-optical system, in the center the surface neutralizer, and to the right the Absolute Beam Monitor. Units are shown at different scales.

The necessary low-energy ENA beams are produced by converting a 3 keV ion beam using surface neutralization at grazing incidence angle. For this purpose, a surface neutralizer [19] is installed in front of the ion beam entrance into the vacuum chamber (Figure 1, center). The ion beam enters into the neutralizer, and is decelerated by floating the neutralizer to an electrical potential of up to 3 kV. The energy  $E_{ion}/q$  of the ion beam striking the neutralizing tungsten single crystal surface is set by adjusting the float high voltage in combination with a 20° electrostatic analyzer (ESA) in the neutralizer.

$$\frac{E_{ion}}{q} = U_{extr} - U_{float} = k_{eff} \cdot U_{ESA}$$

The effective neutralizer ESA constant is  $k_{eff} \cong 10$ , and  $-U_{ESA}$  and  $+U_{ESA}$  are the bias voltages applied to the inner and outer ESA electrodes, respectively.

After on-surface neutralization, remaining positive and converted negative ions are removed from the scattered beam by two electrostatic deflection plates. The neutral atom beam is collimated through a  $16 \times 16 \text{ mm}^2$  exit aperture, resulting in an angular beam spread of approximately  $\pm 5.5^\circ$  in horizontal and  $\pm 4^\circ$  in vertical extent. The surface neutralizer is mounted on a two-axis linear translation stage, which allows for precise positioning of the neutralizer entrance aperture with respect to the ion beam in the plane perpendicular to the ion beam axis. This is important, as the ion beam location may vary with the plasma conditions in the ion source and the optimisation of the ion beam path.

The beam neutralization process using a neutralizing surface causes a reduction of the beam energy and an increase in the neutral beam angular divergence. This implies that the produced ENA beam exiting the neutralizer needs to be characterized separately. Until recently, the neutral beam flux was determined using a standard particle detector such as an MCP detector. The accuracy of the neutral atom flux measurement is however limited by the knowledge of the detector's detection efficiency for neutral atoms at the energies of interest. To improve on this problem, we recently developed Absolute Beam Monitor (ABM) [8] that allows us to experimentally determine the absolute neutral atom flux  $F_n$  from the neutralizer without relying on prior knowledge of detector efficiencies.

Aside from the primary ion beam energy and species, the actual ENA beam intensity largely depends on the ion beam intensity from the ion source, which is strongly affected by the detailed plasma conditions in the ion source and is subject to optimization of the downstream ion-optical system. Consequently, the intensity of the ion beam into the neutralizer varies from day to day and may also vary during operating time. We keep track of this ion beam intensity variations by real-time monitoring the current recorded on the neutralizer surface used for beam-neutralizing using a pico-amperemeter installed in the neutralizer itself.

We verified that the neutral atoms flux into the chamber, for a given species and beam energy, is proportional to the neutralizer surface current. This is justified as in particle scattering surface

interactions at grazing incidence angles, the fraction of neutralized ions and the angular scatter distribution vary with incident ion energy, species, and incidence angle, but are not observed to deviate from proportionality with ion beam intensity. Since the neutraliser surface is a tungsten metal surface even high ion intensities will not lead to surface charging. To calibrate the neutralizer we relate the ENA flux  $F_n$  out of the neutralizer measured by the ABM to the neutralizing surface current  $I_{ncs}$  measured in the neutralizer itself. The surface current  $I_{ncs}$  then serves as a secondary reference during the ENA calibrations, and converts to the ENA flux by a calibration factor

$$CF(E_{ion}) = F_n / I_{ncs}$$

as function of the ion beam energy  $E_{ion}$  for a set of ion species of interest. For example, for a neutralizer surface current of  $I_{ncs} = 1$  nA, the calibration factor  $CF = 1000 \text{ s}^{-1}\text{cm}^{-2}\text{pA}^{-1}$  corresponds to a neutral atom beam flux of  $F_n = 10^6 \text{ s}^{-1}\text{cm}^{-2}$  in the test chamber. With the ABM we measure the absolute neutral atoms flux locally in the test chamber, as described in [8].

We calibrated the MEFISTO laboratory neutral beam source for a set of atomic species of particular interest in regard of the IMAP-Lo calibration campaign, using the ABM as an independent primary calibration standard.

### 3. Results and Discussion

#### a) Absolute Neutral Atom Flux

In Figure 2 to Figure 6, the calibration factor  $CF$  as determined from the ABM flux and simultaneous neutralizer surface current measurements is plotted as a function of the primary ion beam energy, for hydrogen, helium, deuterium, oxygen and sulfur atom beams, respectively. The measured data were fitted with a three-parameter Weibull distribution function [8]:

$$f(x) = a \exp(-(b x)^d) \quad (1)$$

Above a characteristic energy around 100 eV, the ENA flux out of the neutralizer does not depend on ion energy, and is proportional to the neutralizer surface current. Below this roll-over energy, there is an additional power-law relation between the  $CF$  and primary ion energy, depending on the ENA species.

The primary contributions to the measurement uncertainty of the  $CF$  in the low-energy range are the low coincidence counting statistics from the ABM. The uncertainty in the energy results from the limited accuracy of the voltage difference between neutralizer float potential, ion-source extraction voltage, and the plasma potential of the ion source. This difference defines the ion energy onto the neutralizer surface. The relative scatter of data points is attributed to the overall system alignment accuracy, which comprises the optimized ion beam path from the source through the ion-optical system to the neutralizer and the ABM.

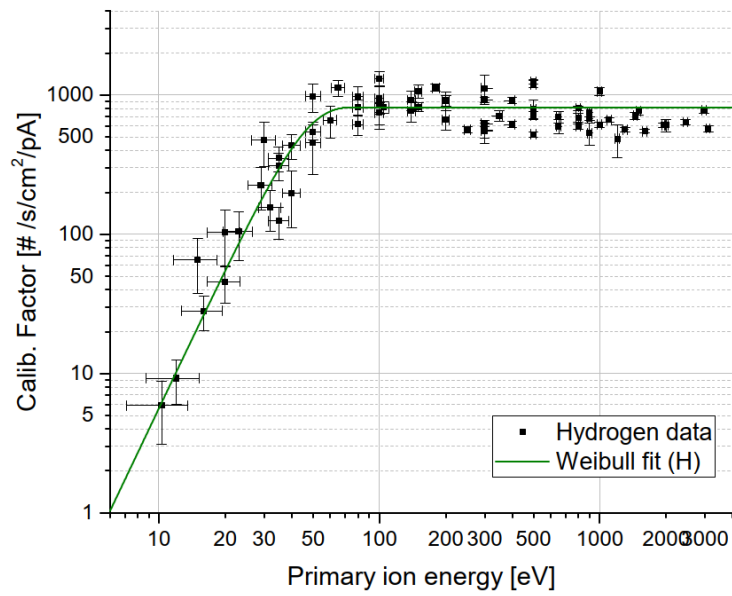


Figure 2: Calibration Factor ( $CF = F_n/I_{ncs}$ ) for hydrogen in the ion energy range 10 eV to 3 keV.

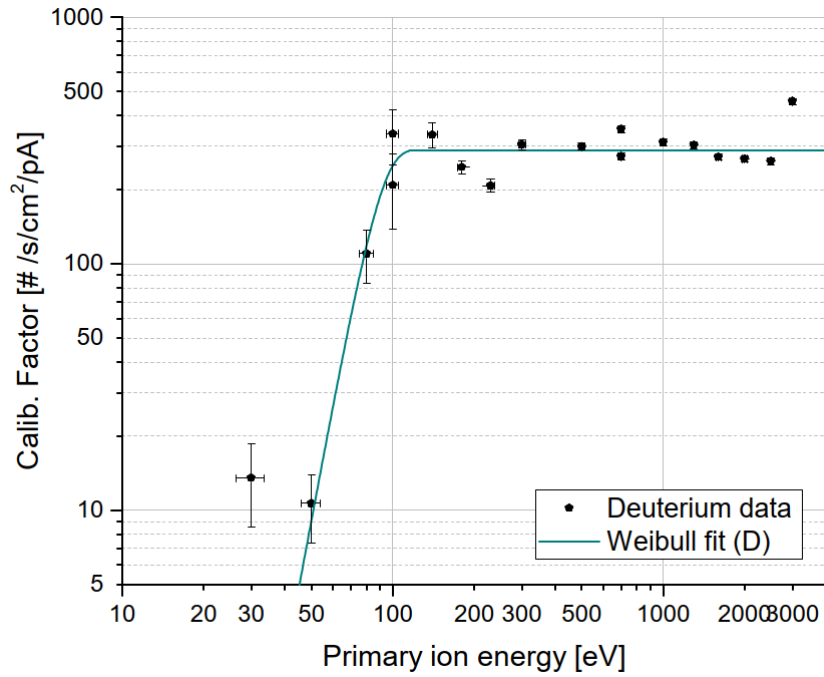


Figure 3: Neutralizer Calibration Factor for deuterium in the energy range 30 eV to 3 keV.

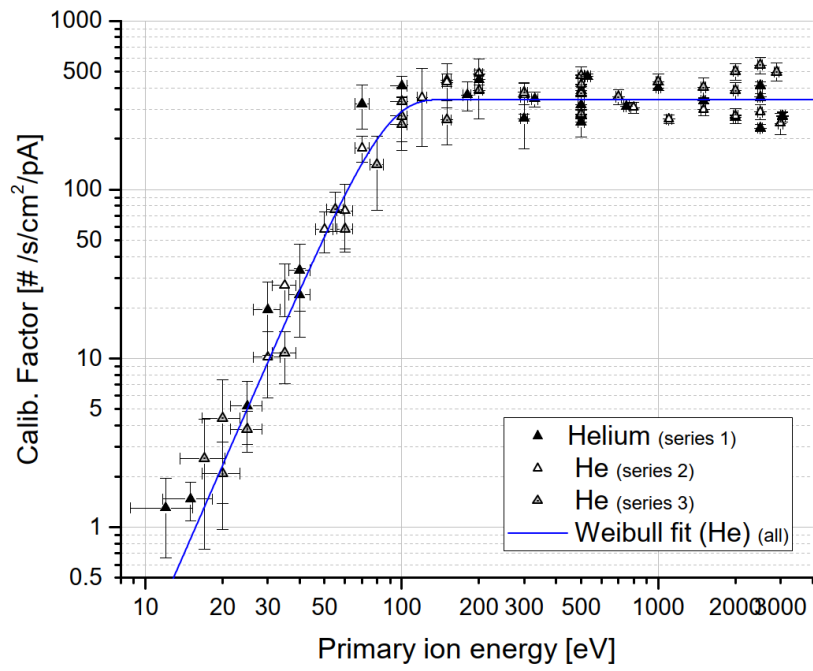


Figure 4: Neutralizer Calibration Factor for helium in the energy range 10 eV to 3 keV.

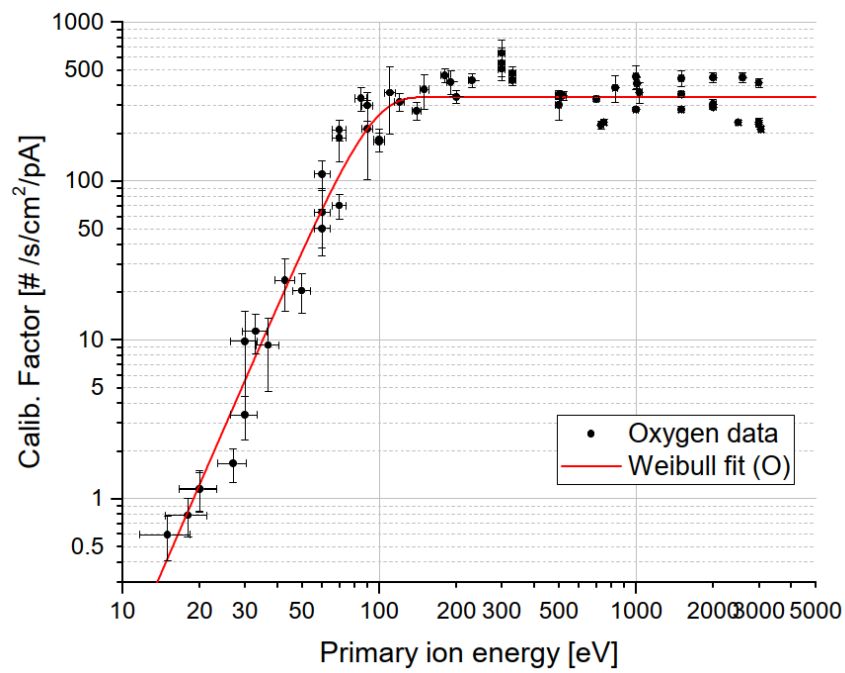


Figure 5: Neutralizer Calibration Factor for oxygen in the energy range 15 eV to 3 keV.

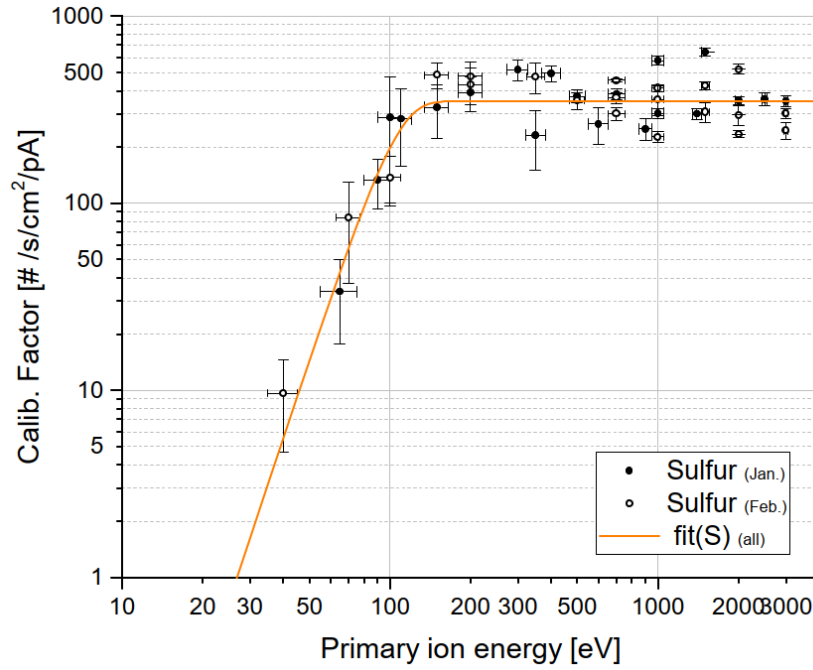


Figure 6: Neutralizer Calibration Factor for sulfur in the energy range 40 eV to 3 keV.

### b) Energy Loss in the Neutralizer

In the ABM, time-of-flight (ToF) spectra of coincident start and stop events were recorded for ENA species H, D, He, O, and Ne at energies of the primary ion beam into the neutralizer from 3 keV down to 100 eV. From the peaks in the ToF spectra, the mean energy  $\langle E \rangle_{tof}$  of neutral atoms scattered off the ABM's start surface was retrieved by finding the center of the ToF peak by means of a Gaussian fit [8]. The results are shown in Figure 7; the dashed line indicates the situation if no kinetic energy loss occurred on the scattering surface, i.e.,  $\langle E \rangle_{tof} = E_{ion}$ . The standard error of mean of the neutral atoms energy was estimated as the half-width at 95 % of the maximum of the Gaussian fit to the energy distribution obtained from the ToF spectra.

Figure 7 illustrates that over the full energy range, the reduction in kinetic energy tends to be more pronounced for higher atomic mass, except for the noble gas neon, for which the results are comparable to hydrogen. However, Ne spectra have just been evaluated down to 1000 eV due to low peak signal and comparably high background in the spectra.

On their trajectory through the neutralizer and into the ABM, the atoms that generate a signal in the ToF peak were scattered at a polished W surface twice: once on the neutralizing surface in the neutralizer and once on the ABM start surface (SS). Assuming that the atoms' energy is reduced by the same fraction at each surface, we obtain the relative energy loss per surface interaction as given in Eq. (10) in [8]. The results are shown in Figure 8 to Figure 12, respectively, for H, D, He, O, and Ne. A log-linear two-parameter fit ( $y(x) = b \cdot \ln(x) - a$ ) was added to guide the eye. The fit represents the measured data reasonably well at beam energies above 100 eV (above 300 eV for deuterium).

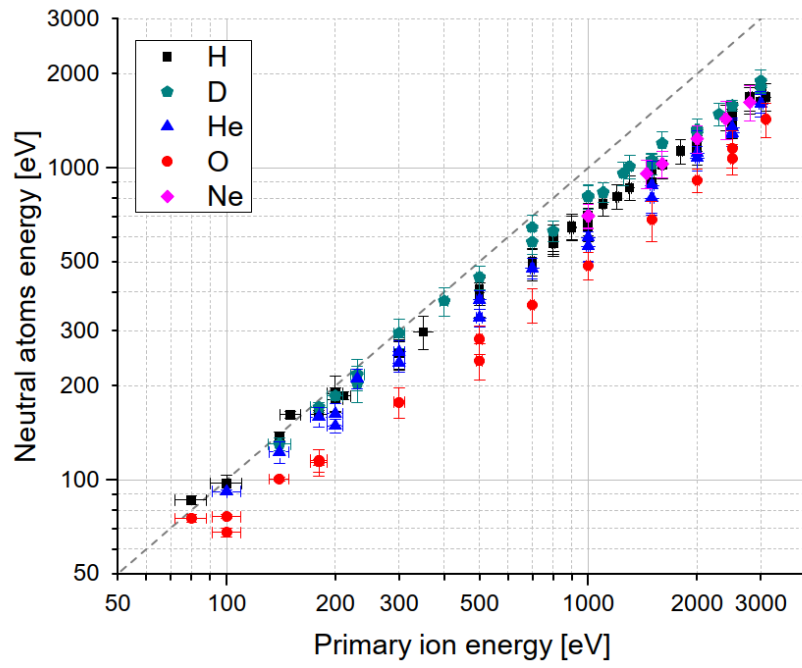


Figure 7: ENA kinetic energy obtained from ABM ToF spectra as function of the primary ion energy into the neutralizer, for atomic species H, D, He, O, and Ne. The dashed line indicates the hypothetical case of surface scattering without energy loss.

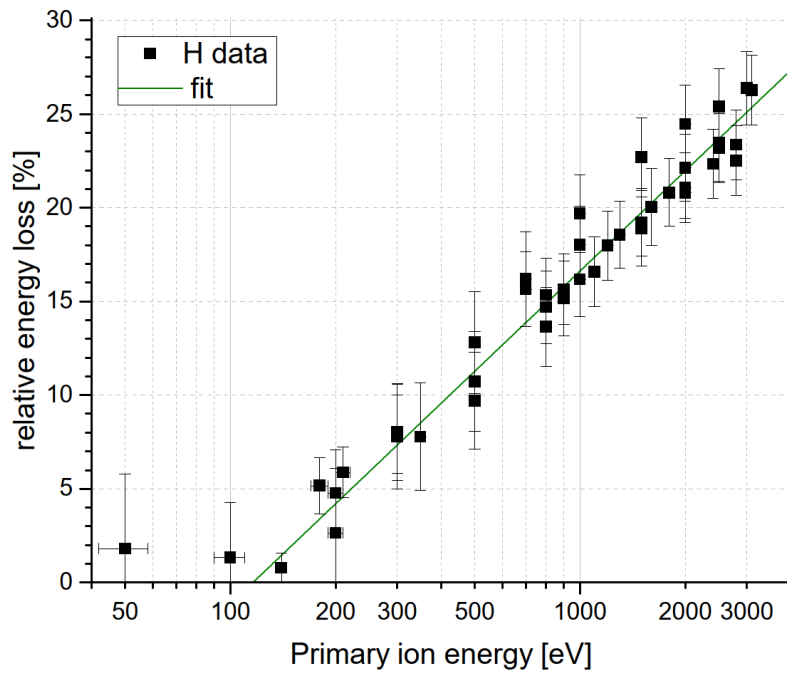


Figure 8: Fraction of kinetic energy lost at the W surface in the neutralizer for hydrogen atoms.



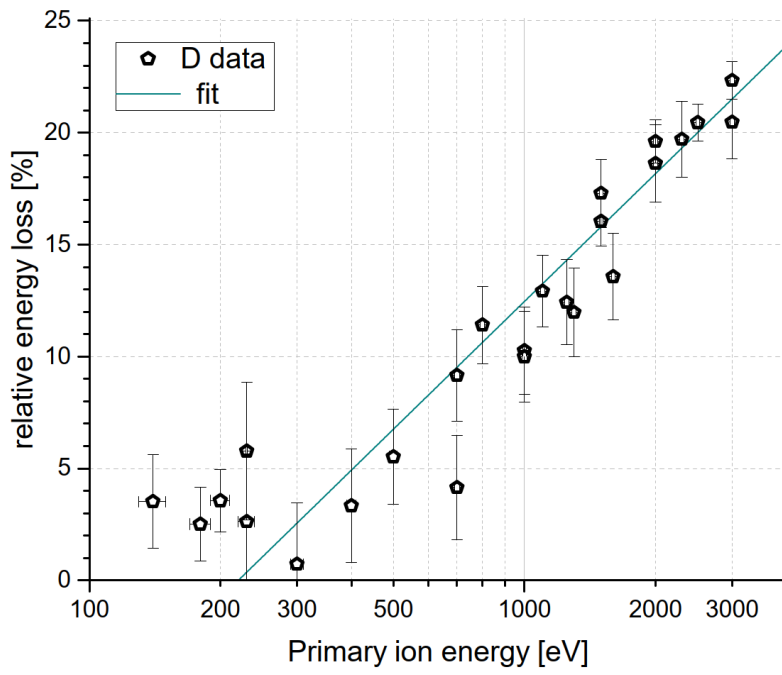


Figure 9: Fraction of kinetic energy lost at the W surface in the neutralizer for deuterium atoms.

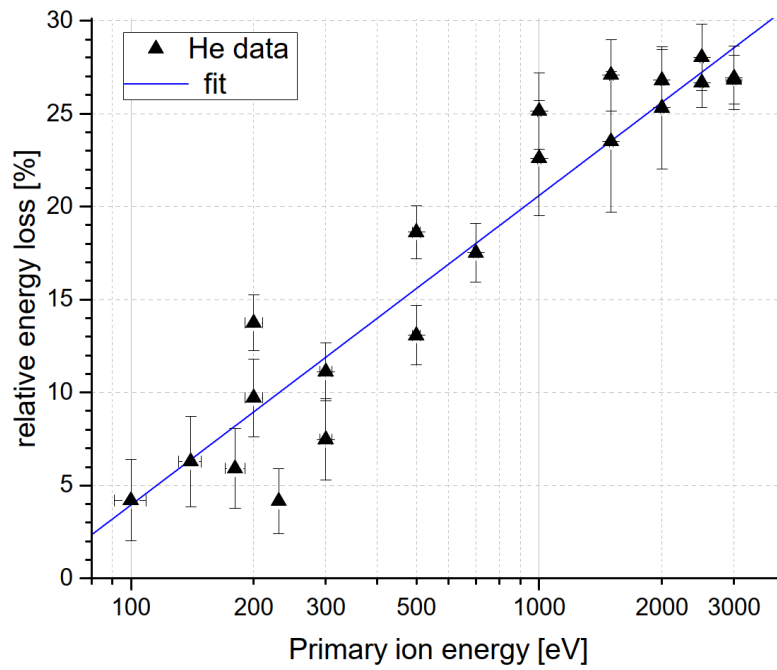


Figure 10: Fraction of kinetic energy lost at the W surface in the neutralizer for helium atoms.

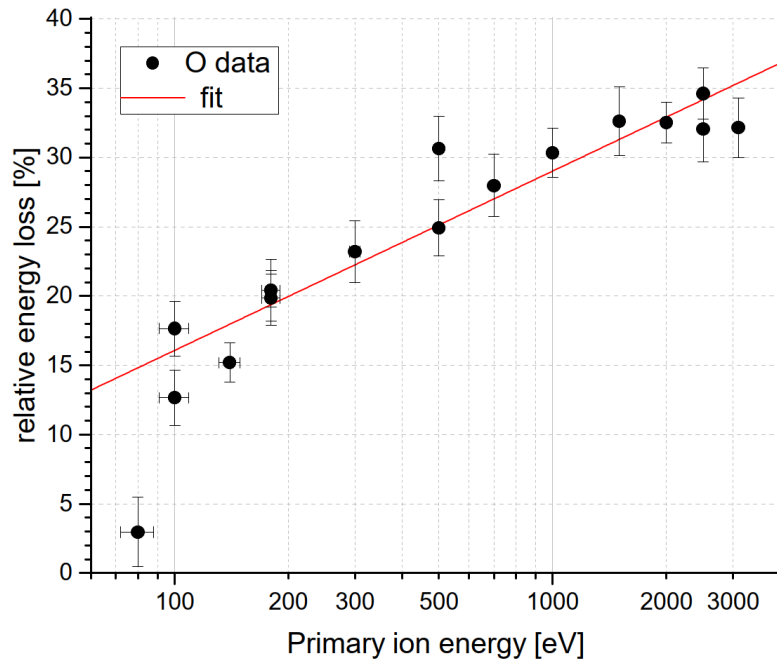


Figure 11: Fraction of kinetic energy lost at the W surface in the neutralizer for oxygen atoms.

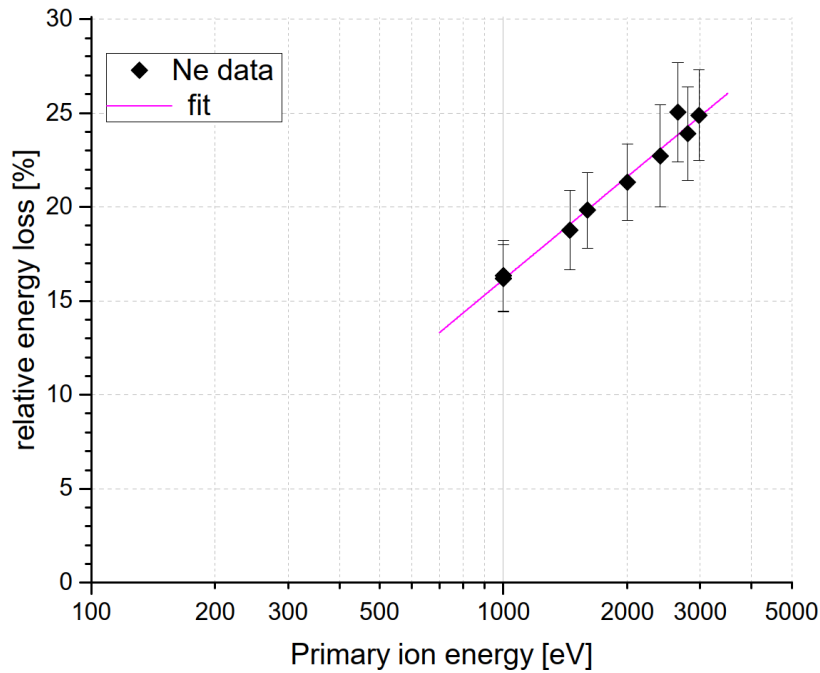


Figure 12: Fraction of kinetic energy lost at the W surface in the neutralizer for neon atoms.

The results presented in Figure 8 to Figure 12 show that a considerable fraction of kinetic energy is lost in the interaction with the neutralizing surface. At energies above 100 eV, the relative energy loss increases monotonically with primary ion energy from just a few percent to 20–35 % at 3 keV depending on atomic species. The fraction of energy lost tends to increase with atomic mass and is highest for oxygen among the measured atomic species.

During the instrument calibration of IBEX-Lo, the fraction of energy loss at the instruments' conversion surface was determined based on the discrepancy between instrument energy step and the set beam center energy (see Fuselier et al. [5], Section 3.9 and Figure 18). At energies from 100 eV to 2 keV, the fraction of energy lost was found to be [5] about 15 % to 30 % for H, and between 35 % and 50 % for O, with relative error bars (+0.68, −0.34). Those values were clearly higher than the 15 % relative energy loss estimated before the IBEX-Lo calibration campaign, but still agreed within the uncertainty range.

In comparison, the ABM measured data for hydrogen shown in Figure 8 amount to a lower energy loss at the surface interaction, i.e., less than 10 % at energies below about 400 eV, but still up to 25 % at the highest measured energies. For oxygen (see Figure 11), we obtained values about 10 – 20 % lower than in [5]. Note, however, that the IBEX-Lo CS were DLC coated Si wafers (in contrast to W single crystal in the neutralizer and in the ABM), and that the CS are installed at 15° nominal incidence angle in IBEX-Lo. Both differences could explain part of the larger energy loss derived for IBEX-Lo conversion surfaces. Overall, those results are still in agreement with the ones shown here considering the uncertainties.

Based on the available data at low energies and the observed general trend, we expect the relative energy loss not to exceed 5 % for H, D, and He at beam energies below 100 eV.

## 4. Summary

The low-energy neutral atom beam source in the MEFISTO laboratory [11] at the University of Bern was calibrated using the Absolute Beam Monitor [8] by relating the measured absolute neutral atom flux to the neutralizer surface current  $I_{ncs}$  [19]. With the derived calibration factors for the energy range and species of interest, the ENA flux available during calibration can be determined by real-time monitoring the current on the neutralizer surface,  $I_{ncs}$  and converting it to the ENA flux with the presented calibration. This work was done for the upcoming calibration campaign of the IMAP-Lo instrument. The results will also be valuable to calibrate other future ENA instruments.

Moreover, the ABM ToF spectra allowed us to determine the mean fraction of ENA kinetic energy lost at the neutralizer surface. With this knowledge, we can account for the energy loss and compensate for it by adjusting the primary ion beam accordingly.

## Bibliography

- [1] F. Allegrini, R. W. Ebert, and H. O. Funsten. Carbon foils for space plasma instrumentation. *Journal of Geophysical Research: Space Physics*, 121 (5): 3931–3950, 2016. doi: [10.1002/2016JA022570](https://doi.org/10.1002/2016JA022570).
- [2] M. Bodendorfer, P. Wurz, and M. Hohl. Global plasma simulation of charge state distribution inside a 2.45 GHz ECR plasma with experimental verification. *Plasma Sources Science and Technology*, 19 (4): 045024, 2010. doi: [10.1088/0963-0252/19/4/045024](https://doi.org/10.1088/0963-0252/19/4/045024).
- [3] H. Funsten, F. Allegrini, P. Bochslers, G. Dunn, S. Ellis, D. Everett, M. Fagan, S. Fuselier, M. Granoff, M. Gruntman, A. Guthrie, J. Hanley, R. Harper, D. Heirtzler, P. Janzen, K. Kihara, B. King, H. Kucharek, M. Manzo, M. Maple, K. Mashburn, D. McComas, E. Möbius, J. Nolin, D. Piazza, S. Pope, D. Reisenfeld, B. Rodriguez, E. Roelof, L. Saul, S. Turco, P. Valek, S. Weidner, P. Wurz, and S. Zaffke. The Interstellar Boundary Explorer high energy (IBEX-Hi) neutral atom imager. *Space Science Reviews*, 146: 75–103, 2009. doi: [10.1007/s11214-009-9504-y](https://doi.org/10.1007/s11214-009-9504-y).

- [4] S. Fuselier, A. Ghielmetti, T. Moore, M. Collier, J. Quinn, G. Wilson, P. Wurz, S. Mende, H. Frey, C. Jamar, J.-C. Gerard, and J. Burch. Ion outflow observed by IMAGE: Implications for source regions and heating mechanisms. *Geophysical Research Letters*, 28 (6): 1163–1166, 2001. doi: [10.1029/2000GL012450](https://doi.org/10.1029/2000GL012450).
- [5] S. Fuselier, P. Bochsler, D. Chornay, G. Clark, G. Crew, G. Dunn, S. Ellis, T. Friedmann, H. Funsten, A. Ghielmetti, J. Googins, M. Granoff, J. Hamilton, J. Hanley, D. Heirtzler, E. Hertzberg, D. Isaac, B. King, U. Knauss, F. Kudirka, H. Kucharek, J. Lobell, S. Longworth, D. McComas, E. Möbius, A. Moore, T. Moore, R. Nemanich, P. Nolin, M. O’Neal, D. Piazza, S. Pope, P. Rosmarynowski, L. Saul, J. A. Scheer, C. Schlemm, J. Scherrer, C. Tillier, S. Turco, J. Tyler, M. Vosbury, M. Wieser, P. Wurz, and S. Zaffke. The IBEX-Lo Sensor. *Space Science Reviews*, 146: 117–147, 2009. doi: [10.1007/s11214-009-9495-8](https://doi.org/10.1007/s11214-009-9495-8).
- [6] A. Galli, P. Wurz, N. Schwadron, K. Fairchild, D. Heirtzler, E. Möbius, H. Kucharek, R. Winslow, M. Bzowski, M. Kubiak, I. Kowalska-Leszczynska, S. Fuselier, J. M. Sokół, P. Swaczyna, and D. McComas. One solar cycle of heliosphere observations with the Interstellar Boundary Explorer: Energetic neutral hydrogen atoms observed with IBEX-Lo from 10 eV to 2 keV. *Astrophysical Journal Supplement Series*, 261 (2), 2022. doi: [10.3847/1538-4365/ac69c9](https://doi.org/10.3847/1538-4365/ac69c9).
- [7] J. Gasser, M. Föhn, A. Galli, E. Argegnani, A. Romeo, and P. Wurz. Cadmium telluride as a potential conversion surface. *Journal of Applied Physics*, 129: 045303, 2021. doi: [10.1063/5.0033701](https://doi.org/10.1063/5.0033701).
- [8] J. Gasser, A. Galli, and P. Wurz. Absolute beam monitor: A novel laboratory device for neutral beam calibration. *Review of Scientific Instruments*, 93 (9): 093302, 2022. doi: [10.1063/5.0092065](https://doi.org/10.1063/5.0092065).
- [9] M. Hohl, P. Wurz, and P. Bochsler. Investigation of the density and temperature of electrons in a compact 2.45 GHz electron cyclotron resonance ion source plasma by X-ray measurements. *Plasma Sources Science and Technology*, 14 (4): 692–699, 2005. doi: [10.1088/0963-0252/14/4/008](https://doi.org/10.1088/0963-0252/14/4/008).
- [10] M. Liehr, R. Trassl, M. Schlapp, and E. Salzborn. A low power 2.45 GHz ECR ion source for multiply charged ions. *Review of Scientific Instruments*, 63 (4): 2541–2543, 1992. doi: [10.1063/1.1142882](https://doi.org/10.1063/1.1142882).
- [11] A. Marti, R. Schletti, P. Wurz, and P. Bochsler. Calibration facility for solar wind plasma instrumentation. *Review of Scientific Instruments*, 72, 2001. doi: [10.1063/1.1340020](https://doi.org/10.1063/1.1340020).
- [12] D. McComas, F. Allegrini, P. Bochsler, M. Bzowski, E. Christian, G. Crew, R. DeMajistre, H. Fahr, H. Fichtner, P. Frisch, H. Funsten, S. Fuselier, G. Gloeckler, M. Gruntman, J. Heerikhuisen, V. Izmodenov, P. Janzen, P. Knappenberger, S. Krimigis, H. Kucharek, M. Lee, G. Livadiotis, S. Livi, R. MacDowall, D. Mitchell, E. Möbius, T. Moore, N. Pogorelov, D. Reisenfeld, E. Roelof, L. Saul, N. Schwadron, P. Valek, R. Vanderspek, P. Wurz, and G. Zank. Global observations of the interstellar interaction from the Interstellar Boundary Explorer (IBEX). *Science*, 326 (5955): 959–962, 2009. doi: [10.1126/science.1180906](https://doi.org/10.1126/science.1180906).
- [13] D. McComas, F. Allegrini, P. Bochsler, M. Bzowski, M. Collier, H. Fahr, H. Fichtner, P. Frisch, H. Funsten, S. Fuselier, G. Glöckler, M. Gruntman, V. Izmodenov, P. Knappenberger, M. Lee, S. Livi, D. Mitchell, E. Möbius, T. Moore, S. Pope, D. Reisenfeld, E. Roelof, J. Scherrer, N. Schwadron, R. Tyler, M. Wieser, P. Wurz, and G. Zank. IBEX - Interstellar Boundary Explorer. *Space Science Review*, 146: 11–33, 2009. doi: [10.1007/s11214-009-9499-4](https://doi.org/10.1007/s11214-009-9499-4).
- [14] D. McComas, E. Christian, N. Schwadron, N. Fox, J. Westlake, F. Allegrini, D. Baker, D. Biesecker, M. Bzowski, G. Clark, C. Cohen, I. Cohen, M. Dayeh, R. Decker, G. de Nolfo, M. Desai, R. Ebert, H. Elliott, H. Fahr, P. Frisch, H. Funsten, S. Fuselier, A. Galli, A. Galvin, J. Giacalone, M. Gkioulidou, F. Guo, M. Horanyi, P. Isenberg, P. Janzen, L. Kistler, K. Korreck, M. Kubiak, H. Kucharek, B. Larsen, R. Leske, N. Lugaz, J. Luhmann, W. Matthaeus, D. Mitchell, E. Möbius, K. Ogasawara, D. Reisenfeld, J. Richardson,

C. Russell, J. Sokól, H. Spence, R. Skoug, Z. Sternovsky, P. Swaczyna, J. Szalay, M. Tokumaru, M. Wiedenbeck, P. Wurz, G. Zank, and E. Zirnstein. Interstellar Mapping and Acceleration Probe (IMAP): A new NASA mission. *Space Science Reviews*, 214: 116, 2018. doi: [10.1007/s11214-018-0550-1](https://doi.org/10.1007/s11214-018-0550-1).

[15] J. Scheer, P. Wahlström, and P. Wurz. Scattering of light molecules from thin Al<sub>2</sub>O<sub>3</sub> films. *Nuclear Instruments and Methods in Physics Research B*, 267: 2571–2574, 2009. doi: [10.1016/j.nimb.2009.05.016](https://doi.org/10.1016/j.nimb.2009.05.016).

[16] N. Schwadron, E. Möbius, S. Fuselier, D. McComas, H. Funsten, P. Janzen, D. Reisenfeld, H. Kucharek, M. Lee, K. Fairchild, F. Allegrini, M. Dayeh, G. Livadiotis, M. Reno, M. Bzowski, J. M. Sokól, M. Kubiak, E. Christian, R. DeMajistre, P. Frisch, A. Galli, P. Wurz, and M. Gruntman. Separation of the ribbon from globally distributed Energetic Neutral Atom flux using the first five years of IBEX observations. *The Astrophysical Journal Supplement Series*, 215 (1): 13, 2014. doi: [10.1088/0067-0049/215/1/13](https://doi.org/10.1088/0067-0049/215/1/13).

[17] N. Schwadron, F. Allegrini, M. Bzowski, E. Christian, M. Dayeh, M. Desai, K. Fairchild, P. Frisch, H. Funsten, S. Fuselier, A. Galli, P. Janzen, M. Kubiak, D. McComas, E. Möbius, D. Reisenfeld, J. Sokól, P. Swaczyna, J. Szalay, P. Wurz, and E. Zirnstein. Time dependence of the IBEX ribbon and the globally distributed energetic neutral atom flux using the first 9 years of observations. *The Astrophysical Journal Supplement Series*, 239 (1): 1, 2018. doi: [10.3847/1538-4365/aae48e](https://doi.org/10.3847/1538-4365/aae48e).

[18] P. Wahlström, J. Scheer, P. Wurz, E. Hertzberg, and S. A. Fuselier. Calibration of charge state conversion surfaces for neutral particle detectors. *Journal of Applied Physics*, 104 (034503), 2008. doi: [10.1063/1.2957064](https://doi.org/10.1063/1.2957064).

[19] M. Wieser and P. Wurz. Production of a 10 eV - 1000 eV neutral particle beam using surface neutralization. *Measurement Science and Technology*, 16: 2511–2516, 2005. doi: [10.1088/0957-0233/16/12/016](https://doi.org/10.1088/0957-0233/16/12/016).

[20] P. Wurz. Detection of energetic neutral particles. *The Outer Heliosphere: Beyond the Planets*, Copernicus Gesellschaft e.V., Katlenburg-Lindau, Germany, pages 251–288, 2000.

[21] P. Wurz, R. Schletti, and M. Aellig. Hydrogen and oxygen negative ion production by surface ionization using diamond surfaces. *Surface Science*, 373 (1): 56–66, 1997. doi: [10.1016/S0039-6028\(96\)01146-6](https://doi.org/10.1016/S0039-6028(96)01146-6).

## 5. Conclusion

---

Contempla las cosas sin presa.  
Solo así serás capaz de verlas.

Almeida <sup>1</sup>

---

ENA imaging is an important observation technique in space science for the *in situ* and remote observation of space plasma populations. Today's low-energy ENA imaging instruments for space applications rely on surface scattering at grazing incidence angles as an efficient and low-consumption ionization technique prior to the ENA analysis and detection by ion-optical and electrical means. On these charge-conversion surfaces, ENA are converted into negative ions with efficiencies depending on their species, energy, incidence angle, the surface material and surface properties. The widest-used and well-established charge-conversion surface materials for space instrumentation are aluminum oxide and diamond-like carbon thin film coatings deposited on a highly polished silicon wafer substrate.

The characterization and qualification of produced conversion surfaces for flight instruments, as well as the search for novel potential conversion surface materials is carried out experimentally in a dedicated ion-scattering test facility. Within the scope of this thesis, several conversion surface samples were characterized regarding their negative ionization efficiency and scattering distribution width: a set of aluminum oxide samples was tested for the Jovian Neutrals Analyzer instrument on the upcoming JUICE mission; and three sets of DLC test samples manufactured by the Southwest Research Institute were characterized as part of the IMAP-Lo instrument development, with results reported in Chapter 2 of this thesis.

Furthermore, a few new surface materials were tested regarding their suitability to serve as an alternative conversion surface material. Among these, a cadmium telluride coating showed promising results as a potential conversion surface.

---

<sup>1</sup>whom I met on the *Camino de Santiago* in 2018: "Consider the things without hurry. Only then you are able to see them."

Apart from a well-suited ENA ionization and detection method, low-energy ENA instruments also require a thorough pre-flight instrument calibration against well-characterized and calibrated low-energy laboratory ENA beams for the ENA species of interest. The production of neutral atoms beams from 3 keV down to as low as 10 eV is already quite involved. It is achieved by on-surface neutralization of a 3 keV ion beam, which is decelerated to the desired beam energy before neutralization. The ion beam neutralization itself is again an application of grazing-incidence surface scattering off a polished tungsten single crystal surface.

Due to the surface scattering interaction, the neutralized laboratory beam is only poorly characterized in energy and intensity.

The main focus of this thesis project was the development and successful application of the Absolute Beam Monitor (ABM), a novel laboratory device that allows the absolute measurement of a low-energetic neutral atoms beam flux in the test facility. The ABM development is reported on in detail in Chapter 3 of this thesis. Its measurement principle relies on the coincident counting of neutral atoms reflected off a polished tungsten start surface inside the device, and of secondary electrons released from this start surface. The neutral beam energy is obtained from simultaneous time-of-flight measurements of the coincidence events.

The ABM serves as a primary standard for the calibration of the laboratory neutral beam source. Its successful application in calibrating the laboratory neutral atoms beam for several species of interest is described and discussed in Chapter 4.

Here are five important lessons learnt from the work on this PhD project:

1. The measurement of neutral atoms at very low energies naturally implies low detection efficiencies and consequently low count rates, long integration times, and therefore requires very good long-term beam stability ... and much patience!
2. These are the major challenges for very-low energy ENA beam calibration: low signal rates require a very strict suppression and elimination of background signals.
3. Proper beam adjustment and voltage optimization is crucial for successful calibration measurements.
4. In the development of a novel instrument – even if its principle is indeed very simple at first sight – there are eventually unforeseen issues coming up, which can make the simple tasks challenging in practice.
5. The development of a novel instrument can ultimately become a success despite sometimes measurements and strategies do not work out as planned, and one has to try alternative solutions.

In conclusion, I am convinced that the present work, the undertaken development and results contained in this thesis constitute an effective contribution towards improved calibration of ENA space instrumentation.

# Bibliography

- [1] F. Allegrini, R. W. Ebert, and H. O. Funsten. Carbon foils for space plasma instrumentation. *Journal of Geophysical Research: Space Physics*, 121(5):3931–3950, 2016. doi: 10.1002/2016JA022570.
- [2] M. Allenbach. Evaluation of potential conversion surfaces for the IMAP mission, 2016. Master Thesis, University of Bern.
- [3] M. Allenbach, M. Neuland, A. Riedo, and P. Wurz. Scattering of low-energetic atoms and molecules from a boron-doped CVD diamond surface. *Applied Surface Science*, 427: 427 – 433, 2017. doi: 10.1016/j.apsusc.2017.08.237.
- [4] A. Borisov and V. Sidis. Theory of negative-ion conversion of neutral atoms in grazing scattering from alkali halide surfaces. *Physical Review B*, 56(16):10628–10643, 1997. doi: 10.1016/S0039-6028(96)01146-6.
- [5] H.-Y. Chang, A. Alvarado, and J. Marian. Calculation of secondary electron emission yields from low-energy electron deposition in tungsten surfaces. *Applied Surface Science*, 450:190–199, 2018. ISSN 0169-4332. doi: <https://doi.org/10.1016/j.apsusc.2018.04.155>.
- [6] M. Föhn. Application of surface physics for instruments in space science, 2017. Master Thesis, University of Bern.
- [7] S. Fuselier, P. Bochslers, D. Chornay, G. Clark, G. Crew, G. Dunn, S. Ellis, T. Friedmann, H. Funsten, A. Ghielmetti, J. Googins, M. Granoff, J. Hamilton, J. Hanley, D. Heitzler, E. Hertzberg, D. Isaac, B. King, U. Knauss, F. Kudirka, H. Kucharek, J. Lobell, S. Longworth, D. McComas, E. Möbius, A. Moore, T. Moore, R. Nemanich, P. Nolin, M. O’Neal, D. Piazza, S. Pope, P. Rosmarynowski, L. Saul, J. A. Scheer, C. Schlemm, J. Scherrer, C. Tillier, S. Turco, J. Tyler, M. Vosbury, M. Wieser, P. Wurz, and S. Zaffke. The IBEX-Lo Sensor. *Space Science Reviews*, 146:117–147, 2009. doi: 10.1007/s11214-009-9495-8.
- [8] Y. Futaana, M. Wieser, and S. Barabash. Low energy energetic neutral atom imaging in the Jovian system. page 12291, 2013.
- [9] A. Galli, J. Gasser, and P. Wurz. Contamination control and effects of UV exposure for IMAP-Lo, 2020.
- [10] A. Galli, P. Wurz, N. Schwadron, K. Fairchild, D. Heitzler, E. Möbius, H. Kucharek, R. Winslow, M. Bzowski, M. Kubiak, I. Kowalska-Leszczyńska, S. Fuselier, J. M. Sokół,



- P. Swaczyna, and D. McComas. One solar cycle of heliosphere observations with the Interstellar Boundary Explorer: Energetic neutral hydrogen atoms observed with IBEX-Lo from 10 eV to 2 keV. *Astrophysical Journal Supplement Series*, 261(2), 2022. doi: 10.3847/1538-4365/ac69c9.
- [11] J. Gasser, M. Föhn, A. Galli, E. Artegiani, A. Romeo, and P. Wurz. Cadmium telluride as a potential conversion surface. *Journal of Applied Physics*, 129:045303, 2021. doi: 10.1063/5.0033701.
- [12] J. Gasser, A. Galli, and P. Wurz. Absolute beam monitor: A novel laboratory device for neutral beam calibration. *Review of Scientific Instruments*, 93(9):093302, 2022. doi: 10.1063/5.0092065.
- [13] R. Gerber. Molecular scattering from surfaces: Theoretical methods and results. *Chemical Reviews*, 87(1):29–79, 1987. doi: 10.1021/cr00077a003.
- [14] A. Ghielmetti. Improved ion optics for low energy neutral atom imaging with high sensitivity. *Nuclear Instruments and Methods in Physics Research A: Accelerators, Spectrometers, Detectors and Associated Equipment*, 914, 2018. doi: 10.1016/j.nima.2018.06.013.
- [15] M. Gruntman and V. Morozov. H atom detection and energy analysis by use of thin foils and TOF technique. *Journal of Physics E: Scientific Instruments*, 15(12):1356, 1982. doi: 10.1088/0022-3735/15/12/021.
- [16] M. A. Gruntman. Energetic neutral atom imaging of space plasmas. *Review of Scientific Instruments*, 68(10):3617–3656, 1997. doi: 10.1063/1.1148389.
- [17] Z. Insepov, V. Ivanov, S. Jokela, I. Veryovkin, A. Zinovev, and H. Frisch. Comparison of secondary electron emission simulation to experiment. *Nuclear Instruments and Methods in Physics Research A*, 639(1):155–157, 2011. doi: 10.1016/j.nima.2010.10.048. Proceedings of the Seventh International Workshop on Ring Imaging Cherenkov Detectors.
- [18] S. Jans, P. Wurz, R. Schletti, K. Brüning, K. Sekar, W. Heiland, J. Quinn, and R. Leuchtner. Scattering of atoms and molecules off a barium zirconate surface. *Nuclear Instruments and Methods in Physics Research B*, 173:503–515, 2001. doi: 10.1016/S0168-583X(00)00421-3.
- [19] J. Kleimann, K. Dialynas, F. Fraternali, A. Galli, J. Heerikhuisen, V. Izmodenov, M. Kornbleuth, M. Opher, and N. Pogorelov. The structure of the large-scale heliosphere as seen by current models. *Space Science Reviews*, 218(36), 2022. doi: 10.1007/s11214-022-00902-6.
- [20] J. Lienemann, D. Blauth, S. Wethekam, M. Busch, H. Winter, P. Wurz, S. A. Fuselier, and E. Hertzberg. Negative ion formation during scattering of fast ions from diamond-like carbon surfaces. *Nuclear Instruments and Methods in Physics Research B*, 269:915–918, 2011. doi: 10.1016/j.nimb.2010.11.054.

- [21] A. Marti, R. Schletti, P. Wurz, and P. Bochsler. Calibration facility for solar wind plasma instrumentation. *Review of Scientific Instruments*, 72, 2001. doi: 10.1063/1.1340020.
- [22] M. Neuland, A. Riedo, J. Scheer, and P. Wurz. Self-supporting CVD diamond charge state conversion surfaces for high resolution imaging of low-energy neutral atoms in space plasmas. *Applied Surface Science*, 313:293–303, 2014. doi: 10.1016/j.apsusc.2014.05.206.
- [23] M. B. Neuland. Investigation of diamond-like carbon charge state conversion surfaces for low energy neutral atom imaging detectors in space applications, 2011. Master Thesis, University of Bern.
- [24] H. Niehus, W. Heiland, and E. Taglauer. Low-energy ion scattering at surfaces. *Surface Science Reports*, 17(4-5):213–303, 1993. ISSN 0167-5729. doi: 10.1016/0167-5729(93)90024-J.
- [25] M. Opher, A. Loeb, J. Drake, and G. Toth. A small and round heliosphere suggested by magnetohydrodynamic modelling of pick-up ions. *Nature Astronomy*, 4:675–683, 2020. doi: 10.1038/s41550-020-1036-0.
- [26] B. Peko and T. Stephen. Absolute detection efficiencies of low energy H, H<sup>-</sup>, H<sup>+</sup>, H<sub>2</sub><sup>+</sup> and H<sub>3</sub><sup>+</sup> incident on a multichannel plate detector. *Nuclear Instruments and Methods in Physics Research B*, 171(4):597–604, 2000. doi: 10.1016/S0168-583X(00)00306-2.
- [27] A. Pontoni. *Development and simulated observations of the Jovian Neutrals Analyzer*. PhD thesis, Umeå University, Department of Physics, 2022.
- [28] A. Riedo. Optimization of the detection-technique for Energetic Neutral Atoms for the BepiColombo mission, 2010. Master Thesis, University of Bern.
- [29] A. Riedo, P. Wahlström, J. Scheer, P. Wurz, and M. Tulej. Effect of long duration UV irradiation on diamondlike carbon surfaces in the presence of a hydrocarbon gaseous atmosphere. *Journal of Applied Physics*, 108:114915, 2010. doi: 10.1063/1.3517832.
- [30] A. Riedo, M. Ruosch, M. Frenz, J. Scheer, and P. Wurz. On the surface characterization of an Al<sub>2</sub>O<sub>3</sub> charge state conversion surface using ion scattering and atomic force microscope measurements. *Applied Surface Science*, 258:7292–7298, 2012. doi: 10.1016/j.apsusc.2012.03.139.
- [31] Y. Saito, J. Sauvaud, M. Hirahara, S. Barabash, D. Delcourt, T. Takashima, and K. Asamura. Scientific objectives and instrumentation of Mercury Plasma Particle Experiment (MPPE) onboard MMO. *Planetary and Space Science*, 58(1):182–200, 2010. doi: 10.1016/j.pss.2008.06.003. Comprehensive Science Investigations of Mercury: The scientific goals of the joint ESA/JAXA mission BepiColombo.

- [32] J. Scheer, W. Brüning, T. Fröhlich, P. Wurz, and W. Heiland. Scattering of small molecules from a diamond surface. *Nuclear Instruments and Methods in Physics Research B*, 157(1):208–213, 1999. doi: 10.1016/S0168-583X(99)00444-9.
- [33] J. Scheer, P. Wurz, and W. Heiland. Scattering of slow ions from insulator surfaces at the example of molecular oxygen from LiF(1 0 0). *Nuclear Instruments and Methods in Physics Research B*, 212:291–296, 2003. doi: 10.1016/S0168-583X(03)01838-X.
- [34] J. Scheer, M. Wieser, P. Wurz, P. Bochsler, E. Hertzberg, S. Fuselier, F. Köck, R. Nemanich, and M. Schleberger. High negative ion yield from light molecule scattering. *Nuclear Instruments and Methods in Physics Research B*, 230:330–339, 2005. doi: 10.1016/j.nimb.2004.12.063.
- [35] J. Scheer, P. Wahlström, and P. Wurz. Scattering of light molecules from thin Al<sub>2</sub>O<sub>3</sub> films. *Nuclear Instruments and Methods in Physics Research B*, 267:2571–2574, 2009. doi: 10.1016/j.nimb.2009.05.016.
- [36] J. A. Scheer, P. Wahlström, and P. Wurz. Scattering of light molecules from Al<sub>2</sub>O<sub>3</sub> surfaces. *Nuclear Instruments and Methods in Physics Research B*, 256(1):76–80, 2007. doi: 10.1016/j.nimb.2006.11.093.
- [37] P. Sigmund. Theory of sputtering. I. sputtering yield of amorphous and polycrystalline targets. *Physical Review*, 184(2):383–415, 1969. doi: 10.1103/PhysRev.187.768.
- [38] P. Sigmund. Mechanics and theory of physical sputtering by particle impact. *Nuclear Instruments and Methods in Physics Research B*, 27(1):1–20, 1987. doi: 10.1016/0168-583X(87)90004-8.
- [39] T. M. Stephen and B. Peko. Absolute calibration of a multichannel plate detector for low energy O, O<sup>−</sup>, and O<sup>+</sup>. *Review of Scientific Instruments*, 71(3):1355–1359, 2000. doi: 10.1063/1.1150462.
- [40] E. Taglauer. *Surface Characterization by Low-Energy Ion Scattering*, volume SPPHY 22, pages 150–159. Springer Proceedings in Physics, 1987. ISBN 978-3-642-72969-0. doi: 10.1007/978-3-642-72967-6\_14.
- [41] M. Thompson. Atomic collision cascades in solids. *Vacuum*, 66:99–114, 2002.
- [42] N. Utterback and G. Miller. Fast molecular nitrogen beam. *Review of Scientific Instruments*, 32:1101–1106, 1961.
- [43] P. Wahlström. Optimization of the detection-technique for Energetic Neutral Atoms for the IBEX mission, 2007. Master Thesis, University of Bern.
- [44] P. Wahlström, J. Scheer, P. Wurz, E. Hertzberg, and S. A. Fuselier. Calibration of charge state conversion surfaces for neutral particle detectors. *Journal of Applied Physics*, 104(034503), 2008. doi: 10.1063/1.2957064.

- [45] P. Wahlström, J. Scheer, A. Riedo, P. Wurz, and M. Wieser. Test facility to study surface-interaction processes for particle detection in space. *Journal of Spacecraft and Rockets*, 50:402–410, 2013. doi: 10.2514/1.A32134.
- [46] R. Wei. Development of new technologies and practical applications of plasma immersion ion deposition (PIID). *Surf. Coat. Tech.*, 204(18):2869–2874, 2010. doi: 10.1016/j.surfcoat.2010.01.046.
- [47] M. Wieser and P. Wurz. Production of a 10 eV - 1000 eV neutral particle beam using surface neutralization. *Measurement Science and Technology*, 16:2511–2516, 2005. doi: 10.1088/0957-0233/16/12/016.
- [48] M. Wieser, P. Wurz, E. Möbius, S. Fuselier, E. Hertzberg, and D. McComas. The ion-optical prototype of the low energy neutral atom sensor of the Interstellar Boundary Explorer mission (IBEX). *Review of Scientific Instruments*, 78:124502:01–14, 2008. doi: 10.1063/1.2821235.
- [49] H. Winter. Collisions of atoms and ions with surfaces under grazing incidence. *Physics Reports-Review Section of Physics Letters*, 367:387–582, 2002. doi: 10.1016/S0370-1573(02)00010-8.
- [50] M. Wüest, D. S. Evans, and R. von Steiger. *Calibration of Particle Instruments in Space Physics*, volume SR-007. ESA Communications, ISSI Scientific Report, 2007.
- [51] P. Wurz. Detection of energetic neutral particles. *The Outer Heliosphere: Beyond the Planets*, Copernicus Gesellschaft e.V., Katlenburg-Lindau, Germany, pages 251–288, 2000.
- [52] P. Wurz, R. Schletti, and M. Aellig. Hydrogen and oxygen negative ion production by surface ionization using diamond surfaces. *Surface Science*, 373(1):56–66, 1997. doi: 10.1016/S0039-6028(96)01146-6.
- [53] P. Wurz, T. Frölich, K. Brüning, J. Scheer, W. Heiland, E. Hertzberg, and S. Fuselier. Formation of negative ions by scattering from a diamond (111) surface. pages 257–262. Charles University, Prague, MATFYZPRESS, 1998. ISBN 80-85863-29-4.
- [54] P. Wurz, A. Balogh, V. Coffey, B. Dichter, W. Kasprzak, A. Lazarus, W. Lennartsson, and J. McFadden. Calibration techniques. In M. Wüest, D. Evans, and R. von Steiger, editors, *Calibration of Particle Instruments in Space Physics*, volume SR-007, chapter 3, pages 117–276. ESA Communications, ISSI Scientific Report, 2007.

# A. Appendix

---

All science is either physics or stamp collecting.

*attributed to Ernest Rutherford*

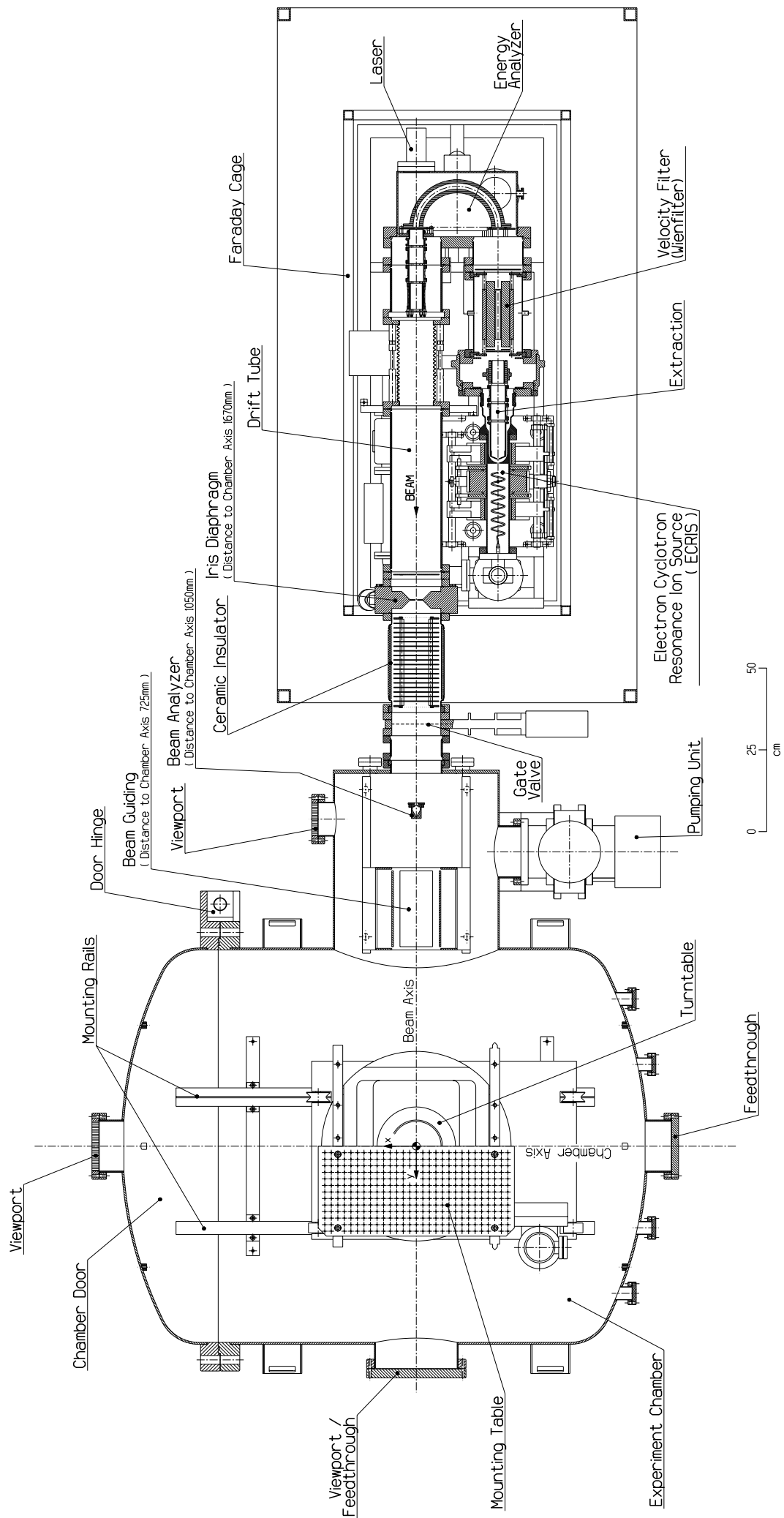
---

## A.1. Test facility drawing

Below you find a top view drawing of the entire MEFISTO test facility (*Courtesy: Space Research division, University of Bern*).

## A.2. Neutralizer Quick Start Guide

A short 'cheatsheet' for the neutralizer installation in the vacuum chamber and for the neutralizer operation in combination with an ion beam from the ECRIS are included on p. 153ff below.



## Neutralizer Installation Cheatsheet:

### Inside the vacuum chamber:

- Put the neutralizer on the table in the clean-bench, ready for installation
- Vent and open the vacuum chamber
- Move the hexapod close to the ion beam shroud (coordinates  $[X,Y,Z] = [0,0,50]$  )
- Put the neutralizer on the hexapod table. Make sure the pair of screws at the top plate of the YZ-stage are on the left side and the single screw (front) on the right side.
- Lift the two distance disks on the YZ-stage top, lift the neutralizer and slide the two screws into the corresponding notches in the metal strip.
- Then tighten the two screws (yet loosely), and insert the third screw in the protruding metal holder
- Crucial: Align the neutralizer front exactly parallel to the hexapod edge (Y-coordinate), and make sure the neutralizer sits exactly horizontal ! Then tighten all three mounting screws tightly.
- Attach the grounding metal stripe on one corner of the hexapod (screw, cable lug)
- The HV banana cables 1...6 should already be connected correctly at the vacuum feedthrough inner side: otherwise, do and check that.
- Connect the HV banana pins 1...6 at the hexapod front side (make sure the grounding stripe does not touch a pin!)
- Insert the five thermal heater and sensor pins at the hexapod.
- Connect the four SMA cables A...D of the neutralizer entrance plates to the neutralizer case. The cables should also be connected in the SMA feedthrough (vacuum side).
- Connect the pico-amperemeter plug to the pA-Meter.
- Make sure the pA-Meter power pin (SMA) is connected to the pA-Meter box and at the feedthrough.
- Check the coordinate limitation of the hexapod (negative X coords are crucial)

### Laboratory / air side:

- Make sure the SMA cables A-D from the BNC switch are connected to the correct feedthrough, and that the BNC switch output leads into the Keithley Amperemeter.
- Make sure the LEMO HV cables are connected correctly from the neutralizer HVPS to the rear LEMO flange, as follows:
 

1. ESA +	4. Float HV
2. Float HV	5. Deflect +
3. ESA –	6. Deflect –
- Make sure a voltmeter is plugged in to the “float monitor” output at the power supply
- For proper  $U_{\text{ESA}}$  measurement, connect a voltmeter between the two HV cables (ESA+) and (ESA-) to directly measure the output potential difference  $\Delta\text{ESA} = (\text{ESA+}) - (\text{ESA-})$ .  
**CAUTION:** this voltmeter will be floating at  $U_{\text{float}}$  **High Voltage !!**
- The neutralizer pico-amperemeter cube must be connected as follows:
  - Power plug (Netzstecker)
  - An SMA cable to the feedthrough (for LV DC power)
  - D-Sub connector to the feedthrough underneath the chamber for data transmission
  - D-Sub connector to the PC for communication and data readout
- An LVPS is used for the surface heater. Connect it at the respective feedthrough pins.

## Neutralizer Operation Cheatsheet

### Initialization:

- Switch ON the neutralizer power supply. Make sure all HV knobs are turned down before then switching ON the HV.
- Initial HV setting, depending on ENA energy  $E_1 = e U_1$  first needed:
  - Deflection: slightly below 200 V
  - ESA voltage: switch to high range, then set approx.  $U_{ESA} = U_1/10$ .
  - Float: set approx.  $U_{float} = 3 \text{ kV} - U_1$ .

### Positioning:

- Produce a stable and optimized ion beam in the Mefisto ECRIS (gate slider open). Then move the beam-scanner out of the beam line ("park")
- Check the beam-induced current on the neutralizer aperture plates A-D via the Keithley nano-ampere-meter by mutually switching in and out each current line.
- Use the LabView routine "yz-stage.vi" (@ COM port 10) to move the neutralizer Y (horizontal) and Z (vertical) position
- Iteratively balance the current on plates A-C (up/down) and B-D (left/right), respectively:
  - $I(A) > I(C)$ : move up  $\rightarrow (+)$  vertical
  - $I(B) > I(D)$ : move right (seen in beam direction)  $\rightarrow (-)$  horizontal
- Adjust the hexapod coordinates (with DUT and test setup) accordingly

### Energy adjustment:

- For beam energies  $E > 100 \text{ eV}$ :
  - Adjust  $U_{float}$  at the "float monitor" (1:10'000) display [mV] to the nominal value
  - Set  $U_{ESA}$  to the corresponding voltage (high range)
  - Check at the pA-meter (at *high* range) that it is approx. at the optimum value. (evt.) adjust the  $U_{float}$  slightly.

Remark: if the  $I_{ncs}$  maximum is at  $U_{float}$  strongly deviating from the nominal value, this is a hint that the neutralizer is possibly not well aligned with the beam.
- For beam energies  $E < 100 \text{ eV}$ :
  - Set  $U_{float}$  and  $U_{ESA}$  as before, but with the low ESA voltage range
  - Maximize the Neutralizer surface current at the pA-meter (at *low* range if  $I_{ncs} < 0.5 \text{ nA}$ ) by varying  $U_{float}$  as before. Make sure to properly zero-check the pA-meter.
  - At very low energies, if no satisfactory stable beam (current) can be found, try to reach by "handling down" the beam energy from a configuration  $E = 100 \text{ V}$ : iteratively increase  $U_{float}$  a bit and reduce  $U_{ESA}$  a bit.
  - At  $U_{ESA} < 3.0 \text{ V}$  (corresp.  $E = 30 \text{ eV}$ ), an additional resistor may need to be in place across the external ESA voltmeter to pull the  $\Delta U_{ESA}$  further down.

**CAUTION:** turn down all neutralizer High Voltages before (un-)installation !!



## **Declaration of consent**

on the basis of Article 18 of the PromR Phil.-nat. 19

Name/First Name: Jonathan Gasser

Registration Number: 11-101-748

Study program: Physics

Bachelor ☐ Master ☐ Dissertation ☒

Title of the thesis: Towards better Calibration of Space Instrumentation  
for Measurements of Energetic Neutral Atoms

Supervisor: Prof. Dr. Peter Wurz

I declare herewith that this thesis is my own work and that I have not used any sources other than those stated. I have indicated the adoption of quotations as well as thoughts taken from other authors as such in the thesis. I am aware that the Senate pursuant to Article 36 paragraph 1 litera r of the University Act of September 5th, 1996 and Article 69 of the University Statute of June 7th, 2011 is authorized to revoke the doctoral degree awarded on the basis of this thesis.

For the purposes of evaluation and verification of compliance with the declaration of originality and the regulations governing plagiarism, I hereby grant the University of Bern the right to process my personal data and to perform the acts of use this requires, in particular, to reproduce the written thesis and to store it permanently in a database, and to use said database, or to make said database available, to enable comparison with theses submitted by others.

Bern, 20.12.2022

Place/Date

Signatu

